



**HAL**  
open science

# Seasonal deformation of the Earth induced by variations in hydrology : impact on seismicity

Kristel Chanard

## ► To cite this version:

Kristel Chanard. Seasonal deformation of the Earth induced by variations in hydrology : impact on seismicity. Geophysics [physics.geo-ph]. Ecole normale supérieure - ENS PARIS, 2015. English. NNT : 2015ENSU0031 . tel-01598509

**HAL Id: tel-01598509**

**<https://theses.hal.science/tel-01598509>**

Submitted on 29 Sep 2017

**HAL** is a multi-disciplinary open access archive for the deposit and dissemination of scientific research documents, whether they are published or not. The documents may come from teaching and research institutions in France or abroad, or from public or private research centers.

L'archive ouverte pluridisciplinaire **HAL**, est destinée au dépôt et à la diffusion de documents scientifiques de niveau recherche, publiés ou non, émanant des établissements d'enseignement et de recherche français ou étrangers, des laboratoires publics ou privés.



Laboratoire de Géologie, École Normale Supérieure  
École Doctorale des Sciences de la Terre

Thèse présentée en vue de l'obtention du titre de  
DOCTEUR DE L'ÉCOLE NORMALE SUPÉRIEURE

Spécialité: Géophysique

par

KRISTEL CHANARD

---

# Déformation saisonnière de la Terre sous l'effet des variations hydrologiques, Impact sur la sismicité

---

Soutenance prévue le 21 Octobre 2015, devant le jury composé de:

Tonie Van Dam	Rapporteur	Université du Luxembourg
Christophe Voisin	Rapporteur	ISterre, Grenoble
Marianne Greff-Lefftz	Examinatrice	IPG, Paris
Laurent Bollinger	Examineur	CEA, Bruyères-le-Châtel
Alexandre Schubnel	Directeur de Thèse	École Normale Supérieure, Paris
Eric Calais	co-Directeur de Thèse	École Normale Supérieure, Paris
Jean-Philippe Avouac	Invité	Caltech, Pasadena
Luce Fleitout	Invitée	École Normale Supérieure, Paris



# CONTENTS

<b>Abstracts (Français &amp; English)</b>	<b>vii</b>
<b>Remerciements</b>	<b>xi</b>
<b>Résumé étendu en français</b>	<b>1</b>
<b>Introduction</b>	<b>27</b>
<b>1 Seasonal forcing of the Earth: State of the art</b>	<b>31</b>
1.1 Measuring seasonal deformation and mass variations . . . . .	31
1.1.1 Quantifying deformation with Global Positioning System . . . . .	31
1.1.2 Estimation of surface mass redistributions from satellite gravity measurements . . . . .	33
1.2 Modeling seasonal deformation induced by surface hydrology . . . . .	34
1.2.1 The trampoline effect . . . . .	34
1.2.2 Regional models . . . . .	35
1.2.3 Global models . . . . .	40
1.3 Periodic variations of seismicity . . . . .	47
<b>2 Elastic seasonal deformation in the Himalaya</b>	<b>53</b>
2.1 Introduction . . . . .	55
2.2 Presentation of the GPS and GRACE data used in this study . . . . .	56
2.2.1 The GPS dataset . . . . .	56
2.2.2 Continental regional water mass variations derived from GRACE Level-2 solutions . . . . .	57
2.3 Modeling of seasonal ground deformation induced by surface load variations . . . . .	62
2.3.1 Modelling of seasonal ground deformation for a homogeneous elastic half-space . . . . .	65
	iii

## Contents

---

2.3.2	Green's functions for a spherical, layered elastic Earth model . . . . .	67
2.3.3	Comparison of Green's functions for the half-space and spherical layered elastic Earth models . . . . .	68
2.3.4	Modeling of seasonal ground deformation for a spherical, layered Earth model . . . . .	72
2.4	Constraints on the crust depth-dependent elastic structure using geodetic seasonal surface displacements . . . . .	76
2.5	Implications and Conclusions . . . . .	78
	Supplements . . . . .	82
<b>3</b>	<b>Global seasonal deformation</b>	<b>85</b>
3.1	Introduction . . . . .	85
3.2	Estimating global variations of surface hydrology and surface ground displacement	88
3.2.1	Continental water mass variations derived from GRACE Level-2 solutions	88
3.2.2	The GPS dataset . . . . .	93
3.3	Global elastic modeling of seasonal ground deformation induced by surface load variations . . . . .	98
3.3.1	Description of the model . . . . .	98
3.3.2	Model for Earth . . . . .	99
3.3.3	Data-model comparison . . . . .	101
3.4	Potential contributors to missing seasonal signals . . . . .	126
3.4.1	Differences in GPS processing software . . . . .	126
3.4.2	Phase center modeling . . . . .	128
3.4.3	Environmental factors . . . . .	131
3.4.4	GPS draconitic year . . . . .	132
3.4.5	Bedrock thermal expansion . . . . .	136
3.4.6	Differences in GRACE processing . . . . .	137
3.4.7	Degree-one deformation and reference frame issue . . . . .	139
3.5	Seasonal variations and implications for the Earth mechanical properties . . .	158
3.5.1	Influence of shallow elastic properties . . . . .	158
3.5.2	Influence of low viscosity in the asthenosphere . . . . .	159

3.5.3 Mantle phase transitions . . . . .	176
3.6 Implications and Conclusions . . . . .	189
Supplements . . . . .	192
<b>4 Periodic stress perturbations and seismicity</b>	<b>207</b>
4.1 Introduction . . . . .	207
4.2 Seasonal stress and seismicity . . . . .	210
4.2.1 Global stress and strain induced by seasonal hydrology . . . . .	210
4.2.2 Seismicity in Nepal & seasonal Coulomb stress variations . . . . .	213
4.3 Dynamic acoustic emission triggering by small periodic pore pressure variations during brittle creep experiments . . . . .	217
4.3.1 Brittle creep deformation . . . . .	218
4.3.2 Experimental setup and sample preparation . . . . .	219
4.3.3 Experimental Results . . . . .	223
4.4 Conclusions . . . . .	233
<b>Conclusions</b>	<b>235</b>
<b>A GRACE seasonal amplitude</b>	<b>239</b>
<b>B Code associated with Chapter 2</b>	<b>245</b>
B.1 Contents . . . . .	245
B.2 Set up & Computation . . . . .	246
B.3 Plotting tools . . . . .	247
<b>Bibliography</b>	<b>284</b>



## RÉSUMÉ

Cette thèse a pour objectif de modéliser les déformations saisonnières de la Terre associées aux redistributions de masses d'eau de l'hydrosphère. Pour cela, nous tirons profit de la mesure des déplacements saisonniers du sol par Global Positioning System (GPS) et de l'estimation des variations spatio-temporelles de l'hydrosphère déduite du champs de gravité terrestre mesuré par la mission Gravity and Recovery Climate Experiment (GRACE). Ces données ouvrent la voie à des modèles précis de la déformation saisonnière, discutés dans le *Chapitre 1*, qui auront des implications importantes pour la définition des référentiels terrestres, l'identification d'événements tectoniques de glissement de période comparable ou encore pour la compréhension du lien entre déformation et sismicité saisonnière. Dans le *Chapitre 2*, nous montrons que les déformations saisonnières mesurées en Himalaya sont expliquées par la réponse de la Terre à la charge saisonnière de GRACE qui produit des déplacements de surface cohérents au premier ordre avec les observations horizontales et verticales simultanément à condition d'utiliser un modèle de Terre réaliste, sphérique et stratifié. Nous étendons ensuite le modèle à l'échelle globale dans le *Chapitre 3*, et comparons les déplacements induits par la charge saisonnière à 195 stations GPS, en tenant compte des contributions de degré-1 dans le signal GRACE (Swenson et al., 2008). Alors que la composante verticale est raisonnablement prédite, les composantes horizontales sont systématiquement sous-estimées et leur phase est mal reproduite. Nous montrons que ce désaccord entre modèle et observations horizontales à l'échelle mondiale peut être associé au premier ordre à une contribution de degré-1 sous-estimée, et non à la grande résolution spatiale de GRACE. Nous proposons de l'estimer à posteriori grâce à une transformation d'Helmert, représentant le mouvement du géocentre ainsi qu'une partie de la déformation de degré-1. La corrélation entre modèle et données horizontales est nettement améliorée, sans que les prédictions verticales soient affectées. Au second ordre, nous montrons que les variations de volume dans le manteau terrestre liées aux changements de phase des minéraux qui le composent peuvent jouer un rôle dans la déformation saisonnière. Enfin, nous montrons qu'il est possible d'utiliser la déformation saisonnière pour déterminer une borne inférieure de la viscosité transitoire de l'asthénosphère, paramètre clé des modèles de déformation postsimique. Afin de tester l'hypothèse d'un impact des charges saisonnières sur la sismicité, nous examinons les variations de contrainte liées aux chargements saisonniers de surface. Nous menons également des expériences de déformation triaxiale sur des grès de Fontainebleau, saturés en eau soumis à des paliers de contrainte simulant un chargement tectonique, ainsi qu'à des oscillations sinusoïdales de la pression de pore simulant les marées ou l'hydrologie continentale. Nos observations expérimentales, détaillées dans le *Chapitre 4* suggèrent que les chargements périodiques de faible amplitude peuvent jouer un rôle important dans la longue phase de nucléation des séismes.

Mots clefs: géodésie, GPS, hydrologie, GRACE, déformation saisonnière, sismicité périodique.



## ABSTRACT

In this thesis, we aim at modeling accurately seasonal deformation of the Earth induced by redistribution of hydrosphere masses. We take advantage of seasonal ground displacements measured by continuous stations of the Global Positioning System (cGPS) and the estimate of the spatio-temporal evolution of surface hydrology derived from the Gravity and Recovery Climate Experiment (GRACE) measurements. Precise geophysical models of the seasonal deformation, discussed in *Chapter 1*, of the Earth have far-reaching implications in defining international terrestrial reference frame, detecting potential transient deformation with comparable period or even understanding the link between induced stress perturbations and seasonal seismicity. In *Chapter 2*, we show that seasonal ground displacements recorded by cGPS stations in the Himalaya are fairly well explained by the Earth's response to seasonal hydrology derived from GRACE, which induces coherent surface displacements, in first order approximation, with horizontal and vertical observations simultaneously, provided that a realistic elastic, spherical and layered model for Earth is used. We extend the model to a global scale in *Chapter 3*, and compare displacements induced by the seasonal load at 195 cGPS stations globally distributed. We account for the degree-1 contribution in GRACE using results from [Swenson et al. \(2008\)](#). We find that, while the vertical displacements are well predicted by the model, the horizontal components are systematically underpredicted and out-of-phase with the observations. We show a significant improvement when we do not apply a priori degree-1 coefficients but estimate and apply a posteriori a Helmert transform to the horizontal components. The fit in phase and amplitude of the seasonal deformation model to the horizontal components is improved and does not affect the fit to the vertical measurements. We conclude that horizontal misfits result mostly from degree-one deformation plus reference frame differences between model and observations, and not from the limited spatial resolution of GRACE. However, the amplitude of global seasonal horizontal displacement remains slightly underpredicted. We show that mantle volume variations due to mineral phase transitions may play a role in the seasonal deformation and, as a by-product, use this seasonal deformation to provide a lower bound of the transient asthenospheric viscosity. Finally, in order to test the impact of seasonal forcing on seismicity, we estimate the amplitude of periodic stress perturbations induced by seasonal loading. To further investigate the question, we perform a set of triaxial deformation experiments on water-saturated Fontainebleau sandstones. Rock samples are loaded by the combined action of steps of constant stress, intended to simulate tectonic loading and small sinusoidal pore pressure variations, analogous to tides or seasonal loading. Our experimental results suggest that the correlation of small stress perturbations and acoustic emissions depends primarily on the state stress of the rock and that emissions occur more likely when cracks are unclamped. In other words, our observations suggest that tidal triggering might occur favorably during the long nucleation phase of earthquake.

Key words: geodesy, GPS, hydrology, GRACE, seasonal deformation, periodic seismicity.



## REMERCIEMENTS

Ce manuscrit est l'aboutissement d'une thèse. Cependant, tout a commencé il y a six ans, lorsque j'ai eu la chance de rencontrer Jean-Philippe Avouac, et de commencer à réfléchir avec lui aux interactions entre la Terre solide et les variations saisonnières des masses d'eau à sa surface. C'est donc naturellement que j'aimerais le remercier en premier lieu pour sa disponibilité, son enthousiasme scientifique contagieux, son extrême gentillesse à mon égard, et bien-sûr son soutien professionnel et personnel sans faille. L'aventure ne s'arrête pas là, j'en suis convaincue. Je tiens également à remercier vivement Alexandre Schubnel, qui même si, avec modestie, vous dira ne pas avoir fait grand chose, m'a convaincue de me lancer dans une thèse après une belle expérience de recherche avec lui en master, et a été l'inspirateur et le pilier du projet expérimental qui m'a permis de la terminer. Ses idées incessantes, son extrême enthousiasme, sa rigueur scientifique et sa gentillesse font de lui un encadrant exceptionnel. Jean-Philippe et Alex, merci d'avoir cru pour moi en cette thèse depuis le départ. J'ai également eu la chance de travailler avec Luce Fleitout et je lui suis extrêmement reconnaissante d'avoir accepté de m'aider et me guider avec bienveillance sur le projet principal de ma thèse. J'ai beaucoup appris et compris en travaillant avec elle, et je pense qu'il n'y avait pas meilleure collaboration pour mener à bien ce projet. Enfin, merci à Eric Calais d'avoir rattrapé ma thèse en chemin et de m'avoir conseillée et encadrée pendant ces deux années à l'ENS. J'ai eu la chance d'avoir un sur-encadrement de luxe pendant ma thèse, et je vous remercie tous les quatre pour votre disponibilité et votre soutien moral au cours de ces dernières années.

Au moment où j'écris ces lignes, je ne peux que remercier le jury d'avoir accepté d'y participer. Mais, d'avance, je sais que vos commentaires m'aideront à améliorer mon travail et que vos questions soulèveront des points importants auxquels il me faudra réfléchir et travailler.

Je souhaiterais aussi remercier quelques personnes avec qui j'ai appris beaucoup scientifiquement en discutant et en interagissant. Guillaume Ramillien, qui participe à ce projet depuis le début et qui a toujours répondu à mes nombreuses questions avec une grande gentillesse et humilité. Sylvain Barbot, avec qui j'ai commencé à compliquer les choses en passant le cap du modèle viscoélastique. Et bien-sûr, Raúl Madariaga, Raphael Grandin et Laurent Bollinger qui, en faisant partie de mon comité de thèse ont sû me conseiller dans l'avancement de mes travaux de recherche. J'ai aussi beaucoup appris sur le terrain grâce à John Galetzka et aux collègues du National Seismological Center au Népal.

Bien-sûr, une thèse c'est aussi de nombreuses heures passées au laboratoire, et des rencontres qui comptent et qui marquent. Interagir avec les chercheurs et personnels à l'ENS a été un vrai bonheur. J'ai reçu conseils et aide de bien des gens depuis que j'ai mis un pied à l'ENS en L3, que je ne me risquerais pas à citer ici de peur d'en oublier!

## Remerciements

---

La bonne ambiance au cours de ces années de thèse a été un élément fondamental pour mener à bien mon travail et un soutien important pendant des périodes difficiles. Je tiens donc à remercier les gens qui m'ont entourée, à l'ENS comme à Caltech, pendant cette aventure: Audrey, Emilie, Jan, Damian, Amaya, Olga, Thomas F, Rémi, Gianina, Céline, Alexis, Fred, Aurélien B., Steve, Stephen, Frank, Erika. Une thèse c'est des amitiés qui naissent, et j'ai eu la chance de rencontrer des personnes que j'estime beaucoup: Aurélien (dit "gnogno"), Jean-Baptiste, Ben, Tim, Hélène, François (dit "traquenard"), Luca, et Heather. C'est aussi et surtout des amitiés qui se consolident. Et là, je me vois forcée de commencer par dire un grand merci à Marianne (dit "meuf") qui a été un soutien constant pendant ma thèse, et qui a toujours trouvé les mots (ou les vidéos) pour me faire rire quand j'en avais besoin ou me secouer quand il le fallait. Et tout naturellement, un grand merci à Jean-Arthur (dit "roux"), Seb, Nico, Adri, Pierre, Cédric, Célestine, Romain, Thibaut, Meriem et Quentin sur qui j'ai pu compter et avec qui j'ai continué à passer de très bon moments.

Pour finir, je remercie ma famille et particulièrement mon père, ma mère, ma soeur, mon frère et sa famille, pour m'avoir toujours encouragée et soutenue, et m'avoir changé les idées dans cette folle aventure.

# RÉSUMÉ ÉTENDU EN FRANÇAIS

## Introduction

La déformation de la Terre sous l'effet de variations de charges à sa surface reflète la réponse des matériaux la composant ainsi que la nature de la charge (distribution spatiale, masse, fréquence de chargement). Mesurer et comprendre la réponse spatio-temporelle de la Terre à des épisodes de charge et de décharge en surface ou en profondeur permet donc de contraindre sa rhéologie, paramètre clé de la compréhension de la physique de la Terre.

La Terre est soumise à un large spectre de chargements à différentes échelles de temps et d'espace auxquels elle répond différemment selon l'échelle de temps. Chacun de ces modes de chargement apporte une information différente sur la rhéologie de la Terre. Il est par exemple commun de considérer que, pour des périodes allant de la seconde à l'année, elle réagit comme un solide élastique. Cette élasticité se manifeste par exemple par les déformations de la surface terrestre engendrées par le passage des ondes sismiques et les phénomènes de marées. Pour des périodes plus longues, il est admis que la Terre se comporte comme un solide viscoélastique. On observe par exemple encore aujourd'hui un soulèvement du sol en Scandinavie et en Amérique du Nord traduisant la relaxation de la Terre à la décharge rapide de sa surface dû à la dernière déglaciation, il y a environ 10 000 ans.

Une question importante est de savoir à partir de quelle période de chargement la réponse de la Terre n'est plus instantanée mais en déphasage avec la charge, et avec une amplitude différente de celle prédite par un modèle purement élastique. A l'échelle de l'année par exemple, la Terre se déforme sous l'effet des variations saisonnières de l'hydrosphère (hydrologie continentale, marées non-tidales et masses atmosphériques), et son mode de déformation est considéré comme purement élastique. Nous disposons à présent d'une mesure précise

de la déformation saisonnière du sol ainsi que d'une estimation fiable des variations spatio-temporelles de l'hydrosphère déduite des variations du champs de gravité terrestre obtenu par satellite. Ces données ouvrent la voie vers des modèles précis de la déformation saisonnière de la Terre, trop souvent estimée empiriquement. En plus d'apporter des informations sur la structure interne de la Terre et ses modes de déformation, complémentaires à celles déduites des observations sismiques ou des données liées au rebond post-glaciaire, ces modèles précis ont une importance pour la définition des référentiels terrestres, l'estimation des vitesses de déformation séculaire ainsi que pour la détection potentielle d'évènements de glissement transitoires.

Le *Chapitre 1* de cette thèse propose une introduction générale à la modélisation de la déformation et à la sismicité saisonnières et présente les enjeux qui ont motivés cette thèse au départ.

Le premier enjeu de cette thèse, qui fait l'objet du *Chapitre 2*, est de **modéliser la réponse élastique de la Terre aux cycles hydrologiques saisonniers en Himalaya**, zone où les oscillations annuelles des déplacements du sol observés sont de forte amplitude. Au premier ordre, les déplacements en surface prédits par un modèle de Terre élastique réaliste, soumis aux variations spatio-temporelles de l'hydrologie de surface sont en bon accord avec les observations mesurées par le positionnement des stations du "Global Positioning System" (GPS).

Dans le *Chapitre 3*, nous étendons les prédictions de ce modèle élastique à des stations réparties sur le globe et discutons sa validité à l'échelle mondiale. Un désaccord entre modèle et données à l'échelle mondiale, en particulier pour les composantes horizontales suggère l'existence d'une source d'erreur systématique, qu'elle provienne du traitement des données géodésiques ou d'un phénomène géophysique mal modélisé. **Le deuxième enjeu de cette thèse est donc de mieux comprendre la déformation saisonnière globale, en particulier les déplacements horizontaux.** Nous montrons que la déformation et le mouvement du géocentre associés à des charges de degré harmonique un, non mesurées par GRACE, doivent être pris en compte avec précaution pour modéliser précisément la déformation saisonnière, en particulier ses composantes horizontales, et améliorons nettement l'accord entre modèle et observations. Cependant, une différence d'amplitude résiduelle nous amène aussi à question-

ner la validité de l'utilisation d'un modèle purement élastique, dérivé de données sismiques, à l'échelle de l'année. Nous montrons que, en prenant en compte les variations de volume dans le manteau terrestre liées aux changements de phases de certains minéraux, nous améliorons encore le modèle de déformation saisonnière de la Terre. Nous excluons les faibles viscosités asthénosphériques ainsi que l'inexactitude des paramètres élastiques comme candidat potentiel au signal globalement manquant. Ces résultats ont potentiellement des conséquences intéressantes pour la compréhension du comportement de la Terre soumise à un chargement périodique et l'amélioration de l'analyse des données géodésiques souvent bruitées par les signaux saisonniers.

Une fois la réponse de la Terre aux variations de chargements de surface correctement modélisée, la question de l'importance des perturbations de contraintes périodiques engendrées par ces déformations sur les failles et de leur rôle dans le cycle sismique se pose. Des variations saisonnières de micro-sismicité ont en effet été détectées dans plusieurs régions et reliées à un forçage hydrologique saisonnier. Cependant, les mécanismes de déformation en profondeur associés et leur influence sur la sismicité restent à éclaircir. Dans le *Chapitre 4*, nous testerons expérimentalement l'influence de petites variations cycliques de la pression de pore sur les émissions acoustiques produites par un échantillon de roche sous pression afin de **mieux comprendre les mécanismes de la sismicité périodique**. Bien que préliminaires, nos résultats suggèrent l'importance de l'état de contrainte d'une roche sur l'influence ou non de petites perturbations périodique des contraintes sur la micro-sismicité.

### **Déformation élastique de la Terre sous l'effet des variations saisonnières de l'hydrologie en Himalaya**

Avec le développement de satellites artificiels depuis les années 1960, les constellations de satellites de positionnement ("Global Navigation Satellite System") ont remplacé peu à peu les systèmes de localisation au sol. Le plus connu de ces systèmes, le "Global Positioning System" (GPS), développé aux États-Unis à des fins militaires à partir des années 1970 et est

## Résumé étendu en français

---

opérationnel depuis le début des années 1990, suivi par d'autres systèmes comme GLONASS (Russie), Galileo (Europe) ou encore BeiDou (Chine).

Tous ces systèmes de positionnement par satellites utilisent le même principe de fonctionnement qui s'appuie sur les méthodes de triangulation classique. Chaque satellite émet en permanence un signal transportant une information sur sa position et l'heure précise de l'émission (déterminée par une horloge atomique embarquée dans le satellite). Des antennes récepteurs, ancrées dans le sol, mesurent les instants de réception des signaux provenant des satellites dans son champ de visibilité. La détermination de la position du récepteur consiste en la résolution d'une équation à quatre inconnues : la position géographique du récepteur (latitude, longitude), son altitude et le biais de l'horloge de mesure du récepteur. Il faut donc quatre satellites "visibles" pour déterminer une position. Pour que le récepteur fonctionne sur toute la surface du globe, il faut qu'il puisse voir en permanence au minimum 4 satellites et que la répartition géométrique des satellites positionnés au-dessus de lui soit la plus uniforme possible. Une constellation de 24 satellites à une distance d'environ 20 000 km de la surface terrestre est le minimum requis pour le bon fonctionnement du GPS par exemple. Afin d'améliorer la précision de la position calculée par le GPS, les scientifiques ont ensuite développé de nombreuses méthodes d'analyse et de corrections des signaux GPS qui permettent aujourd'hui un positionnement avec une précision de l'ordre du millimètre.

Les campagnes de mesure géodésiques menées au Népal ont commencé au début des années 1990. Depuis, plusieurs réseaux permanents ont vu le jour et le réseau népalais de stations continues du "Global Positioning System" (cGPS) se compose de trois stations installées en 1997 par une collaboration entre le département des Mines et de Géologie local (DMG, Nepal) et le Laboratoire de Détection et Géophysique (CEA/LDG, France), ainsi que de 26 stations déployées entre 2003 et 2014 au travers d'une autre collaboration avec le California Institute of Technology (États-Unis). Ces réseaux sont coûteux et demandent un effort d'installation, d'amélioration et de maintenance régulier auquel j'ai eu la chance de participer pendant 8 mois.

Une station GPS permanente typique au Népal se compose d'une antenne "Choke ring",

protégée par un dôme et montée sur un trépied en acier inoxydable solidement ancré dans le sol. L'antenne est reliée à un récepteur GPS enregistrant les signaux provenant des satellites visibles par l'antenne, alimentée par un système de batteries et panneaux solaires (Figure 1.1). Ces stations, en plus d'autres réseaux proches (Inde, Tibet), ont d'abord permis de converger

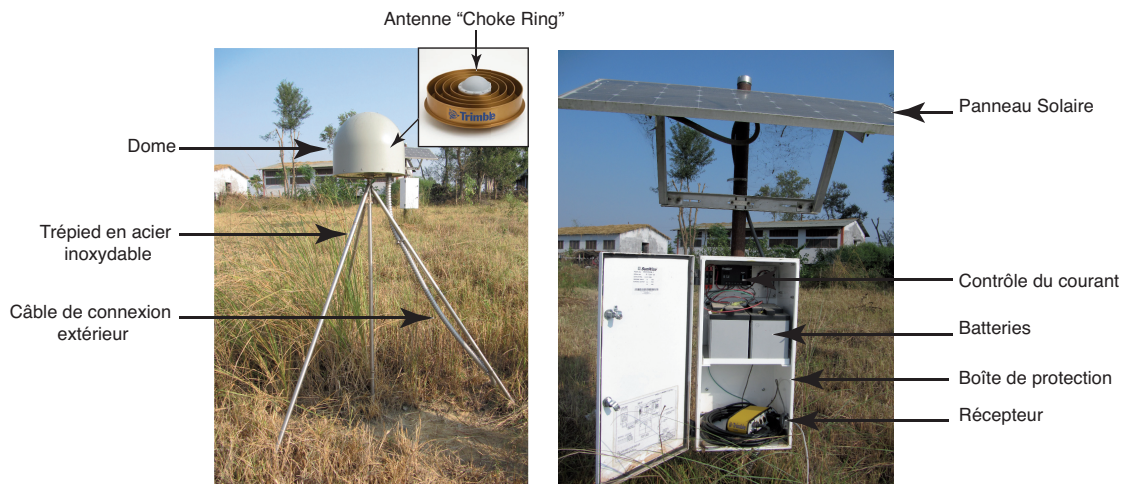


Figure 1 – Photographies de la station permanente NPJG située dans une coopérative agricole à Nepalganj, au Sud-Oest du Népal

vers une estimations de la vitesse de collision Inde-Eurasie autour de 20 mm/an, ainsi que le degré de couplage (ou potentiel sismogénique) des failles de la région et en particulier du chevauchement frontal himalayen (Bettinelli et al., 2006, Ader et al., 2012a).

Grâce à la haute précision des positions calculées, les données GPS exhibent également des phénomènes de plus petite amplitude, en particulier saisonniers (Dong et al., 2002). La Figure 1.2 montre à gauche les déplacements brutes de la station LHAZ située au Tibet, avec une claire tendance "long" terme de convergence entre l'Inde et l'Eurasie, et un léger soulèvement vertical. A droite, les déplacements saisonniers sont mis en avant une fois les tendances long terme retirées. Ces déplacements saisonniers sont présents partout sur Terre, avec une amplitude plus ou moins importante, à la fois sur les composantes horizontales et verticale. Il a été établi que ces variations saisonnières ne sont pas un artefact de traitement mais ont bien une explication géophysique. En effet, la Terre se déforme à l'échelle de l'année sous l'effet des variations saisonnières importantes de l'hydrologie continentale, des masses atmosphériques et océaniques (Van Dam et al., 2001).

LHAZ

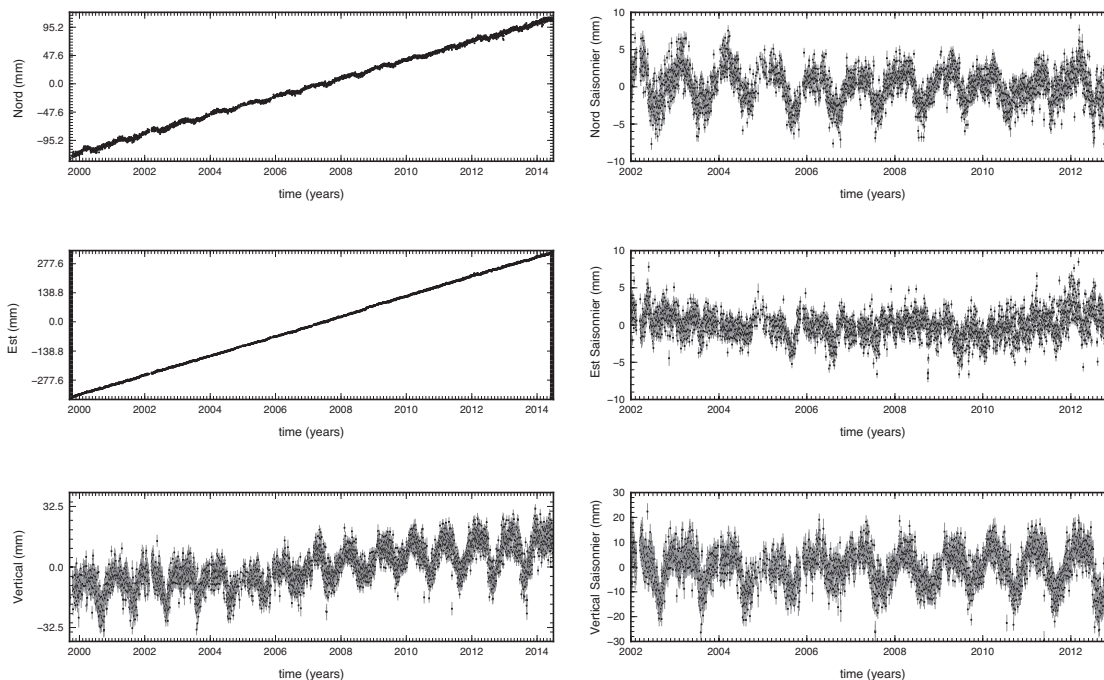


Figure 2 – Séries temporelles de déplacement séculaires (gauche) et saisonniers (droite) avec les barres d’erreurs associées aux incertitudes 1- $\sigma$ , enregistrés à la station LHAZ, Tibet.

Un modèle simple pour expliquer ces déplacements saisonniers en Asie est la réponse de la Terre au cycle de la mousson. En été, le poids de l’eau, de la végétation et des sédiments déplacés dans le bassin du Gange exercent une pression non-négligeable qui attire vers le nord et vers le bas les stations GPS situées en Inde alors que les stations du Népal et du Tibet sont elles attirées vers le sud et vers le bas. En hiver, le rebond élastique du sol lié au déchargement du bassin produit des déplacements opposés aux stations (Figure 3). L’avancée récente de la géodésie spatiale à également vu naître des projets de mesure des variations du champ de gravité terrestre permettant d’accéder aux redistributions des masses à la surface du globe et de tester cette hypothèse.

La mission qui nous intéresse ici, communément appelée GRACE, acronyme de Gravity Recovery and Climate Experiment, s’inscrit dans le cadre d’un projet international coordonné par les agences spatiales américaines et allemande, NASA et DLR respectivement (Tapley et al., 2005). Le but de cette mission est de cartier les variations spatio-temporelles du champ de gravité de la Terre avec une précision d’un 1 cm de hauteur du géoïde pour 275 km. La mission

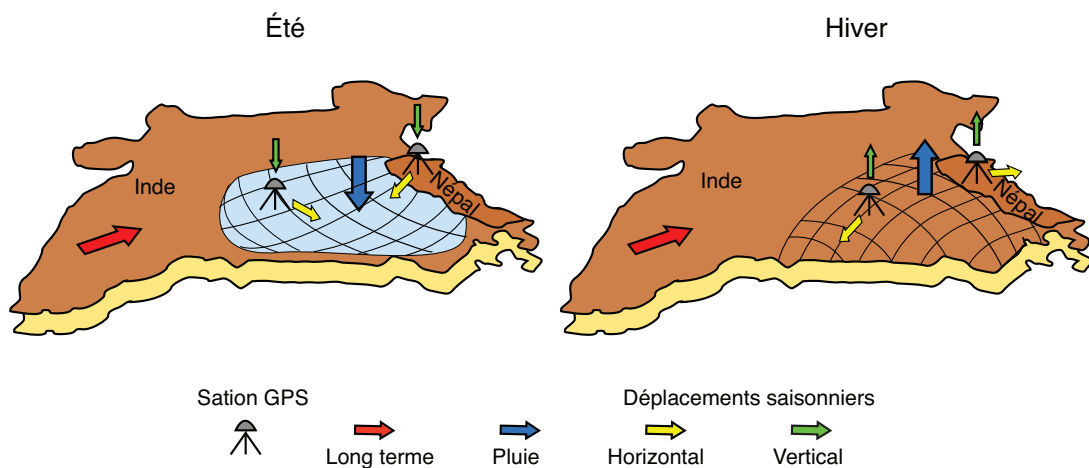


Figure 3 – Schéma de principe des déplacements saisonniers observés aux stations GPS en Inde et au Népal induits par les variations de l'hydrologie de surface (cycle de la mousson).

GRACE, lancée en mars 2002 et initialement prévue pour 5 ans, est toujours en marche et a jusqu'ici permis d'obtenir 12 ans de mesure des variations du champ de gravité. Le principe est simple: deux satellites en tandem volent sur une orbite basse quasi-polaire à approximativement 220 km de distance. Les deux satellites subissent les perturbations de l'orbite liées à la non-uniformité du champ de gravité. En effet, le champ de gravité étant directement relié à la distribution des masses sur Terre, la force de gravité appliquée à un satellite en orbite terrestre dépend des masses au-dessus desquelles il vole. Toutes ces perturbations causent un changement continu de la distance inter-satellite, ensuite utilisée pour déterminer la distribution et la progression des perturbations du champ de gravité. Les satellites GRACE tournent autour de la Terre 15 fois par jour, et permettent une résolution temporelle de 10 jours pour le champ de gravité global.

Après correction de tous les phénomènes connus et modélisables faisant varier le champ de gravité dans l'espace et dans le temps, GRACE offre un accès unique aux redistributions des grandes masses à la surface du globe: hydrologie continentale, masses océaniques et atmosphériques, difficilement mesurables in-situ (Lemoine et al., 2007, Bruinsma et al., 2010, Ramillien et al., 2005). La Figure 4 montre l'amplitude pic à pic de la variation de ces masses en Asie du Sud, principalement saisonnière car dominée par le cycle de la mousson, entre mars 2002 et août 2012 ainsi qu'une indication de la variations spatio-temporelle de la charge entre les points A et B indiqués sur la carte. Une fois les variations temporelles de charge à la surface du globe connues, nous pouvons modéliser la réponse de la Terre à ce chargement et

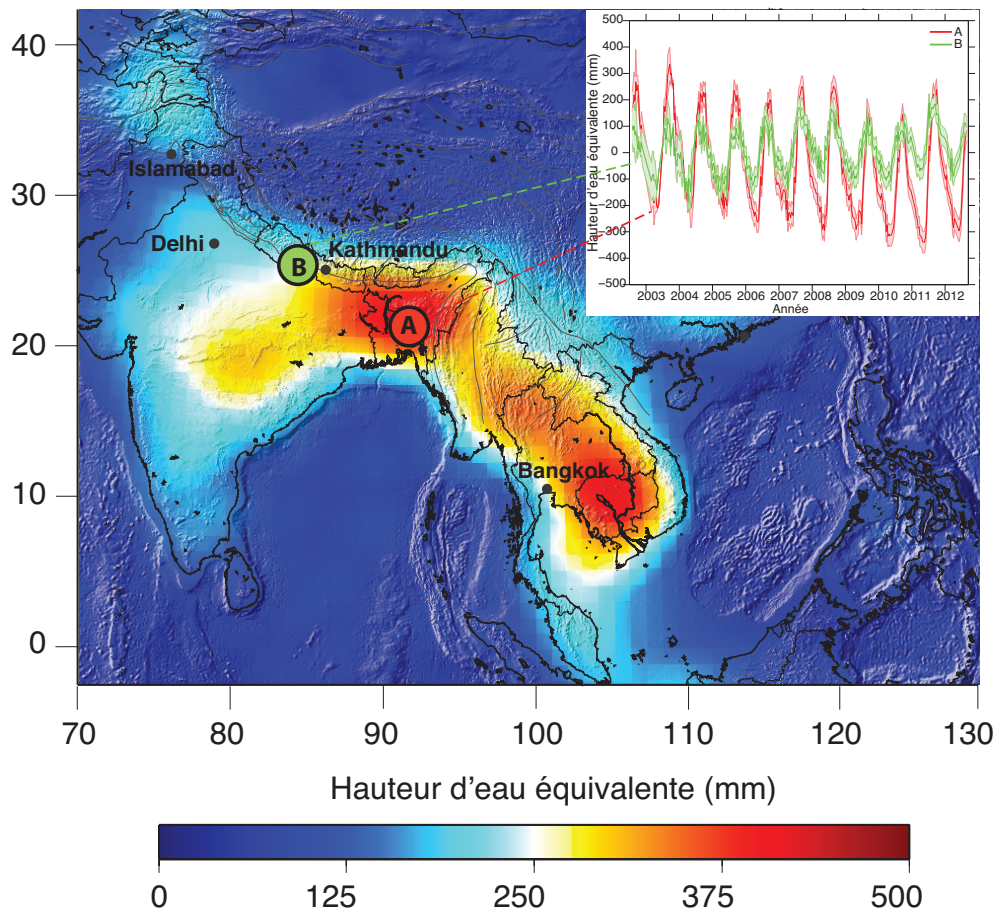


Figure 4 – Amplitude pic à pic de la hauteur d’eau équivalente déduite de GRACE en Asie du Sud pendant la période 2002-2012 et série temporelles associées aux points A et B indiqués sur la carte.

la comparer aux observables GPS.

Dans cette partie, nous nous plaçons dans l’hypothèse des déformations élastiques, approximation raisonnable au premier ordre à l’échelle de l’année.

Les déplacements horizontaux et verticaux  $U_i$  en un point  $M$  à la surface de la Terre à un instant  $t$  induits par les colonnes d’eau de masse volumique  $\rho$  et de hauteur  $h_s$  peuvent être modélisés par:

$$U_i(M, t) = \rho \int_S h_s(m, t) G_i(M - m) dm. \quad (1)$$

où  $G_i$  représente le déplacement de la  $i$ -ème composante en  $M$  causé par une charge unitaire, i.e. une fonction de Green. L’hypothèse principale de cette modélisation est donc le choix du

modèle de Terre dont les fonctions de Green dépendent.

L'hypothèse communément faite, car simple et analytique (Boussinesq, 1885), est celle d'un demi-espace élastique homogène (Bevis et al., 2005, Steckler et al., 2010). Ces études se concentrent cependant sur la composante verticale, de plus grande amplitude, et ajuste le seul paramètre non-contraint, le module d'Young  $E$  (le coefficient de Poisson étant supposé égal à 0.25). Pourtant, Farrell (1972) a établi depuis plusieurs décennies que seul un modèle sphérique et stratifié pouvait prédire correctement à la fois les déplacements horizontaux et verticaux induits par des charges de surfaces. Considérant le nombre d'études récentes utilisant un l'approximation de Boussinesq, nous présentons dans un premier temps les prédictions d'un demi-espace élastique homogène soumis à la charge saisonnière dérivée de GRACE.

La Figure 5 souligne la difficulté de modéliser simultanément l'amplitude des déplacements horizontaux et verticaux avec un seul modèle de ce type et la phase des composantes horizontales. Au sens des moindres carrés, nous obtenons deux meilleurs modèles pour les déplacements horizontaux et verticaux avec respectivement  $E = 90GPa$  et  $E = 170GPa$ , suggérant une sensibilité différente des composantes à une charge de surface. En effet, les déplacements horizontaux et verticaux n'évoluent pas de la même façon avec la distance à la charge dans un modèle réaliste de Terre, alors que leur rapport est constant avec la distance à la charge dans l'approximation de Boussinesq.

Nous construisons donc ensuite un modèle sphérique et stratifié (Farrell, 1972) s'appuyant sur les paramètres élastiques du "Preliminary Reference Earth Model" (PREM, Dziewonski & Anderson (1981)), avec une croûte continentale (CRUST 5.1, Mooney et al. (1998)). La Figure 6 donne un exemple de la prédiction d'un tel modèle soumis aux charges déduites des données GRACE à la station LHAZ. Sur l'ensemble des 28 stations utilisées dans cette étude régionale, l'utilisation d'un modèle de Terre plus réaliste améliore la prédiction des signaux saisonniers de la composante Est de 24%, Nord de 40% et verticale de 15%.

Le code sphérique et stratifié développé au cours de ma thèse calculant la réponse de la Terre aux charges saisonnières déduites des données GRACE est maintenant documenté et accessible en ligne (Annexe B).

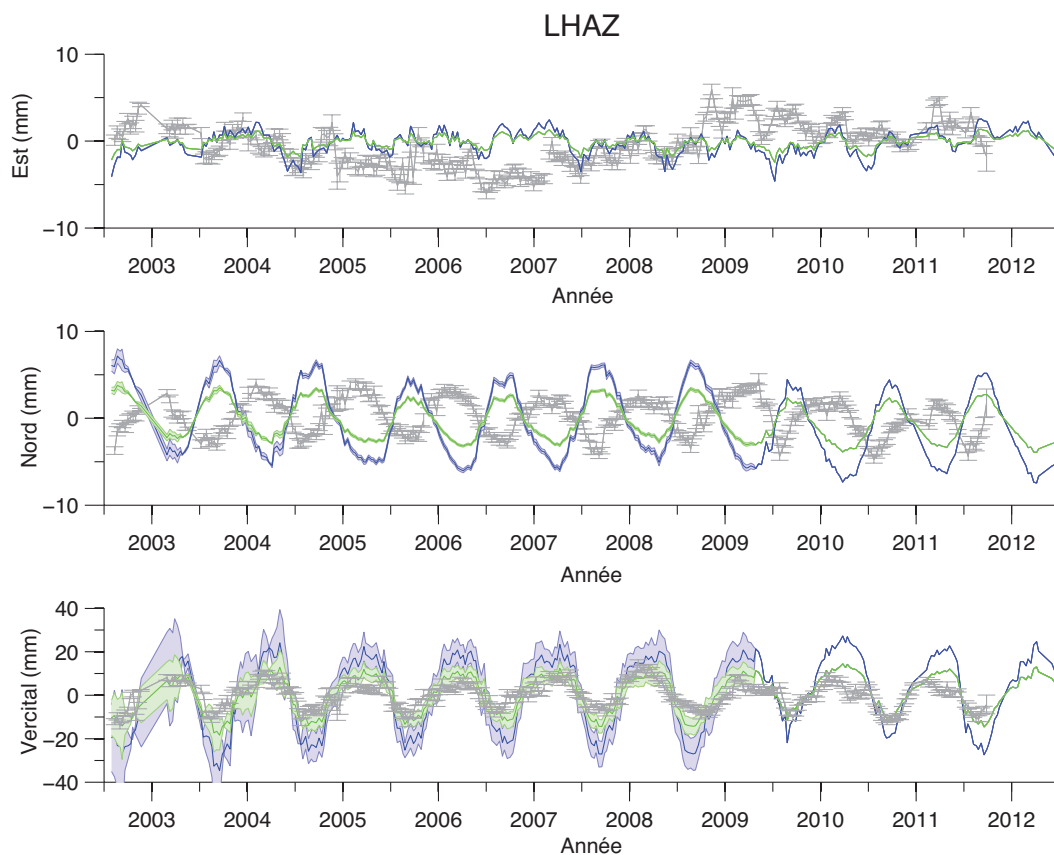


Figure 5 – Positions géodésiques saisonnières, moyennées sur une période de 10 jours, à la station LHAZ (gris). Les barres d’erreur représentent les incertitudes  $1-\sigma$ . Les courbes bleues et vertes montrent les déplacements induits par les variations d’hydrologie de surface dérivées de GRACE pour des demi-espaces élastiques homogènes. La courbe bleue correspond à un module d’Young  $E = 90GPa$ , reproduisant au mieux les données horizontales pour l’ensemble des 28 stations GPS de l’étude. La courbe verte correspond à un module d’Young  $E = 170GPa$ , meilleur modèle prédisant les données verticales. Les barres d’erreurs sur les modèles proviennent des incertitudes sur l’estimation de la charge de surface.

Même si la prédiction des variations saisonnières observées aux stations GPS dans la région est meilleure avec un modèle de Terre élastique réaliste, elle n’est pas parfaite. Des différences d’amplitude et de phase sont visible à de nombreuses stations entre données et modèle. Dans le contexte Himalayen, la structure de la lithosphère est très différente de celle d’un modèle 1D moyen de Terre. Afin d’améliorer le modèle, j’ai donc voulu ajuster localement les paramètres (ratio des vitesses sismiques et densité) des premiers 150 km du modèle de Terre en réalisant une inversion bayésienne.

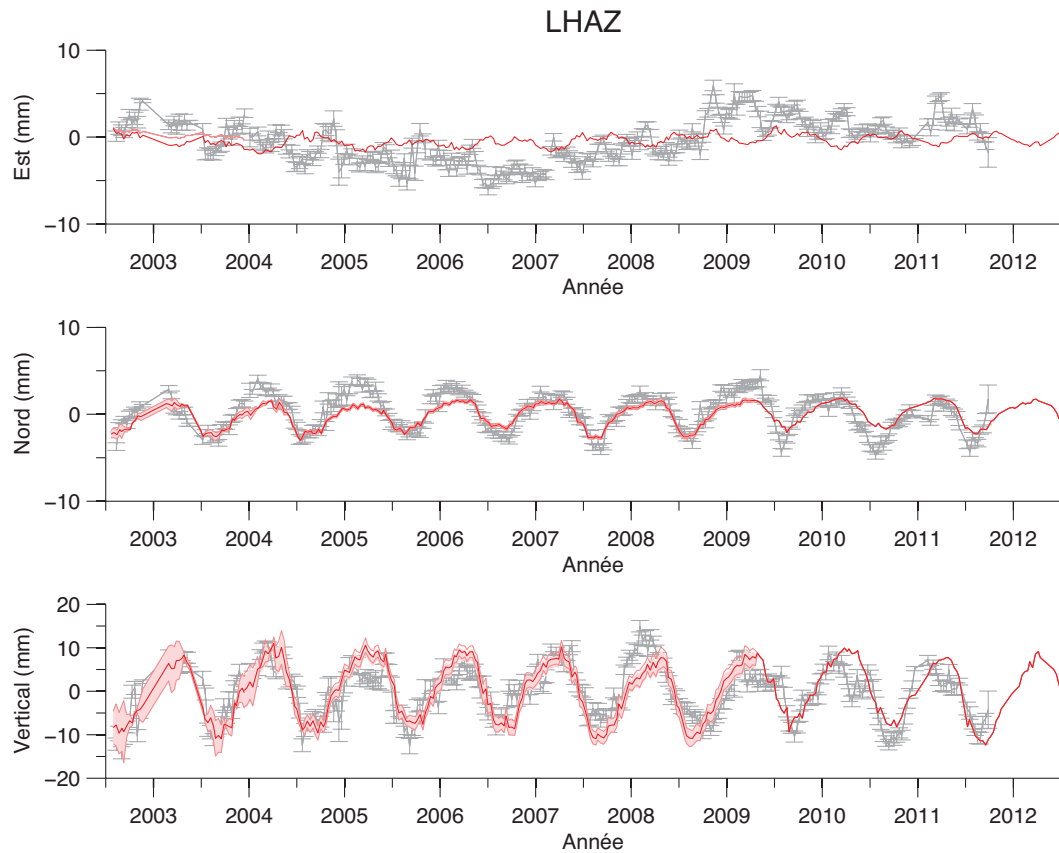


Figure 6 – Positions géodésiques saisonnières, moyennées sur une période de 10 jours, à la station LHAZ (gris). Les barres d’erreur représentent les incertitudes  $1-\sigma$ . La courbe rouge montre les déplacements induits par les variations d’hydrologie de surface dérivées de GRACE pour un modèle sphérique stratifié s’appuyant sur PREM (Dziewonski & Anderson, 1981). Les barres d’erreurs sur les modèles proviennent des incertitudes sur l’estimation de la charge de surface.

La Figure 7 montre une comparaison de plusieurs modèles de Terre 1D pour les premiers 150 km. Le modèle moyen déduit des déplacements saisonniers mesurés par les stations GPS du Népal et du Sud-Tibet (MGrace, rouge) prédit un ratio de vitesses et une densité plus proche des modèles régionaux (noir) que du modèle moyen global (bleu), capturant grossièrement des caractéristiques propres à la chaîne Himalayenne et améliorant la prédiction des observations saisonnières d’environ 20%.

Cependant, ce modèle n’est pas suffisant pour prédire de façon satisfaisante le signal saisonnier de la région, en particulier horizontal. Les différences entre modèle et données pouvant

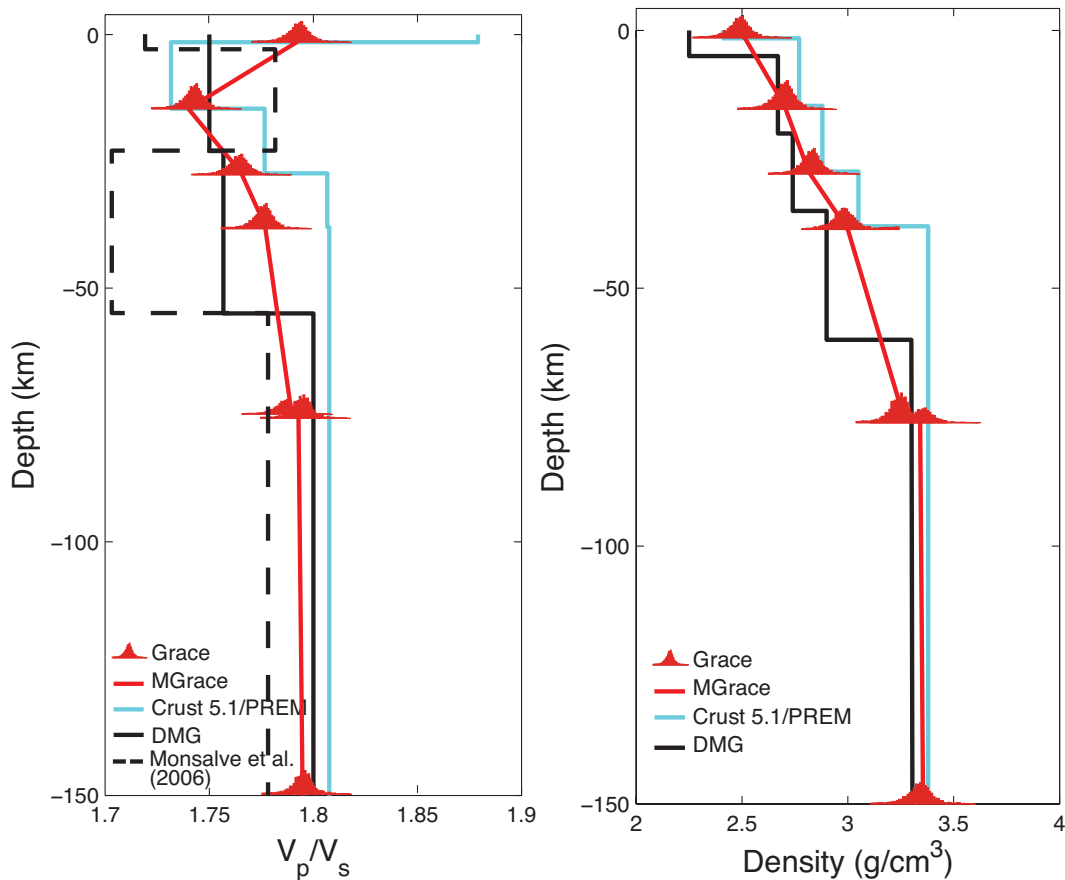


Figure 7 – Comparaison de modèles de Terre 1D pour les premiers 150 km en Himalaya pour le ratio des vitesses des ondes P et S (a) ainsi que la densité (b): Crust 5.1/PREM (bleu), modèles régionaux (noir d'après Pandey et al. (1995)), noir pointillé d'après Monsalve et al. (2006)), Grace (histogrammes rouges représentant les densités de probabilité à posteriori) et MGrace (rouge, dérivé de Grace).

apporter des contraintes intéressantes sur la structure interne de la Terre, j'ai ensuite étendu l'étude régionale à une étude globale afin de mieux comprendre la répartition spatiale de ces différences et d'envisager leurs sources potentielles..

## Modélisation globale de la déformation saisonnière de la Terre

La modélisation globale des signaux saisonniers observés dans les séries temporelles GPS a attiré beaucoup d'attention ces dernières années (Van Dam et al., 2001, Davis et al., 2004). Dong et al. (2002) a montré que la nature de ces variations annuelles, pour la composante verticale au moins, était majoritairement expliquées sur le globe par les redistributions des

masses d'eau à la surface du globes (marées, chargements océaniques et atmosphériques, hydrologie continentale, neige et glace, etc.). Modéliser ces variations à partir des données GRACE présentées dans la section 1.1, et en utilisant un modèle réaliste élastique de Terre, s'avère satisfaisant pour la composante verticale mais les composantes horizontales sont problématiques dans bien des régions (Fu et al., 2013). Cette étude suggère en effet une bonne corrélation entre modèle élastique, sphérique et stratifié, et données pour la composante verticale mais relèvent certains problèmes de phase et d'amplitude pour les composantes horizontales. Ces problèmes, décelés à l'échelle régionale, sont très souvent expliqués par le manque de résolution de la charge provenant de GRACE, mais n'ont pas été décrits et étudiés en détails.

Dans un premier temps, nous proposons donc un modèle élastique global de déformations, verticale et horizontales, induites par des redistributions de charge à la surface de la Terre. Ce modèle, développé au départ par Luce Fleitout pour l'étude du rebond post-glaciaire, s'appuie sur une décomposition en harmoniques sphériques et en fréquences de la charge de surface, et sur la théorie des nombres de Love (Wu & Peltier, 1983, Cathles, 1975).

La charge est déduite des données GRACE, comme décrit précédemment. La Figure 1.3 montre l'amplitude pic à pic des variations de charge de surface dérivées de GRACE. La contribution des charges de degré 1, c'est à dire la déformation et le mouvement du géocentre associé, n'étant pas mesurée par GRACE, nous l'ajoutons dans un premier temps en bénéficiant des résultats produits par Swenson et al. (2008). Une caractéristique importante de la charge est la variété de ses longueurs d'onde car, d'après la Figure 9, la réponse de notre modèle de Terre, et en particulier le ratio des déplacements horizontaux et verticaux, dépend directement de la taille du chargement (inversement proportionnel au nombre harmonique).

Nous comparons ensuite les résultats de ce modèle avec des observations de signaux saisonniers à 195 stations GPS réparties sur Terre. La Figure 10 montre un exemple de série temporelle GPS, où les déformations long terme ont été estimées et retirées (gris) et de la prédiction du modèle élastique (bleu). On remarque que les données verticales sont relativement bien modélisées, en amplitude et en phase, alors que les composantes horizontales, ici Nord en

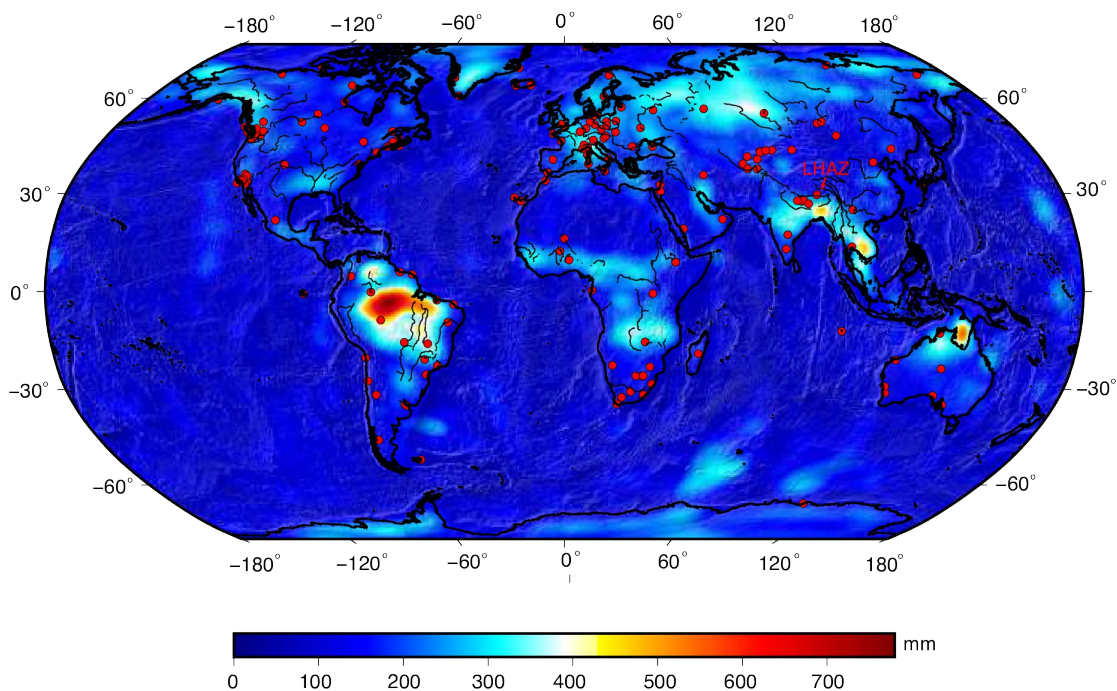


Figure 8 – Amplitude globale pic à pic de la hauteur d'eau équivalente saisonnière déduite de GRACE pendant la période 2002-2012 (mm).

particulier, sont sous-prédites et déphasées par rapport au modèle élastique.

Cette remarque n'est pas propre à cette station. Les cartes de la Figure 11 représentent les erreurs quadratiques moyennes normalisées par l'amplitude moyenne du signal entre les prédictions d'un modèle élastique et les observations. Les données horizontales sont donc globalement mal prédites alors que les données verticales sont raisonnablement bien modélisées. De nombreux facteurs peuvent influencer l'amplitude et la phase des déplacements saisonniers. Parmi eux, des problèmes de traitement géodésique (GRACE ou GPS), ou encore des phénomènes non-hydrologiques, comme l'expansion thermique du sol, que nous écartons au premier ordre.

Nous nous arrêtons sur l'incohérence de référentiels entre les données GRACE, ne mesurant pas les charges de degré 1 ni le mouvement du géocentre associé, alors remplacés empiriquement, et des données GPS saisonnières centrées sur le centre de figure de la Terre. Nous montrons que le désaccord entre modèle et observations horizontales à l'échelle mondiale

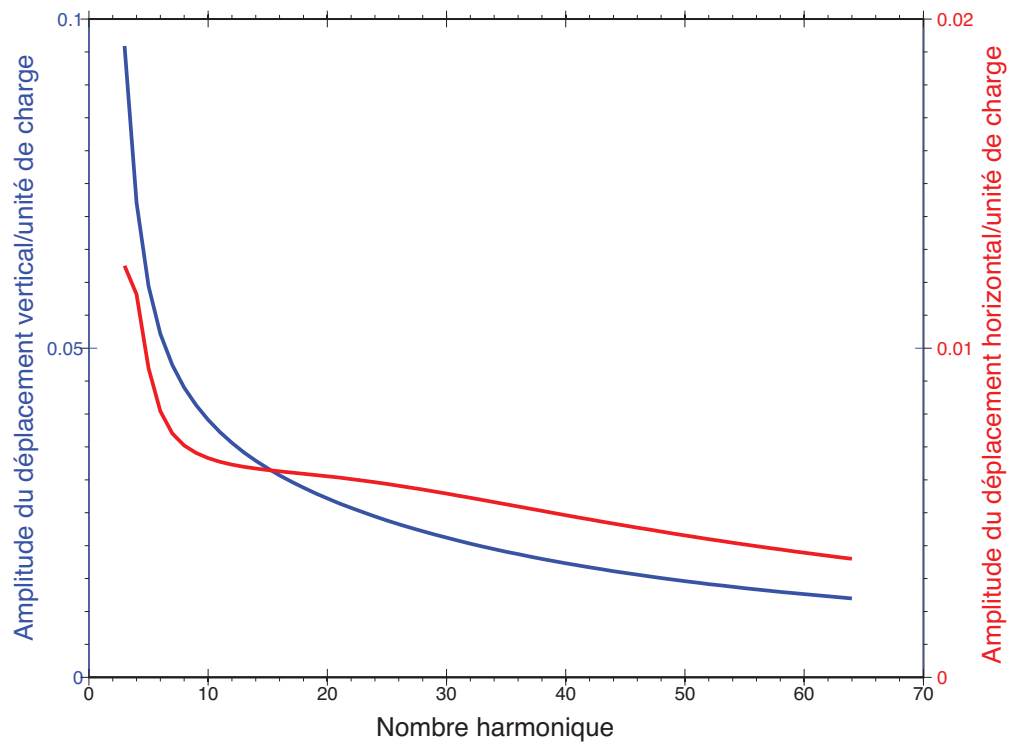


Figure 9 – Amplitude du déplacement vertical (bleu) et horizontal (rouge) en fonction du nombre harmonique et, en réponse à un chargement annuel saisonnier.

peut être associé au premier ordre à une contribution de degré-1 sous-estimée et proposons de l'estimer a posteriori grâce à une transformation d'Helmert à 6 paramètres, représentant le mouvement rigide du géocentre ainsi que, potentiellement, une partie de la déformation de degré-1 (voir Figure 12). La corrélation entre modèle et données horizontales est nettement améliorée, sans que les prédictions verticales soient affectées comme le montre les Figures 10 et 13. Cette transformation, principalement une translation et rotation sur l'axe Z de période annuelle, est déduite des données horizontales uniquement, car les deux composantes sont affectées différemment par les charges de degré-1, et est représentée en Figure 12.

Au second ordre, les variations de volume dans le manteau terrestre liées aux changements de phase des minéraux qui le composent peuvent jouer un rôle dans la déformation saisonnière. En effet, PREM, déterminé à l'aide de données sismique, n'est théoriquement valable que pour des échelles de temps allant jusqu'à l'heure. Les transitions larges de phase des minéraux (pyroxène-grenat-perovskite) du manteau engendrent des variations de volume

LHAZ

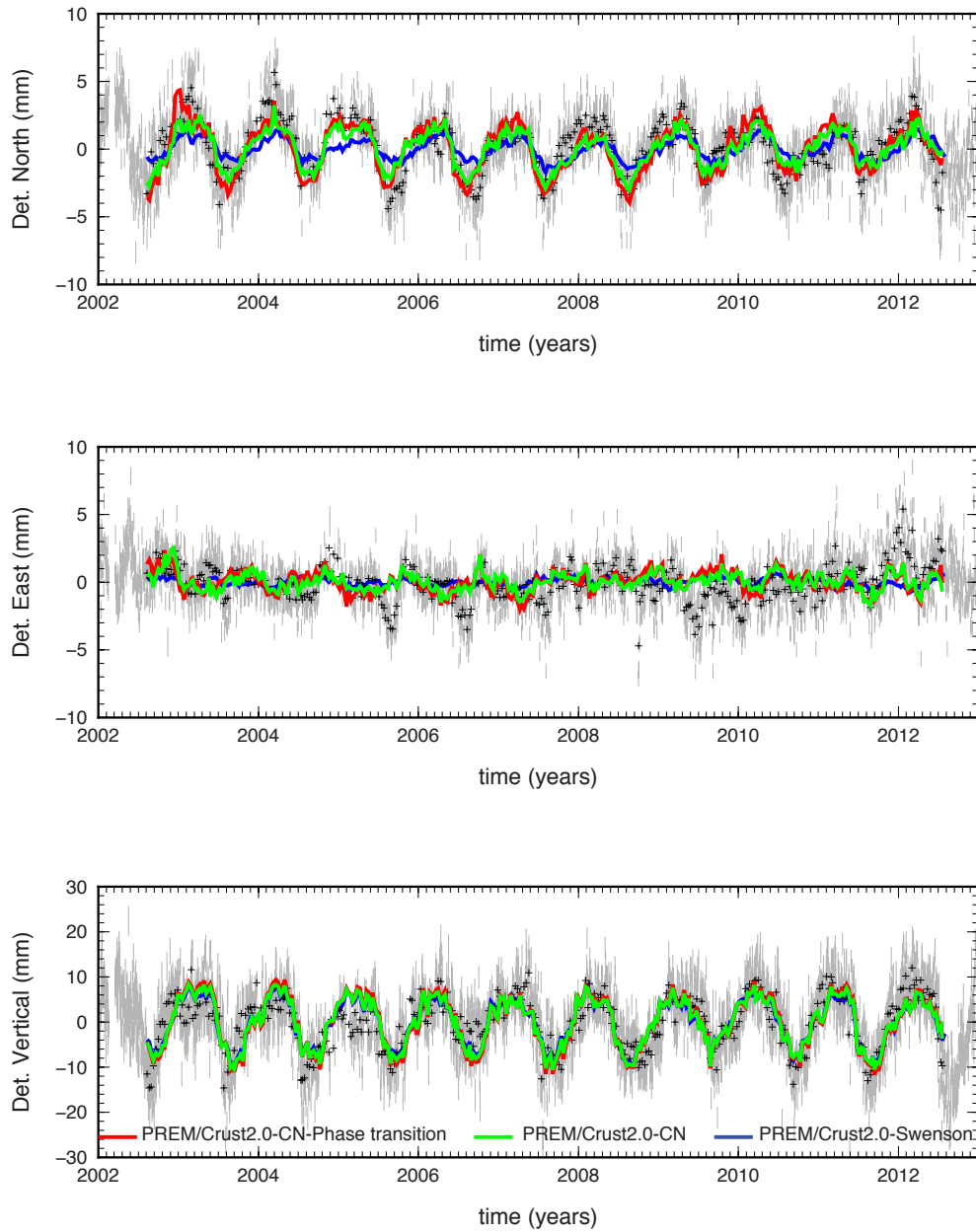


Figure 10 – Positions géodésiques annuelles à la station LHAZ, Tibet (voir figure 1.3 pour la localisation) et barres d’erreurs pour les incertitudes à  $1-\sigma$  (gris). Les points noirs représentent une moyenne glissante sur 10 jours des positions géodésiques journalières. Les courbes sont les prédictions des déplacements induits le signal de GRACE avec un modèle de terre élastique sphérique stratifié: contribution de degré-1 d’après Swenson et al. (2008) (bleu), contribution de degré-1 estimées a posteriori sans (vert) ou avec (rouge) variations de volume dans le manteau.

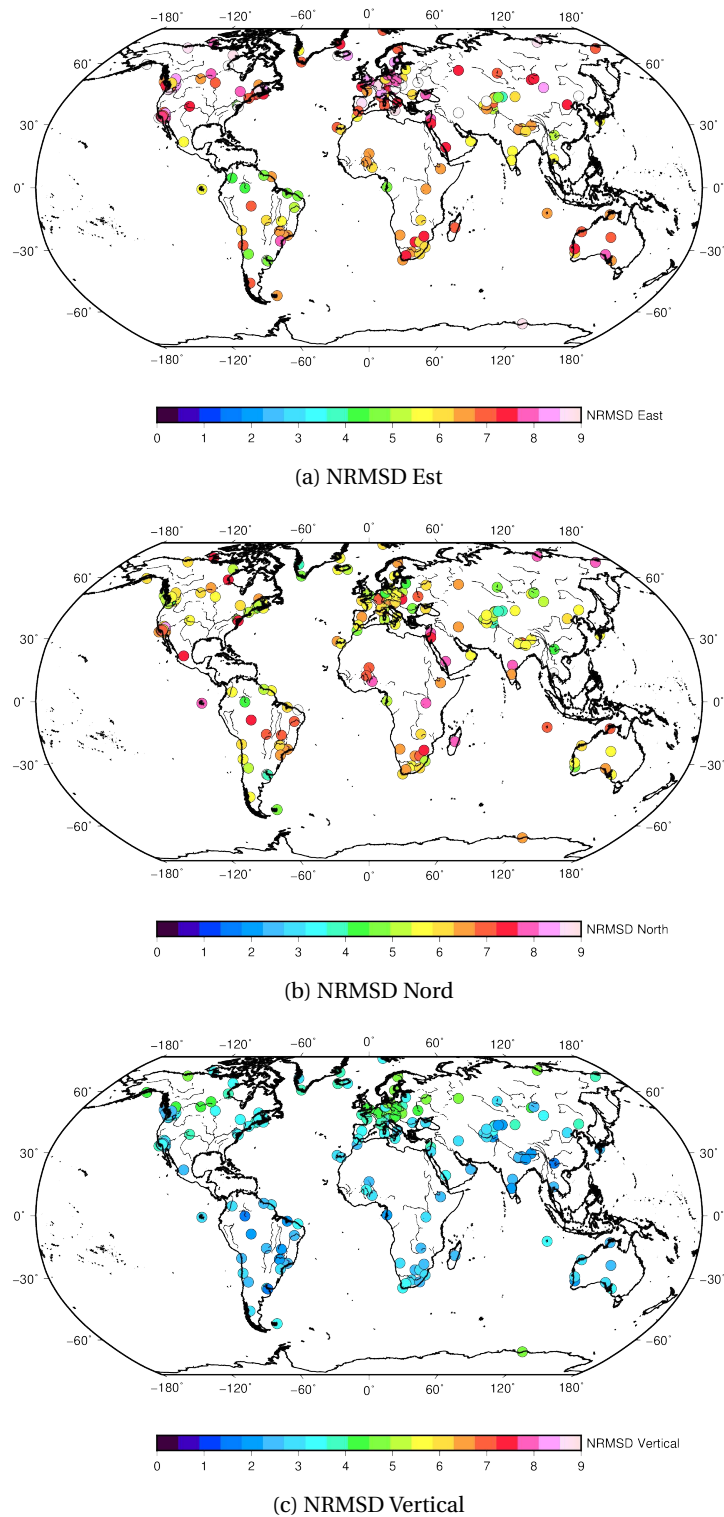


Figure 11 – Erreur quadratique moyenne normalisée par l'amplitude moyenne du signal entre les prédictions d'un modèle élastique dont le degré-1 de charge est ajouté d'après [Swenson et al. \(2008\)](#) et les observations sur les composante (a) est, (b) nord et (c) verticale. Les composantes horizontales sont nettement moins bien prédites que la composante verticale par le modèle.

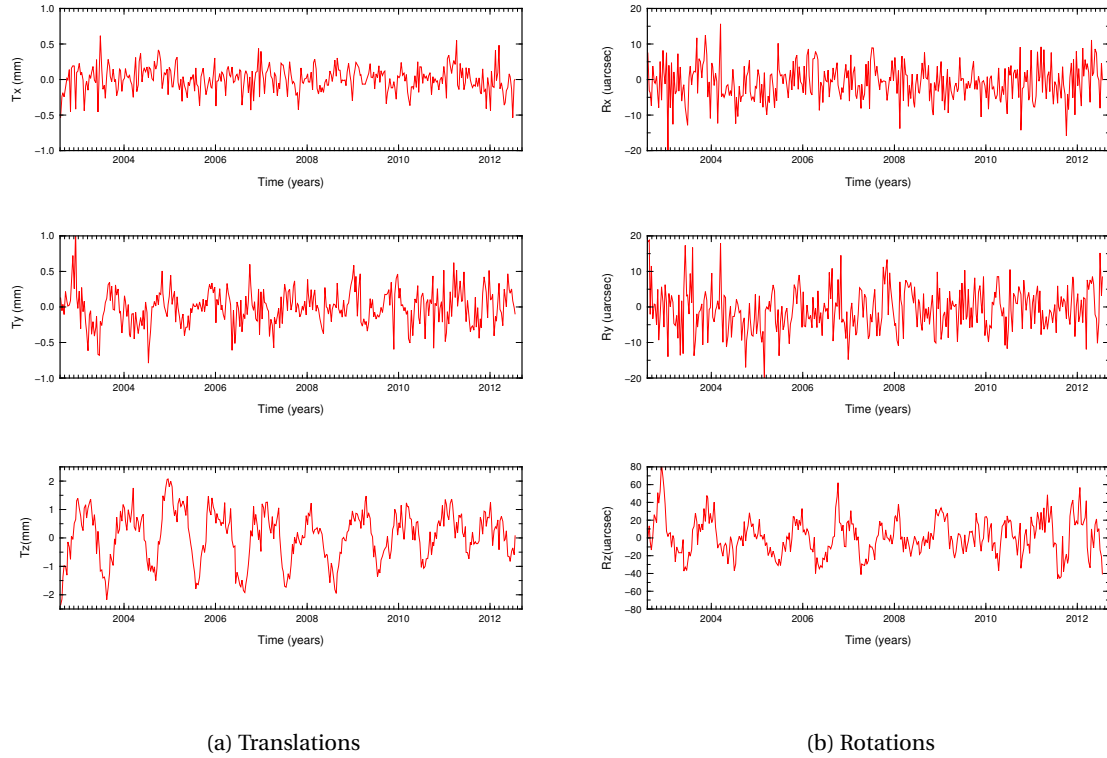
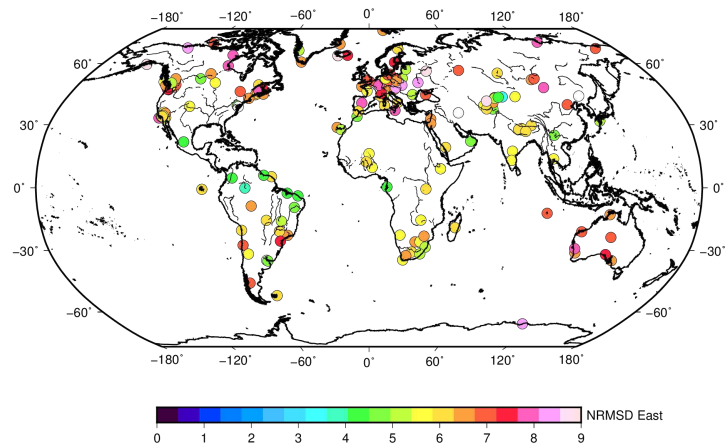
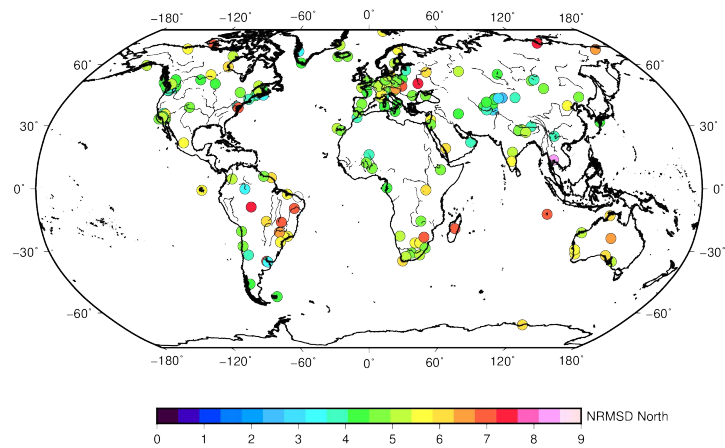


Figure 12 – Best-fitting (a) translations  $T_x, T_y, T_z$  and (b) rotations  $R_x, R_y, R_z$  derived from a global least square inversion of the horizontal and time series of the 195 cGPS sites of our study.

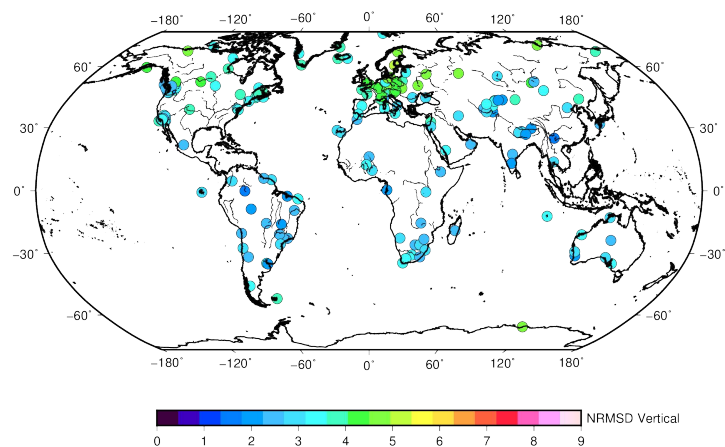
non-négligeables mais les cinétiques de ces réactions sont très mal connues. En effet, les contraintes sur la vitesse de ces réactions, obtenues de l'étude de l'atténuation des ondes sismiques et de la circulation mantellique suggèrent qu'elles se font entre 7000 secondes (Durand et al., 2012, Resovsky et al., 2005) et  $10^5$  années (Čadek & Fleitout, 2003). Ces réactions ont un effet sur les propriétés des matériaux en profondeur. En particulier, le module d'incompressibilité peut être redéfini en fonction de la fréquence de chargement de surface et modélisé dans notre modèle, cette fois-ci viscoélastique, avec des éléments types ressorts et vérins simples. L'incompressibilité de la zone de transition du manteau soumise à un chargement périodique de surface dépend alors de sa fréquence. Une limite peut-être placée sur le module d'incompressibilité relaxée en le redéfinissant à partir des variations de la masse volumique avec la profondeur.



(a) NRMSD East



(b) NRMSD North



(c) NRMSD Vertical

Figure 13 – Erreur quadratique moyenne normalisée par l'amplitude moyenne du signal entre les prédictions d'un modèle élastique dont le degré-1 de charge est estimé à posteriori et les observations sur les composantes (a) est, (b) nord et (c) vertical.

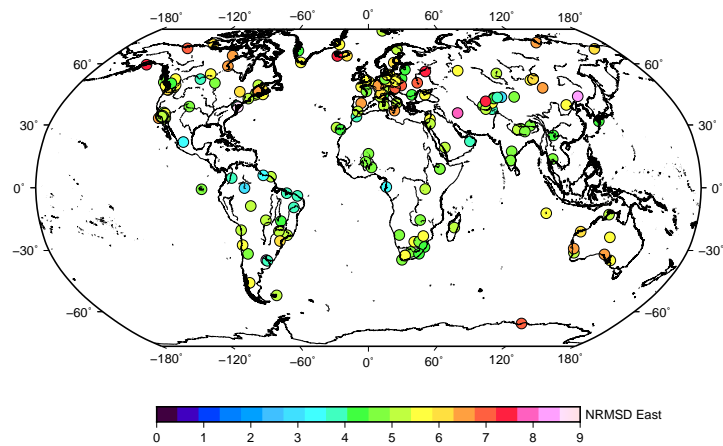
Nous incluons ces réactions dans notre modèle, et déterminons un meilleur modèle, incluant les variations de volumes de la zone de transition du manteau liées aux transformations des minéraux en profondeur entre 410 et 660 km. Ce meilleur modèle est déterminé comme le modèle expliquant au mieux les variations saisonnières observées (verticales et horizontales), à partir de deux paramètres: (1) un facteur du module d'incompressibilité sismique (fréquence infini de chargement) et (2) une pseudo-viscosité représentant la cinétique de phase et permettant à la réaction de s'amorcer.

Notre meilleur modèle incluant ces variations de volume décrit mieux les données et suggère que la transformation pyroxène-grenat-perovskite à le temps, en partie, de se faire en l'espace d'un an. Un exemple des prédictions de ce modèle est donné pour LHAZ, Tibet (Figure 10, courbe rouge) et la corrélation entre modèle et données horizontales à l'échelle globale est améliorée, sans que les prédictions verticales soient affectées comme le montre la Figure 14.

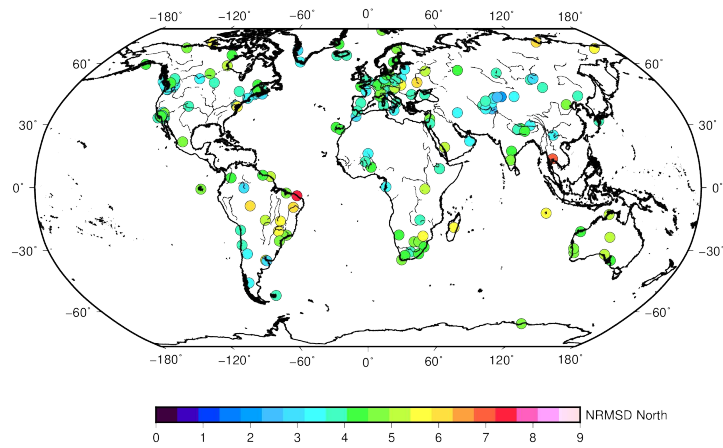
Notre étude suggère que l'utilisation du signal saisonnier de GRACE, même avec sa grande résolution spatiale, pour décrire la déformations annuelles mesurées localement par les stations GPS est possible. Les différences entre modèle et données horizontales ne sont pas majoritairement dues à des effets locaux de charge mais plutôt à l'estimation de la déformation de degré-1 et au mouvement du géocentre associé, non mesuré par GRACE. Potentiellement, la charge annuelle peut également aider à contraindre la rhéologie de la Terre à l'échelle de l'année.

## Variations périodique de sismicité & approche expérimentale

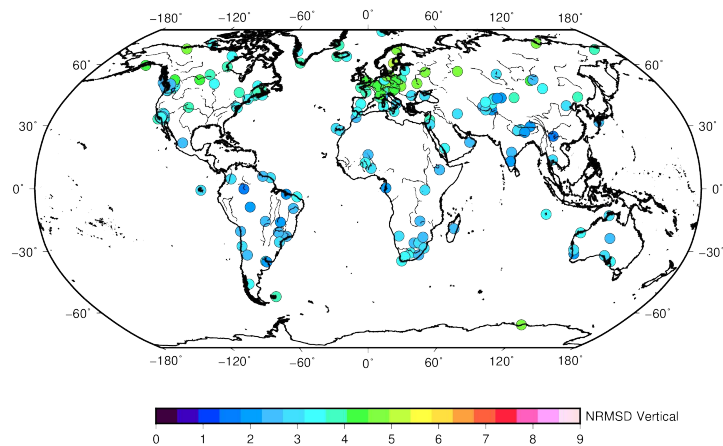
Une fois les déformations saisonnières de la Terre précisément modélisées, la question de leur influence sur la sismicité se pose. De nombreuses études ont en effet montré une corrélation entre sismicité et forçage périodique, qu'il soit journalier sous l'effet des marées (Métivier et al., 2009, Cochran et al., 2004, Thomas et al., 2012, Tanaka et al., 2002, 2004, Ide & Tanaka, 2014), ou saisonnier, soumis aux variations de l'hydrosphère (Bollinger et al., 2007, Heki, 2003, Saar & Manga, 2003, Bettinelli et al., 2008, Christiansen et al., 2005, Ader & Avouac, 2013, Costain & Bollinger, 1996, Braunmiller et al., 2014). Cependant, cette corrélation n'est pas



(a) NRMSD East



(b) NRMSD North



(c) NRMSD Vertical

Figure 14 – Erreur quadratique moyenne normalisée par l'amplitude moyenne du signal entre les prédictions d'un modèle élastique dont le degré-1 de charge est estimé à posteriori incluant les variations de volume du manteau liées aux transformations minéralogiques et les observations sur les composantes (a) est, (b) nord et (c) vertical.

systématique (Vidale et al., 1998, Beeler & Lockner, 2003), et les paramètres clés du lien entre forçage périodique et sismicité sont peu connus. L'importance de l'amplitude et la fréquence du forçage ont été mis en évidence à travers des expériences de laboratoire (Lockner & Beeler, 1999, Beeler & Lockner, 2003), tandis que le rôle de l'état de contrainte de la faille dans la modulation périodique de la sismicité a été mis en évidence par l'augmentation de la corrélation entre les marées et la sismicité d'une zone de nucléation précédent de grands tremblements de Terre (Tanaka, 2010, 2012).

Dans cette partie du manuscrit, nous estimons dans un premier temps l'évolution spatio-temporelle des contraintes induites par les variations saisonnières de l'hydrosphère mesurées par GRACE. La Figure 15 montre l'amplitude du second invariant du tenseur des contraintes déviatoriques induites par la charge de GRACE (2002-2012) à 20 km de profondeur. La charge saisonnière affecte donc de façon significative des régions d'intérêt sismique comme l'Himalaya, l'Alaska ou encore le Pérou.

Nous nous intéressons ensuite plus particulièrement à la région Himalayenne, où de nombreux séismes se concentrent sur la partie profonde du Main Frontal Thrust (MHT) (Ader et al., 2012a, Cattin & Avouac, 2000), et sont capturés par le réseau sismique du National Seismological center (NSC), Népal. Il a été montré que, dans cette région, le taux de sismicité est plus élevé pendant les mois d'hiver que les mois d'été. Cette observation a été attribuée aux variations de contraintes induites par l'hydrologie de surface, principalement contrôlée par le cycle de la mousson (Bollinger et al., 2007, Bettinelli et al., 2008, Ader & Avouac, 2013).

Nous calculons l'effet de la charge saisonnière de GRACE sur le MHT, et trouvons une corrélation entre le taux de la contrainte de Coulomb, souvent utilisée pour décrire la possibilité de rupture d'une faille, et la sismicité ( $M_L \leq 3$ ). La Figure 16 montre le taux de la contrainte de Coulomb (rouge) ainsi que la sismicité par mois, sommé sur un an.

Afin de mieux comprendre les mécanismes en jeu dans la modulation périodique de la sismicité par un forçage climatique, nous menons une étude expérimentale. Nous déformons par fluage des échantillons de grès de Fontainebleau en laboratoire. Les roches sont saturées en eau et soumises à une contrainte constante, analogue à un chargement tectonique, ainsi

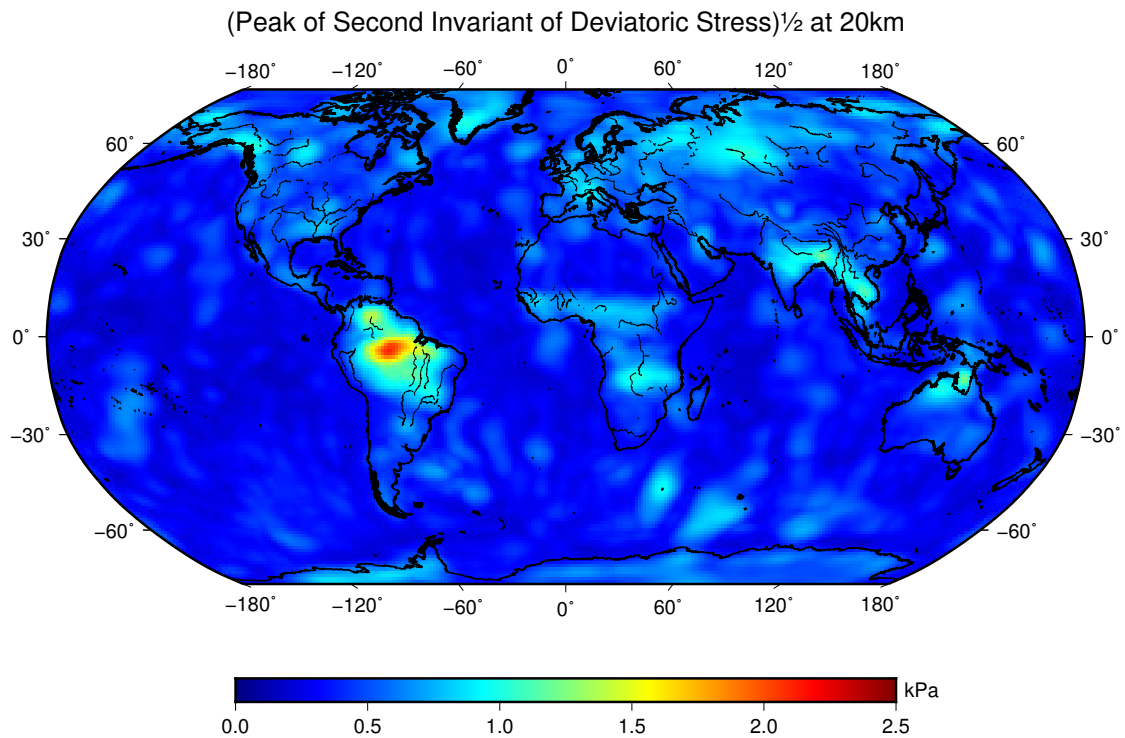


Figure 15 – Amplitude de la racine du second invariant du tenseur des contraintes déviatoriques induites par la charge de GRACE (2002-2012) à 20 km de profondeur.

qu'à des oscillations sinusoidales de la pression de pore, simulant de faibles perturbations de contraintes par forçage hydrologique par exemple. Nos expériences, bien que préliminaires, suggèrent que les faibles variations périodiques de la pression de pore peuvent déclencher des variations cycliques des émissions acoustiques quelques heures avant la rupture. Ces émissions acoustiques se produisent plus significativement lorsque la pression de pore est la plus basse, i.e. lorsque que les micro-fissures de l'échantillon de roche sont soumises à moins de pression (Figure 17).

A plus grande échelle, nos résultats, bien que préliminaires, suggèrent que la modulation ou le déclenchement périodique de séismes par de faibles variations de contrainte oscillantes peut exister pendant la longue phase de nucléation des tremblements de Terre.

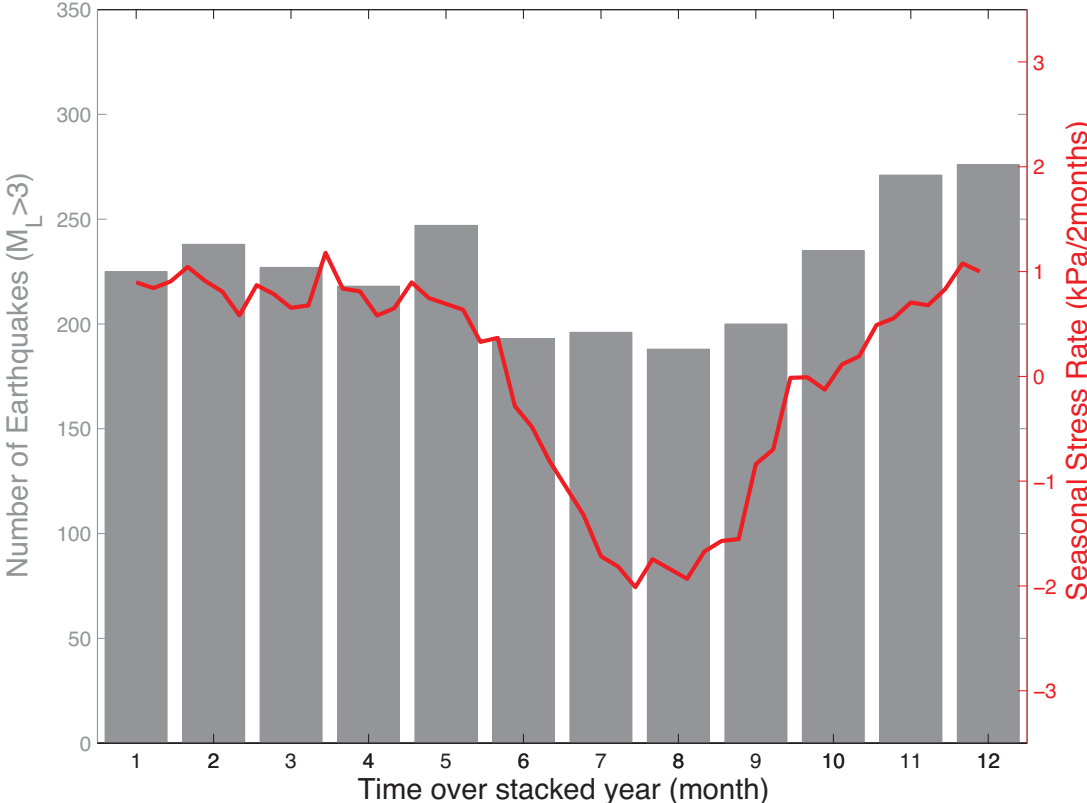
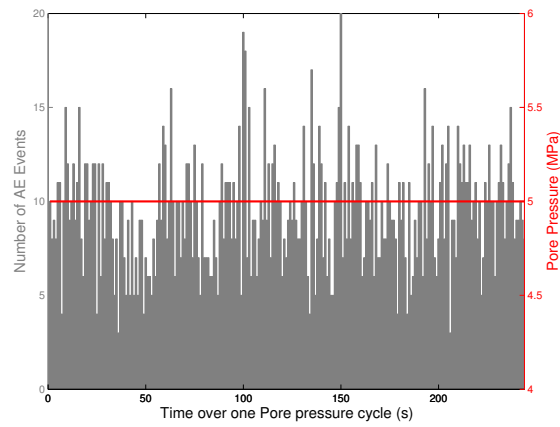
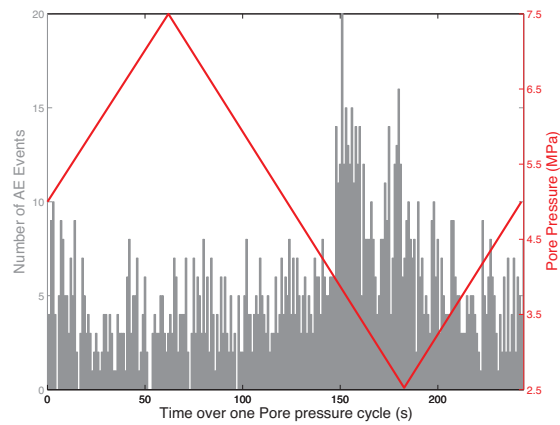


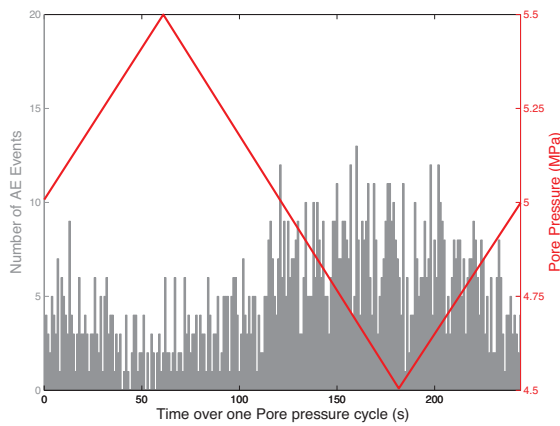
Figure 16 – Evènements de  $M_L \leq 3$  de 1994 à 2009 (catalogue du NSC) sommé sur un an (gris) et taux de la contrainte de Coulomb déduite du signal saisonnier de GRACE chargeant un modèle de Terre sphérique et stratifié, type PREM.



(a) Experiment 1, palier de rupture



(b) Experiment 1, palier de rupture



(c) Experiment 2, palier de rupture

Figure 17 – Moyenne cohérente de la contrainte différentielle avant rupture (rouge) et des émissions acoustiques (gris) pour (a) Expérience 1 ou la Pression de pore ( $P_p$ ) est constante à 5 MPa, (b) Expérience 2,  $P_p=5\pm 2.5$  MPa et (c) Expérience 3,  $P_p=5\pm 0.5$  MPa, sur un cycle d'oscillations de la  $P_p$  (244s).



## INTRODUCTION

The Earth deformation under surface loading variations reflects the rheology of its composing materials and the nature of the load (spatial distribution, loading frequency, etc.). Measuring and understanding the spatio-temporal response of the Earth to surface loading and unloading events is therefore a key parameter to better understand the physics of the Earth.

The Earth deforms under various time and spatial scales, with specific responses. For example, it is common to consider that, for periods from seconds to a year, that the Earth deforms as a purely elastic solid. This elastic response concerns usually, seismic waves, solid and oceanic tides as well as seasonal variations of the hydrosphere. For longer periods, the Earth behaves as a viscoelastic solid. For example, we still observe a significant uplift of Scandinavia and North America due to the relaxation of the Earth following the rapid surface unloading after the last glaciation, 10 000 years ago.

An important question is to define when the Earth's response to surface loading is not instantaneous anymore but exhibits a phase shift and amplitude difference from the prediction of a purely elastic model. At an annual time scale for example, the Earth deforms under the seasonal variations in the hydrosphere (continental water, non-tidal oceanic and atmospheric mass variations). Over the past decade, the recent advances in space geodesy have offered precise measurement of the seasonal ground deformation and a reliable estimate of spatio-temporal evolution of the hydrosphere deduced from variations of the Earth gravity field. First, Global Navigation Satellite Systems (GNSS) opened the way to measures of the ground deformation with a millimeter resolution, and therefore rapidly became a key tool to the understanding of various geophysical processes. Secondly, the launch of the Gravity and Recovery Climate Experiment (GRACE) mission in 2002 ([Tapley et al., 2004](#)) marked an important transition from local measurements to global high resolution and accuracy monitoring of

## Introduction

---

the mass transport process in the Earth system. GRACE has since then provided an incredible dataset of spatio-temporal variations of the hydrosphere.

The manuscript you have in hands takes advantage of the long term effort of several teams to acquire and process geodetic measurements. First, GNSS time series were processed by the Nevada Geodetic Laboratory at a global scale and the California Institute of Technology (Caltech) at the regional scale. The valuable stations located in Nepal were installed and are successfully maintained by the collaboration between the Nepal Seismological Center, the Centre à l'Énergie Atomique and Caltech. Finally, GRACE data used in this work were processed by the Research Group for Space Geodesy, in Toulouse. When we started this work, the idea was to bring these two datasets together and model seasonal horizontal and vertical variations observed in GPS time series as the response of the Earth to seasonal hydrology variations. Along the way, numbers of questions arose from what we thought, at first, was a straight forward problem.

Accurately modeling the Earth's response to seasonal surface hydrology has attracted much attention since the early 2000's ([Van Dam et al., 2001](#)), and even more so as long time series of both deformation and surface load data became available. Comparable to tides ([Farrell, 1972](#)), once properly modeled, physics-based seasonal deformation models have far reaching implications in global geodesy. First, unless accounted for, they can bias estimations of GNSS site velocities intended for high accuracy purposes such as plate tectonics and reference frames ([Blewitt & Lavallée, 2002](#)). Accurate seasonal deformation models are also crucial for the detection of transient deformation of similar amplitude and close periodicity ([Dragert et al., 2001](#)). Understanding the Earth's deformation under loads of multiple wavelengths at an annual time scale can also provide useful constraints on its rheology. These indications may have implications for the understanding of the post-seismic response of the Earth, occurring at comparable spatial and temporal scales. Finally, once the link between hydrological redistributions and GNSS observations is fully understand, GNSS time series can be used to determine water storage at a shorter spatial scale ([Fu et al., 2015](#)).

During the past decade, numbers of studies have modeled seasonal deformation as the re-

sponse of surface loading, regionally or globally, using simple elastic homogeneous half-space or more realistic spherical and layered models for Earth. Most authors focused on the vertical deformation induced by continental water mass redistributions, due to its large amplitude compared to the horizontal seasonal deformation. Yet, precise models of the seasonal horizontal displacements are essential for increasing site velocities accuracy, detect potential transient deformation or fully understand the annual deformation of the Earth.

The central ideas of my thesis is to model accurately the interaction between the solid Earth and its fluid envelops by focusing on the seasonal redistributions of water and atmospheric masses. I also investigated whether or not seasonal deformation can be used to place constraints on the Earth's elastic and viscoelastic structure at an annual time scale. Using a satisfying seasonal deformation model, I then estimated annual stress perturbations induced by surface hydrology. Finally, from an experimental point of view, I questioned the role of small periodic perturbations on seismicity.

In this manuscript, we review in *Chapter 1* previous studies of seasonal deformation and potentially induced seismicity that have brought us to further investigate these questions.

*Chapter 2* focuses on building a **regional elastic model of seasonal deformation in the Himalayas, where the monsoon cycle induces both horizontal and vertical ground motion**. At a first order approximation, the predicted displacements by a realistic elastic Earth model, under seasonal surface loading derived from GRACE are in good agreement with the observations recorded at continuous stations from the Global Positioning System (GPS). However, we show that regional seasonal displacements can be used to adjust locally the elastic parameters of the first 150 km of the Earth.

In *Chapter 3*, we extend the model to a global scale and show that there is a systematic underprediction and phase lag of the horizontal observations while the vertical displacements are fairly well predicted. **The second concern of my thesis is therefore to better understand and model global horizontal and vertical seasonal deformation**. We show that, degree-one deformation and associated geocenter motion are of importance when modeling seasonal

## Introduction

---

ground deformation and that existing models to replace GRACE uncaptured degree-one components are not necessarily appropriate for modeling seasonal horizontal displacements. We then question the validity of a purely elastic model derived from seismic measurements at an annual time scale using seasonal observations. We show that including mantle volume variations due to phase transformations may improve the accuracy of our model. We also discard the use of a transient viscosity lower than  $5 \cdot 10^{17} Pa \cdot s$  using a Burger rheology in the asthenosphere, as for postseismic studies, that would significantly affect the seasonal deformation.

Once the seasonal deformation is modeled, the question of the role of the associated small periodic stress perturbations in the seismic cycle arises. Indeed, numbers of studies suggest the existence of a correlation between seasonal hydrological forcing and seismicity (Bollinger et al., 2007, Heki, 2003). However, the mechanisms of the effect of periodic surface loading on seismicity remain unclear. In *Chapter 4*, we propose to **experimentally investigate the effect of small cyclic pore pressure oscillations on the acoustic emissions of a creeping rock sample**. Even if only preliminary, our experiments suggest that the modulation of laboratory earthquake by small periodic pore pressure variations depends on the state of stress of the rock.

In this *Chapter 1*, we first present geodetic datasets essential to the work that will follow. We also review previous studies of seasonal deformation and point out potential models incompleteness that motivated at first this thesis. Finally, we discuss the occurrence of seasonal seismicity and its relation with surface loading.

## **1.1 Measuring seasonal deformation and mass variations**

### **1.1.1 Quantifying deformation with Global Positioning System**

With the development of artificial satellites since the early 1960s, positioning satellites constellations, also called Global Navigation Satellite System (GNSS) have been replacing ground localization systems. The most famous of the GNSS is the Global Positioning System (GPS), developed in the United States for military purposes since the 1970s, and operational since the early 1990s. It was rapidly followed by competitors such as the russian GLONASS, the european GALILEO or the chinese BeiDou system.

All these satellite positioning systems use the same positioning principle, inspired by classical triangulation methods. Each satellite continuously sends a signal with an information on its position and the precise time of emission, determined by an on-board atomic clock). Receivers on the ground measure the reception time of these signals from all visible satellites. The receiver position is given by solving a system of equations with four unknowns: the position (latitude and longitude) of the receiver, its altitude and the bias from the time measure of the receiver. Thus, four satellites are required to determine a receiver geographical position.

## Chapter 1. Seasonal forcing of the Earth: State of the art

For a receiver to function anywhere on the globe, it needs to see at least four satellites at any time, positioned as uniformly as possible. A constellation of 24 satellites, at a 20 000 km distance of the Earth surface is the minimum required for a working GPS. In order to improve the precision of positioning, numbers of analysis methods and correction techniques have been developed over the past decades, leading to a millimeter positioning precision. A

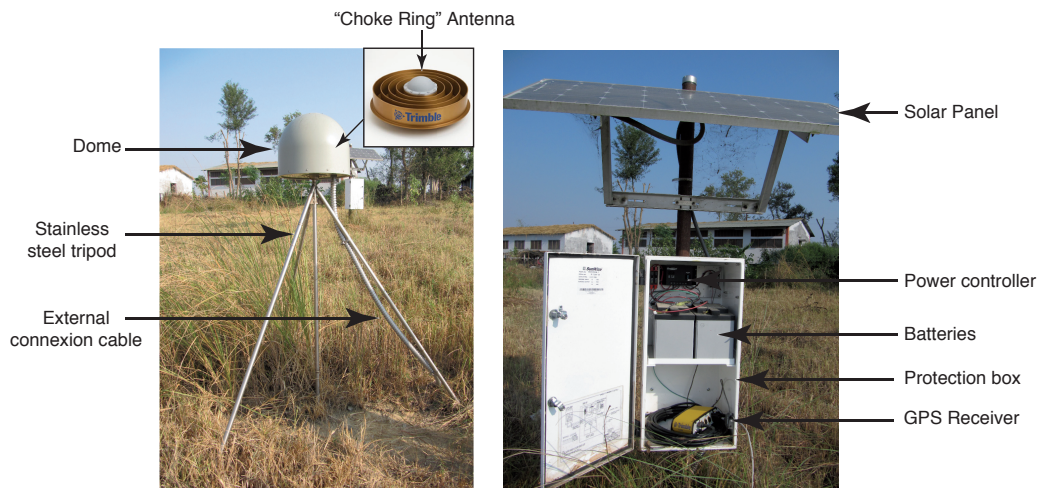


Figure 1.1 – Photos of continuous GPS station NPGJ in Nepalganj, South-West Nepal

typical continuous station is composed of an antenna, protected by a dome and mounted on a quadpod made of stainless steel and strongly anchored in the ground. The antenna is linked to a GPS receiver recording signals from satellites visible by the antenna. The system is powered by solar panels and batteries. Figure 1.1 shows photos of a continuous GPS (cGPS) station located in Nepal as an example. Thanks to the high precision of site positions, cGPS stations record the central observation of this thesis: small seasonal displacements (Van Dam et al., 2001). Figure 1.2 shows, on the left, raw displacements at site LHAZ in Tibet. The obvious signal here is the convergence between India and Eurasia, clearly visible on horizontal components, associated with a small vertical uplift. On the right, detrended time series are shown. Seasonal displacements can be observed clearly on the north and vertical components. These seasonal signals are measurable at a global scale, with various amplitudes and have been satisfyingly explained, at least for the vertical component, as the elastic response of the Earth to mass variations in the hydrosphere (Van Dam et al., 2001, Davis et al., 2004, Bevis et al., 2005, Bettinelli et al., 2008, Steckler et al., 2010, Elósegui et al., 2003, Fu & Freymueller, 2012, Fu et al., 2012, Wahr et al., 2013, Fu et al., 2013).

## 1.1. Measuring seasonal deformation and mass variations

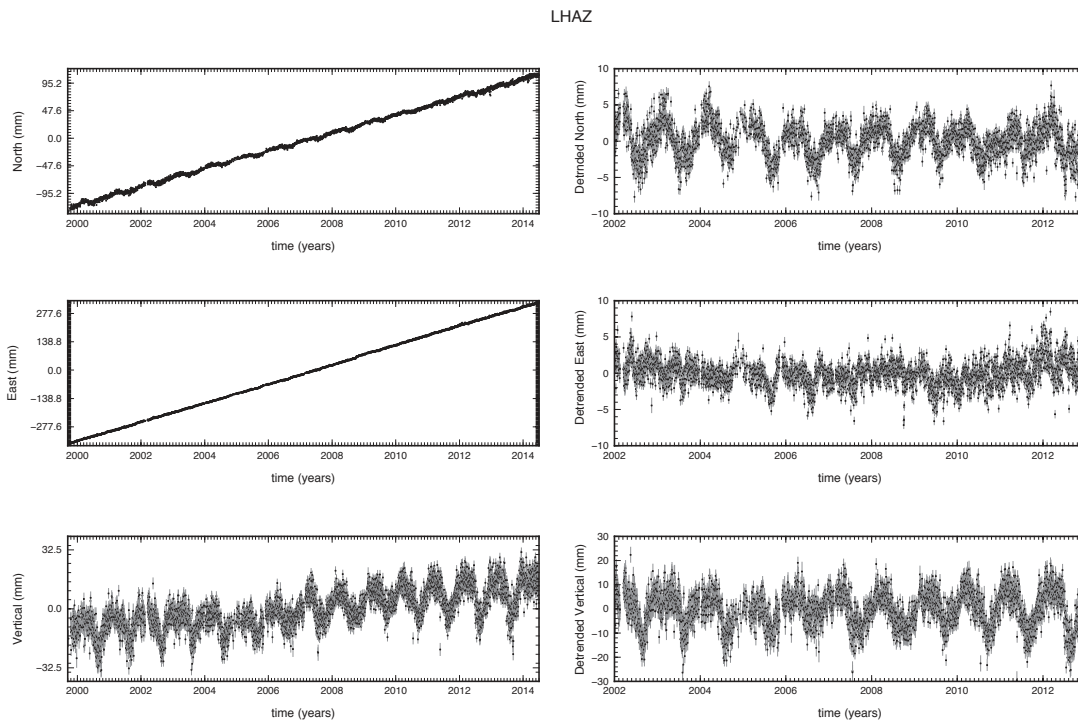


Figure 1.2 – GPS secular (left) and seasonal (right) site positions at station LHAZ located in Lhasa, China, with associated  $1\text{-}\sigma$  uncertainties.

### 1.1.2 Estimation of surface mass redistributions from satellite gravity measurements

In order to model seasonal deformation observed in GPS time series as the response of the Earth to seasonal hydrology, one needs an estimate of global redistribution of hydrosphere masses. Recent advances in geodesy have permitted global measurements of the variations in the Earth gravity field, giving access to this surface mass redistribution. In this work, we take advantage of the Gravity and Recovery Climate Experiment (GRACE), an international project coordinated by the American and German spatial agencies: NASA and DLR (Tapley et al., 2004).

The mission's goal is to map the spatio-temporal variations of the Earth gravity field with a 1 cm geoid height precision over 275 km. GRACE, launched in March 2002 and initially planned for 5 years, is still working and up to now, has offered 12 years of valuable gravity field variations measurements.

The mission is composed of two satellites, flying in tandem, on a quasi-polar orbit and a distance of approximately 220 km. The satellites undergo the orbit perturbations induced by the non-uniform Earth gravity field. Indeed, the gravity field is directly related to the distribution of mass on Earth and the gravity force applied on a satellite in orbit is thus a function of the mass it flies over.

All perturbations induce variations of the distance between satellites, which is later on used to determine variations in in gravity field. GRACE satellites fly around the Earth 15 times per day, leading to a 10 days time resolution for the global gravity field variations.

After correcting GRACE data from all known and modeled time-varying phenomena that affect the Earth's gravity field, and estimate and remove long term trends and large co-seismic contributions, GRACE gives access to redistributions of large scale surface mass, mainly continental water and oceanic and atmospheric masses, difficult to measure in-situ ([Lemoine et al., 2007](#), [Ramillien et al., 2008, 2005](#)). Figure 1.3 shows global seasonal peak to peak amplitudes of equivalent water height between March 2002 and August 2012. Signals from continental water variations are dominant: from precipitation cycles (Amazon, Asia, Africa) or snow and ice changes (Canada, Alaska, Russia).

## 1.2 Modeling seasonal deformation induced by surface hydrology

### 1.2.1 The trampoline effect

The two sets of geodetic data presented in 1.1, GPS and GRACE, can be linked using a simple assumption: the Earth responds to surface loading. As shown in Figure 1.4, during the loading season, GPS stations located around the loading area will record a vertical down-lift and an horizontal motion towards the load. The opposite occurs during the unloading season: stations will record a vertical uplift and be pulled away from the loading area. Of course, the rheology of the Earth is crucial to describe the observed deformation at GPS sites, as the response of the Earth to seasonal loading derived from GRACE.

## 1.2. Modeling seasonal deformation induced by surface hydrology

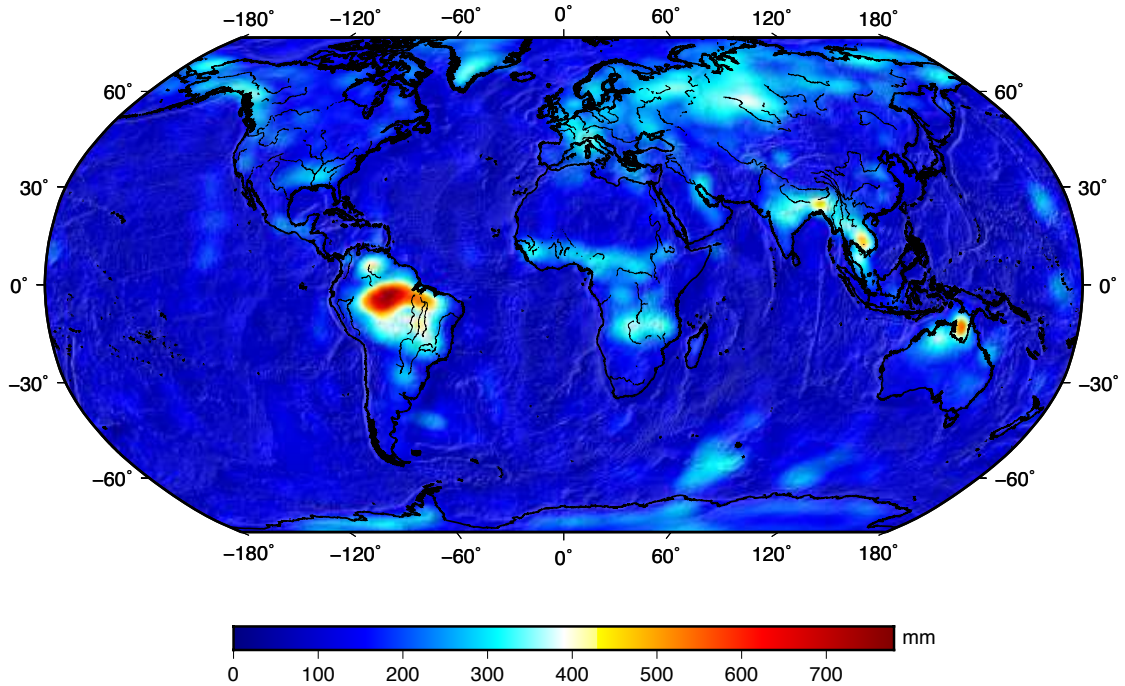


Figure 1.3 – Peak to Peak amplitude of global seasonal Equivalent Water Height derived from GRACE (mm).

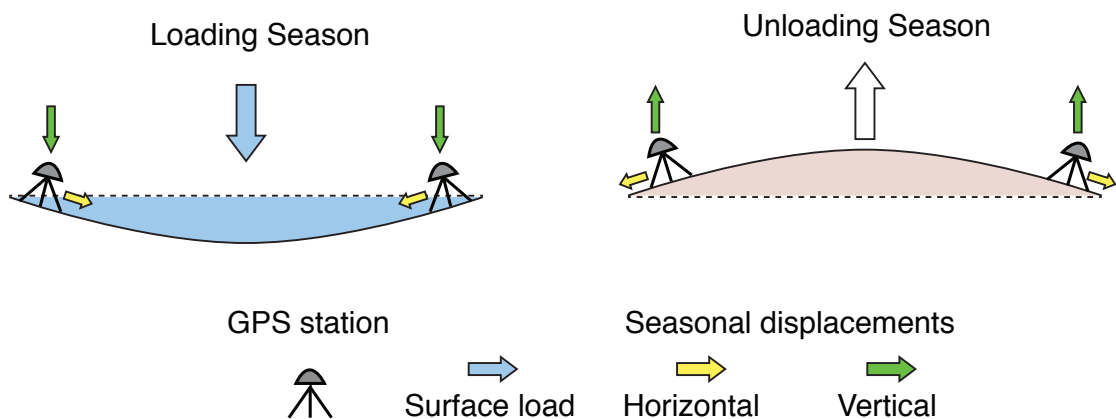


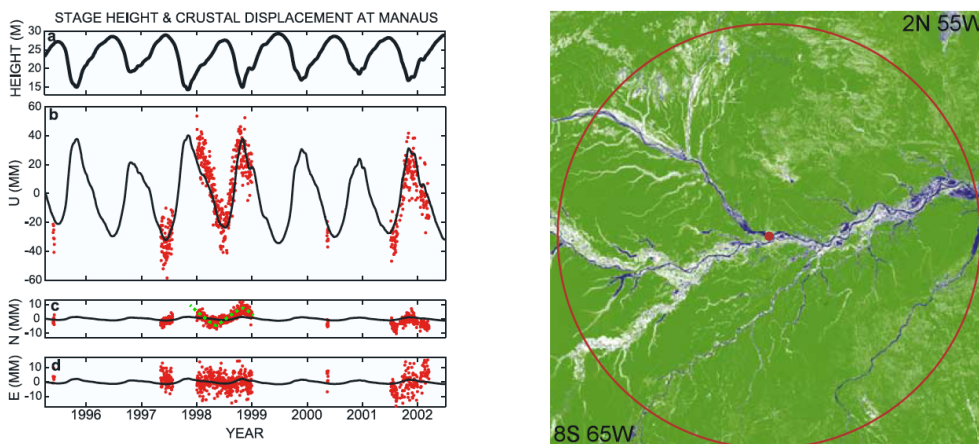
Figure 1.4 – Scheme of seasonal deformation at GPS sites induced by surface loading and unloading.

### 1.2.2 Regional models

When modeling surface deformation induced by variations in surface load, one needs to choose a model for Earth. Recently, several studies have proposed simple elastic homogeneous half-space models and predicted seasonal horizontal and vertical displacements induced by variations in hydrology at a regional scale. However, it has been well established

by Farrell (1972) for several decades now that a spherical and layered model is the correct one to model both horizontal and vertical components simultaneously. The reason for ignoring this statement is that a simple analytic solution to the surface loading problem for a elastic homogeneous half-space exists, the Boussinesq approximation and gives satisfying results for horizontal and vertical components separately once the elastic parameters of the model, the Young's modulus and the Poisson ratio, are estimated to best-fit a single component of the GPS observations.

The first study looking at seasonal deformation using a Boussinesq approximation was proposed by Bevis et al. (2005). The authors observed an annual cycle in GPS measurements at station MANA located in Manaus, in the middle of the Amazon basin, with peak to peak amplitude reaching 50 to 75 mm (Figure 1.5 (a)). They use a simple model to relate the esti-



(a) Stage height in Manaus and vertical, north and east geodetic displacements at MANA (b) Pattern of flooding around MANA

Figure 1.5 – Figures from Bevis et al. (2005). Stage height in Manaus (solid black line). Vertical, north and east geodetic displacements at MANA (red dots) with model predictions using a Boussinesq approximation (solid black lines). We added a green dashed line on the north component to highlight the misfit of the model.

mate of the Amazon river height variations to the regional flooding pattern (Figure 1.5 (b)) and argue that the seasonal vertical deformation at MANA is a direct elastic response of the Earth to surface hydrology in the surrounding 200 km. Their best-fitting model to the vertical component is obtained with an "effective" Young's modulus value of 137.3 GPa. Note that the model is insensitive to the Poisson's ratio which can be fixed to 0.25. Using this result,

## 1.2. Modeling seasonal deformation induced by surface hydrology

which can be related to global 1D models at a given depth, the authors claim that GPS seasonal measurements can be used to place constraints on the crustal elastic structure of the Earth. But the physical meaning of an effective Young's modulus is unclear as this model does not explain satisfyingly the horizontal observed displacements as shown by the green dashed line on Figure 1.5 (a).

As a consequence, other studies, using a similar approach, found significantly different values of the Young's modulus when including the horizontal component of the deformation. First,

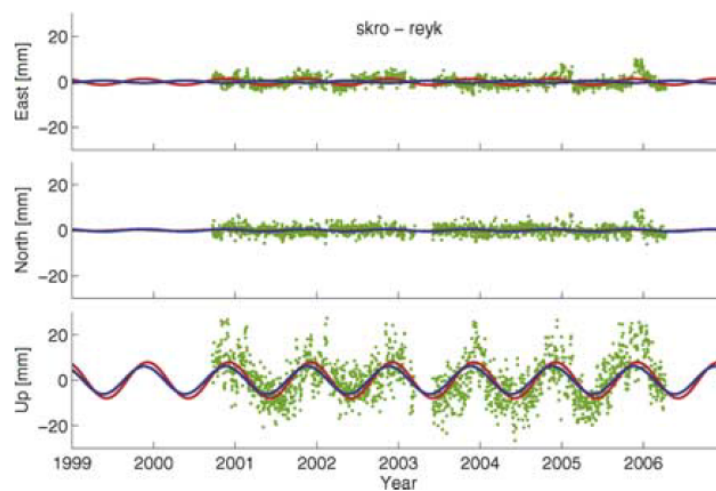


Figure 1.6 – Figure from (Grapenthin et al., 2006). Comparison of observed displacements at station SKRO, Iceland (green dots and best fitting function to the time series in red) and predicted seasonal signals using a sinusoidal loading history on an elastic half-space with a Young's modulus of 40 GPa (blue line).

Grapenthin et al. (2006) observed a strong annual signal in time series of GPS stations located in Iceland. As Bevis et al. (2005), the authors modeled these displacements as the response of an elastic homogeneous half-space using a simple sinusoidal load history for islandic ice caps. A best-fitting value for the Young's modulus of 40 GPa is proposed for a set of cGPS stations, and the variability of the best-fitting Young's modulus at each station is proposed to correlate with the age of the bedrock in Iceland. However, the meaning of this effective Young's modulus and geological explanations of its values seem questionable as the fit to the data is not entirely satisfactory. For example, Figure 1.6 shows an example of observations and predictions at station SKRO, Iceland. The East component shows a non-negligible misfit between the best-fitting sine function to the seasonal observations (red line) and the predicted

## Chapter 1. Seasonal forcing of the Earth: State of the art

displacements (blue line). While the vertical component is fairly well predicted by the model, the east component is underestimated and not in phase with the model.

Similarly, [Bettinelli et al. \(2008\)](#) using GRACE data as a loading input in the Himalayan

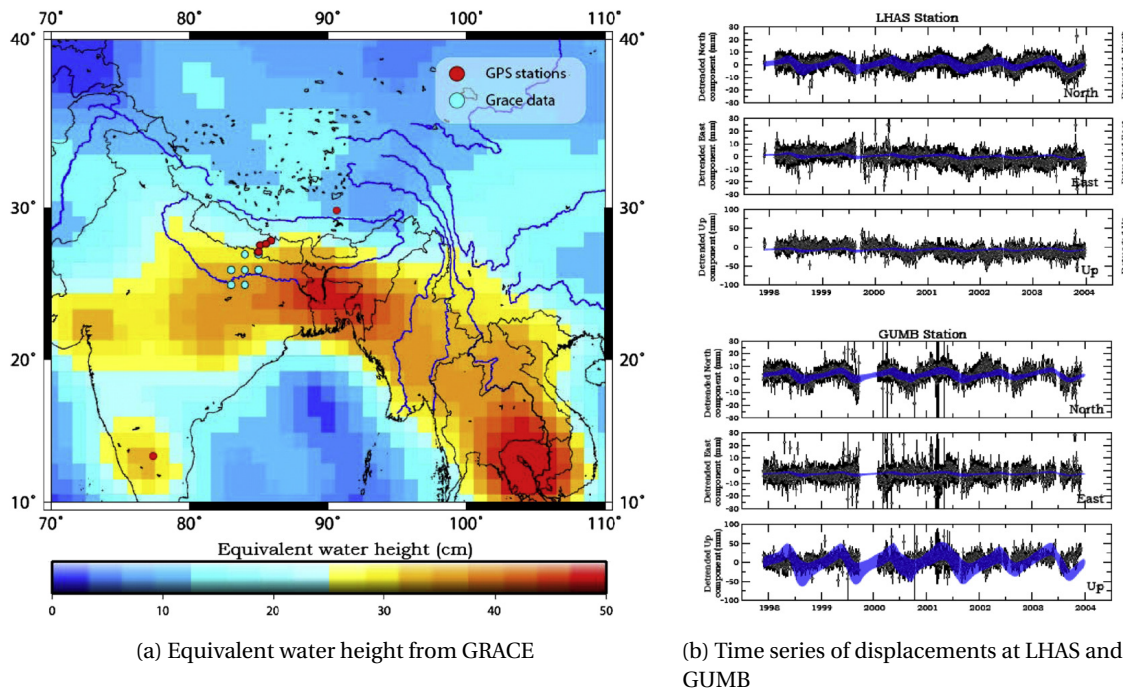


Figure 1.7 – Figures from [Bettinelli et al. \(2008\)](#). (a) Peak to Peak seasonal amplitudes of equivalent water height derived from GRACE. (b) Observed and predicted seasonal north, east and vertical displacements at GPS sites LHAS, Tibet and GUMB, Nepal. Predictions are computed using an elastic half-space model assuming a Young's modulus of 40 GPa.

region (Figure 1.7 (a)), also determined a best fitting Young's modulus for an homogeneous half-space of 40 GPa over or under-predicting vertical displacements, at depending on the station as shown on Figure 1.7 (b).

Finally, [Steckler et al. \(2010\)](#) modeled only the seasonal vertical displacements due to variations in surface hydrology in Bangladesh using an uniform elastic half-space. Their best-fitting values for the Young's modulus range between 117 and 135 GPa (Figure 1.8 (a)), and proposed that these estimates lie between local sediment (30-75GPa) and mantle (190GPa) values, indicating that response to loading is sensitive to structure throughout the lithosphere and is not

## 1.2. Modeling seasonal deformation induced by surface hydrology

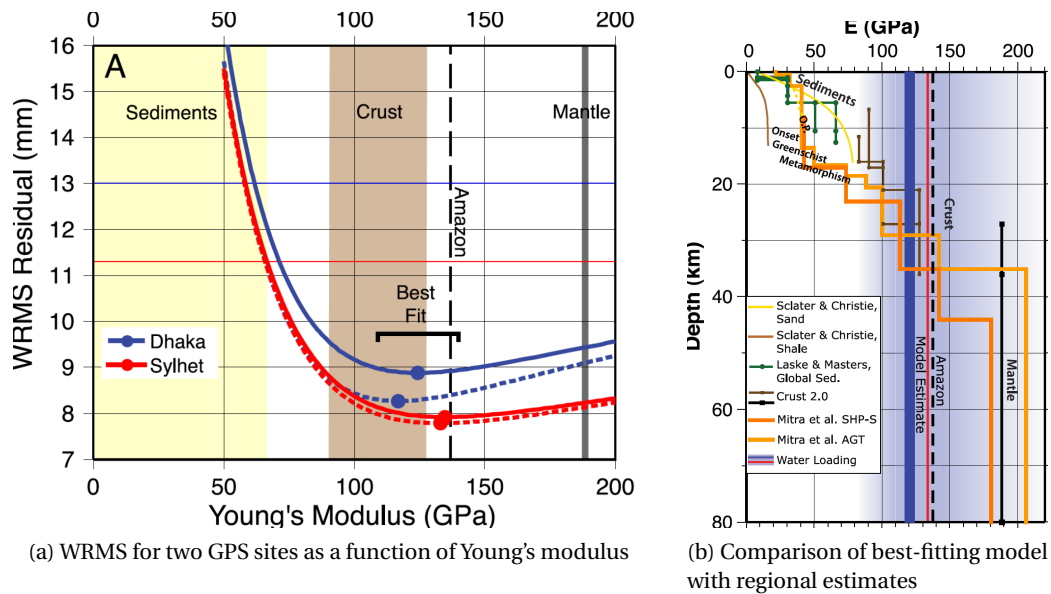


Figure 1.8 – Figures from [Steckler et al. \(2010\)](#). (a) WRMS misfit at two cGPS stations located in Bangladesh as a function of the Young's modulus, only parameter of the elastic half-space model. (b) Comparison of best-fitting Young's modulus with literature estimates. Blue and Red vertical lines correspond to stations in (a). Purple vertical band shows range of values derived in the author's study.

absorbed by the weak sediments.

Discrepancies in values of an effective Young's modulus between studies arise from the use of horizontal or vertical separately, and the various range of distances between observation stations and loading area when determining its best fitting value. Indeed, in a realistic spherical and layered Earth model, horizontal and vertical surface displacements have different distance dependent responses to a load, as already shown by [Farrell \(1972\)](#) for tidal loading.

One of the first motivations of my work, in *Chapter 2*, was to show that, even at regional scales, seasonal deformation modeled as the response of an elastic homogeneous half-space models could not be used to infer local elastic properties of the Earth as a single model could not model both horizontal and vertical components satisfyingly.

### 1.2.3 Global models

Several studies used more realistic models for Earth to investigate the seasonal deformation of the Earth. These models are based on [Love \(1911\)](#) which marked a turn in models of the Earth by proposing a general solution to the elastic Earth deformation problem. He showed that the deformation can be expressed using two numbers,  $h$  and  $k$ , the Love numbers. The number  $h$  gives the amplitude of surface deformation (ground uplift) while  $k$  give the amplitude of the gravity potential perturbations induced by the Earth deformation (the change in the Earth figure induces a its attraction capacity). Later on, [Shida \(1912\)](#) added a third Love number,  $l$ , which was needed to obtain a complete overall description of the solid Earth's response to the tides.  $h$ ,  $k$  and  $l$  depend on the Earth's structure and particularly on its rigidity and density profile: they contain the physics of the problem. [Farrell \(1972\)](#) numerically computed the Love's numbers and Green's functions for the surface mass-load problem on an elastic spherical, stratified and gravitating problem. His tables have been largely used to compute the response of a realistic Earth model to seasonal loading.

[Van Dam et al. \(2001\)](#) convolved Farrell's Green functions with an estimate of surface load

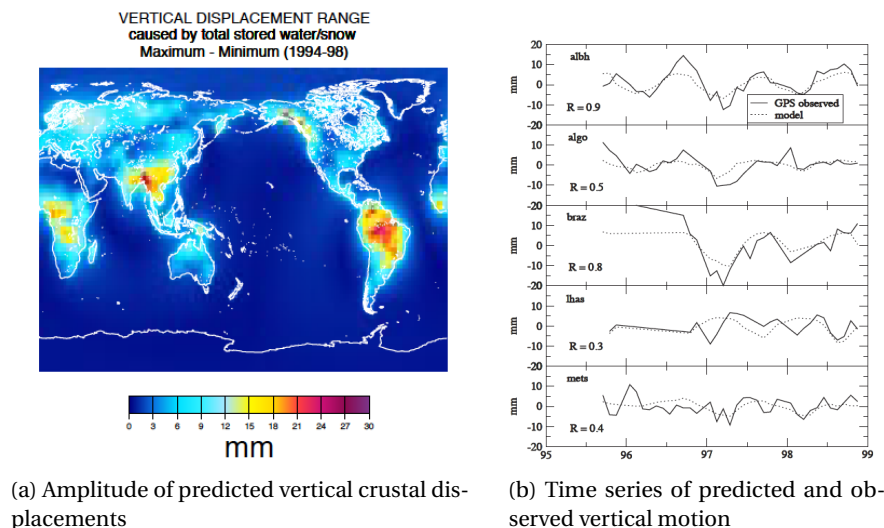


Figure 1.9 – Figures from [Van Dam et al. \(2001\)](#). (a) Maximum range in vertical crustal displacement during 1994-1998 in mm induced by variations in continental water storage. (b) Modeled vertical displacements (dotted lines) and observed monthly-averaged GPS height at selected sites, after correction from atmospheric pressure, tidal and non-tidal annual contribution (solid lines).

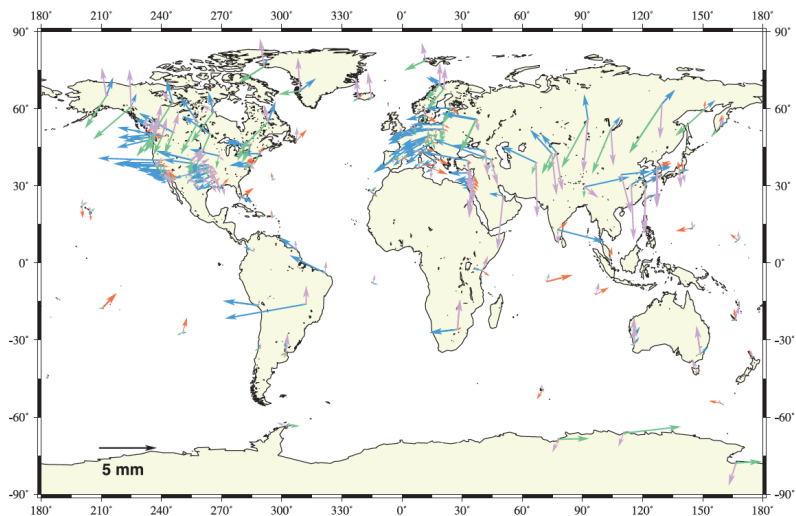
## 1.2. Modeling seasonal deformation induced by surface hydrology

---

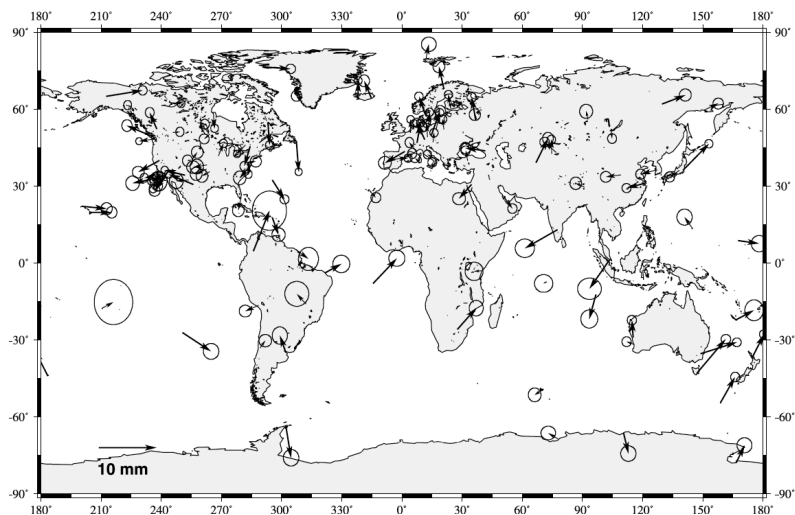
between 1994 and 1998 derived from several combined climate and precipitation models and predicted global vertical displacements (Figure 1.9 (a)). By comparing predictions with observations at 147 globally distributed GPS sites, they showed a good agreement between their model and GPS time series, with a significant variance reduction (Figure 1.9 (b)).

[Dong et al. \(2002\)](#) further investigated the question, listed and tested numbers of potential contributors to the observed vertical seasonal signals in GPS site positions. They showed that ~ 40 % of the observed annual vertical signal can be explained by the joint contribution of surface hydrological mass redistribution (atmosphere, non-tidal ocean, snow, and soil moisture). Figure 1.10 (a) shows individual contribution of each of these factors and (a) shows the final residuals after all mentioned load corrections have been estimated and applied. Note that there are still unmodelled signals that if not understood and accurately modeled may bias site velocity estimates.

The study by [Davis et al. \(2004\)](#) marked a turn in global seasonal deformation models by using a global estimate of mass redistributions inferred from gravity measurements, with a high spatio-temporal resolution, derived from GRACE. Focusing on the Amazon region, they found that the radial displacement predictions from GRACE measurements correlated well with observed seasonal signals at cGPS stations, as shown by Figure 1.11. This conclusion demonstrated that GRACE can provide a reliable estimate of the seasonal mass variations at the Earth's surface and help understanding seasonal deformation of the Earth. However, one major issue when using GRACE to study global seasonal deformation is the reference frame issue as pointed out by [Davis et al. \(2004\)](#). Indeed, the GRACE data are acquired by two co-orbiting satellites that respond to changes in the gravity of the total Earth system (solid Earth and fluid envelopes) as explained in section 1.1.2. Deformations inferred from GRACE, contrary to GPS site positions, therefore have no degree-one contribution. Indeed, long wavelength mass redistribution, that is to say mass exchange from one hemisphere to the other upon the season, will induce a compression of the northern hemisphere, and associated expansion of the southern hemisphere during February to March. The opposite deformation will occur during August to September. This global mode of the Earth deformation has been first detected by [Blewitt et al. \(2001\)](#) in GPS records and will translate mostly



(a) Contributors to the vertical seasonal signal



(b) Residuals between data and modeled contributors in (a)

Figure 1.10 – Figures from Dong et al. (2002). (a) Atmosphere (purple), non tidal ocean (red), snow (green) and soil wetness (blue) caused vertical annual variations at 128 globally distributed site. Amplitude  $A$  and phase  $\phi$  are defined as  $A \sin(\omega(t - t_0) + \phi)$ . (b) Vertical annual terms after correction from (a).

into a global  $Z$ -translation and affect significantly globally distributed stations, differently for horizontal and vertical components. Comparisons between seasonal observations at GPS sites with predicted displacements induced by GRACE can thus provide insights on degree-one deformation.

## 1.2. Modeling seasonal deformation induced by surface hydrology

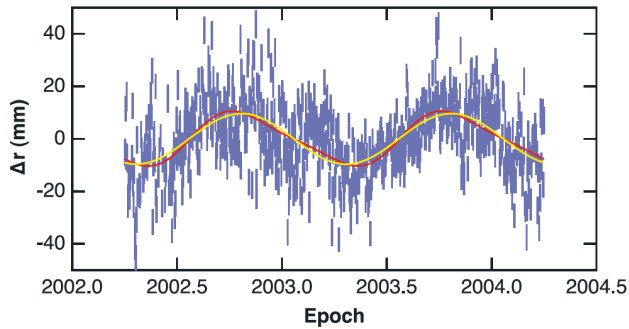


Figure 1.11 – Figure from [Davis et al. \(2004\)](#). Time series of observed vertical position at station BRAZ, Brasil and  $1-\sigma$  errorbars (blue), best-fit to the annual and semi-annual variations (red line) and predicted displacement from GRACE (yellow line).

As highlighted by Figure 1.12, this global mode of deformation can reach to 3 mm and 2 mm amplitude for vertical and horizontal displacements respectively. Note that compared to the observed seasonal signals arising from all wavelengths loading events, the understanding and accurate modeling of this global mode is a crucial for horizontal components.

Up to this point, most studies of seasonal deformation had focused on modeling vertical displacements, due to their larger amplitude. However, as we enter the age of millimeter precision in geodesy, more and more studies need to extract as accurately as possible seasonal vertical but also horizontal signals in order to improve plate velocity estimates and reference frame ([Blewitt & Lavallée, 2002](#)) and detect potential tectonic transient deformation ([Vergnolle et al., 2010](#)).

Transient deformation include, for instance, slow slip events detected using dense GPS arrays in subduction zones (Cascadia, Nankai, Guerrero, etc.). In the Cascadia area, [Dragert et al. \(2001\)](#) first evidenced the existence of these slow slip events on the subduction plane and later on, [Rogers & Dragert \(2003\)](#) showed their correlation with non-volcanic tremors as shown by Figure 1.13. In this area, these events usually last around 10 days and repeats with a period from 11 to 16 months. The amplitude of slow slip events on the East component are about 5 mm. Because of their periodic characteristic close to a year and a similar amplitude to seasonal non-tectonic deformation, accurate physics based models for seasonal horizontal displacements are necessary.

[Tregoning et al. \(2009\)](#) first proposed a global elastic model for both horizontal and verti-

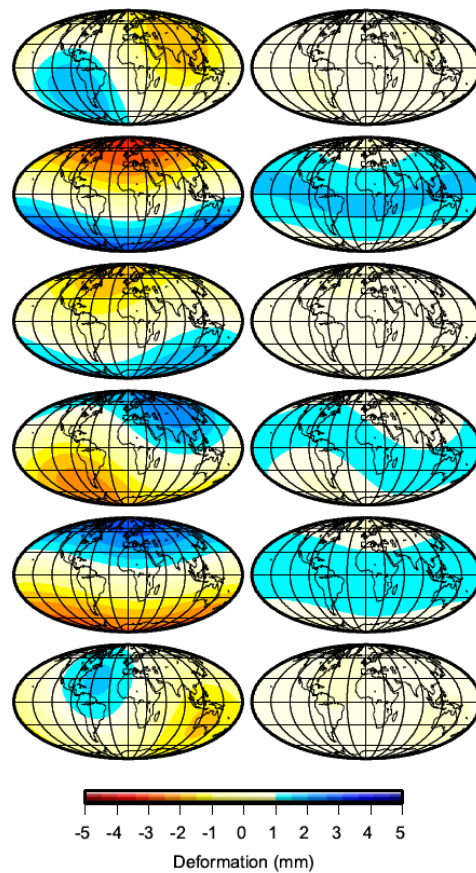


Figure 1.12 – Figures from [Blewitt et al. \(2001\)](#). Observed seasonal variations in the Earth deformation. Degree-one deformation uses two-month stacked solutions of (top to bottom) Dec-Jan to Oct-Nov for vertical (left) and horizontal (right) components.

cal displacements induced by continental water load estimates derived from GRACE, where degree-one contribution have been inserted into the GRGS spherical harmonic field using results from [Munekane \(2007\)](#). The authors find a good correlation between model and observations at GPS sites, in regions where a strong hydrological load occurs, with a better correlation for the vertical component (Figure 1.14, BRAZ). However, the study reports many examples where the horizontal component is out of phase and underpredicted (Figure 1.14, DARW, MATE, POTS). The authors suggest that the misfit might be caused by a geophysical process that is affecting the two observation techniques differently (local hydrological process might affect a GPS time series significantly but be too small spatially to be detected by GRACE).

## 1.2. Modeling seasonal deformation induced by surface hydrology

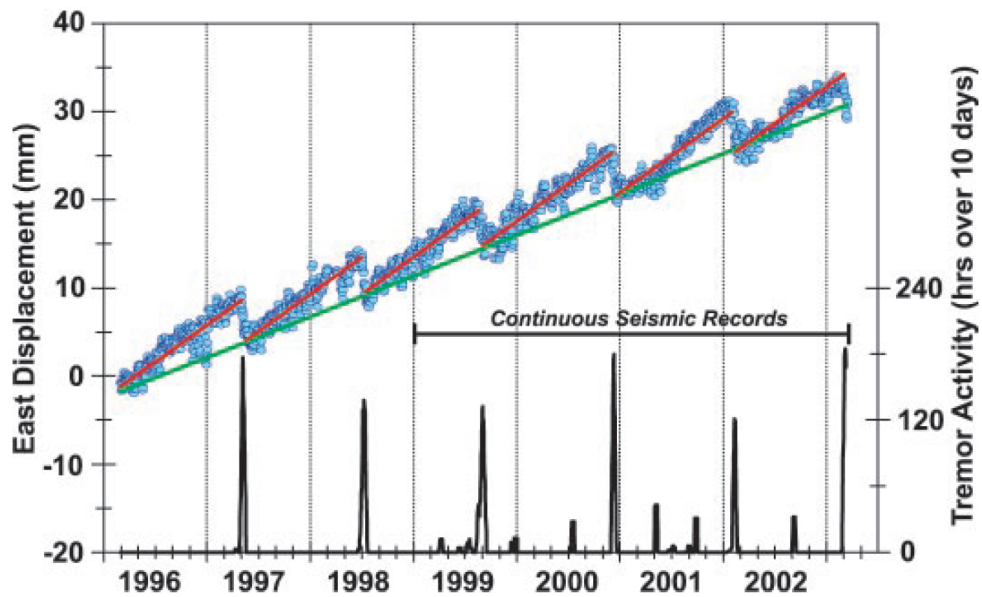


Figure 1.13 – Figures from [Rogers & Dragert \(2003\)](#). Comparison of slip and tremor activity observed for the Victoria area. Blue circles show day-by-day changes in the east component of the GPS site ALBH. The continuous green line shows the long-term eastward motion of the site. Red line segments show the mean elevated eastward trends between the slip events, which are marked by the reversals of motion every 11 to 16 months.

Recently, another study by [Fu et al. \(2013\)](#) tackled the seasonal horizontal displacements problem. The authors compared seasonal observations at GPS stations in the Nepal Himalaya and in the Amazon basin with predicted displacements from GRACE, where degree-one components were replaced using [Swenson et al. \(2008\)](#). They state that both observed and predicted displacements are consistent and attribute discrepancies between observations and model to local effects that would influence GPS measurements and not be captured by GRACE due to its large wavelength spatial resolution. However, from Figure 1.15, the author's model is in good agreement with vertical GPS measurements in both areas (blue and light blue arrows). Therefore, the local effects argument to explain large discrepancies between predictions and observations seem unlikely (green and red arrows). This misfit is also observed when using elastic-half space models ([Bevis et al., 2005](#), [Bettinelli et al., 2008](#)).

The misfit observed between horizontal observations and predictions brings up interesting questions:

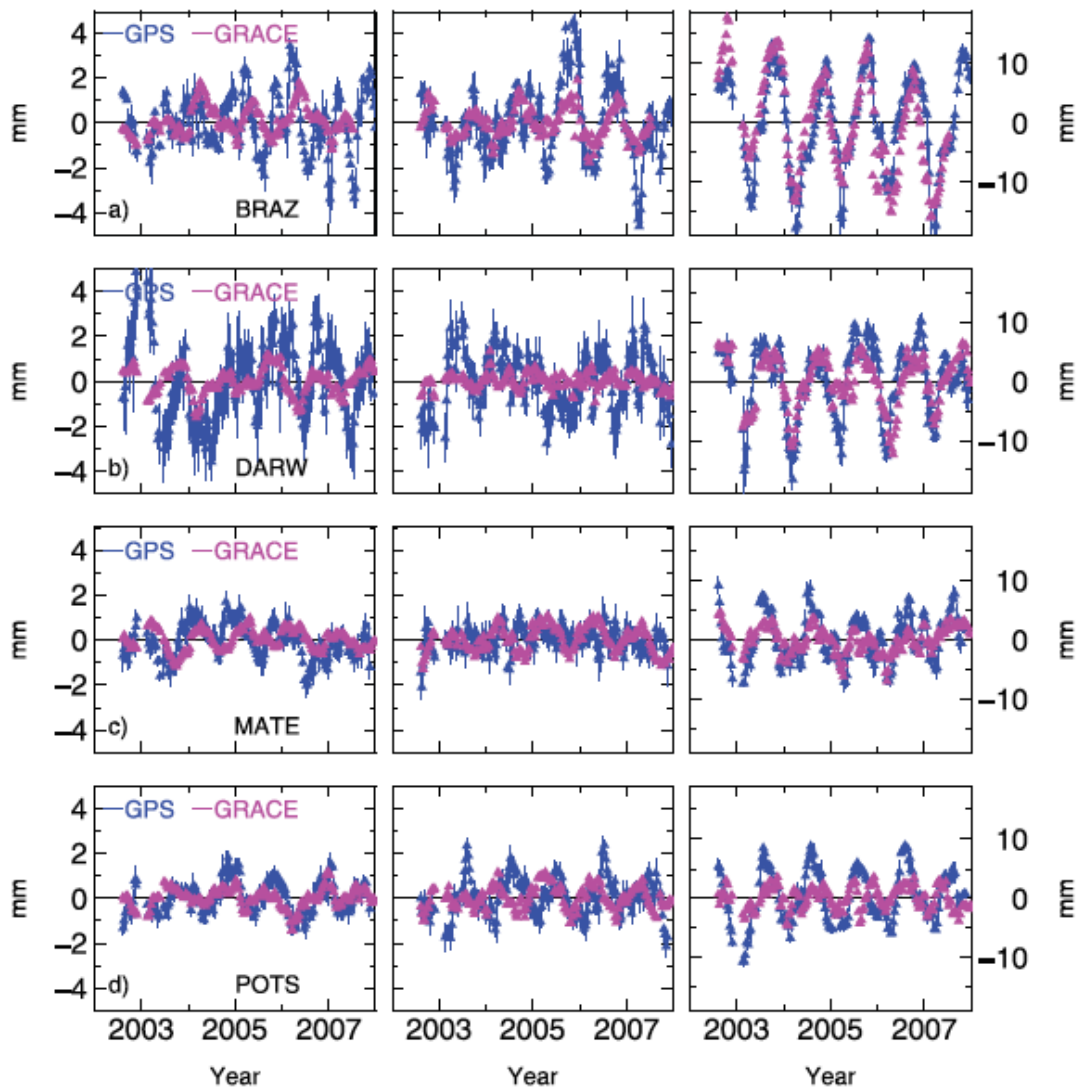
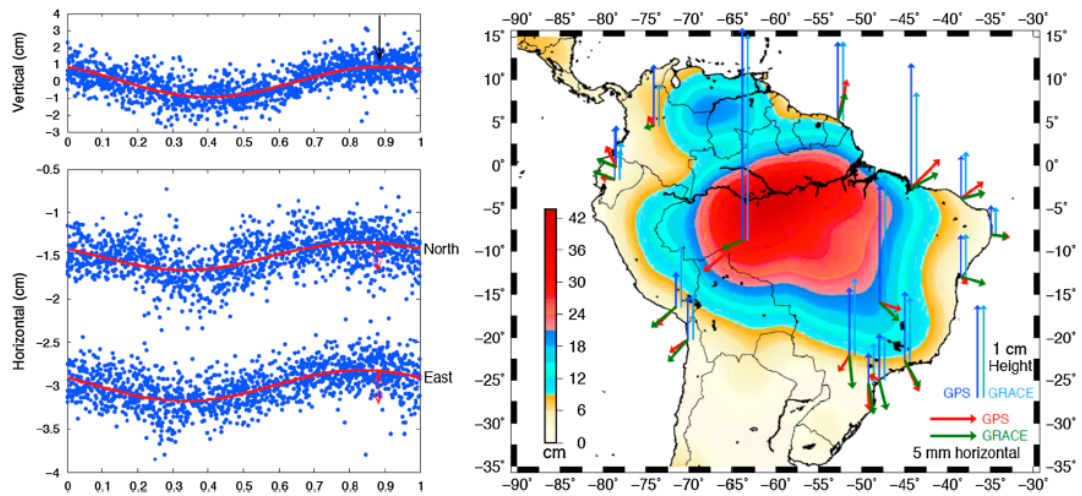


Figure 1.14 – Figures from [Tregoning et al. \(2009\)](#). Time series of GPS coordinate anomalies (blue) with elastic deformation computations superimposed as derived from GRACE surface load estimates (pink) for Brasilia, Brazil, Darwin, Australia, Matera, Italy and, Potsdam, Germany.

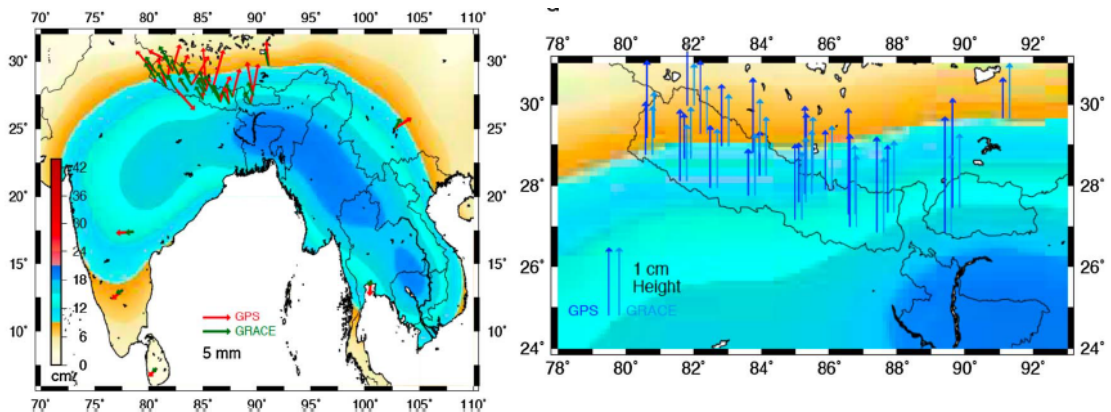
1. Why would the vertical predictions of seasonal displacements be more convincing than the horizontal ones?
2. Is this a global or local phenomena?
3. What potential contributors to the misprediction of the horizontal seasonal signal?

The second motivation of my work was therefore to further investigate horizontal seasonal displacements, regionally in *Chapter 2* and globally in *Chapter 3*, and try to reconcile the

### 1.3. Periodic variations of seismicity



(a) Seasonal observations and predictions around the Amazon basin



(b) Seasonal observations and predictions in South Asia

Figure 1.15 – Figures from Fu et al. (2013). (a) Example (GPS station SALU) of the strategy used to derive the peak to peak amplitude and phase of the seasonal vectors (left). Horizontal observed and predicted seasonal vectors for stations around the Amazon Basin (red and green). Similarly, blue and light blue are for the vertical component (left). (b) Results for South Asia.

model with the observations.

### 1.3 Periodic variations of seismicity

As described in the preceding, the Earth undergoes periodic loading, deforming its surface and inducing periodic stress perturbations. These perturbations are created by solid Earth and oceanic tides, with an amplitude of a few kPa (Bettinelli et al., 2008), or by the seasonal hy-

drology cycles. Earthquakes may be triggered or modulated by these forces, implying a causal link between small periodic loading and the mechanical behavior of the upper crust (Saar & Manga, 2003, Christiansen et al., 2005). Stresses induced by periodic loads have been shown to be sufficient to fracture near-critically stressed rocks either through pore pressure diffusion (Talwani, 1998, Hainzl et al., 2006) or the elastic response of the Earth to loading and unloading (Bollinger et al., 2007, Heki, 2003). However, the link between periodic stress perturbations and seismicity remains unclear. Of course the amplitude and frequency of perturbations play a role in the triggering or modulation of seismicity, but other parameters may be important. For instance, and experimental results may provide insights on the mechanisms controlling the observed seismic periodicities in some regions.

In the Himalaya, a strong correlation between seasonal deformation induced by the Monsoon cycle and seismicity has been observed (Ader & Avouac, 2013, Bettinelli et al., 2008, Bollinger et al., 2007). This signal has been attributed to the normal and shear stress variations on the Main Himalayan Thrust (MHT) induced by the seasonal hydrological load driven by the Monsoon cycle. Indeed, during the summer, the load on the Ganges basin, inducing stress on the MHT, with an estimated amplitude of 3 kPa (Bettinelli et al., 2008), and the opposite occurs over the winter as shown on Figure 1.16.

Seismicity in Nepal is shown on Figure 1.17 and exhibits clearly an annual periodicity. This seasonality correlates with the detrended horizontal North-South displacements observed at cGPS station DAMA located in Nepal.

Other studies show a correlation between seasonal forcing and seismicity in other regions (Heki, 2003, Saar & Manga, 2003, Christiansen et al., 2005, Costain & Bollinger, 1996, Braunmiller et al., 2014). In addition, the tidal forcing has also been shown to correlate with seismicity (Métivier et al., 2009, Cochran et al., 2004, Thomas et al., 2012, Tanaka et al., 2002, 2004, Ide & Tanaka, 2014). However, the correlation is not always obvious as show by Vidale et al. (1998), and the parameters controlling dynamic triggering of earthquakes by small periodic stress perturbations are unclear. Of course, the amplitude and frequency of stress oscillations are of importance. In a rate and state frame work, largely used to model faults behavior, the critical threshold is determined by a competition between loading and healing (Dieterich, 1994,

1979). It has been proposed that short-period stress transients are not effective at triggering earthquakes if they occur faster than nucleation times (Dieterich, 1992). Lockner & Beeler (1999) estimated a nucleation time of  $\sim$  one year from stick slip laboratory experiments in a triaxial apparatus on granite samples, with a periodic loading function varying in frequency and amplitude. Later on, they used this estimate to explain the poor correlation between tidal loading and earthquakes (Beeler & Lockner, 2003). However, some robust studies suggest a strong correlation between Earth tides and earthquakes, and even at higher frequencies between dynamic triggering from seismic waves and earthquakes.

Another parameter which may play an important role in triggering or modulation of earth-

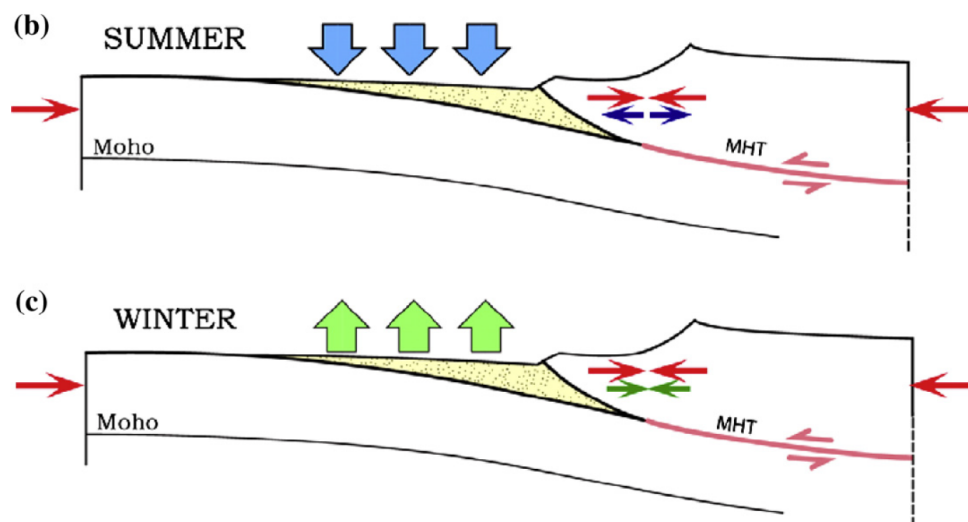


Figure 1.16 – Figure from Bettinelli et al. (2008). (b) In the summer, this seasonal strain implies horizontal extension at seismogenic depth (2–15 km, blue arrows) in the Himalaya, which reduces the effect of secular horizontal compression due to interseismic strain buildup (red arrows). (c) The opposite occurs in the winter so that unloading, as water level drops, implies some horizontal compression (green arrows) that adds to the secular interseismic contraction (red arrows).

quakes by perturbation loading is the state of stress of a fault. This idea is supported by the observation of an increase in correlation between tidal loading and seismicity localized in nucleation zones of large earthquakes: the Sumatra megathrust earthquakes of 26 December 2004 (Mw 9.0), 28 March 2005 (Mw 8.6), and 12 September 2007 (Mw 8.5) (Tanaka, 2010), and the 2011 Tohoku-Oki earthquake (Mw 9.1) (Tanaka, 2012). Intuitively, faults in a critical state

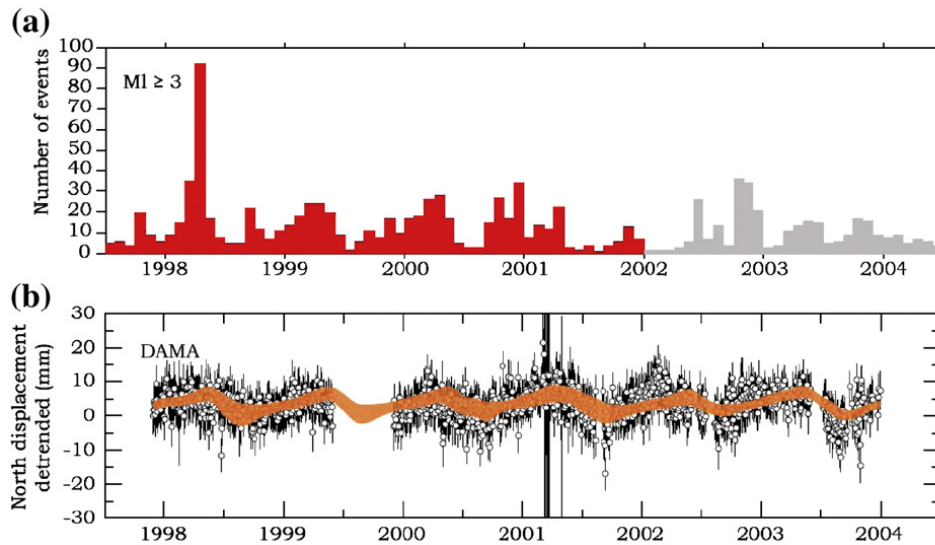
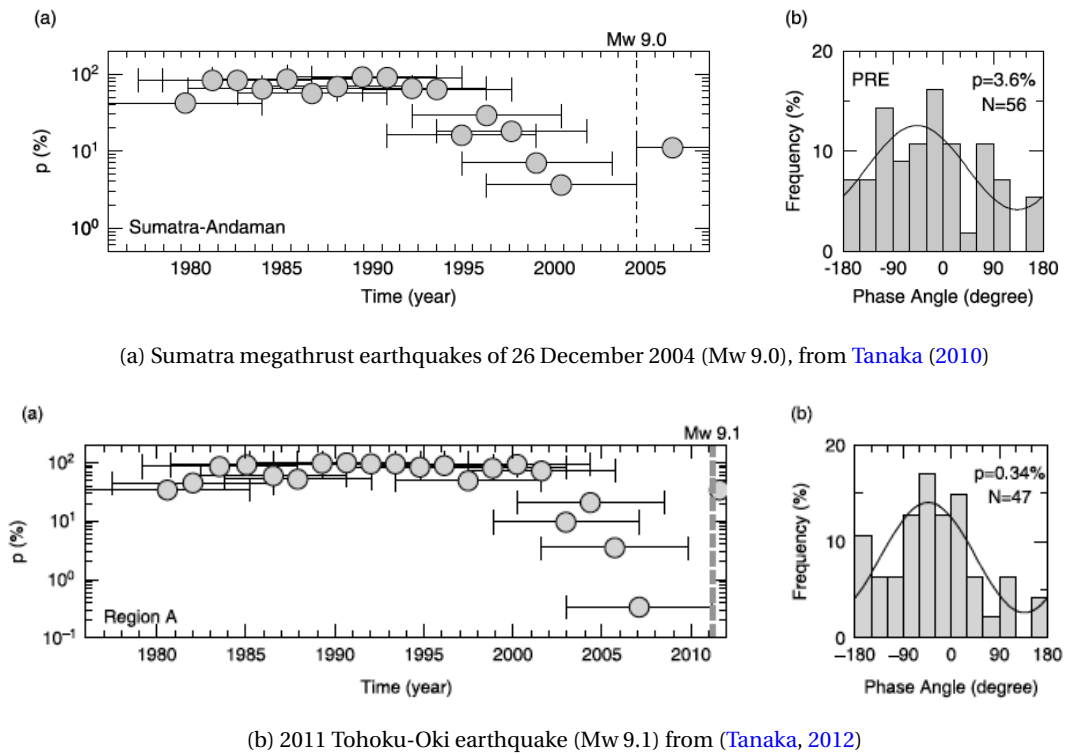


Figure 1.17 – Figure from [Bettinelli et al. \(2008\)](#). (a) Seismicity ( $M_I > 3$ ) is shown in red for the period over which the geometry of the seismic network has not changed. It is shown in grey for the period over which the detection level varied due to discontinuous operation of the seismic stations (the apparent drop in January 2002 in particular is an artifact of technical failure of about 50% of the seismic stations during that winter). Variations from the secular trend of the geodetic position shown for stations DAMA (b).

should be sensitive to small stress perturbations that may contribute, when added to a high pre-existing stress, to failure. On the contrary, faults far from failure would be insensitive to small periodic loading. Figure 1.18 shows the temporal evolution of p-value in nucleation regions the (a) Sumatra-Andaman and (b) Tohoku-Oki earthquakes. The p-value began to drop gradually with time, which lasted up to the occurrence of the mainshocks. Until then, the p-value had been stable, indicating the absence of significant correlation between tides and earthquakes over a  $\sim 10$  years time period. After the earthquakes, the p-value returned again to the level of insignificant correlation. Figure 1.18 also shows the phase distribution of earthquakes in the 3000 days prior to the earthquakes. Earthquakes occur more significantly when shear stresses enhancing slip are highest.

These observations motivated another part of my work, the estimation of global stress perturbations caused by seasonal hydrology. We were also motivated by testing experimentally the effect of the stress of state of a fault on dynamic triggering of acoustic emissions, to investigate in the laboratory interesting results from [Tanaka \(2010, 2012\)](#).

### 1.3. Periodic variations of seismicity



(a) Sumatra megathrust earthquakes of 26 December 2004 (Mw 9.0), from [Tanaka \(2010\)](#)

(b) 2011 Tohoku-Oki earthquake (Mw 9.1) from [Tanaka, 2012](#)

Figure 1.18 – Temporal variation of p-value in the area of nucleation of major earthquake. A time window of 3000 days, which is represented by horizontal bar, is shifted by 500 days and Frequency distribution of tidal phase angles in the 3000 days prior to the (a) Sumatra-Andaman and (b) Tohoku-Oki earthquakes. Solid curve represents a sinusoidal function fitted to the distribution.



## ELASTIC DEFORMATION INDUCED BY SEASONAL HYDROLOGY IN THE HIMALAYA

Mountains ranges have fascinated from explorers to scientists through history. The Himalaya, as the most impressive example of it, has attracted the curiosity of explorers who attempted and succeeded in climbing Himalayan peaks in the past few centuries helping to better constrain vertical elevation of the area. The highest mountains also interested geologists, for example Emile Argand, whose work marked a transition from traditional geology to modern geosciences and helped understanding the main geological structures of the region. [Argand \(1924\)](#) gives a first and general overview of orogeny and the tectonic history of Asia, as mentioned in the title of its work.

In the past decades, the advances in geodetic measurements revealed interesting informations about the long term evolution of the mountain range but also shorter deformation modes, such as seasonal variations of geodetic strain. [Bettinelli et al. \(2008\)](#) first showed that seasonal surface strain variations are measurable in the region and could be modelled as the Earth's response to annual changes in continental hydrology. Moreover, they related annual loading to variations of seismicity, already observed by [Bollinger et al. \(2007\)](#), possibly providing information on the potential failure of the main frontal thrust. This point will be discussed in chapter 4.

In this chapter, we show that seasonal geodetic deformation in the Himalaya can be fairly well explained by seasonal variations of continental water storage driven by the Monsoon cycle, for both horizontal and vertical surface displacements provided a realistic elastic Earth structure model. In order to improve the fit of the model to geodetic data, we adjust the Earth structure

parameters based on an inversion method, and discuss limits of this hypothesis.

**Modeling deformation induced by seasonal variations of  
continental water in the Himalaya region: sensitivity to Earth  
elastic structure**

K. Chanard<sup>1,2</sup>, J.P. Avouac<sup>1</sup>, J. Genrich<sup>1</sup> and G. Ramillien<sup>3</sup>

<sup>1</sup> Tectonics Observatory, Caltech, Pasadena, USA.

<sup>2</sup> Laboratoire de Géologie, Ecole Normale Supérieure, Paris, FRANCE.

<sup>3</sup> Géophysique Environnement Toulouse, FRANCE.

Published in J. of Geoph. Res.: Solid Earth, Volume 119, Issue 6, pages 5097–5113, 2014

---

**Abstract** Strong seasonal variations of horizontal and vertical positions are observed on GPS times series from stations located in Nepal, India and Tibet (China). We show that this geodetic deformation can be explained by seasonal variations of continental water storage driven by the Monsoon. For this purpose, we use satellite data from the Gravity Recovery and Climate Experiment (GRACE) to determine the time evolution of surface loading. We compute the expected geodetic deformation assuming a perfectly elastic Earth model. We consider Green's functions, describing the surface deformation response to a point load, for an elastic homogeneous half-space model and for a layered non-rotating spherical Earth model based on the Preliminary Reference Earth Model (PREM) and a local seismic velocity model. The amplitude and phase of the seasonal variation of the vertical and horizontal geodetic positions can be jointly adjusted only with the layered Earth model while an elastic half-space model fails, emphasizing the importance of using a realistic Earth elastic structure to model surface displacements induced by surface loading. We demonstrate, based on a formal inversion, that the fit to the geodetic data can be improved by adjusting the layered earth model. Therefore the study also shows that the modelling of geodetic seasonal variations provides a way to probe the Elastic structure of the Earth, even in the absence of direct measurements of surface load variations.

---

## **2.1 Introduction**

Geodetic time series recorded by the Global Positioning System (GPS) have revealed that surface load variations can induce measurable surface strain. Variations of surface loading can result from various sources: tidal loading (Agnew, 1996, 1997), continental water storage (Blewitt et al., 2001, Bevis et al., 2005, Van Dam et al., 2001, Davis et al., 2004, Bettinelli et al., 2008, Steckler et al., 2010, Elósegui et al., 2003, Fu & Freymueller, 2012, Fu et al., 2012, Wahr et al., 2013), ice and snow (Grapenthin et al., 2006, Matsuo & Heki, 2010, Jiang et al., 2010) and atmospheric pressure (Kaniuth & Vetter, 2006). The analysis of these signals has attracted much attention. One reason is that GPS can provide a way to monitor mass variations of the hydrosphere or cryosphere which are rather difficult to monitor otherwise. Another reason is that correcting for these variations is important to measure accurately secular geodetic velocities (Blewitt & Lavallée, 2002) and to detect potential aseismic tectonic transients. It has been shown that, in some instance, surface load induced deformation had been misinterpreted as tectonic transients or had obscured subtle tectonic transients (Vergnolle et al., 2010). Finally, the measurements and modeling of the Earth response to surface load variations provides a way to probe the density and elastic structure of the Earth as has been shown recently from the analysis of geodetic deformation induced by oceanic tides (Ito & Simons, 2011).

In this study, we focus on the Himalaya region where the Monsoon regime induces large variations of continental water storage and where strong seasonal geodetic strain has been documented (Bettinelli et al., 2008, Steckler et al., 2010, Flouzat et al., 2009, Fu & Freymueller, 2012). Variations of continental water storage are actually measurable using satellite gravity measurements provided by the Gravity Recovery and Climate Experiment (GRACE) missions, as shown by Ramillien et al. (2008) for example (Figure 2.1) while geodetic displacements are measured by continuous GPS (cGPS) stations. The Himalaya region is also a place where deformation transients associated with Himalayan tectonics could be occurring but would have remained undetected so far.

In a previous study, Bettinelli et al. (2008) have modeled the geodetic strain expected from surface load annual variations, as determined from GRACE, and assuming an elastic half-space.

They found a relatively good fit with the GPS seasonal signal but noticed a difficulty to match simultaneously the amplitude and phase of the vertical and horizontal components. They were using data from a single transect across the Himalaya at the longitude of Kathmandu. This problem is even more conspicuous when data from cGPS stations more widely distributed over the Nepal Himalaya and India are considered (Figure 2.3). Here, we investigate further that issue and show that the amplitude and phase of the vertical and horizontal components of the seasonal strain are explained significantly better if a PREM layered spherical Earth model is considered rather than an elastic half space. However, the model does not explain perfectly the phase total amplitude of the observed seasonal signals. Keeping the elastic approximation, we then exploit geodetic displacements induced by seasonal variations of continental water storage to constrain a shallow depth dependent PREM-like regional model. In the following we present first the GPS and GRACE data analyzed in this study, and next our modeling and inversion results.

## 2.2 Presentation of the GPS and GRACE data used in this study

### 2.2.1 The GPS dataset

We use data from 3 IGS stations available in the study area and from the Geodetic network of Nepal (see stations location in Figure 2.1). The Nepal network consists of three cGPS stations which were installed in 1997 under a collaboration between the Laboratoire de Détection et Géophysique (CEA/LDG, France) and the Department of Mines and Geology (DMG, Nepal), and 25 stations which were deployed since 2003, by the Tectonics Observatory (<http://www.tectonics.caltech.edu>).

The daily station positions in ITRF2005 were computed from 24 hours GPS dual-frequency phase and code observations with the GAMIT/GLOBK processing software in a 2-step procedure (King & Bock, 2005, Herring, 2005). We used the GMF model for the tropospheric mapping function (Boehm et al., 2006) and estimated horizontal tropospheric gradients at each station. We include data sampled at a 2-minute interval from reference stations DGAR, GUAM, GUAO, HYDE, IISC, KUNM, LHAS, LHAZ, POL2, SELE, URUM and WUHN to obtain

## 2.2. Presentation of the GPS and GRACE data used in this study

---

a very loosely constrained regional solution. Satellite orbital parameters used were those published by IGS as final. The regional solution was combined with solutions at the normal equation level from five global IGS sub-networks (SOPAC IGS1 through IGS5) to arrive at final site positions.

The detrended time series, after removal of a best fitting linear trend, are shown in Figure 2.3 for 4 continuous GPS stations. The errorbars represent formal 1 standard deviations derived from the Kalman filter solution of the joint networks (Nepal regional network plus IGS1 through IGS5). They rely on tight position constraints for the IGS reference sites and assume that monument noise is white (Flicker noise is not accounted for). These time series show strong seasonal variations at all stations. The gray dots and error-bars represent a 10-day averaged signal used to reduce the daily scatter. The location of the three stations are plotted in Figure 2.1.

### 2.2.2 Continental regional water mass variations derived from GRACE Level-2 solutions

We are interested in seasonal variations of surface loading driven by surface hydrology. We take advantage of the data collected by the GRACE experiment, a tandem satellite mission launched in March 2002. GRACE provides a global mapping of the gravity field variations from monthly to decade time scales (Tapley et al., 2005), and thus gives access to redistributions of large-scale surface water mass (atmosphere, oceans, continental water storage) once the static geoid is corrected. Gravitational contributions of the known time-varying phenomena (tides, polar movements) are removed from the raw GRACE measurements, and then monthly and 10-day Level-2 solutions are obtained by least-square orbit adjustment of the residual observations for each period of time (Lemoine et al., 2007, Bruinsma et al., 2010).

Atmospheric and non-tidal oceanic loading contributions should not be corrected in the GRACE data as they are not accounted for in the GPS processing. We therefore add back the non-tidal ocean model forced by air pressure and wind on ocean: Mog-2D (Carrère & Lyard, 2003), provided by the European Centre for Medium-Range Weather Forecasts (ECMWF).

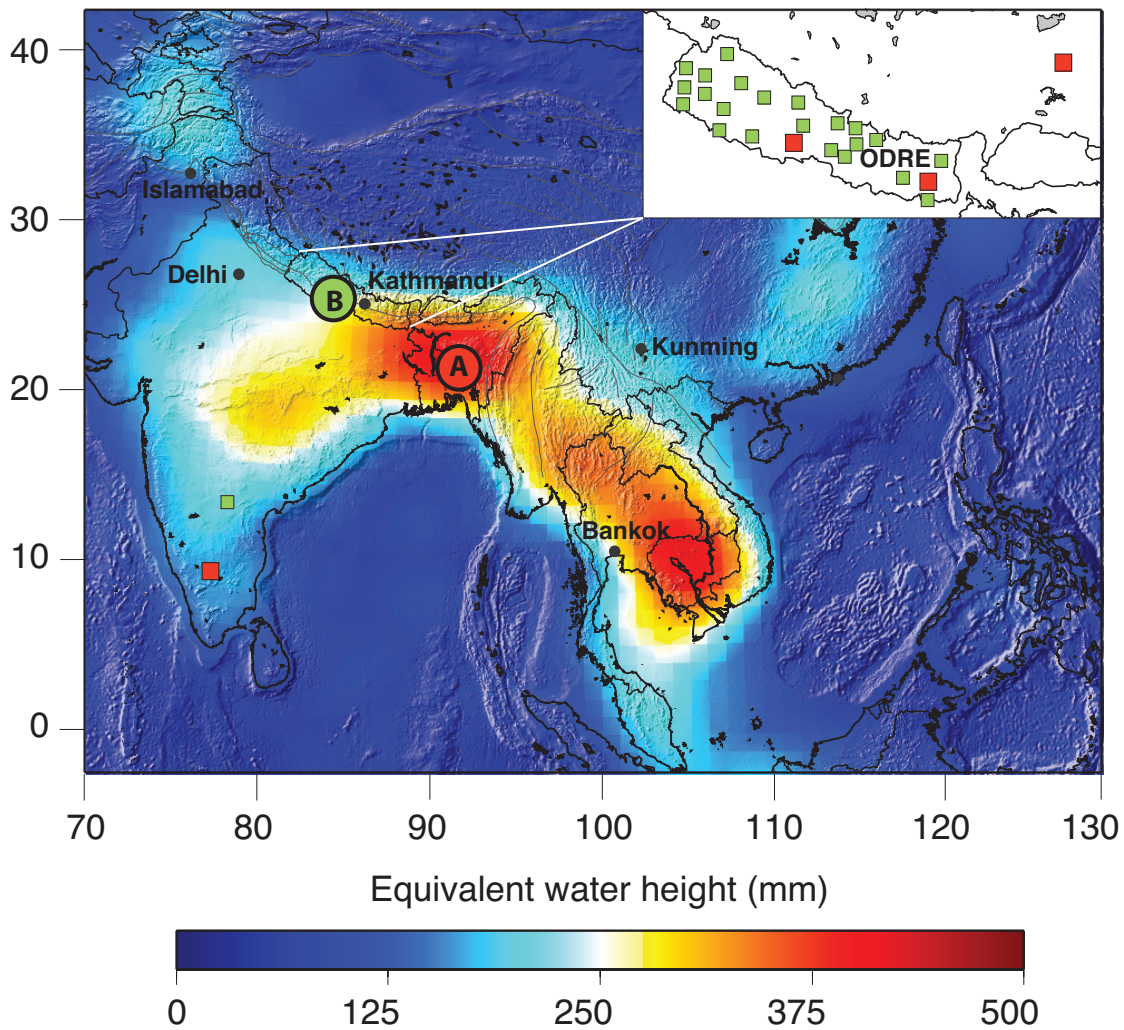


Figure 2.1 – Peak to peak surface load variations, expressed in equivalent water height (in mm), derived from GRACE for the 2002-2012 period and corrected from earthquake co and postseismic contributions. Green dots show location of the cGPS stations used in this study and red squares highlight the cGPS stations for which time series are plotted on Figures 2.3 and 2.6. Circles labeled A and B show location of the surface load time-series of Figure 2.2. Point A, in Bangladesh, is located approximately where the seasonal variation is maximum.

We notice however that amplitudes of atmospheric and non-tidal loading in this region are relatively low (a few mm) compared to the annual variations of continental loading.

In this study, we use 10-day solutions provided by the CNES/GRGS, available at <http://grgs.obs-mip.fr/>. These solutions are expressed in terms of Stokes coefficients (i.e., non-dimensional spherical harmonic coefficients of the geopotential) which represent the gravitational effects

## 2.2. Presentation of the GPS and GRACE data used in this study

---

of non-modeled phenomena, mainly continental hydrology (the degree 1 Stokes coefficients have been omitted in our study because the estimate of annual degree-1 contribution given by [Swenson et al. \(2008\)](#) remains negligible compared to the amplitude of seasonal displacements induced by higher degrees loads). The solutions also contain polluting noise, aliasing effects, leakage and errors in the correction models. Several post-processing filtering approaches of the residual Stokes coefficients have been proposed to extract realistic continental hydrology signals, and to get rid of the high frequency energetic North-South striping that is due to orbit resonance during the Stokes coefficient determination ([Wagner et al., 2006](#)) and aliasing of the not-well resolved short term phenomena. Stokes coefficients can be converted into geoid and water mass coefficients (expressed in terms of mm of equivalent-water height) by isotropic filtering ([Ramillien et al., 2005](#)). Then, 10-day 1-by-1 degree grids of water mass are simply interpolated from the water mass coefficients and a time-average is removed to each 10-day solution so that the solutions are expressed with respect to the mean solution over the time span of analysis.

In our study, we estimate the uncertainty on regional water mass averages from: (1) formal errors from processed Stokes coefficients adjustment, (2) inside leakage error induced by very dominant hydrological signals from outside of the studied area, up to 10 cm of equivalent water height on the signal amplitude at our GPS stations (e.g., important water mass change drainage basins), and (3) outside leakage error or uncertainties due to the spectrum truncation up to cut-off degree 50 (yielding a spatial resolution of 300-400 km) that could represent up to 6% of the estimate of equivalent water height ([Ramillien et al., 2005, 2006, 2008](#)). The errors from spectrum truncation-type (2) and (3) are estimated as a function of time by using an existing global hydrology model (WGHM developed by [Döll et al. \(2003\)](#)) for our studied region and converting it to GRACE-like observations (with similar spatial resolution, i.e. using Stokes coefficients up to order 50). In addition, we also suspect errors from correcting models of known gravitational forces, including tides, and time-aliasing effects, but these errors remain difficult to quantify. A logical way to address these uncertainties is to compare different GRACE solutions available from various processing centers, which handle the noise in the L1B satellite observations differently, use different orbit integration methods, and different correction models. [Sakumura et al. \(2014\)](#) show that differences between the four centers CSR, GFZ, JPL,

GRGS solutions are small, at least for seasonal variations, of the order 8.3 to 17.6mm rms of equivalent water height (compared to the 600mm amplitude of variation, Figure S.1). In addition, these authors show that correlations between solutions decrease with the harmonic degree and are better for mid and small frequencies, i.e. for radial displacements. We conclude that these errors remain small in our area of study, compared to our estimated uncertainties.

In this study, we use continental water variations time-series from February 2002 to August 2012 (Figure 2.1). In this region, tectonic signals represent another source of error. Indeed, [Han et al. \(2006\)](#) reported the detection by GRACE of large coseismic gravity changes due to the 2004  $M_w$ 9.3 Sumatra-Andaman earthquake. Post-seismic recovery of the geoid depression is also observed ([Han et al., 2008](#), [Ogawa & Heki, 2007](#)) and causes apparent variations in equivalent water height ([Chen et al., 2007](#)). Moreover, [Sun & Okubo \(1993\)](#) have shown that measurable co- and postseismic geoid and gravity changes can be induced by large earthquakes ( $M \geq 7.5$ ). For the purpose of our study, we empirically model and remove earthquake-induced mass redistribution observable in the gravity field measurements of each  $M > 7.5$  which occurred within the 2002-2012 period (M9.1 December 2004 Sumatra-Andaman, M8.5, 7.9, 7.1 October 2007 Sumatra sequence, M7.8 April M7.7 October 2010 Sumatra earthquakes), using the empirical formulation:

$$h_s(m, t) = h(m, t) - \sum_i \alpha_i \mathcal{H}(t - t_i) + \sum_i \beta_i \mathcal{H}(t - t_i) \ln\left(1 + \frac{t - t_i}{\tau}\right) \quad (2.1)$$

where  $h_s$  refers to the seasonal equivalent water height measured by GRACE at point  $m$  at the Earth surface, after earthquake contributions have been removed from the equivalent water height  $h$ .  $\mathcal{H}$  is the Heaviside function representing abrupt coseismic changes of the gravity field at time  $t_i$ , and  $\tau$  is the characteristic time of postseismic relaxation described by [Hoechner et al. \(2011\)](#).  $\alpha_i$  and  $\beta_i$  are constants estimated by a least-square inversion.

Figure 2.1 shows the averaged annual peak to peak amplitude of the equivalent water height (in mm) at the Earth surface for the 2002-2012 time period. Figure 2.2 presents the spatio-temporal variations of the equivalent water height at the surface. The peak to peak amplitude of seasonal variations reaches a maximum of 70 cm in Bangladesh (red line). The amplitude of the signal decreases westwards towards Nepal and shows a phase lag of about 3 to 4 months

## 2.2. Presentation of the GPS and GRACE data used in this study

(green line).

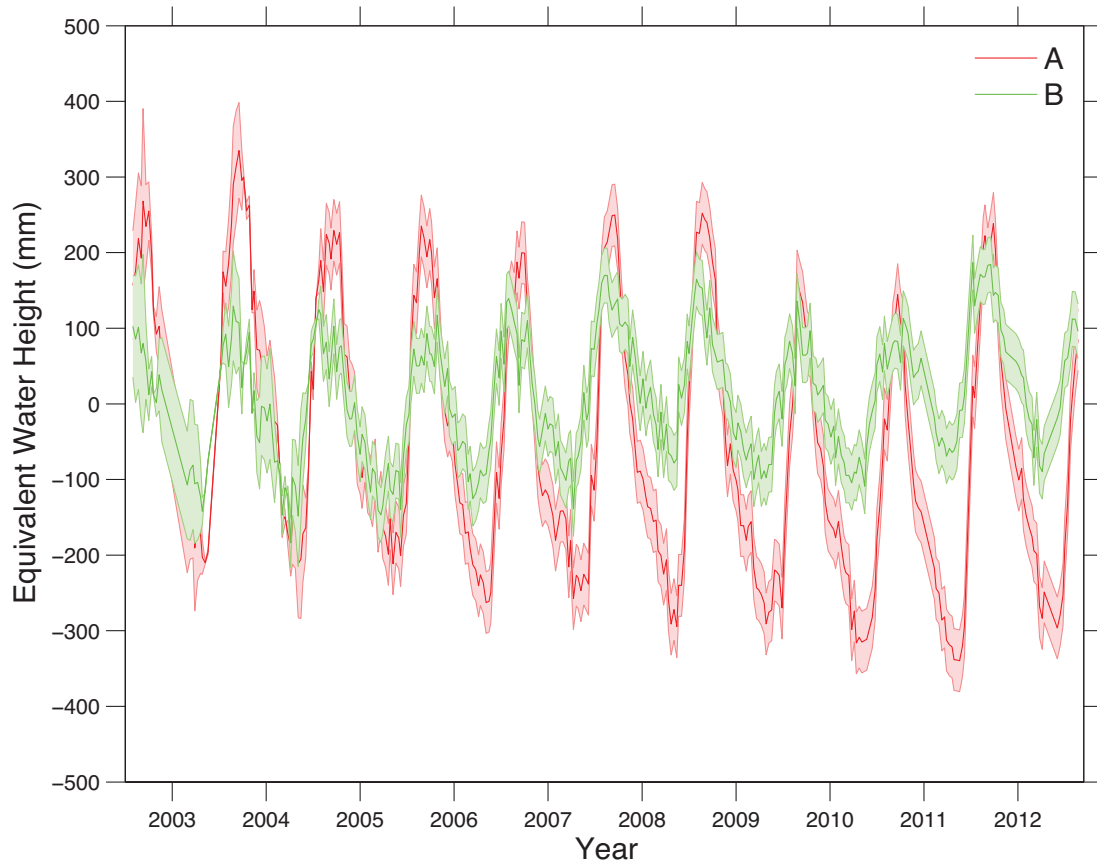


Figure 2.2 – Surface load variations at locations of points A (red line) and B (green line) reported in Figure 2.1. Note that surface load variations at point B, in the Nepal Himalaya, is shifted by about two months with respect to the time series at point A in Bangladesh. Shaded areas represent the final uncertainty on regional water mass averages from (1) formal errors from processed Stokes coefficients adjustment, (2) inside leakage error induced by very dominant hydrological signals from outside of the studied area, up to 10 cm of equivalent water height on the signal amplitude at our GPS stations (e.g., important water mass change drainage basins), and (3) outside leakage error or uncertainties due to the spectrum truncation up to cut-off degree 50 (yielding a spatial resolution of 300-400 km) that could represent up to 6% of the estimate of equivalent water height (Ramillien et al., 2005, 2006, 2008).

### 2.3 Modeling of seasonal ground deformation induced by surface load variations

Let us consider a time-varying distributed surface load expressed in terms of a seasonal equivalent water thickness,  $h_s(m, t)$ , with density  $\rho$ , where  $t$  is time and  $m$  refers to the point location at the Earth surface. We assume a purely elastic deformation so that the superposition principle applies. The assumption of a perfectly elastic Earth model is a good first order approximation at an annual time scale as the Maxwell time associated with viscous relaxation of the crust and lithosphere ranges from years (postseismic deformation) to thousands of years (postglacial rebound).

The time varying geodetic displacement  $U_i(M, t)$ ,  $i = 1, 3$  at a point  $M$  is then obtained by convolving the load distribution over a surface  $S$  with the Green's functions  $G_i(M)$ :

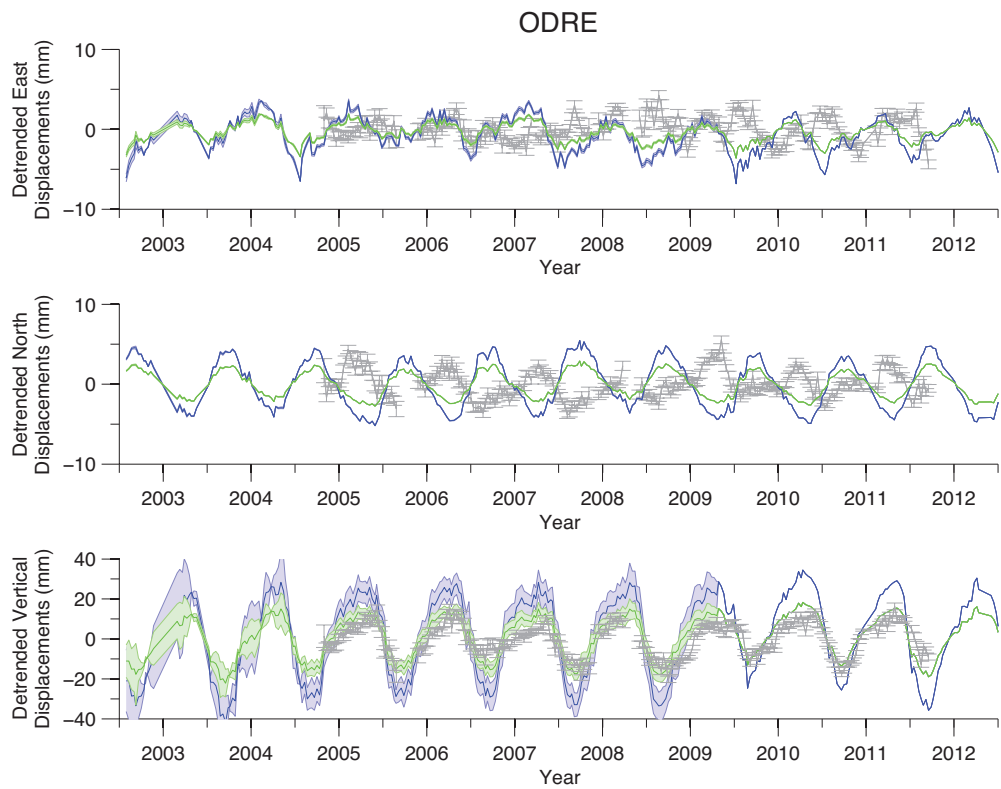
$$U_i(M, t) = \rho \int_S h_s(m, t) G_i(M - m) dm. \quad (2.2)$$

Here  $G_i$  refers to the  $i$ -th component of the geodetic displacement at point  $M$  at the Earth surface due to a surface point load, a Dirac function, at the origin. For numerical computation the Earth surface is meshed and a discrete version of equation (2) is adopted, e.g. the integral in (2.2) is approximated by a sum over the  $1^\circ \times 1^\circ$  GRACE grid. The Green functions must be computed based on assumptions of the elastic structure of the Earth. We first show the results obtained assuming an homogeneous elastic half-space and move next to the case of spherical and layered Earth model.

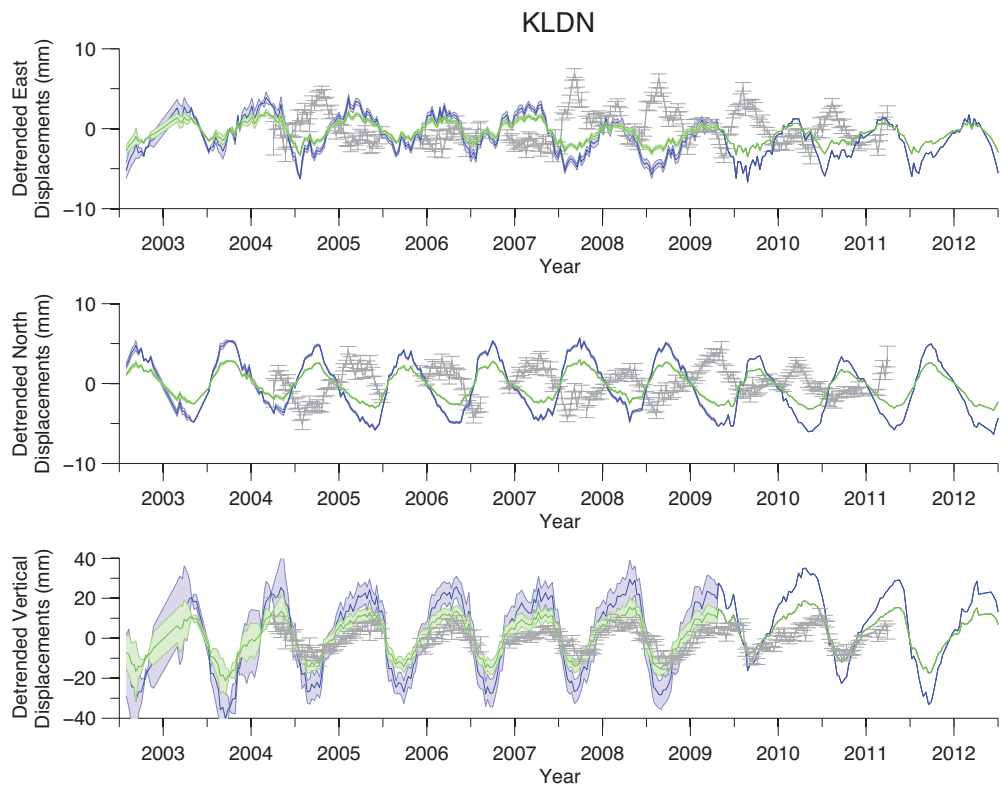
---

Figure 2.3 (following page) – Detrended geodetic positions, averaged over ten days, determined at stations ODRE (a), KLDN (b), LHAZ (c) and IISC (d) (gray symbols). See Figure 2.1 for locations of these stations. Error-bars show  $1-\sigma$  uncertainties. The green and blue lines show predicted surface displacements computed from surface load variations derived from GRACE assuming a homogeneous elastic half space. Blue line corresponds to a Young's modulus  $E$  of 90 GPa, the value found to yield the best overall fit to the horizontal components (Table 1). Green line corresponds to a Young's modulus  $E$  of 170 GPa, the value found to yield the best overall fit to the vertical component (Table 1). Poisson's ratio,  $\nu$  is 0.25 for both models. Shaded areas show uncertainties on predictions derived from uncertainties on estimated surface loads.

### 2.3. Modeling of seasonal ground deformation induced by surface load variations

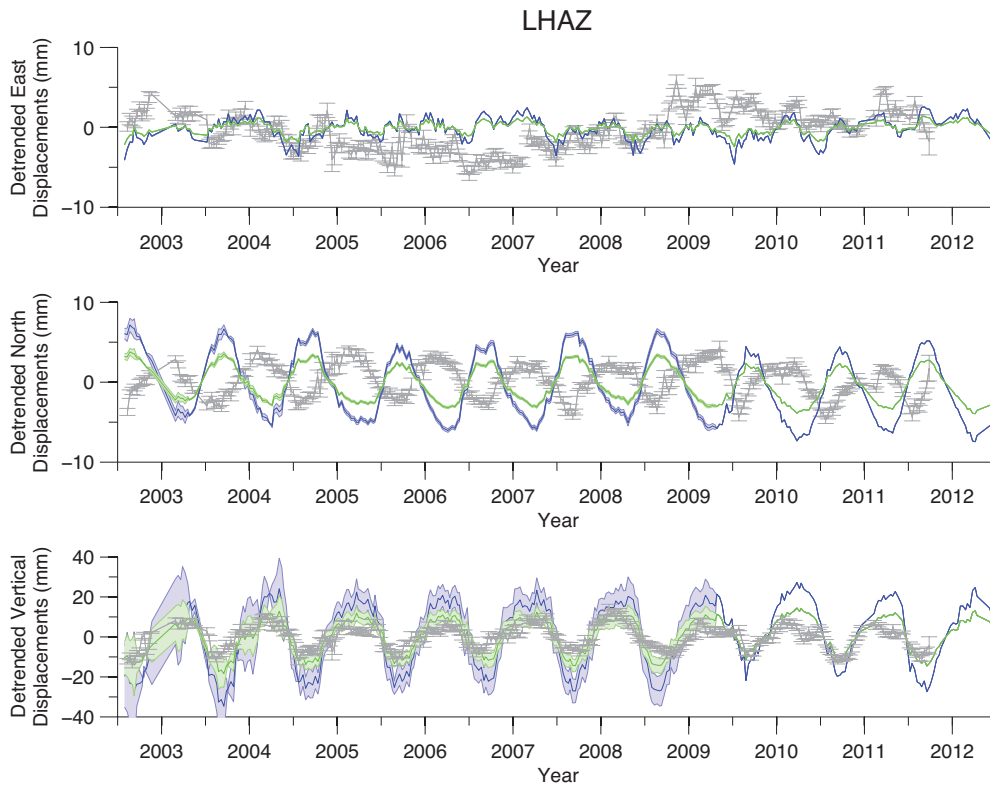


(a) ODRE cGPS station, Odare, Nepal

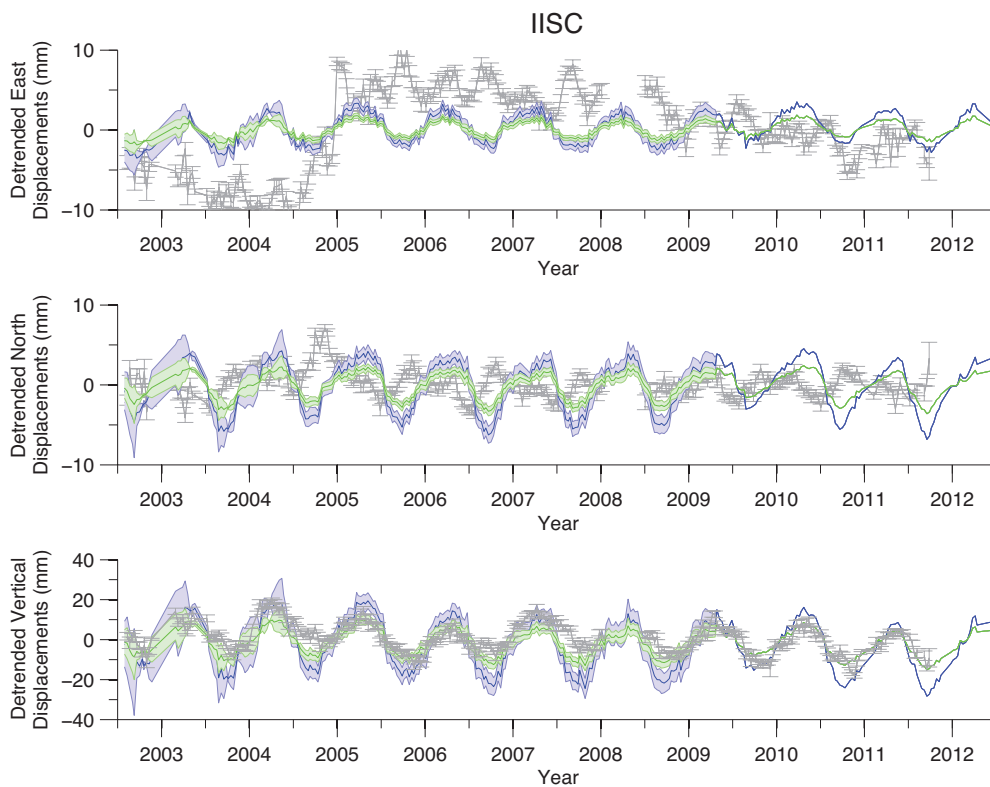


(b) KLDN cGPS station, Koldana, Nepal

## Chapter 2. Elastic seasonal deformation in the Himalaya



(c) LHAZ cGPS station, Lhasa, Tibet



(d) IISC cGPS station, Bangalore, India

### 2.3.1 Modelling of seasonal ground deformation for a homogeneous elastic half-space

A common assumption is that an elastic half-space model would be a satisfying first order approximation to model surface displacements induced by surface loading e.g., [Bevis et al. \(2005\)](#), [Grapenthin et al. \(2006\)](#), [Bettinelli et al. \(2008\)](#), [Steckler et al. \(2010\)](#). The advantage of using that approximation is that the solution is analytical ([Boussinesq, 1885](#)). However, it has been well established by [Farrell \(1972\)](#) for several decades now that a spherical and layered model is the correct one to model both horizontal and vertical components simultaneously. Considering the number of recent studies still using the Boussinesq approximation, we first present results for elastic homogeneous half-space models and emphasize the difficulty to predict surface displacements induced by surface loading for both components using a single model.

Surface displacements of a non-gravitating, homogeneous half-space to surface loading, are commonly referred to as the Boussinesq's problem, for which the Green's functions are obtained by solving the elastic equilibrium equation. Let  $F$  be the norm of a unit mass force applied vertically at the model's surface. We consider a cylindrical coordinates system  $(r, \theta, z)$ , centred on the force application point. The analytical solution then writes:

$$u_R(R, 0) = \frac{-F(1 - 2\nu)(1 + \nu)}{2\pi ER}, \quad (2.3)$$

$$u_\theta(R, 0) = 0, \quad (2.4)$$

$$u_z(R, 0) = \frac{-F(1 - \nu)(1 + \nu)}{\pi ER}, \quad (2.5)$$

where  $R$  is the distance between the observation point and the mass point force,  $\nu$  is the Poisson's ratio and  $E$  the Young's modulus, quantifying the resistance of an elastic body to deformation.

By symmetry,  $u_\theta = 0$  and all components of surface displacements are independent of  $\theta$ . In this approach there are only two adjustable model parameters: the Young's modulus and the Poisson's ratio. The sensitivity to the Poisson's ratio is actually negligible so that in practice

only the Young's modulus is adjusted and  $\nu$  is generally set to a standard value of 0.25, as is the case in this study.

To compute the deformation induced by distributed surface load, we convolve the spatial distribution of surface loads derived from GRACE with the Green's functions corresponding to an elastic homogeneous half-space described above. We use the 10-day Level 2 solutions, expressed in equivalent water height, and a 1-by-1 degree grid of mass point forces, covering a 40 by 60 degrees area around the Himalayan region (Figure 2.1). For consistency the cGPS time series are 10-day averaged. Table 1 shows the best fitting Young's modulus obtained from least-squares inversion of the GPS data by minimizing a L2 norm of the residuals  $r_i$ , weighted by their nominal uncertainties  $\sigma_i$ :

$$\chi_r^2 = \frac{1}{n-p} \sum_i \frac{r_i^2}{\sigma_i^2}. \quad (2.6)$$

$(n-p)$  is the number of degrees of freedom,  $n$  being the number of observations ( $n \sim 4200$  for each displacement component), and  $p$  the number fitted parameters ( $p = 1$ , the Young's modulus, for half-space models, and  $p = 0$  for the PREM model). Note that the misfit criterion ignores a possible serial correlation of uncertainties.

We find, with no surprise, that if the horizontal and vertical time series are inverted jointly the amplitude of the seasonal variations on the vertical components is systematically underpredicted, while the amplitude of the seasonal variations of the horizontal components is systematically overpredicted. We then look at what Young's modulus is needed in the Boussinesq problem in order to approximate the correct spherical Green's functions for our given load and data distribution. We find best fitting values of the Young's modulus ranging from 92 to 113 GPa for the horizontal components, and from 161 to 186 GPa for the vertical components. When all the stations are combined, we find best-fitting Young's modulus of  $\sim 90$  and  $\sim 170$  GPa for the horizontal and vertical components respectively. Figure 2.3 shows 10-day averaged seasonal GPS data in gray, and the predicted displacements time-series for half-space models with  $E=90$  GPa (blue line) and  $E=170$  GPa (green line). Clearly, as predicted by [Farrell \(1972\)](#), the half-space model fails in adjusting simultaneously the amplitude of the seasonal variations of the vertical and horizontal components. This means that the two com-

## 2.3. Modeling of seasonal ground deformation induced by surface load variations

ponents have very different sensitivities to the location and wavelength of the load. The phase is also mispredicted. In particular, it should be noticed that the model predicts a horizontal signal which is clearly out of phase at most stations, being too early by a few months typically, depending on the distance to the load. By contrast, the predicted vertical displacements are approximately in phase with the observations. This could be explained by the fact that, given positive loads, the vertical displacements always add constructively while the horizontal displacements can add destructively depending on the spatial distribution of the load.

### 2.3.2 Green's functions for a spherical, layered elastic Earth model

The Green's functions entering equation (2) can be computed for a spherical perfectly elastic Earth Model based on load Love numbers theory (Longman, 1962, 1963, Farrell, 1972), in which the deformation of the Earth, generated by a surface load, is a function of the spherical harmonic components of the gravitational potential created by this load. To define the load Love numbers, the vertical and horizontal surface displacements, generated by the surface load, are expanded into spherical harmonics. In this study, the load Love numbers are computed for a model based on PREM (Dziewonski & Anderson, 1981), in which the ocean is replaced by a continental crust (Figure 2.4). We use asymptotic expressions to compute numerically the Legendre series in the Green's functions for the load Love numbers, following Farrell (1972) formalism and the numerical method of Guo et al. (2004) which is more accurate than the Farrell's original method. The surface Green's functions for vertical and horizontal displacements, induced by a unit mass point force, are then given by:

$$u_r = \frac{R}{M} \sum_{n=0}^{\infty} h'_n P_n(\cos\theta) \quad (2.7)$$

$$u_\theta = \frac{R}{M} \sum_{n=0}^{\infty} l'_n \frac{\partial P_n(\cos\theta)}{\partial \theta} \quad (2.8)$$

where  $P_n(\cos\theta)$  are the Legendre polynomials of the  $n$ 'th degree,  $\theta$  is the angular distance between the force application point and the observation point.  $h'_n$  and  $l'_n$  are the harmonic coefficients of vertical and horizontal displacement respectively.  $R$  and  $M$  denote the radius and mass of the Earth. Figure 2.5 shows that displacements at the surface of a spherical non-rotating, elastic and isotropic Earth, using PREM structure with a continental crust, are mostly

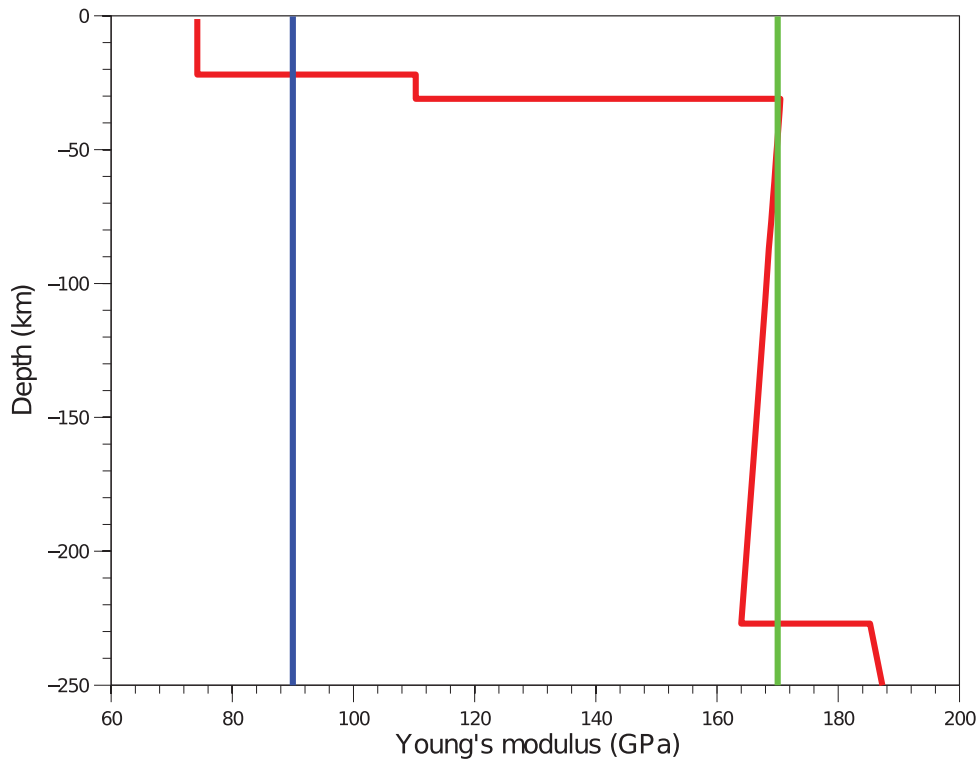


Figure 2.4 – Depth variation of the Young’s modulus in the modified PREM model used to compute the Green functions for a layered spherical Earth model. The crustal structure is based on the seismic velocity model determined for Nepal by Monsalve et al. (2006) (red line). The deeper portion of the model is based on the Preliminary Earth Model (Dziewonski and Anderson, 1981). Also shown is the value of Young’s modulus derived from the modeling of vertical (green) and horizontal (blue) seasonal displacements (Table 1).

controlled by large wavelength loads. Indeed, the evolution of the ratio of radial displacement to the equivalent water height, as a function of the surface load wavelength highlights that for the resolution of GRACE (~400km, or harmonic degree of 50), the radial surface displacement is 100 times smaller than the applied load (expressed in equivalent water thickness). The ratio decreases with decreasing load size. Therefore, we will capture the most significant surface displacement with a the 400km resolution of GRACE data.

### 2.3.3 Comparison of Green’s functions for the half-space and spherical layered elastic Earth models

Figures 2.6(a) and 2.6(b) respectively represent horizontal and vertical displacements computed based on the PREM model described above (red lines) for a point load at origin. The blue

### 2.3. Modeling of seasonal ground deformation induced by surface load variations

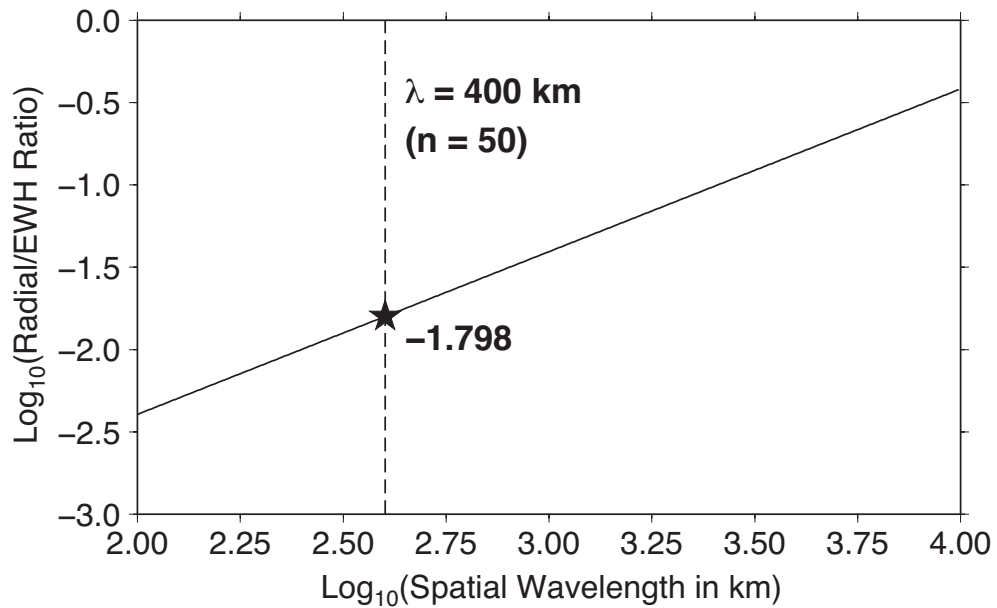
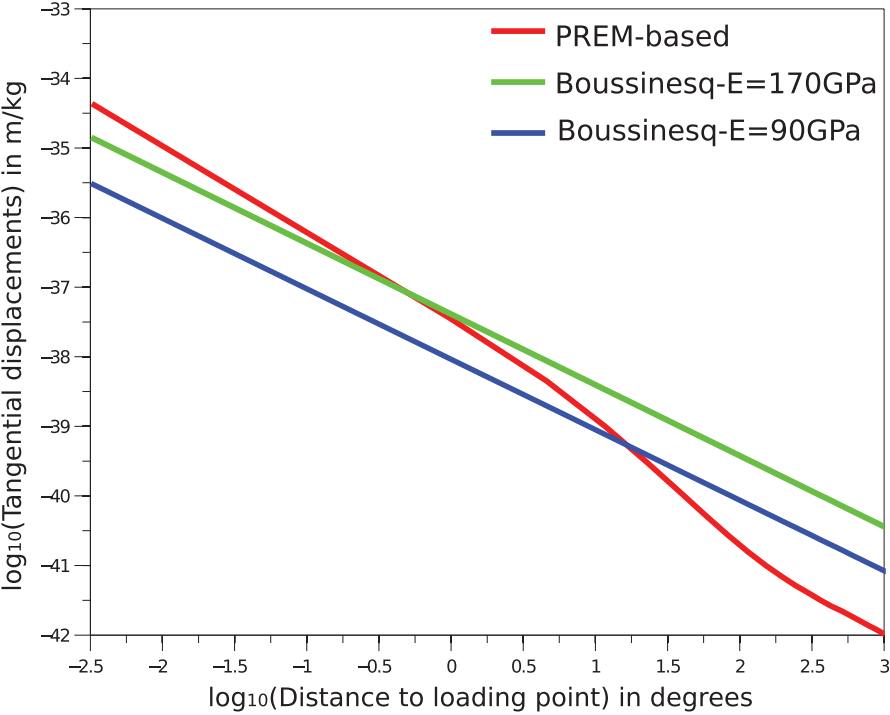


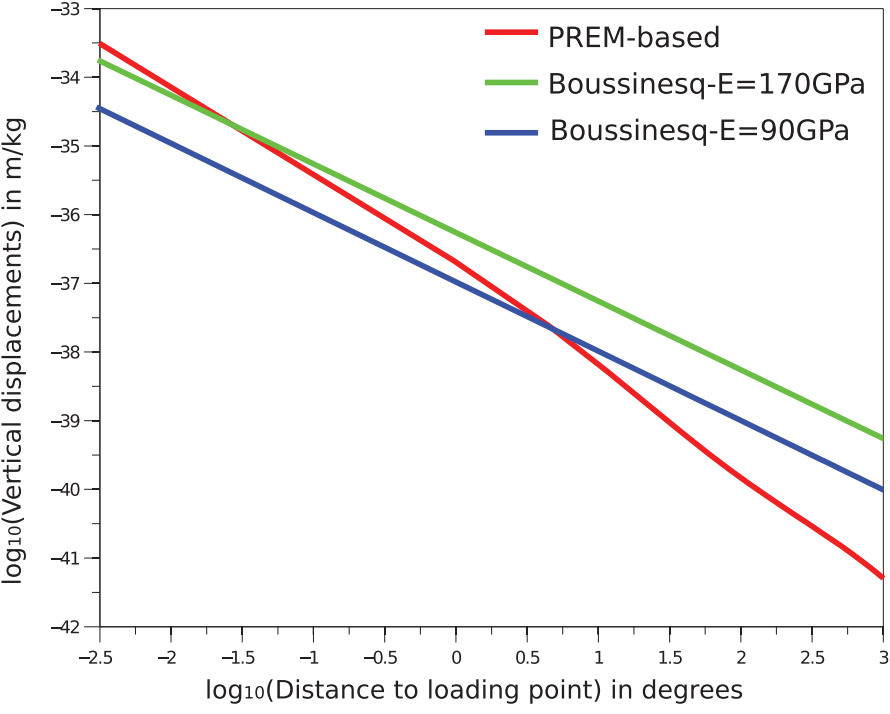
Figure 2.5 – Transfer function of the ratio of radial displacement to equivalent water height, as a function of the surface load wavelength. For the resolution of GRACE ( $\sim 400\text{ km}$ , or harmonic degree  $n = 50$ ), the radial surface displacement is 100 times smaller than the applied load. The transfer function favours large wavelength loads and local hydrology would not affect significantly surface displacements.

and green lines show for comparison the predicted displacements assuming homogeneous half-space models with  $E=90\text{ GPa}$  (the value found to best fit the horizontal geodetic seasonal displacements) and  $E=170\text{ GPa}$  (the value found to best fit the vertical geodetic seasonal displacements). These figures, in agreement with Farrell (1972) results, help visualize that it is not possible to approximate satisfactorily the layered Earth model with an elastic half space even if only one single component (vertical or horizontal) is considered. For example, when only the horizontal displacements are considered, the PREM model predicts approximately the same response as an half-space model with  $E=90\text{ GPa}$  for a only relatively narrow range of distances around  $\sim 30\text{ km}$  ( $-0.5^\circ$ ). When the vertical displacement are considered, this same approximation is valid only at distances of  $\sim 3\text{ km}$  ( $-1.5^\circ$ ).

Figure 2.6(c) shows the ratio between horizontal and vertical displacements for the PREM model in red (note that this figure could be deduced from Farrell (1972) and is in agreement with Wahr et al. (2013)). This ratio is constant for an elastic half-space (blue line) and depends



(a) Tangential displacements induced by a unit load



(b) Vertical displacements induced by a unit load

### 2.3. Modeling of seasonal ground deformation induced by surface load variations

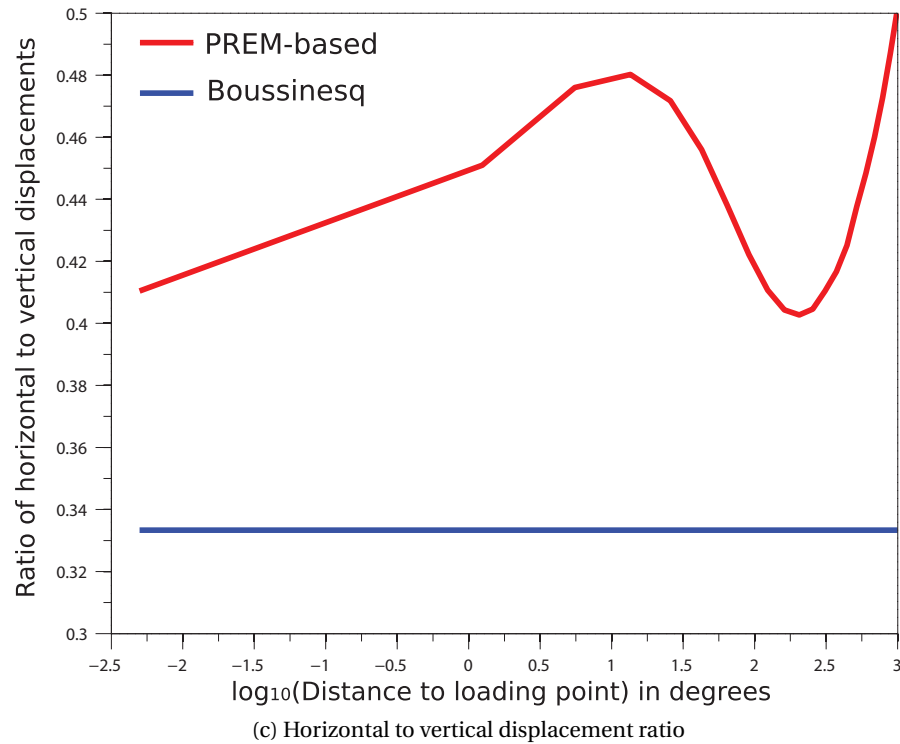


Figure 2.6 – Tangential (a) and vertical (b) surface displacements Green’s functions for the modified PREM model of Figure 2.4. Blue and green lines show Green’s functions for tangential displacements computed for an homogeneous half-space model with a Young’s modulus of respectively 90 GPa and 170 GPa. The Poisson’s ratio is set to 0.25 for all models. (c) shows ratio of horizontal and vertical surface displacements Green’s functions for the modified PREM model of Figure 2.4 (red line) and for an homogeneous half space with a Poisson’s ratio of 0.25 (blue line).

only on the Poisson ratio as it is equal to  $(1 - 2\nu)/(1 - \nu)$  (see Equation 3-5). This shows that if one aims at fitting both the horizontal and vertical components the variations of sensitivity of the components with the distance to the load must be taken into account. This effect explains why fitting the vertical components with an elastic half-space requires a Young’s modulus of 170 GPa significantly larger than the value of 90 GPa inferred from fitting the horizontal components: the two components have different sensitivity to the elastic structure with distance to the load.

The Boussinesq model matches the ratio of horizontal to vertical displacements of the PREM model most closely on average for  $(1 - 2\nu)/(1 - \nu) \sim 0.44$ , i.e.  $\nu \sim 0.35$ . However, even this ad hoc value is chosen, it doesn’t help reconciling entirely the amplitude of horizontal and

vertical displacements. This is due to the specific distribution of the cGPS stations relative to the load distribution. As a result, best fitting Young's modulus for the horizontal and vertical components are of  $\sim 60\text{GPa}$  and  $\sim 140\text{GPa}$  respectively, underestimating the horizontal displacements observed at cGPS stations and overestimating the vertical ones. We show in the next section that this effect explains indeed well the relative amplitudes and phase of the vertical and horizontal surface deformation induced by seasonal variations of surface loading in the Himalayan region.

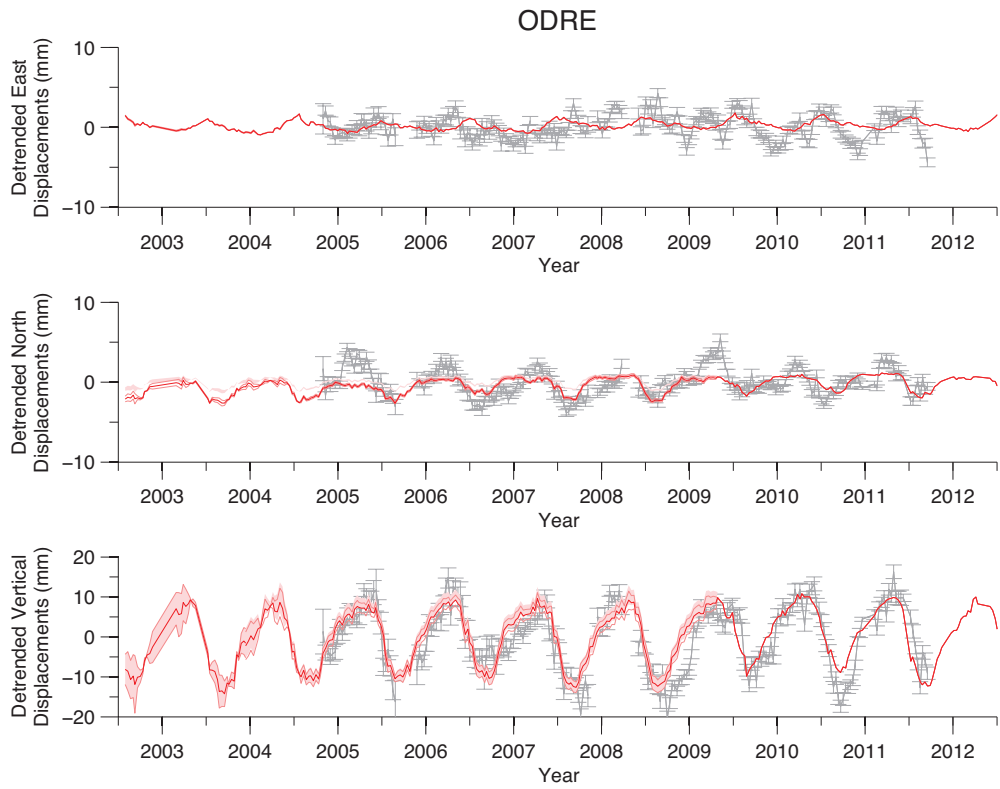
### 2.3.4 Modeling of seasonal ground deformation for a spherical, layered Earth model

We now compute seasonal surface deformation by convolving the spatial distribution of surface loads derived from GRACE with the Green's functions derived for a spherical, layered Earth model described above. The predicted displacements now fit both the horizontal and the vertical components quite well (Figure 2.5). The reduced  $\chi^2$  of the residuals is reduced by 50% (Table 1). This model thus reconciles the relative amplitudes of the horizontal and vertical components as well as their apparent phase shift and shape. It is interesting to note that the model fits the GPS data actually better than the elastic half-space models even when only the vertical or the horizontal components are considered (Table 1). In comparison to the  $E=90\text{GPa}$  half-space model, the fit to the East component is improved on average by 24% (between 5 and 32% depending on the station considered) and the fit to the North component by 40% (between 12 and 64%). In comparison to the  $E=170\text{GPa}$  half-space model, the fit to the vertical data is improved by 15% (between 2 and 36%). This is clear indication that the dependency of the Green's functions on distance to the load predicted by the modified PREM model is more appropriate than the  $1/R$  dependency predicted by the half space model.

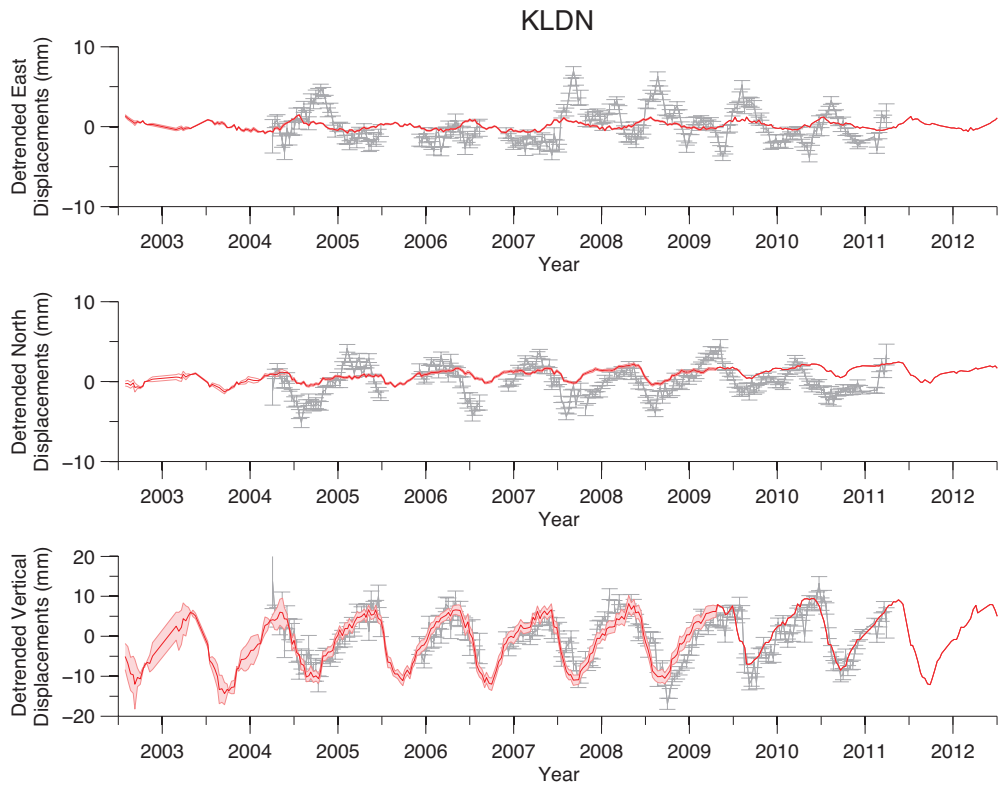
---

Figure 2.5 (*following page*) – Detrended geodetic positions, averaged over ten days, determined at stations ODRE (a), KLDN (b), LHAZ (c) and IISC (d) (gray symbols). See Figure 2.1 for locations of these stations. Error-bars show  $1-\sigma$  uncertainties. The red line shows predicted surface displacements computed from the surface load variations derived from GRACE assuming a the spherical and layered Earth model described in Figure 2.4. Shaded areas show the uncertainties on the predictions derived from the uncertainties on the estimated surface loads.

### 2.3. Modeling of seasonal ground deformation induced by surface load variations

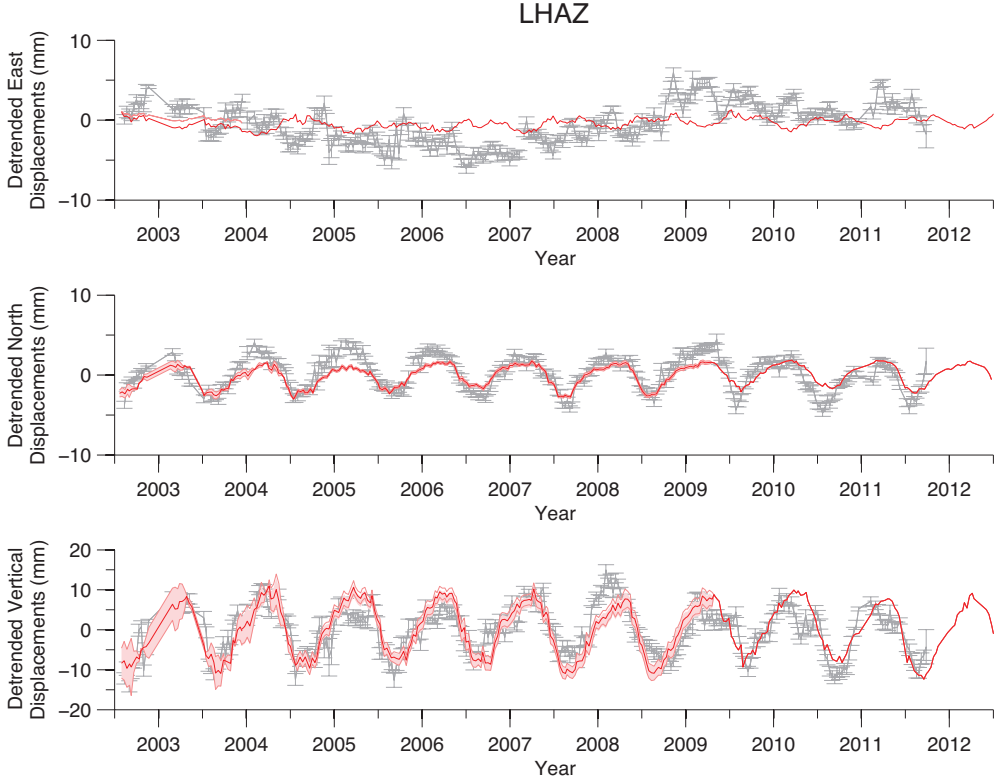


(a) ODRE cGPS station, Odare, Nepal

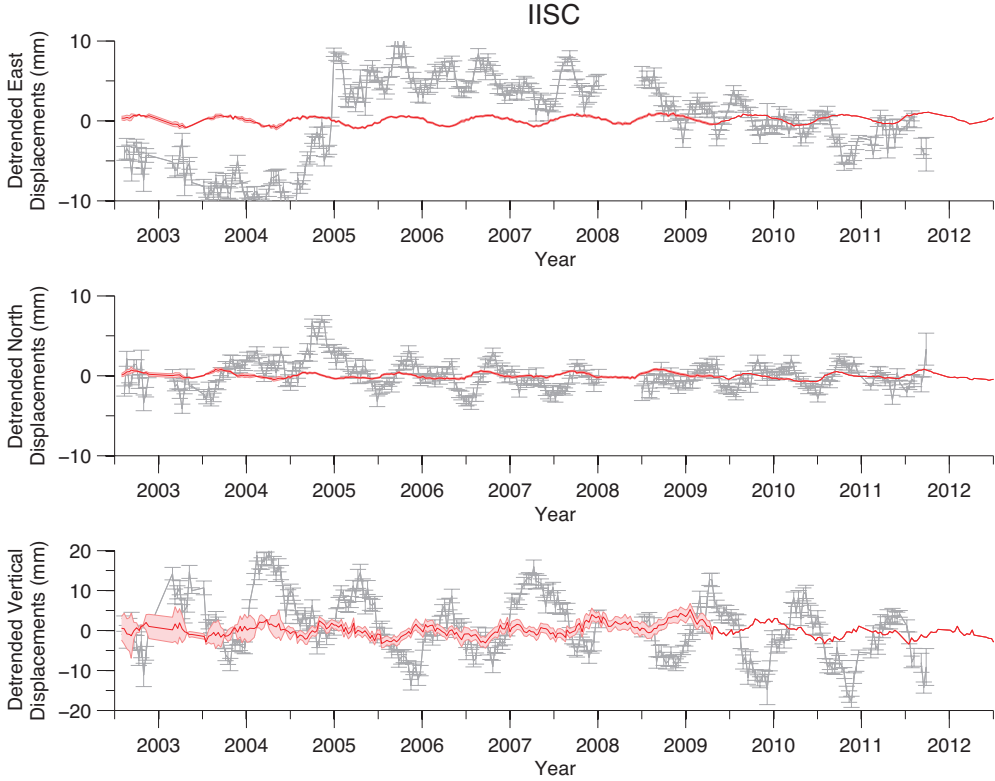


(b) KLDN cGPS station, Koldana, Nepal

**Chapter 2. Elastic seasonal deformation in the Himalaya**



(c) LHAZ cGPS station, Lhasa, Tibet



(d) IISC cGPS station, Bangalore, India

### 2.3. Modeling of seasonal ground deformation induced by surface load variations

---

The phase shift between the horizontal and vertical components arises from the fact that both displacements are sensitive to different wavelengths and distances to the load. It follows that significant subsidence starts at the onset of the Monsoon season as surface loading increases over Bangladesh, but horizontal southward displacements occur only later as the surface load become significant in the Ganges basin immediately to the south of the Nepal Himalayas. Due to the time varying distribution of surface load induced by the Monsoon, combined with the different decrease with distance of their related Green functions, the PREM and the elastic half space models yields quite different temporal evolution of geodetic displacements. Clearly the shape predicted by the PREM model fits the geodetic observations better, and the model does improve significantly the fit to most of the seasonal geodetic variations analysed in this study, but the residuals remain larger than uncertainties on average (Table 1). This could be due partly to underestimated uncertainties on the GPS data, but the misfits show a seasonal residual signal at most stations suggesting the modeling could be improved. These residuals could be due to heterogeneities of surface load distribution, at a scale not resolved by GRACE, or to a non-optimal Earth structure.

We notice furthermore that the fit of our model to the geodetic displacements at station IISC (Figure 2.5(d)) is not significantly better than with the Boussinesq model. This station, located in South India, is probably more sensitive to tides (corrected with GAMIT/GLOBK, assuming a tidal model), non-tidal oceanic loading as it is closer to the ocean than the Nepal stations. Even though we take into account the non-tidal oceanic load variations forced by the atmosphere, the oscillating load might be biased by other oceanic currents.

Another less probable hypothesis is that the PREM Earth structure we used is more appropriate for the Himalaya region than for the Indian craton. In the latter case, modeling of seasonal geodetic strain might be a way to constrain regional variations of elastic properties of the the Earth at shallow depths. We therefore propose to solve this inverse problem, in a probabilistic way, and adjust the shallow material properties of the Earth to improve the prediction of seasonal geodetic displacements induced by variations in surface hydrology. Note that, we restrain ourselves to the elastic case in this chapter. Since the PREM-like model, 1-D globally averaged, has reasons to be significantly different from an Himalayan regional

$\chi_r^2$	Horizontal	Vertical	Horizontal and Vertical
Half-space (E=90GPa)	38.1	30.2	34.1
Half-space (E=170GPa)	42.0	17.3	29.6
Prem	16.2	12.3	14.3
MGrace	13.7	5.1	9.4

Table 2.1 – Reduced Chi-squares  $\chi_r^2$  (see equation (6)) obtained from the inversion of the geodetic time-series ( $\sim 4600$  data points for each displacement component), using the Boussinesq half-space approximation. The values in bold are the minimum values obtained when the Young’s modulus assigned to the elastic half-space is adjusted so as to best fit either the vertical (E=170 GPa) or the horizontal components (E=90 GPa).  $\chi_r^2$  using the Preliminary Reference Earth Model model (Dziewonski & Anderson, 1981). Note the PREM model yields a better fit to both the vertical and horizontal components. Finally,  $\chi_r^2$  using a model based on PREM, MGrace. Material properties for the uppermost 150km are the results of a probabilistic inversion of seasonal geodetic displacements. Note that MGrace leads to an even better fit to both components.

model, and because our spherical layered elastic model predicts most of the seasonal signals, small changes in the elastic structure can improve the fit to the data.

## **2.4 Constrains on the crust depth-dependent elastic structure using geodetic seasonal surface displacements**

Several previous studies have used tidal records to probe the Earth’s structure (Pariisky, 1965, Mantovani et al., 2005). Recently, Ito & Simons (2011) used geodetic displacements induced by tidal ocean loading recorded by a dense array of continuous GPS stations in the Western US. They inverted this dataset, using a fully probabilistic approach, to estimate depth-dependent interior density and elastic moduli and propose a 1D regional radial structure model, significantly improving the prediction of surface displacement induced by tidal loading.

We adopt the same approach, using seasonal geodetic displacements induced by variations in continental water storage. Our initial model is a combination of PREM and a continental crust based on the CRUST 5.1 model (Mooney et al., 1998), which fairly well predicts seasonal geodetic displacements (Figure 2.9). We parametrize the inverse problem in terms of the ratio between the compressional and shear wave velocities,  $V_p/V_s$ , and the density  $\rho$ . We first test the sensitivity of our model by evaluating the effect of small variations of  $V_p/V_s$  and  $\rho$  on

## 2.4. Constrains on the crust depth-dependent elastic structure using geodetic seasonal surface displacements

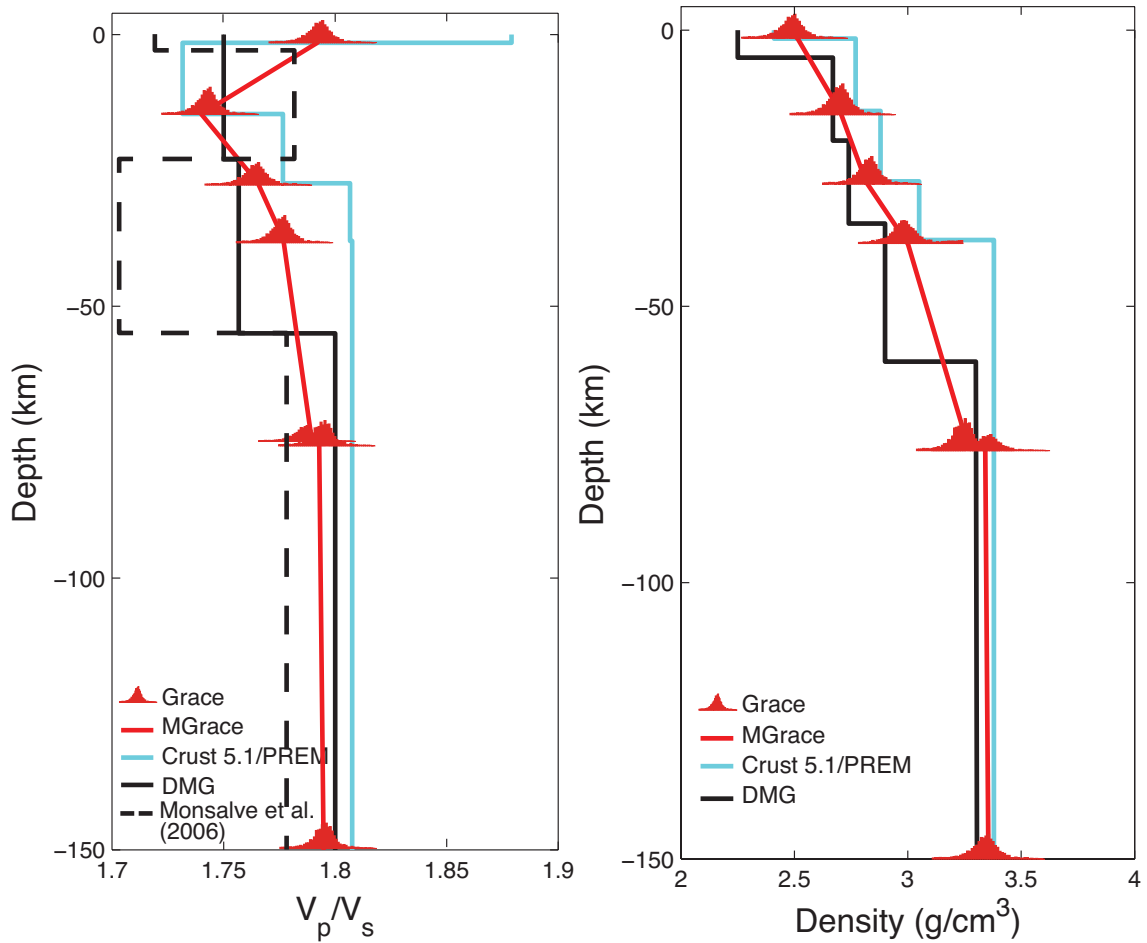


Figure 2.8 – Comparison of 1D models for P-wave/S-wave velocities ratio (a) and density (b) of the upper 150km of the Earth: Crust 5.1/PREM (blue), regional models (solid black from Pandey et al. (1995), dashed black from Monsalve et al. (2006)), Grace (red histograms represent marginal posterior probability density functions) and MGrace, median derived from Grace.

surface radial and tangential displacements, following the method proposed by Ito & Simons (2011). We find that our model is sensitive to the uppermost 150 km of the Earth. Thus, we define  $m$ , a vector of 14 model parameters consisting of  $(\rho, V_p/V_s)$  for each of the 7 layers shallower than 150 km and force deeper parameters to be equal to their PREM values. We then evaluate the equation:

$$d = G(m) + \epsilon \quad (2.9)$$

where  $d$  is the seasonal geodetic data vector,  $G$  the kernel matrix and  $\epsilon$  the vector of errors on observations, with a Gaussian distribution. We adopt a probabilistic approach, where

the posterior probability density function (PDF) is the result of a likelihood function based on the misfit to observations. We use a Bayesian formulation to solve the inverse problem and a Markov Chain Monte Carlo sampling method, with a Metropolis algorithm, to obtain the posterior PDFs of the unknown parameters ( $V_p/V_s$ ) and  $\rho$  (Tarantola, 2005).

Figure 2.8(a) and 2.8(b) show respectively PDFs of ( $V_p/V_s$ ) and  $\rho$  for each layer, and models: median MGrace from this study, PREM and two local velocity models (Pandey et al., 1995, Monsalve et al., 2006). Our density profile shows lower values than the 1D averaged global model, also in agreement with Wang et al. (2013) results, using an inversion of water mass anomalies. The ( $V_p/V_s$ ) profile is closer to the local velocity model found by Pandey et al. (1995) than the Crust 5.1/PREM model but does not capture the low ( $V_p/V_s$ ) zone between 23 and 55 km found by (Monsalve et al., 2006).

Figure 2.9 shows histograms of residual seasonal displacements using Crust 5.1/ PREM (in blue) and MGrace (in red) for horizontal, vertical and both components. MGrace improves significantly the fit to the data, by 20% compared to the fit obtained with PREM (Table 1). Note that we are confident that the inversion is not biased by the relatively low resolution of the GRACE dataset. Indeed, the transfer function converting surface loads into surface displacements on a spherical Earth weights long wavelengths more heavily (Figure 2.5). Thus, a loading signal at shorter wavelength than the GRACE resolution would have a negligible effect on the induced surface displacements. It is also possible that the fit to the data could be improved further by allowing for variations of the Earth elastic properties in 3D. Such an inversion is beyond the scope of this study. The inversion presented here is sufficient to demonstrate the possibility of using seasonal geodetic displacements induced by surface hydrology to probe the shallow elastic structure of the Earth, but requires more data coverage to give significant insights on the Earth local elastic structure.

## 2.5 Implications and Conclusions

Our study confirms the conclusion of Bettinelli et al. (2008) and Fu & Freymueller (2012) that the seasonal strain seen in the Himalaya on the horizontal and vertical components is primarily due to surface load variations induced by continental hydrology. The model

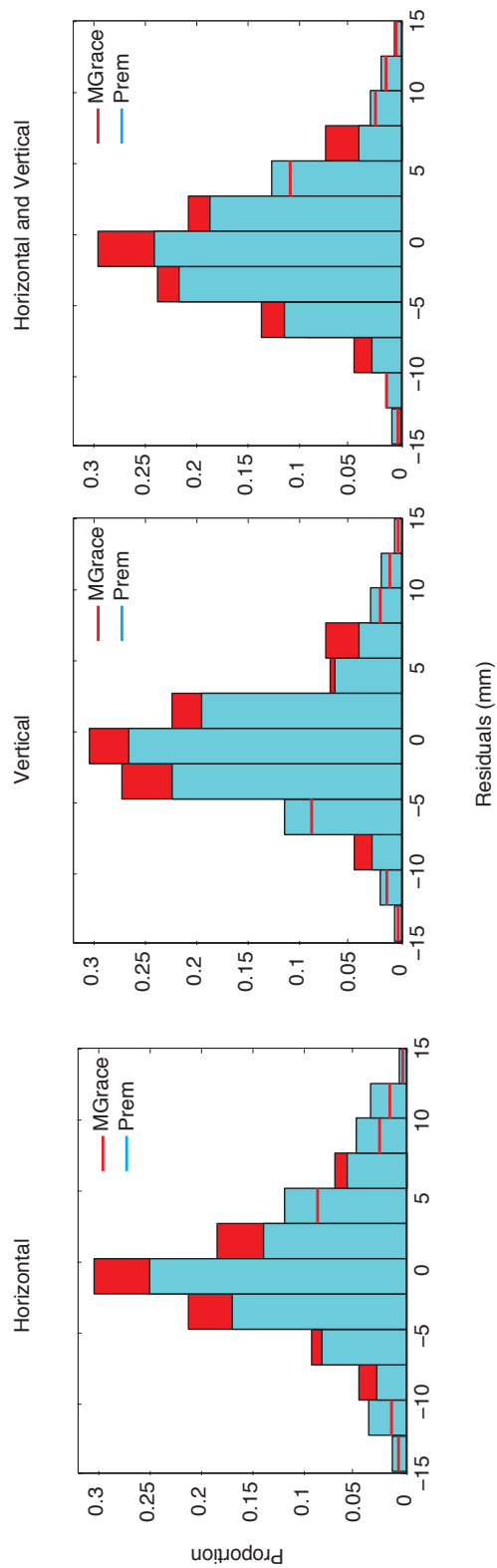


Figure 2.9 – Histograms of residuals of seasonal geodetic displacements using Crust 5.1/PREM (blue) and MGrace (red) for horizontal, vertical, and both components.

## Chapter 2. Elastic seasonal deformation in the Himalaya

---

also explains the seasonal variations seen in Bangladesh (Steckler et al., 2010) as well as in southern India and Tibet as shown in this study. The comparison between the homogeneous elastic half-space and the PREM models shows that vertical and horizontal displacements are sensitive to different distances to the load. As a result, the Young's modulus needed to approximate the correct spherical Green's function using a Boussinesq's approximation from the modeling of vertical displacement is typically of the order of 110 to 190 GPa as found in this and other studies (Bevis et al., 2005, Steckler et al., 2010), while horizontal displacements are better adjusted with significantly lower Young's modulus, 92 to 113 GPa in this study. Also, the value of the Young's modulus derived from inverting geodetic time series based on the Boussinesq's approximation depends on the spatial distribution of the stations, with respect to the distribution of surface load.

This problem is solved when a spherical layered Earth model is considered, as demonstrated by Farrell (1972). The PREM model is also found to reproduce better the temporal structure of the signal seen on individual component in our dataset as the seasonal loading pattern induced by the Monsoon is not stationary. This improvement is due to a better account of dependency of surface deformation to the distance to the load point. The study thus points to the importance of using a realistic model of the Earth structure to model deformation induced by surface loads.

It also shows the possibility to use seasonal geodetic displacements induced by variations in continental hydrology recorded by GRACE to probe the shallow Earth elastic structure (at depths typically shallower than 150 km). We show that the density profile found by inverting seasonal variations of surface displacements induced by continental hydrology shows lower density values for the crust, similar to a local density model. ( $V_p/V_s$ ) profile derived from GRACE is in agreement with one of the local velocity models but lacks at reproducing a lower ( $V_p/V_s$ ) zone between 23 and 55km found by Monsalve et al. (2006). The study shows that to probe the depth-dependent shallow Earth structure properties from the response to surface load variations, it is advantageous to use both the vertical and horizontal components.

However, even with adjusted shallow Earth elastic structure properties, the fit to the data is not perfect, with underpredicted and slightly out of phase signals in the Himalayan region. In order to better understand causes of misfit in phase and amplitude of a purely elastic spherical

and layered model predicting seasonal geodetic displacements, a global and more systematic study is required and described in *Chapter 3*. Indeed, the misfit might for instance depend on the wavelength of the load and a global study will help understanding spatial distribution of the misfit between observations and elastic predictions of seasonal surface displacements and discard potential causes.

Our study, even at this point, also has implications for tectonic geodesy as the accurate determination of secular rates, as well as the detection of transient deformation events requires proper identification and modeling of non-tectonic sources of surface deformation. Therefore, we propose a code written in Matlab to compute surface horizontal and vertical displacements at GPS stations due to atmospheric, non-tidal oceanic loads (MOG-2D) and, residual surface loads (continental hydrology, sediment transport...) inferred from GRACE. The code is available on the Tectonics Observatory website (<http://www.tectonics.caltech.edu/>) and described in Annex B, with a manual and associated Matlab functions.

## Supplements

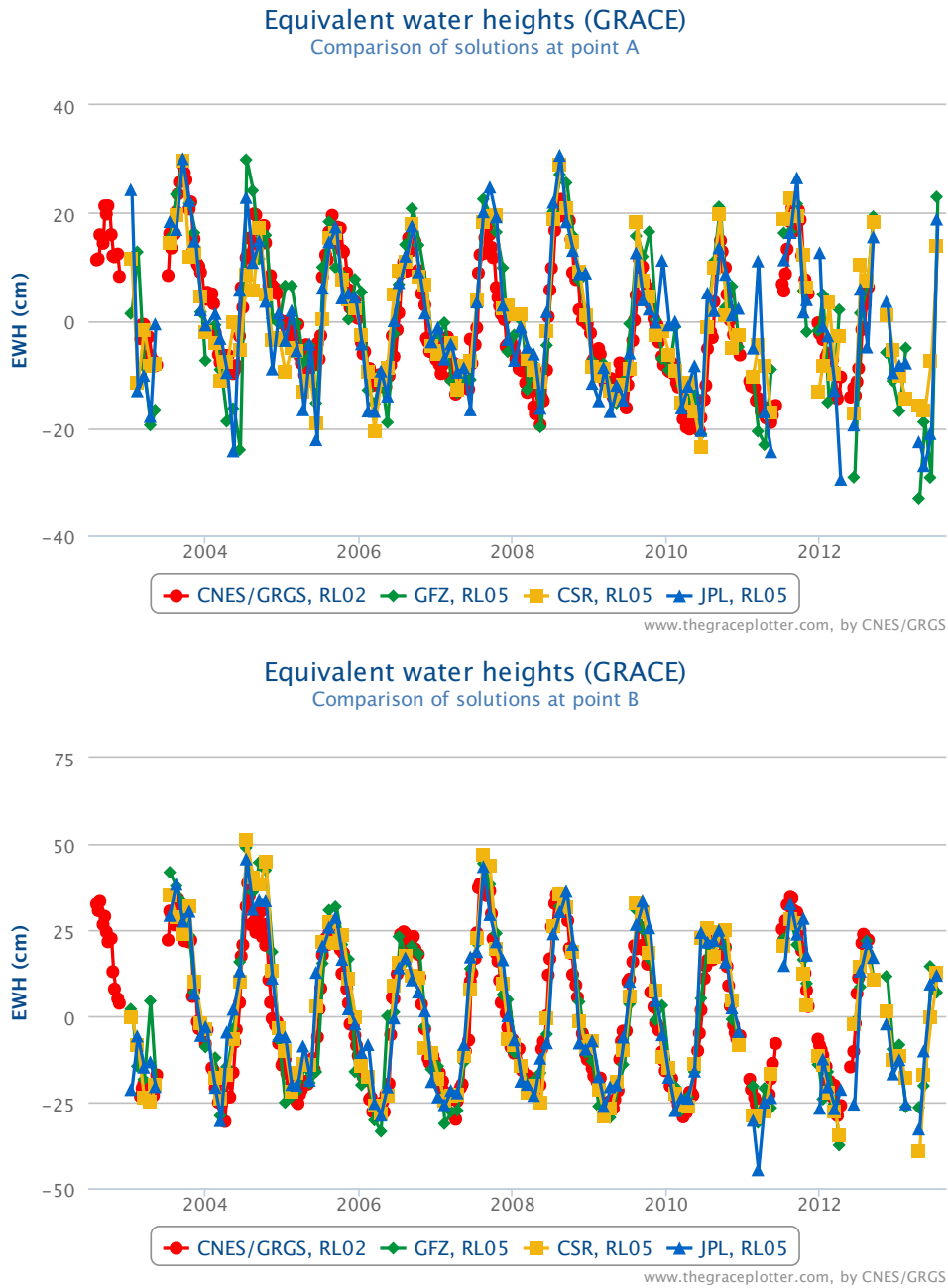


Figure S.1 – Comparison of GRACE solutions at Point A (Nepal) and Point B (Bangladesh) (see figure 1) from the CSR, GFZ, JPL and GRGS processing. Differences between solutions remain within our estimated uncertainties.

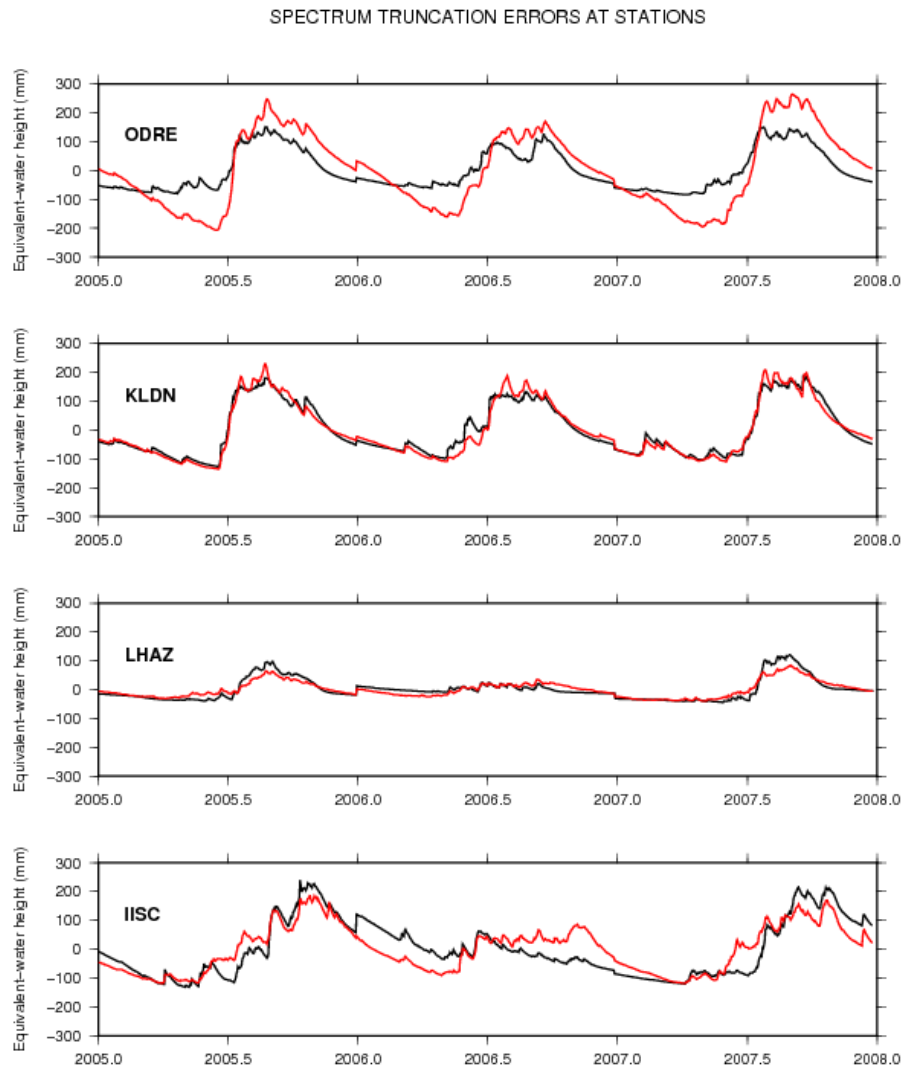


Figure S.2 – Spectrum truncation errors for equivalent water height expressed in mm at GPS stations. Black solid lines are interpolation of WGHM at GPS stations and red solid lines represent the same model, truncated at degree 50 (resolution of GRACE)

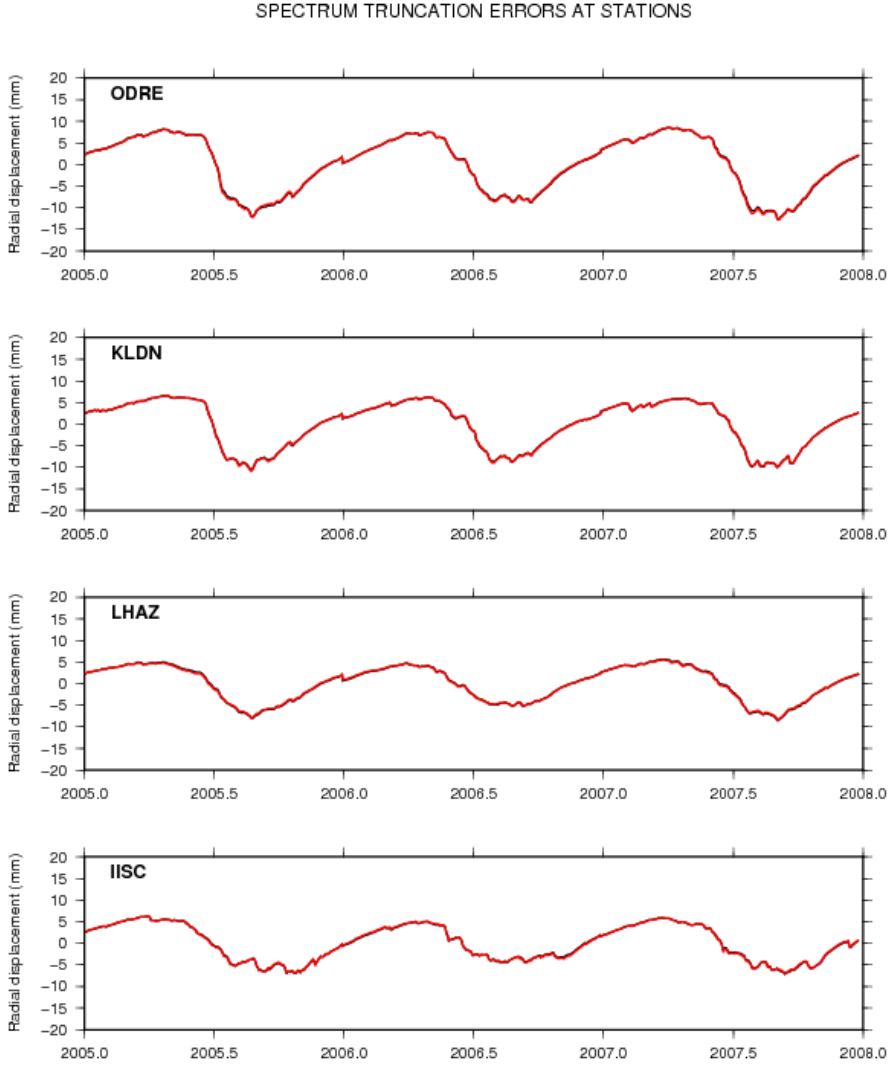


Figure S.3 – Radial displacements computed at 4 GPS stations. The black lines show displacements induced by a load from the WGHM model while the red lines correspond to the displacements induced by the same model, truncated to harmonic degrees lower than 50.

### 3.1 Introduction

Geodetic time series recorded by numerous and globally distributed continuous stations of the Global Positioning System (cGPS) show strong seasonal signals, on both horizontal and vertical component. Potential contributors to seasonal variations in site positions can be attributed to gravitational excitation, mostly from the Sun and the Moon (rotational displacements due to seasonal polar motion, loading induced displacements due to solid Earth tides, ocean and atmospheric tides, pole tides), thermal origins (bedrock thermal expansion), various errors in models (satellite orbits, atmospheric, thermal effects on antenna...), seasonal deformation induced by surface hydrology. [Dong et al. \(2002\)](#) explored the nature of observed seasonal variations in vertical position sites at global GPS sites and showed they can be primarily explained by surface mass redistribution, once other known physical processes such as tides have been accounted for. Seasonal variations of surface loads result from various sources, such as tidal and non-tidal loading ([Agnew, 1996, 1997](#)), continental hydrology ([Blewitt et al., 2001](#), [Bevis et al., 2005](#), [Van Dam et al., 2001](#), [Davis et al., 2004](#), [Bettinelli et al., 2008](#), [Steckler et al., 2010](#), [Elósegui et al., 2003](#), [Fu & Freymueller, 2012](#), [Fu et al., 2012](#), [Wahr et al., 2013](#), [Fu et al., 2013](#), [Chanard et al., 2014](#), [Nahmani et al., 2012](#)), ice and snow ([Grapenthin et al., 2006](#), [Matsuo & Heki, 2010](#), [Jiang et al., 2010](#)), atmospheric pressure ([Kaniuth & Vetter, 2006](#)).

Modeling these signals has attracted much attention recently. It has been established that regional seasonal displacements observed at cGPS stations can be fairly well predicted, particularly the vertical component, using the response of a realistic elastic spherical and layered

### Chapter 3. Global seasonal deformation

---

Earth model to seasonal variations of surface loading, mainly continental water storage and non-tidal and atmospheric masses, measurable using satellite gravity measurements provided by the Gravity Recovery and Climate Experiment (GRACE) missions (Nahmani et al., 2012, Fu et al., 2013, Fu & Freymueller, 2012, Fu et al., 2012, Chanard et al., 2014, Bettinelli et al., 2008).

Accurately modeling seasonal variations of geodetic site positions is of importance to determine more precisely long term velocities and even more to detect potential transient deformation such as slow slip events (Vergnolle et al., 2010). These signals are usually modeled empirically as sinusoidal signals. However, annual variations induced by surface hydrology actually exhibit a more complex behavior, with a spatio-temporal evolution and inter-annual variations. Most studies modeling annual variations in site positions as the response to surface loading focused on the vertical component due to its larger amplitude. However, Wahr et al. (2013), Fu et al. (2012), Chanard et al. (2014), Bettinelli et al. (2008) recently pointed out the importance of modeling the horizontal component of signals induced by surface load which are not necessarily compatible with empirical estimates, and could also provide useful insights on the Earth's mechanical properties.

In this study, we first present GRACE, where we replaced non-observable degree-one components using results from Swenson et al. (2008), and GPS data used in our study in section 3.2. In section 3.3, we propose a global model for horizontal and vertical displacements induced by seasonal hydrology derived from GRACE, where degree-one coefficient are accounted for following Swenson et al. (2008), loading on a spherical, layered and elastic Earth model based on the Preliminary Reference Earth Model (PREM). We compare predicted displacements with observations at 195 globally distributed cGPS stations and show that while the vertical displacements are fairly well modeled, a systematic misfit in phase and amplitude is seen between the predicted horizontal components and the observed data, similar to other regional studies using a comparable Earth model (Fu et al., 2013).

Once other potential contributors (thermal expansion, draconitic effects, processing bias, etc.) are discarded in section 3.4, we interpret these differences as a mismodeled degree-one deformation and reference frame for horizontal deformation in section 3.4.7. The longest

wavelength component of surface mass transfer, the spherical harmonic degree-one, involves the exchange of consequent hydrosphere masses from one hemisphere to the other. These degree-one mass exchanges deform the Earth, as for higher degrees, but also induce geocenter motion between the center of mass (CM) of the total Earth system and the center of figure (CF) of the solid Earth, which affects vertical and horizontal components in a significantly different way. Our initial seasonal model is expressed in a representation of a CM centered reference frame, and then transformed into a CF centered reference frame using an estimate of geocenter motion derived from a combination of GRACE data and the output from ocean models (Swenson et al., 2008). Daily geodetic positions measured by GPS are in a reference frame centered on a representation of CF, derived from horizontal and vertical on-land observations. This suggests that coefficients of geocenter motion from (Swenson et al., 2008) is not directly comparable with geodetic stations anchored to the Earth's surface because positioned by satellites orbiting around CM (Kang et al., 2009, Stolz, 1976, Rietbroek et al., 2012, Bouille et al., 2000), as it affects the definition of the International Terrestrial Reference Frame (ITRF) and therefore geodetic measurements used in geophysical studies. Understanding degree-one deformation, or at least how to circumvent the problem, is therefore essential to model more accurately seasonal deformation. In our study, we do not apply a priori degree-1 coefficients but estimate and apply a posteriori a 6-parameters Helmert transform to the horizontal components and reconcile reference frames to improve the predicted seasonal horizontal displacements. The transformation is essential to improve the fit in phase and amplitude of our seasonal deformation model to the horizontal GPS measurements and does not affect the fit to the vertical component, even if it only accounts for a rigid transformation, and not actual deformation, which was beyond the scope of this thesis and remains to do. However, the amplitude of the horizontal components is still under-predicted.

In order to address this issue, we explore several hypothesis including the validity of a purely elastic model at an annual time scale. Indeed geodetic observations occurring between several hours and decades, such as Chandler Wobble period and damping measurements (Anderson & Minster, 1979, Smith & Dahlen, 1981), tidal variations of the Earth's rotation rate and gravity field (Benjamin et al., 2006) or global tidal displacements (Kang et al., 2015), can all provide constraints on the Earth's mantle anelasticity, in addition to seismic estimates restricted to

time-scales smaller than the longest free oscillation period, i.e. under an hour (Durand et al., 2012). Using a model with mechanical properties derived from seismic records at a one year loading period is therefore questionable, considering the observation of anelastic behavior at comparable time scales, as for viscoelastic postseismic deformation. In section 3.5, we discuss the influence of variations in elastic parameters, viscoelastic Maxwell and Burger rheologies in the asthenosphere on seasonal deformation. We show that annual signals may be used to place rheological constraints on the asthenospheric viscosity. Furthermore, we show the possible role of mantle volume variations induced by mineral phase transitions on modeling seasonal surface displacements induced by variations in surface hydrology. Indeed, we propose a way to improve the fit of our model to the observed seasonal data by adjusting previously unconstrained frequency dependent bulk modulus in the Earth mantle.

Finally, we discuss the implications of seasonal deformation on fault failure and the importance of accurate seasonal models to detect potential transient deformation in section 4.2.

Accurate geophysical models of seasonal deformation, for both horizontal and vertical components, have far-reaching implications. First, seasonal motion is one of the current factors limiting the accuracy and precision of the definition of international terrestrial reference frame. Physics-based models for seasonal deformation will, in turn, help improving the analysis of space geodetic data. In addition, the possible use of deformation of the Earth under forcing from seasonal changes in surface mass loading to place constraints on the Earth rheology may help understand other geophysical processes occurring at comparable time scales.

### **3.2 Estimating global variations of surface hydrology and surface ground displacement**

#### **3.2.1 Continental water mass variations derived from GRACE Level-2 solutions**

In order to estimate global mass redistribution at the Earth surface, we use data collected by the GRACE experiment, a tandem satellite mission launched in March 2002. GRACE provides a global map of the gravity field variations from monthly to decade time scales (Tapley et al.,

### 3.2. Estimating global variations of surface hydrology and surface ground displacement

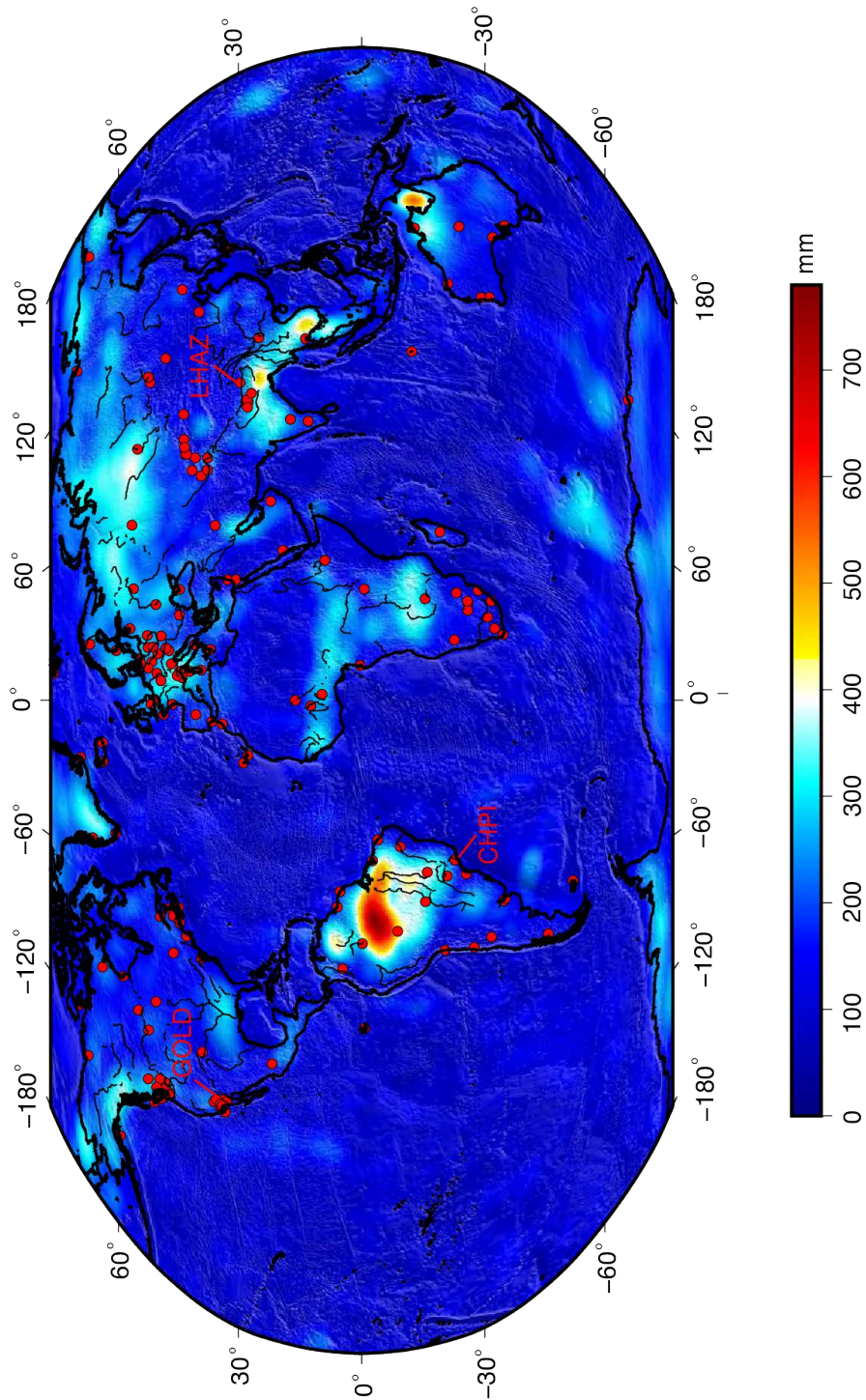
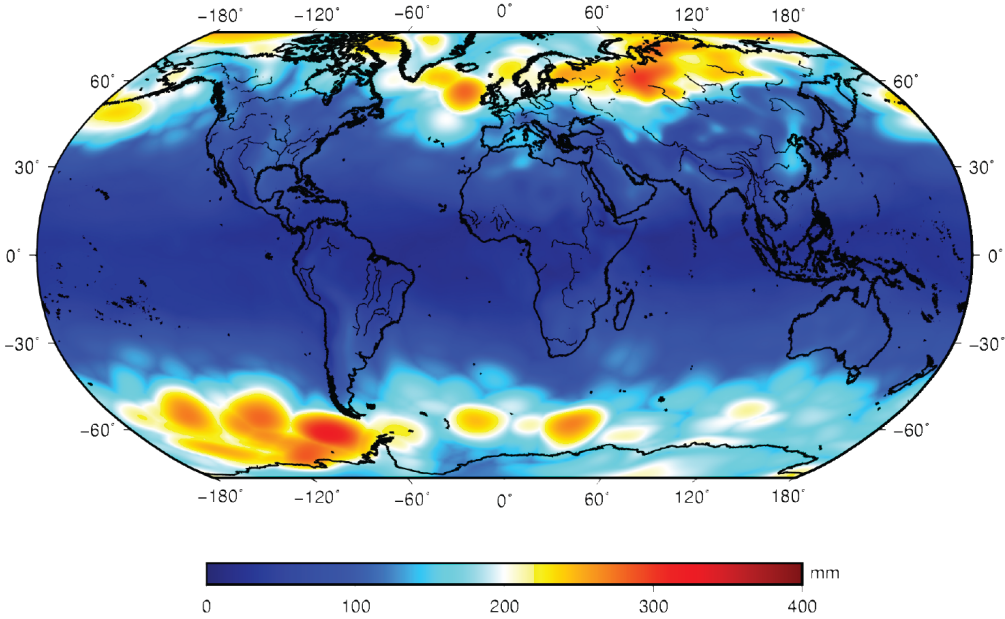
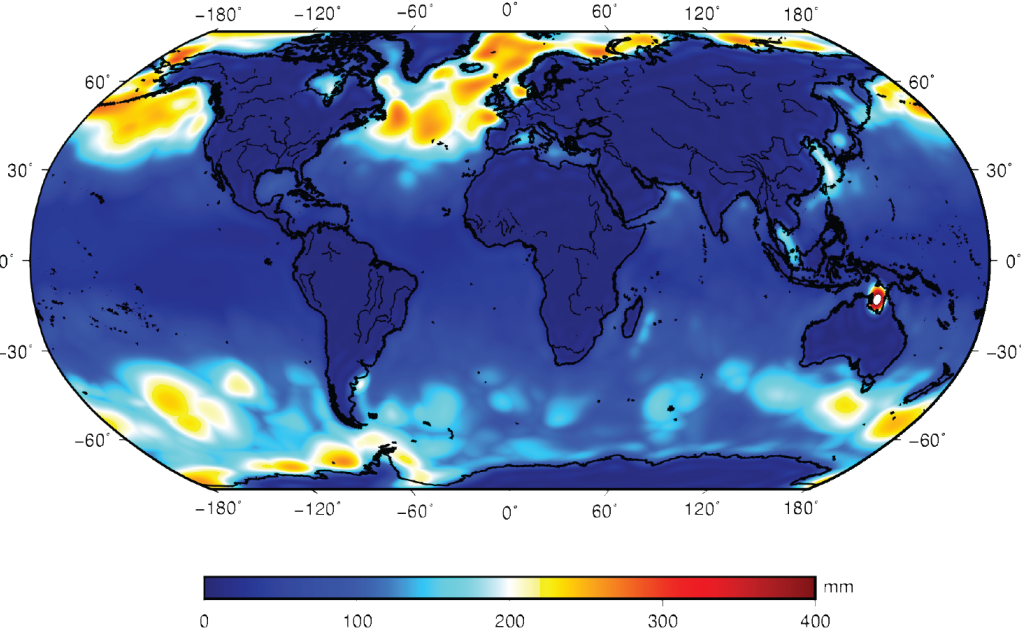


Figure 3.1 – Peak to peak surface load variations, expressed in equivalent water height (in mm), derived from GRACE for the 2002-2012 period and corrected from detectable earthquakes coseismic contributions. Red dots show location of the continuous GPS stations used in this study. LHAZ, GOLD and CHPI are highlighted because time series for these three stations are shown for example later on.



(a) Atmospheric contributions



(b) Non-tidal oceanic contributions

Figure 3.2 – Peak to peak surface (a) atmospheric and (b) non-tidal oceanic variations, expressed in equivalent water height (in mm), derived from Mog-2D (Carrère & Lyard, 2003) for the 2002-2012 period

### **3.2. Estimating global variations of surface hydrology and surface ground displacement**

2005), with a spatial resolution of  $\sim 200$  km. Thus, the mission potentially gives access to large-scale variations within the hydrosphere once the influence of the static geoid is corrected.

To do so, gravitational contributions of all known time-varying phenomena from the raw GRACE data are removed, and monthly and 10-day Level-2 solutions obtained by least-square orbit adjustment of the residual observations for each period of time are released (Lemoine et al., 2007, Bruinsma et al., 2010, Ramillien et al., 2005). These solutions are made available by the CNES/GRGS at <http://grgs.obsmip.fr/>.

Among the gravitational contributions corrected in the 10-day solutions, atmospheric and non-tidal oceanic loads produce non-negligible effects at high and low latitudes while they are not accounted for in the GPS processing. For consistency, we therefore chose to add back to the 10-day GRACE solutions this contribution, using the non-tidal ocean model forced by air pressure and wind on ocean: Mog-2D (Carrère & Lyard, 2003), provided by the European Centre for Medium-Range Weather Forecasts (ECMWF).

The 10-day solutions are expressed in terms of Stokes coefficients (i.e., non-dimensional spherical harmonic coefficients of the geopotential) which represent the gravitational effects of non-modeled phenomena, mainly continental hydrology. Stokes coefficients are converted into geoid and water mass coefficients, expressed in terms of mm of equivalent-water height, by isotropic filtering (Ramillien et al., 2005). Then, 10-day 1-by-1 degree grids of water mass are interpolated from the water mass coefficients and a time-average is removed from each 10-day solution so that the solutions are expressed with respect to the mean solution over the time span of analysis.

We use global continental water, atmospheric and non-tidal mass variations time-series from February 2002 to August 2012 in which large coseismic gravity changes due to mega-earthquakes are recorded (Han et al., 2006). Post-seismic recovery of the geoid variations is also observed (Han et al., 2008, Ogawa & Heki, 2007) and causes apparent variations in equivalent water height (Chen et al., 2007). For example, Sun & Okubo (1993) have shown that measurable co- and postseismic geoid and gravity changes can be induced by large earthquakes ( $M \geq 7.5$ ).

### Chapter 3. Global seasonal deformation

---

For the purpose of our study, we empirically model and remove earthquake-induced mass redistribution observable in the gravity field measurements for each  $M > 7.5$  earthquake which occurred within the 2002-2012 period using the empirical formulation:

$$h_s(m, t) = h(m, t) - \sum_i \alpha_i \mathcal{H}(t - t_i) + \sum_i \beta_i \mathcal{H}(t - t_i) \ln\left(1 + \frac{t - t_i}{\tau}\right) \quad (3.1)$$

where  $h_s$  refers to the seasonal equivalent water height measured by GRACE at point  $m$  at the Earth surface, after earthquake contributions have been removed from the equivalent water height  $h$ .  $\mathcal{H}$  is the Heaviside function representing abrupt coseismic changes of the gravity field at time  $t_i$ , and  $\tau$  is the characteristic time of postseismic relaxation described by [Hoechner et al. \(2011\)](#).  $\alpha_i$  and  $\beta_i$  are constants estimated by a least-square inversion. The main signal removed from the equivalent water level is the co-seismic offset induced by the 2004 Sumatra-Andaman earthquake (see 3.6). Figure 3.1 shows the averaged annual peak to peak amplitude of the equivalent water height ( $h_s$ , in mm) at the Earth surface for the 2002-2012 time period that we will use as our load model in the following. Figure 3.2 gives, for information, the amplitude of the atmospheric and non-tidal oceanic contributions calculated with Mog-2D.

Note that the degree-one Stokes coefficients, which are intimately related to the choice of reference frame, are not observable by GRACE mission. The reference frame origin used in the GRACE gravity field determination is the Earth's center of mass (CM). In this reference frame, the degree-one Stokes coefficients from the combined surface mass plus solid Earth are zero by definition. [Swenson et al. \(2008\)](#), proposed an algorithm to infer the degree one mass coefficients from the GRACE fields, i.e deformation induced by degree one and associated geocenter motion. As proposed by [Swenson et al. \(2008\)](#), we first account for degree-one coefficients to model seasonal deformation recorded by cGPS stations as several other studies such as [Fu & Freymueller \(2012\)](#), [Fu et al. \(2012, 2013\)](#). We add cosine functions using [Swenson et al. \(2008\)](#) amplitude and phase estimates of degree-one contributions to our model a posteriori. Examples of differences between models with no degree-one or including degree-one contributions ([Swenson et al., 2008](#)) are given in Supplement 3.6 for three GPS stations (see Figure 3.1 for location). However, because our predictions presents significant discrepancies with horizontal observations, and due to the large variability in geocenter motion estimates

## **3.2. Estimating global variations of surface hydrology and surface ground displacement**

---

(see [Wu et al. \(2012\)](#), Table 2), we will omit degree-one in the GRACE dataset later on, and will address the problem a posteriori in section 3.4.7.

### **3.2.2 The GPS dataset**

#### **GPS Processing**

In this study, we use data from cGPS stations processed by the Nevada Geodetic Laboratory, as part of a network analysis with over 11000 stations. Data are processed using the GIPSY/OASIS software (Jet Propulsion Laboratory) to estimate daily station coordinates using the Precise Point Positioning method. This is an arbitrary choice and has no significant consequence on the precision of seasonal signals (see section 3.4.1). We describe in the following the processing strategy as stated by the Nevada Geodetic Laboratory (<http://geodesy.unr.edu/>). Ionosphere-free combinations of carrier phase and pseudorange are obtained every 5 min. Calibrations are applied for all antennas, ground receivers and satellite transmitters. To model tropospheric refractivity, the Global Mapping Function was applied, with tropospheric wet zenith delay and horizontal gradients estimated as stochastic randomwalk parameters every 5 min. The observable model includes ocean tidal loading coefficients supplied by Chalmers University. Ambiguity resolution is applied to double differences of the estimated one-way bias parameters, using the wide lane and phase bias method, which phase-connects individual stations to IGS stations in common view. Satellite orbit and clock parameters are provided by the Jet Propulsion Laboratory, who determine these parameters in a global fiducial-free analysis using a subset of the available IGS core stations as tracking sites. Output station coordinates are initially in the loose frame of the Jet Propulsion Laboratory's fiducial-free GPS orbits. These are transformed into reference frame IGS08, using daily seven-parameter transformations supplied by the Jet Propulsion Laboratory (with equal weight on components), which is derived from ITRF2008 ([Altamimi et al., 2011](#)) and consists of 232 globally distributed IGS stations.

### Extracting seasonal signals from time series

We favor data recorded by stations of the International GNSS Service (IGS) network to achieve good quality data at a globally distributed network of sites with long duration time series ( $\leq 4$  years).

In order to extract the non-tectonic signals  $D_s$  of a time series  $D$ , we model and remove from the 452 cGPS stations of this network (i) their initial position  $D(t_0)$ , (ii) steady velocity  $V(t - t_0)$ , (iii) potential earthquake co- and postseismic (with characteristic time  $\tau$ , determined from postseismic studies of each modeled earthquake) contributions (see 3.6), (iv) known material change jumps, described respectively by constants  $(a_i, b_i)$  and  $c_j$  as follows:

$$D_s(t) = D(t) - D(t_0) + V(t - t_0) + \sum_i a_i \mathcal{H}(t - t_i) + \sum_i b_i \mathcal{H}(t - t_i) \ln\left(1 + \frac{t - t_i}{\tau}\right) + \sum_j c_j \mathcal{H}(t - t_j) \quad (3.2)$$

The remaining time series  $D_s$  contain mostly periodic signals. For example, Figure 3.3 shows raw time series  $D^{LHAZ}$  processed by the Nevada Geodetic Laboratory at station LHAZ, China (see Figure 3.1 for location). Origin ordinates for each components represent the initial positions, slopes the steady velocities and material changes are highlighted by dashed lines. Figure 3.4 shows  $D_s^{LHAZ}$ , where seasonal variations are clearly seen on the north and vertical components, with amplitudes of about 5 and 15 mm, respectively.

However, a number of other stations present large data gaps and complexities due to poorly estimates of postseismic deformation, or non-modeled phenomena, for instance, unrelated transient deformation. From the initial 452 stations, we thus remove stations for which  $D_s$  shows significant non-seasonal signals and a large number of missing data.

We retain a subset of 173 cGPS IGS stations to which we add 28 continuous GPS stations from other networks, processed and corrected similarly, in targeted areas where strong seasonal displacements have been reported (Himalaya, Amazonia, Canada, Africa). The location of the 195 stations used in this study is shown on Figure 3.1 and referenced in 3.6. These stations belong to several national and international networks. Further information on each station is available on <http://geodesy.unr.edu/>.

### 3.2. Estimating global variations of surface hydrology and surface ground displacement

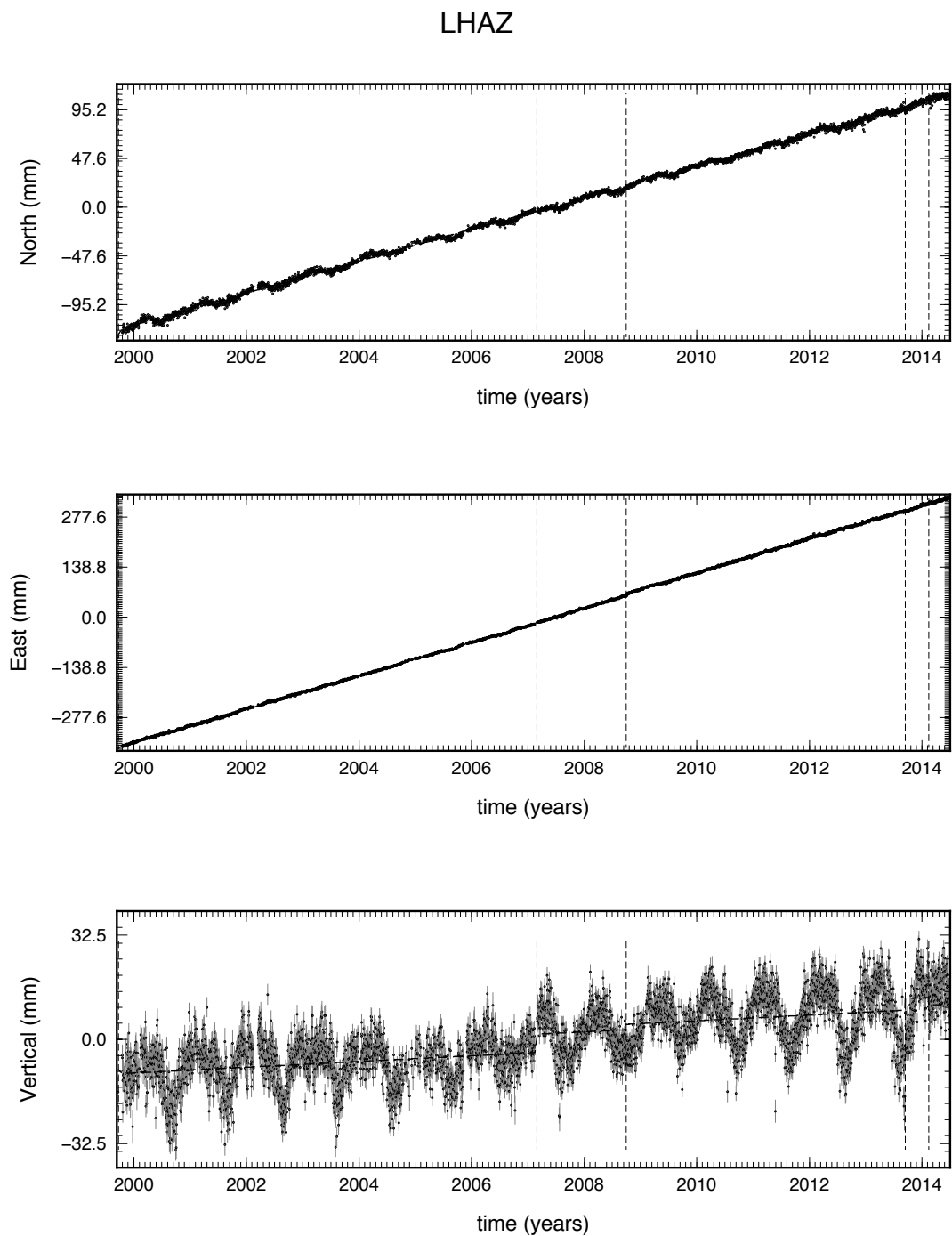


Figure 3.3 – Raw daily geodetic positions, determined at station LHAZ (black dots) by the Nevada Geodetic Laboratory. Error-bars show 1- $\sigma$  uncertainties (gray symbols). Dashed vertical lines show times of material changes and dashed slopes steady velocities.

LHAZ

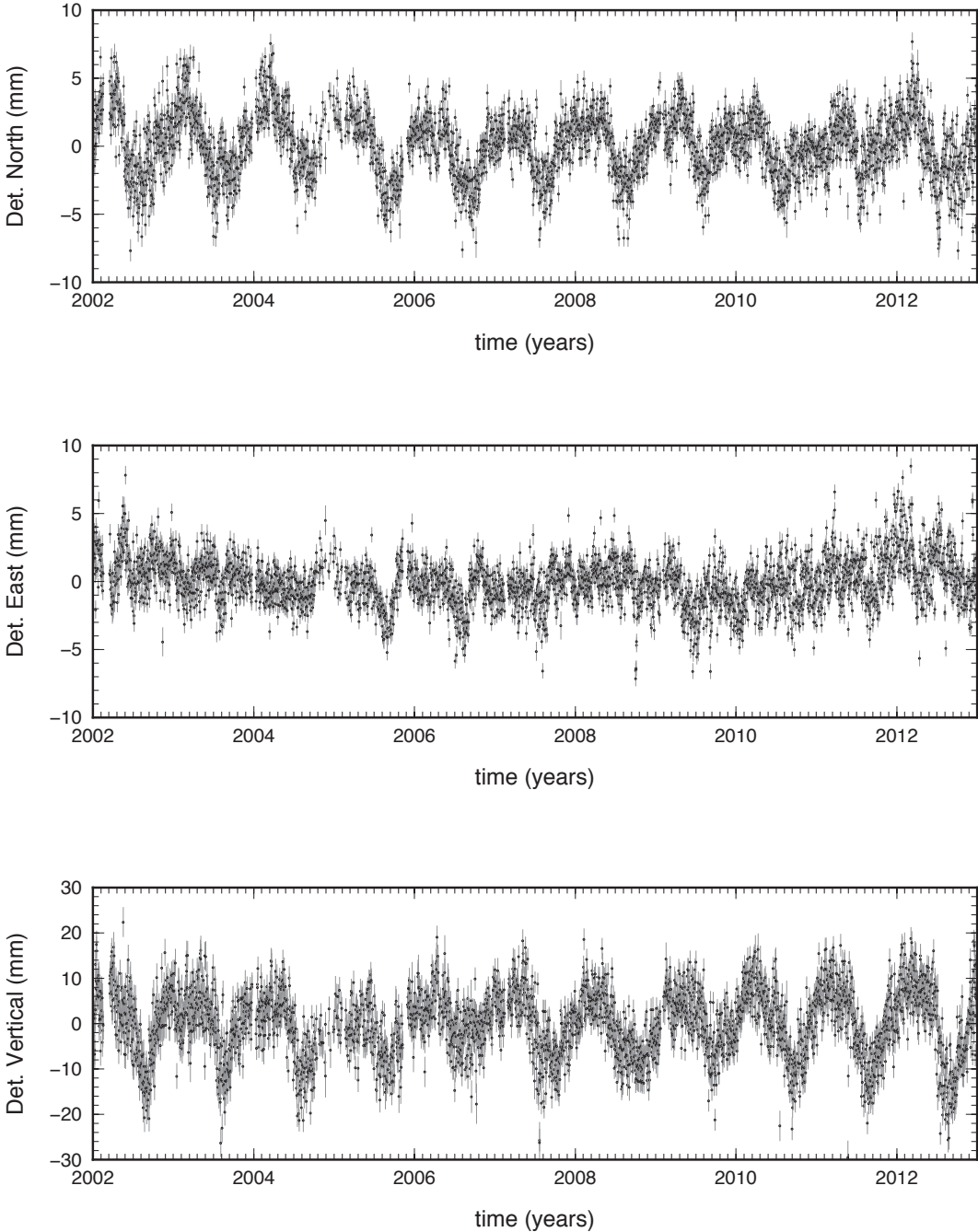


Figure 3.4 – LHAZ daily geodetic positions determined by the Nevada Geodetic Laboratory, detrended and corrected for change in instrument jumps (black dots). Error-bars show 1- $\sigma$  uncertainties (gray symbols). North and Vertical components show clear seasonal signals.

### 3.2. Estimating global variations of surface hydrology and surface ground displacement

---

#### Removing outliers

Our initial dataset of geodetic time series contains outliers. We removed them using a sliding 90-day window on time series that have been detrended and corrected from external contributors mentioned in section 3.2.2 if necessary. For each single window, we compute the median  $M$  of the set of measurements. We then calculate the deviation  $r_i$  from of each point  $d_i$  from the median value  $M$  as  $r_i = d_i - M$ . Let  $M_r$  the median for deviations. A point with  $|r_i| > 2M_r$  is considered as an outlier and removed from the time series. Figure 3.5 shows the example of station LHAZ, Tibet, China. Blue dots are the detrended and corrected site positions. Red dots are data points identified as outliers. For this particular station, we removed 7% of the datapoints on the north and east component, and 5% on the vertical component. For the 195 cGPS stations, the percentage of points removed ranges between:

- [5%,10%], for the north and east components with a mean value of 6.5%,
- [4%,9%] for the vertical component, with a 6.7% mean value.

This is a standard method for removing outliers in GPS time series, with appropriate parameters to fill the seasonal requirements.

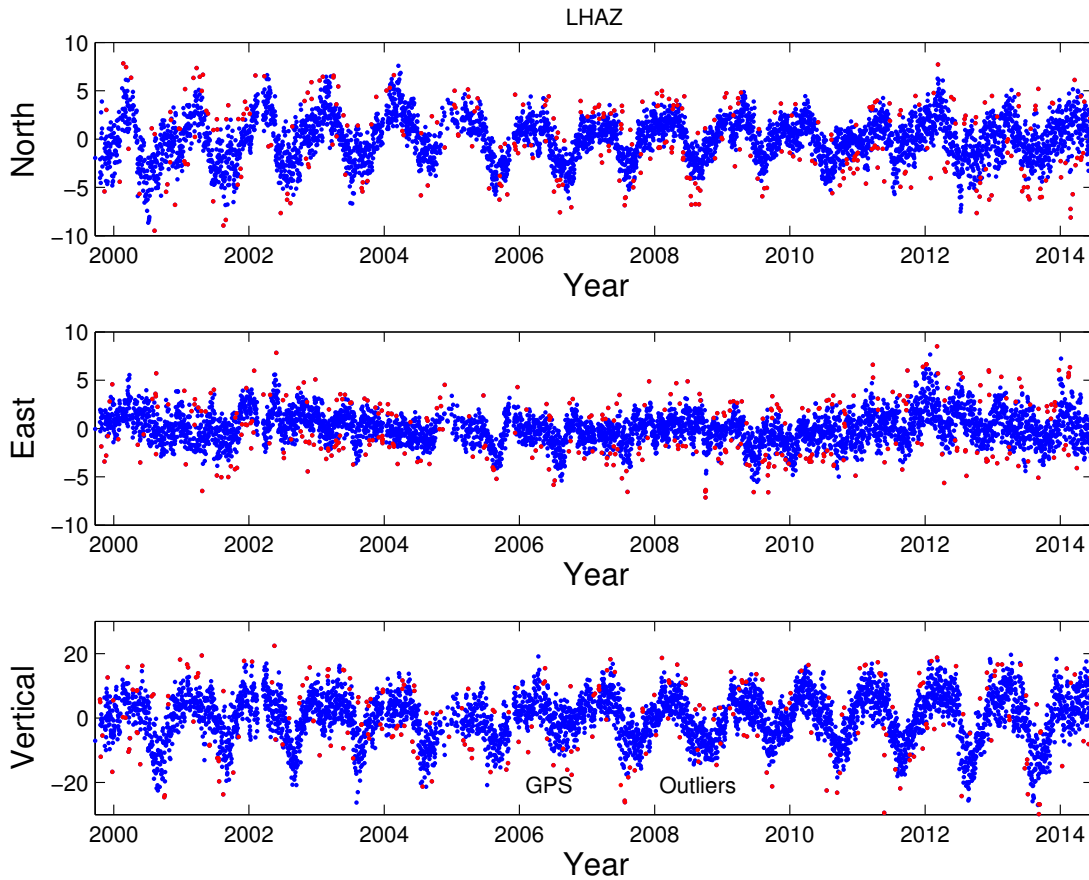


Figure 3.5 – LHAZ daily geodetic positions determined by the Nevada Geodetic Laboratory, detrended and corrected for change in instrument jumps (blue dots). Red dots highlight outliers removed from the time series.

### 3.3 Global elastic modeling of seasonal ground deformation induced by surface load variations

#### 3.3.1 Description of the model

We compute the Earth’s surface displacements induced by variations in seasonal surface hydrology derived from GRACE (see section 3.2.1). The numerical model, originally developed for post-glacial rebound problems by Luce Fleitout, is based on a spherical harmonics and temporal frequencies decomposition of the hydrological loads and uses the Love number theory. A surface load,  $\mathcal{L}(t, \theta, \phi)$ , varying with time ( $t$ ), longitude ( $\theta$ ) and latitude ( $\phi$ ), is decomposed into a load  $\mathcal{L}(\omega, l, m)$  varying with temporal frequency ( $\omega$ ) and spherical harmonics of degree

### 3.3. Global elastic modeling of seasonal ground deformation induced by surface load variations

---

and order  $(l, m)$ .

Surface displacements induced by a unit load are computed for each spherical harmonic of the decomposition and each frequency of the load by solving a system of equations for the elastic deformation of a self-gravitational spheroid body, similar to classical normal modes theory used in seismology. We account for the visco-elastic response of the Earth to surface loading using the correspondence principle, associating the time dependent problem to the initial elastic one in the Fourier domain (Wu & Peltier, 1983, Cathles, 1975). This is equivalent to determining the complex Love numbers  $h(\omega, l)$  and  $\ell(\omega, l)$  for any visco-elastic Earth structure. Displacements for each frequency and spherical harmonic are then combined to obtain surface displacements induced by the global load derived from GRACE at time  $t$ , longitude  $\theta$  and latitude  $\phi$ , and spatially interpolated at cGPS stations coordinates to be directly comparable to geodetic displacement data.

In the purely elastic case, the code reproduces load Love numbers for a realistic compressible Earth. In this section, we focus only on the elastic model, commonly used to model the Earth's response to seasonal hydrological loading based on the assumption that an elastic behaviour is a fair first order approximation for annual deformations (Fu & Freymueller, 2012, Fu et al., 2012, Chanard et al., 2014, Bettinelli et al., 2008). More complex structures will be discussed in section 3.5 in order to test their influence on seasonal model predictions and improve the fit to seasonal geodetic observations.

#### 3.3.2 Model for Earth

We compute load Love numbers for a modified Preliminary Reference Earth Model (PREM), proposed by Dziewonski & Anderson (1981), for which the ocean is replaced by a continental crust as shown in Figure 3.6 and referenced in Table 3.1 (Bassin, 2000). We then compute the Green's functions for horizontal and vertical surface displacements associated to the deformation of this spherical non-rotating elastic and isotropic model for Earth under an harmonic unit loading function, with a 1 year period. Figure 3.7 shows the Green's functions for surface horizontal (red), and vertical (blue) displacements in response to a 1-year period harmonic unit load as a function of the spherical harmonic number  $n$ , or the wavelength  $\lambda$  of

### Chapter 3. Global seasonal deformation

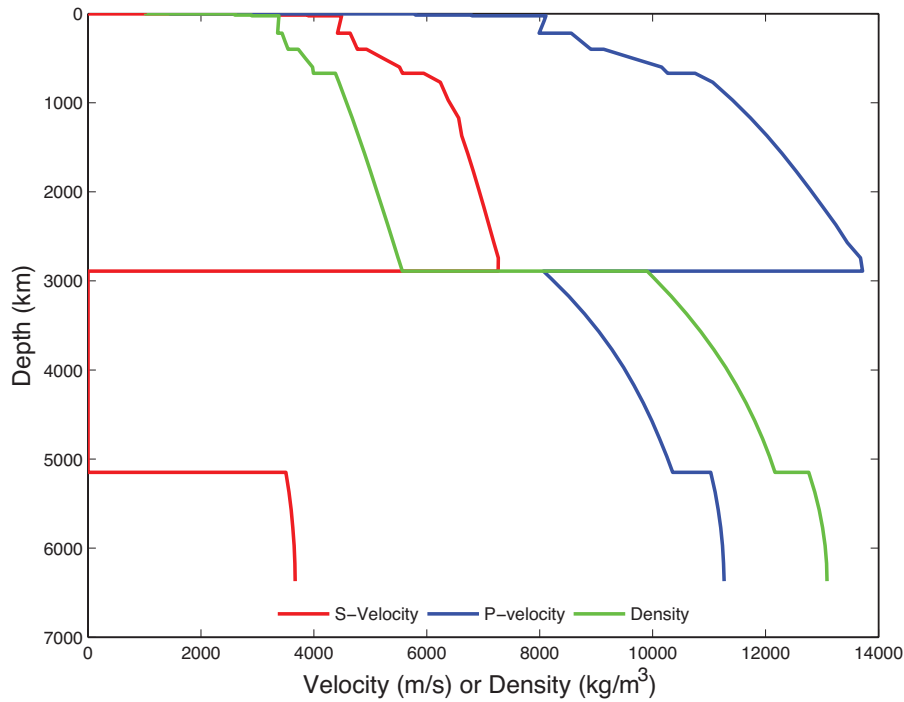


Figure 3.6 – P-wave, S-wave and density profiles for modified continental PREM (with CRUST 2.0)

top of layer ( <i>km</i> )	$V_p$ ( <i>km/s</i> )	$V_s$ ( <i>km/s</i> )	$\rho$ ( <i>g/cm</i> <sup>3</sup> )
-0.31	3.81	2.01	2.38
-1.14	6.13	3.54	2.76
-14.02	6.52	3.67	2.88
-26.63	7.09	3.93	3.05
-37.51	8.15	4.67	3.35

Table 3.1 – Average 1D continental global crustal model CRUST 2.0.

the load defined as  $\lambda = \frac{2\pi R}{n}$ , with  $R$  the radius of the Earth. Because of the spherical geometry and the layering of the Earth model, both surface components of the displacement do not evolve similarly with the wavelength of the load as would be observed for an homogeneous elastic half-space model. We compute the global east, north and vertical displacements induced by seasonal surface hydrological loading derived from GRACE over a 10 years period from 2002 to 2012 and on a 1 by 1 degree grid using our modified elastic PREM model.

Global peak to peak amplitudes of geodetic displacements for each component are shown on Figure 3.8. Predicted horizontal elastic displacements amplitudes remain relatively small, (<4 mm) while vertical seasonal signals are larger (~ 30 mm at maximum). North-South

### 3.3. Global elastic modeling of seasonal ground deformation induced by surface load variations

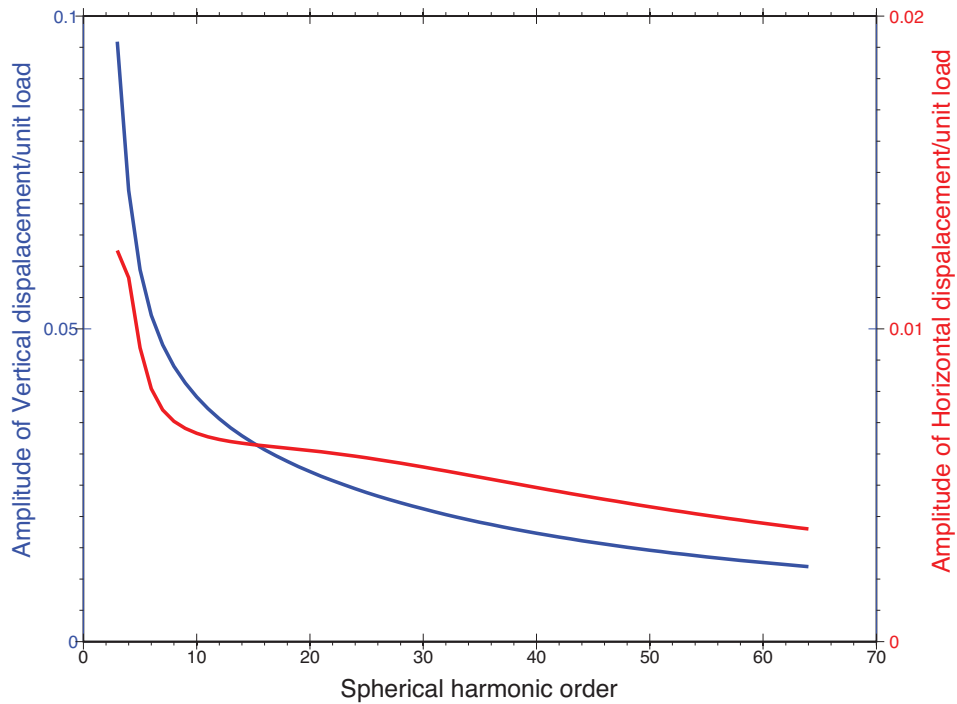


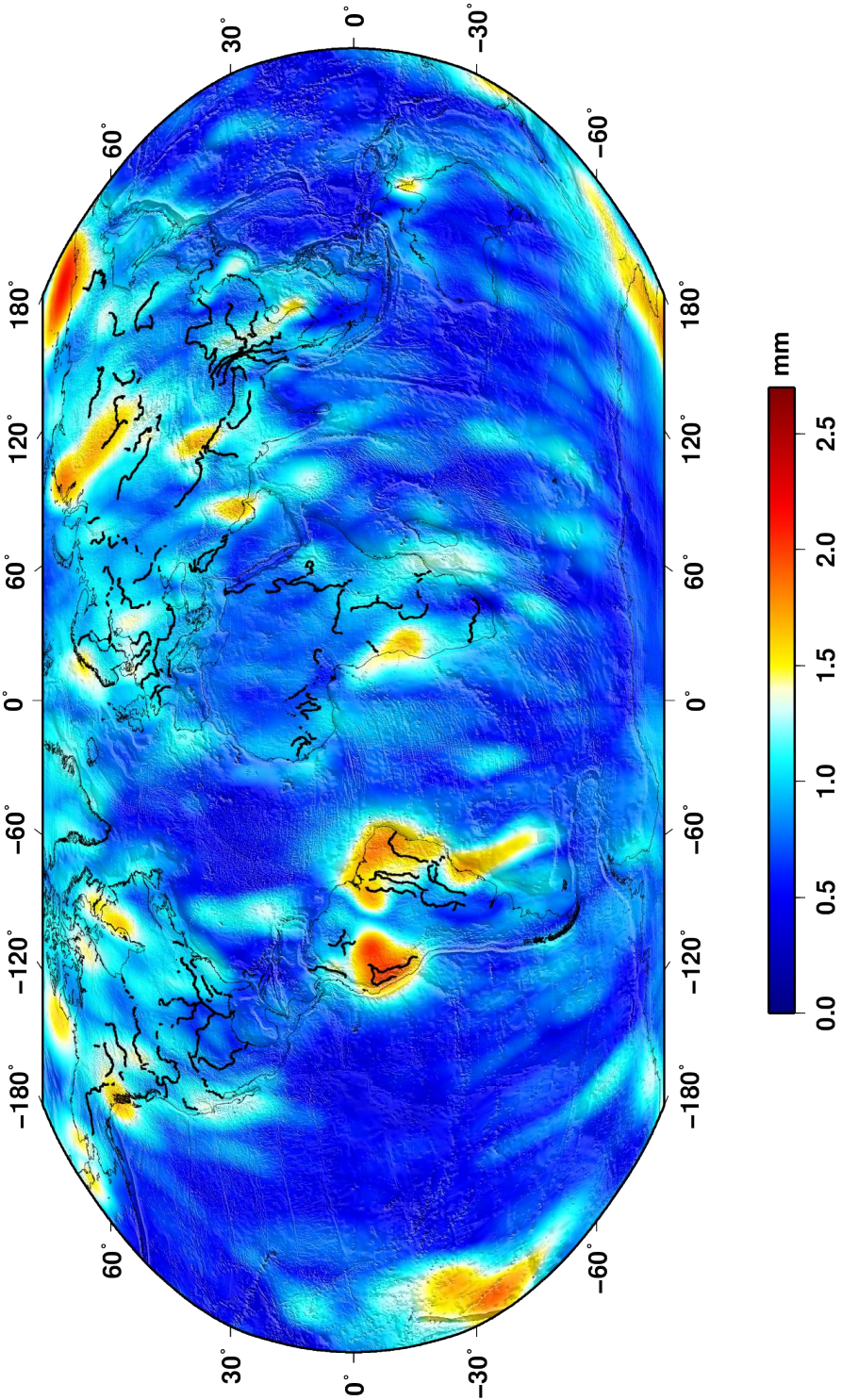
Figure 3.7 – Vertical (blue) and horizontal (red) amplitude of surface displacement as a function of spherical harmonic number, in response to a unit 1 year period harmonic loading function.

stripes appear mostly on the eastern displacements, as a consequence of noise in the Stokes coefficients for high harmonics degrees. Areas most deformed seasonally are, as expected, correlated with large hydrological cycles, such as the Monsoon regime in south Asia, central Africa and the Amazon area. Large seasonal surface displacements are also observed at high and low latitudes, due to snow and glacial loading (Alaska, Canada, Russia, Antarctica).

#### 3.3.3 Data-model comparison

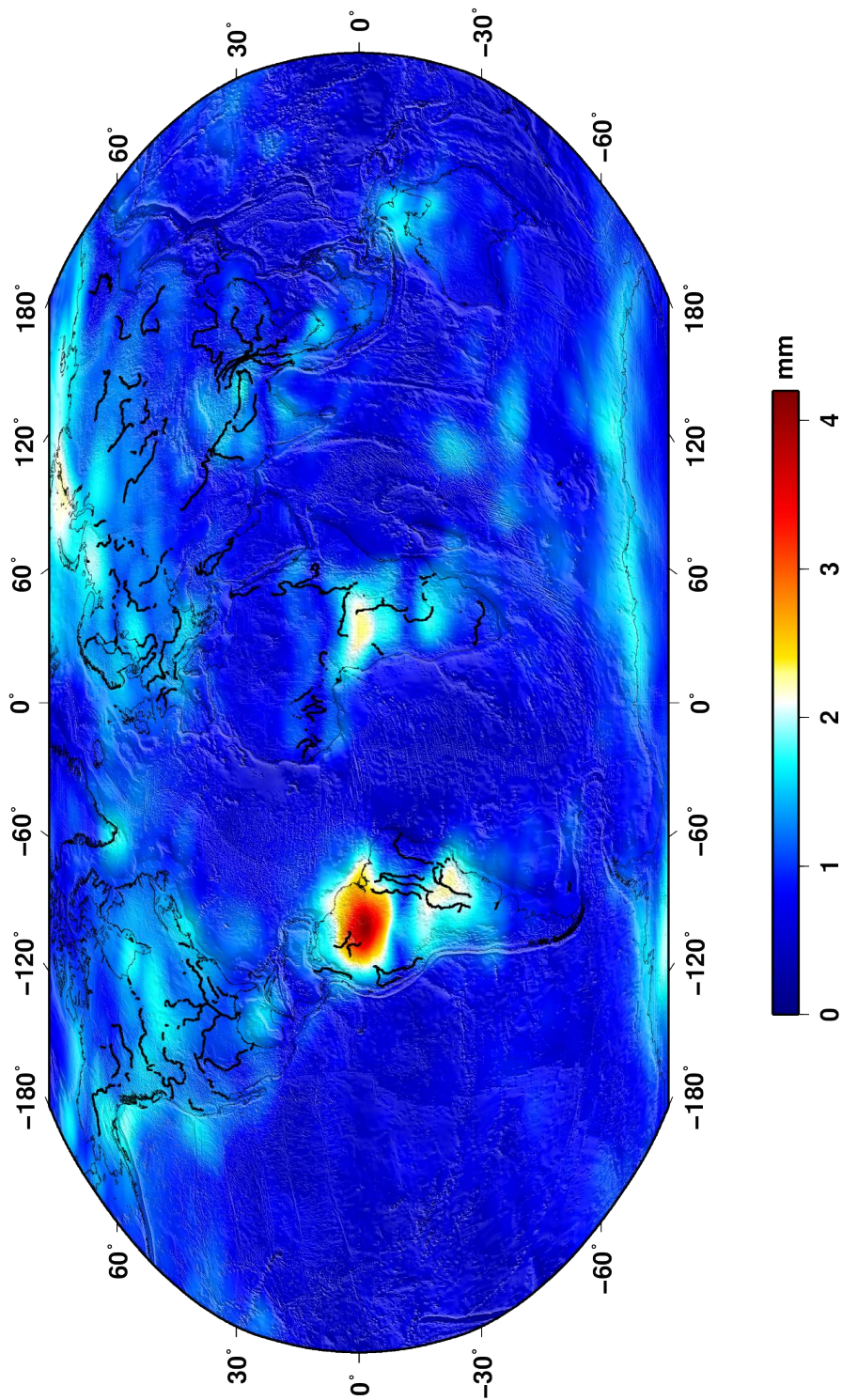
We compute the response of the elastic Earth model presented above to the 2002-2012 variations of surface hydrology derived from GRACE at all cGPS stations referenced in 3.6. Figure 3.9 shows east, north and vertical detrended daily geodetic displacements with error-bars of

Figure 3.8 (*following page*) – Peak to peak amplitude of elastic (continental PREM-like model for Earth) displacements induced by seasonal variations in surface hydrology derived from GRACE, without replacing degree-one components, and using continental-PREM like model for (a) east, (b) north and (c) vertical components.

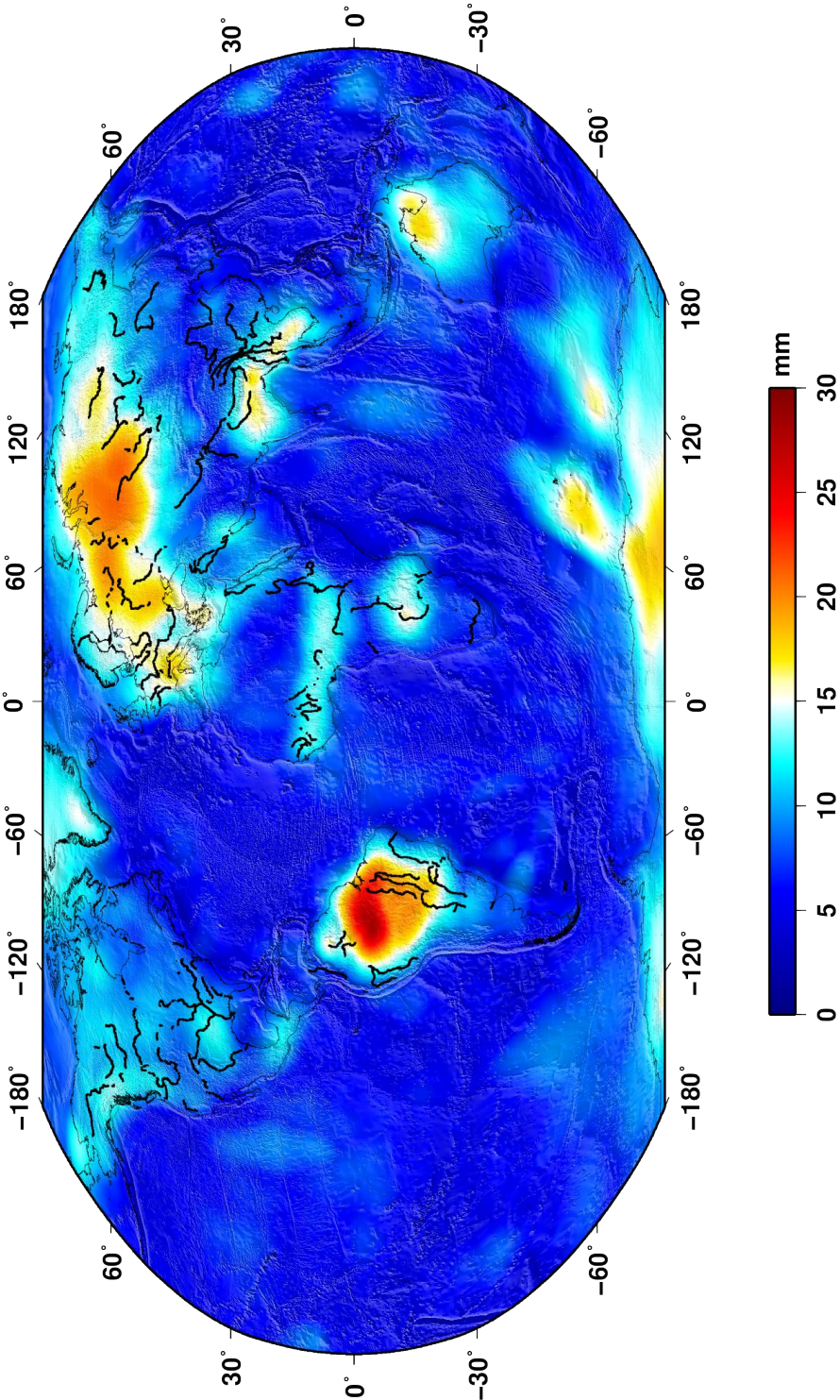


(a) Peak to peak amplitude of elastic east displacements induced by seasonal hydrology derived from GRACE

### 3.3. Global elastic modeling of seasonal ground deformation induced by surface load variations



(b) Peak to peak amplitude of elastic north displacements induced by seasonal hydrology derived from GRACE



(c) Peak to peak amplitude of elastic vertical displacements induced by seasonal hydrology derived from GRACE

### 3.3. Global elastic modeling of seasonal ground deformation induced by surface load variations

---

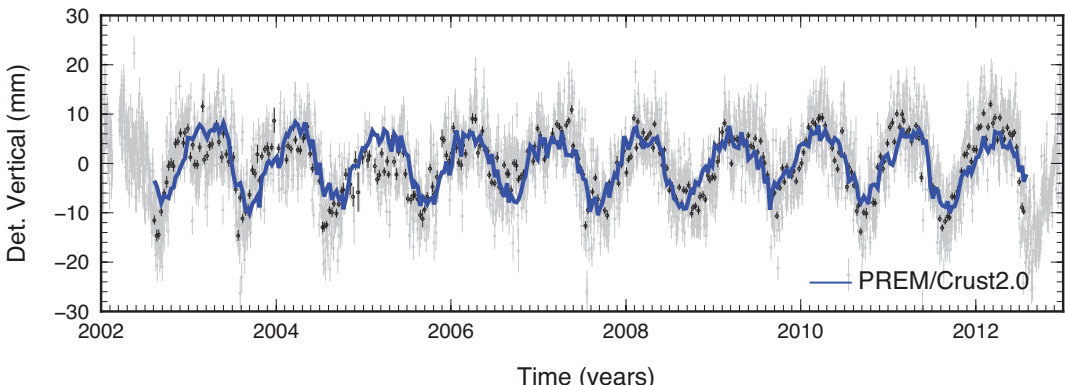
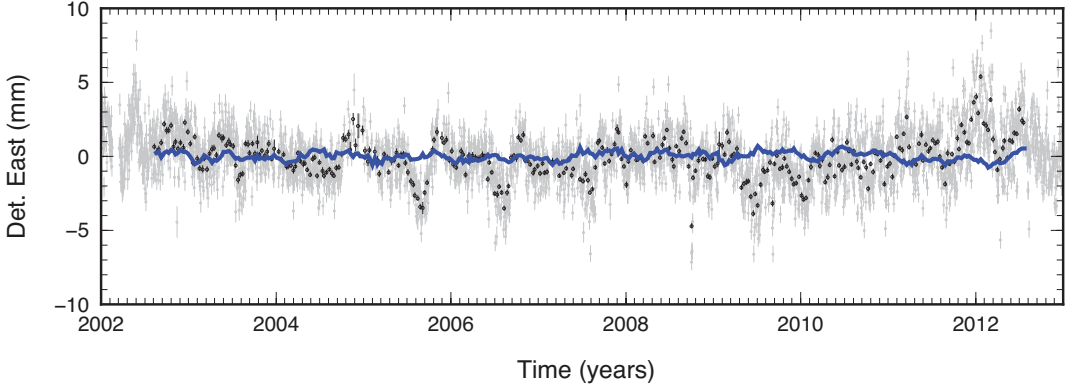
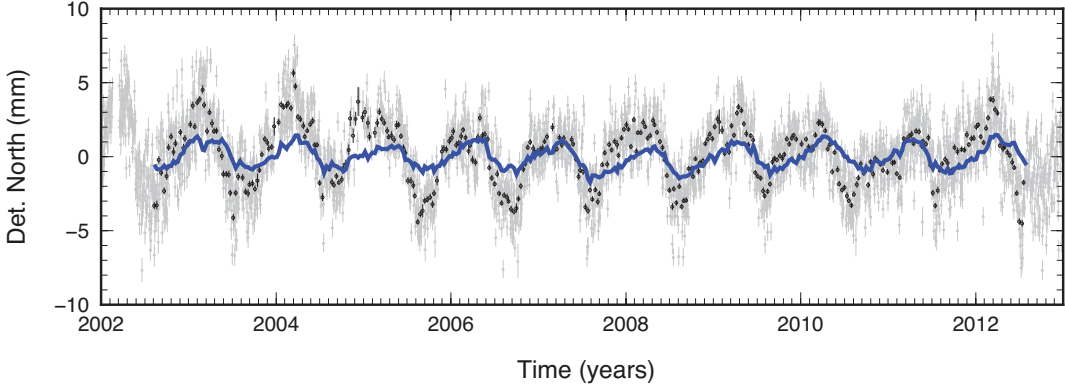
1- $\sigma$  uncertainties (gray) at three stations, (a) LHAZ, China, (b) GOLD, California, (c) CHPI, Brazil (see Figure 3.1 for location) and predicted displacements induced by seasonal surface hydrology variations using a purely elastic continental PREM Earth model described in the previous section (blue). Note that, compared to the modeled time series presented in the previous chapter, the model has no errorbars due to leakage artifacts as we now consider the global load to predict displacement at each station. The elastic model is, as expected, a fairly good approximation to compute seasonal displacements induced by variations in surface loading. However, while the vertical components are well predicted, the horizontal ones are underpredicted and out of phase. As suggested by the three sets of time series recorded at stations globally distributed, the under-prediction of horizontal component does not seem to be a regional artifact. One can also note a time lag between model and observations for the north and east components, obvious for GOLD station (California).

In order to compare efficiently geodetic data and model predictions, we first perform a 10-days moving-average of the daily geodetic observations, over the GRACE time sampling (black dots in Figure 3.9). For all time series, a certain percentage of data points, even after removing outliers, may represent phenomena non-related to large scale variations of surface hydrology (tectonic transient deformation, material change, etc.), and need to be identified and removed. We then propose a simple normalized root mean square error comparison. In order to better understand the data-model misfit, we also look separately at the amplitude and phase fit to the data.

---

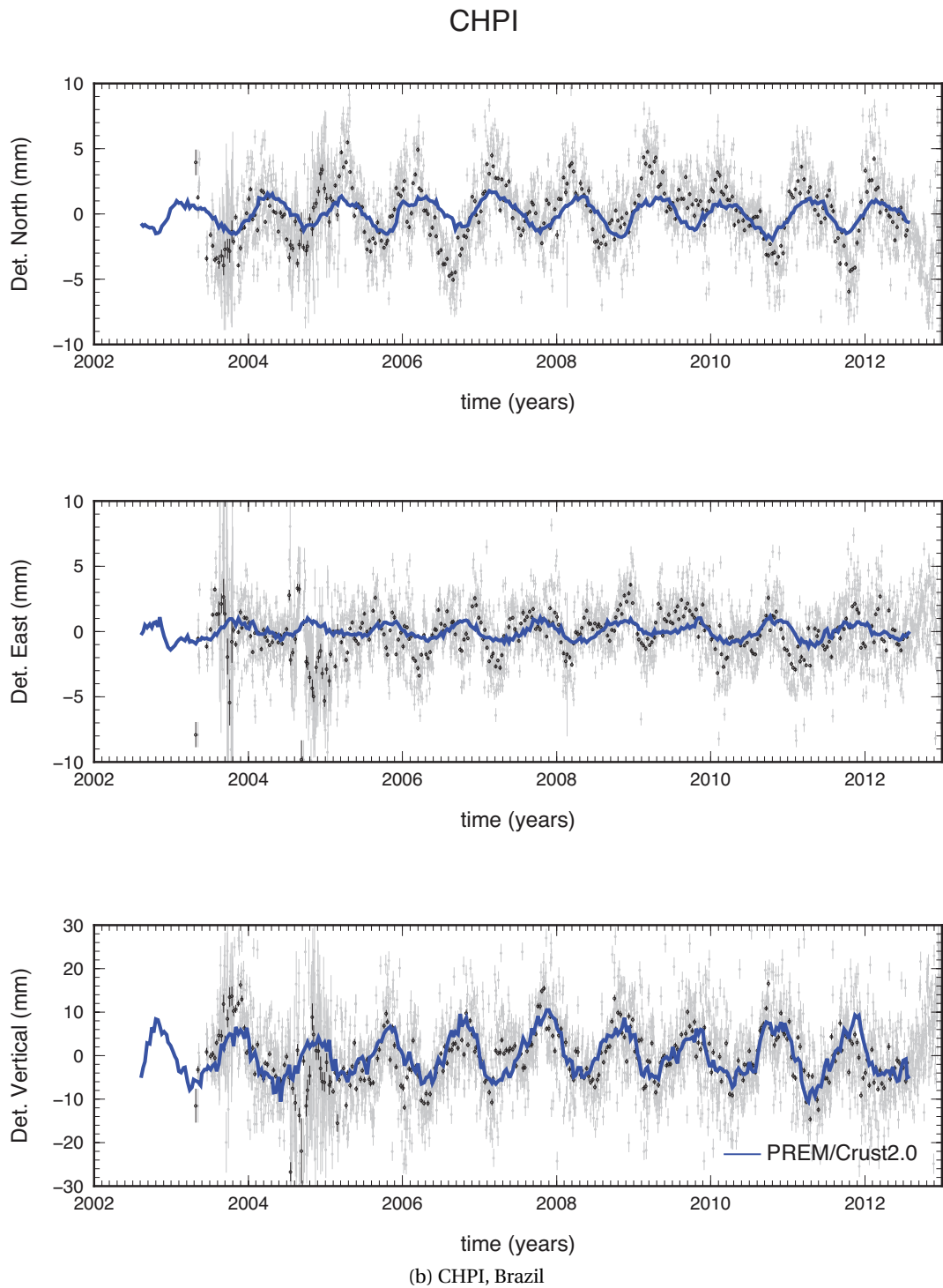
Figure 3.9 (*following page*) – Daily detrended geodetic positions, determined at station (a) LHAZ, (b) CHPI and (c) GOLD GPS stations with error-bars for 1- $\sigma$  uncertainties (gray symbols). See Figure 3.1 for location. Black dots are 10-days moving-average of the daily geodetic observations. Blue line shows predicted displacements induced by seasonal surface hydrology variations derived from GRACE where degree-1 components are accounted for following results from [Swenson et al. \(2008\)](#), using a purely elastic continental PREM Earth model. The elastic model predicts fairly well vertical components while horizontal signals are underpredicted and, in the GOLD case, out of phase.

LHAZ

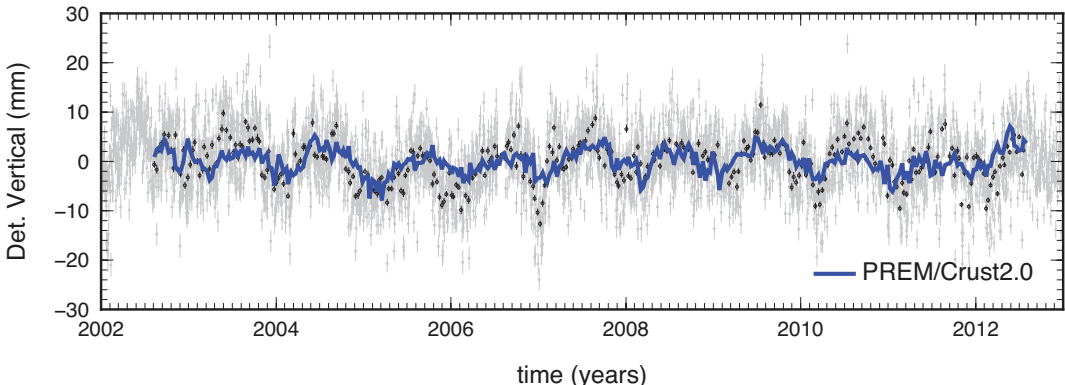
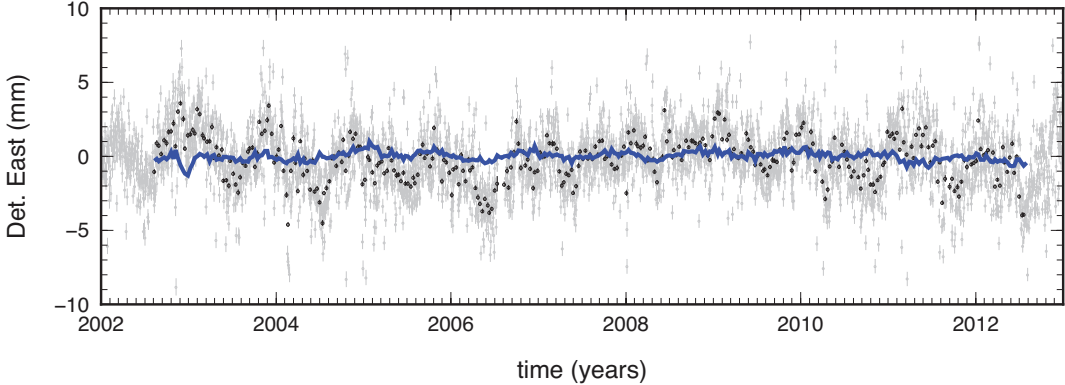
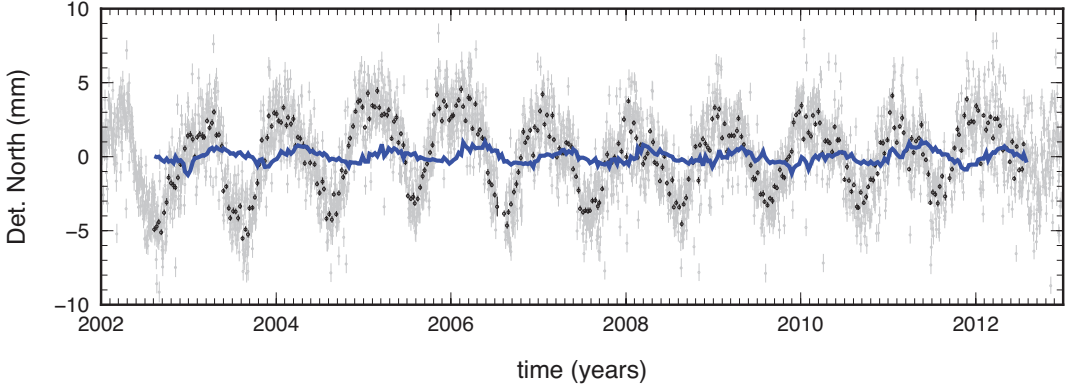


(a) LHAZ, China

### 3.3. Global elastic modeling of seasonal ground deformation induced by surface load variations



GOLD



(c) GOLD, United States (California)

### 3.3. Global elastic modeling of seasonal ground deformation induced by surface load variations

#### Removing non-modeled data points from data-model comparison

In the selected subsets of continuous time series used in our study, small displacements non-related to large scale surface load variations may affect the data-model comparison. To limit from this possible bias, we compute the normalized root-mean-square deviation (NRMSD) and its second derivative between elastic seasonal displacement predictions and observations for each component of each station, including 0 to 100% of the best-fitting set of data points. The NRMSD, defined at each station  $i$  and for each component as the sample standard deviation of the differences between  $N$  predicted values  $m_i$  and observed values  $d_i$ , with errors  $\sigma_i$  and with mean amplitude of the observations  $\overline{\mathcal{A}_i}$  (in order to compare misfit between components):

$$NRMSD_i = \frac{1}{\overline{\mathcal{A}_i}} \frac{\sum_{j=1}^N \left( \frac{d_i(j) - m_i(j)}{\sigma_i(j)} \right)^2}{N} \quad (3.3)$$

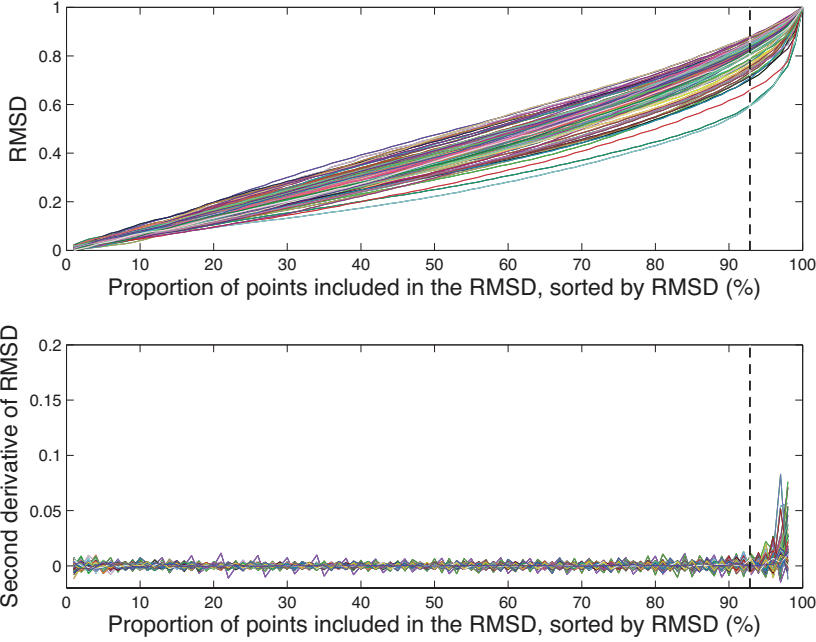
Figure 3.10 shows NRMSD as a function of the percentage of best fitting data points for each component of all stations. We conclude that the worse fitting 8% of the data points to the model bias the data-model comparison and do not take them into account.

#### Normalized root-mean-square deviation maps

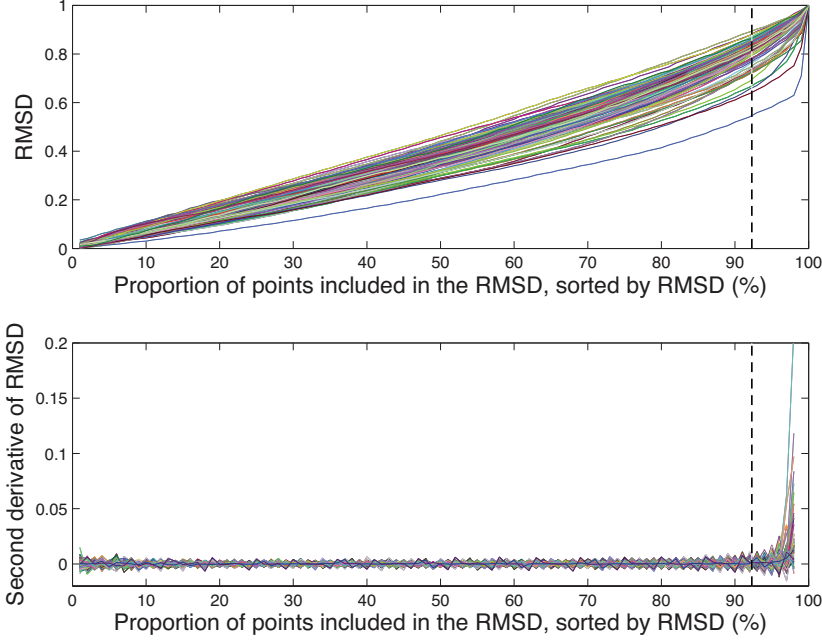
For each station and each component, we compute the NRMSD as stated in equation 3.3. Values of NRMSD range from:

- [3.6, 10.4] for the north component, with a mean value of 6.0,
- [4.0, 11.6] for the east component, with a mean value of 7.1,
- [1.4, 5.4] for the vertical component, with a mean value of 3.2.

Figure 3.11 shows the spatial distribution of misfit between the elastic model and the data for the north (a), east (b) and vertical (c) components. Our model predicts fairly well the vertical seasonal displacements whereas the horizontal components show high NRMSD values. Spatial distribution of the misfit for the horizontal displacements does not show particular pattern. However the vertical component is less well predicted for high and low latitudes. This correlation with latitude could be due to temperature variations and thermal expansion and will be discussed in section 3.4.5. In order to further investigate differences between our



(a) East



(b) North

### 3.3. Global elastic modeling of seasonal ground deformation induced by surface load variations

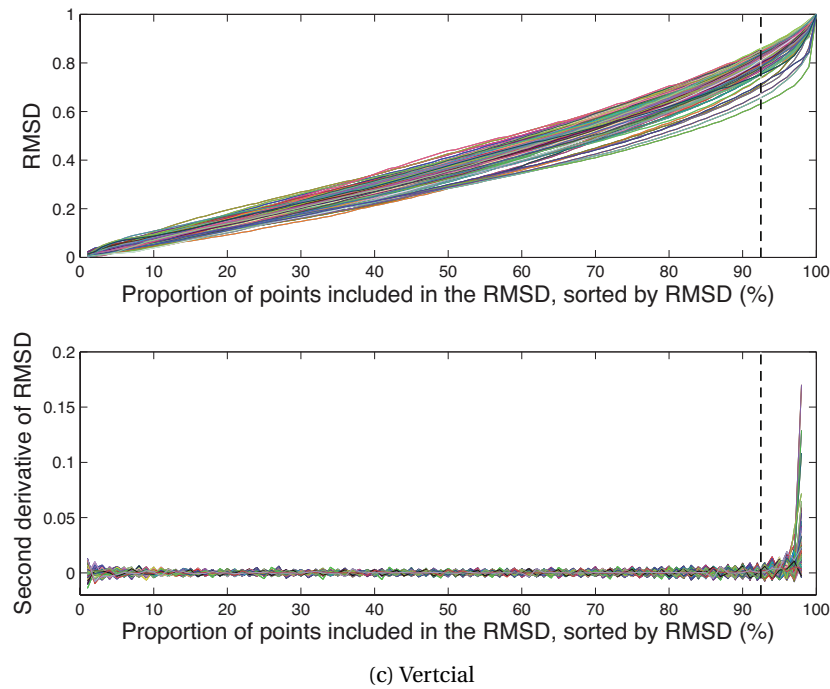


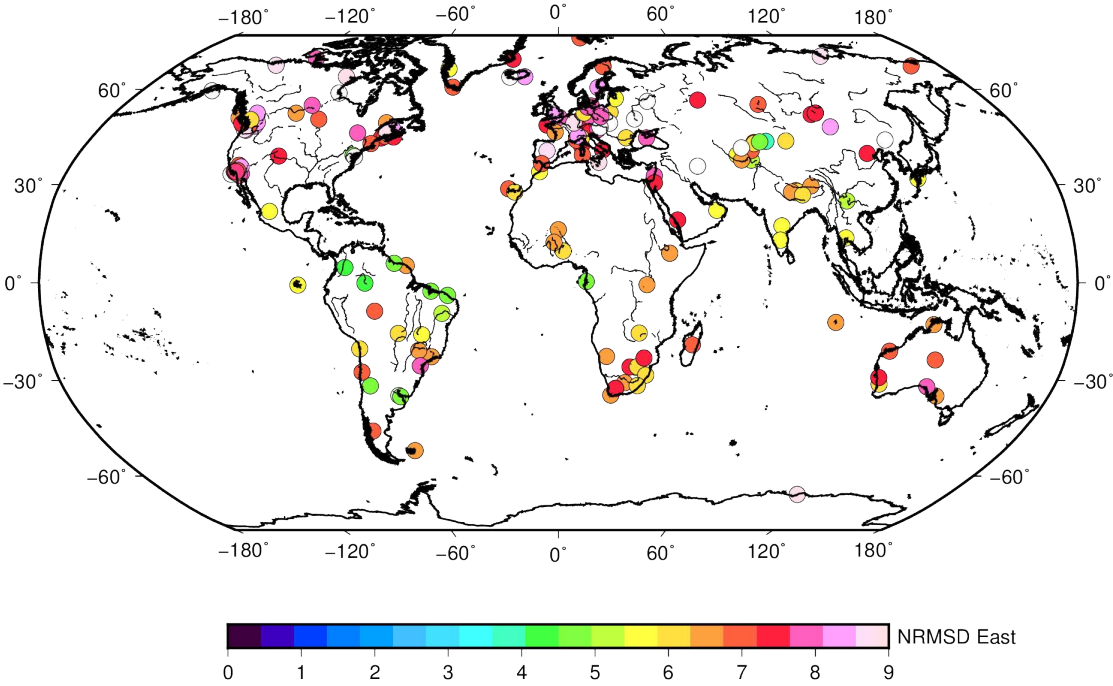
Figure 3.10 – Normalized root-mean-square deviation (NRMSD) and its second derivative between elastic seasonal displacement predictions and observations for each component of each station, including 0 to 100% of the best-fitting set of data points. Dashed line shows the limit of 8% outliers or limited displacements non-related to large scale surface load variations biasing the data-model comparison. Colors represent different stations.

model and data, particularly for the horizontal components, we select components showing a significant seasonal signal, both in observations and model. This will help us focusing on components with actual seasonal signals in order to improve our model. We will then insure that components with no significant seasonal signal are also well described by our final model. To reduce noise in the selected time series, we temporally stack observations and predictions over one year and we compare transfer functions in amplitude and phase between model and data at each station in order to treat these two aspects separately. Techniques used for data-model comparison are described in further details in the following.

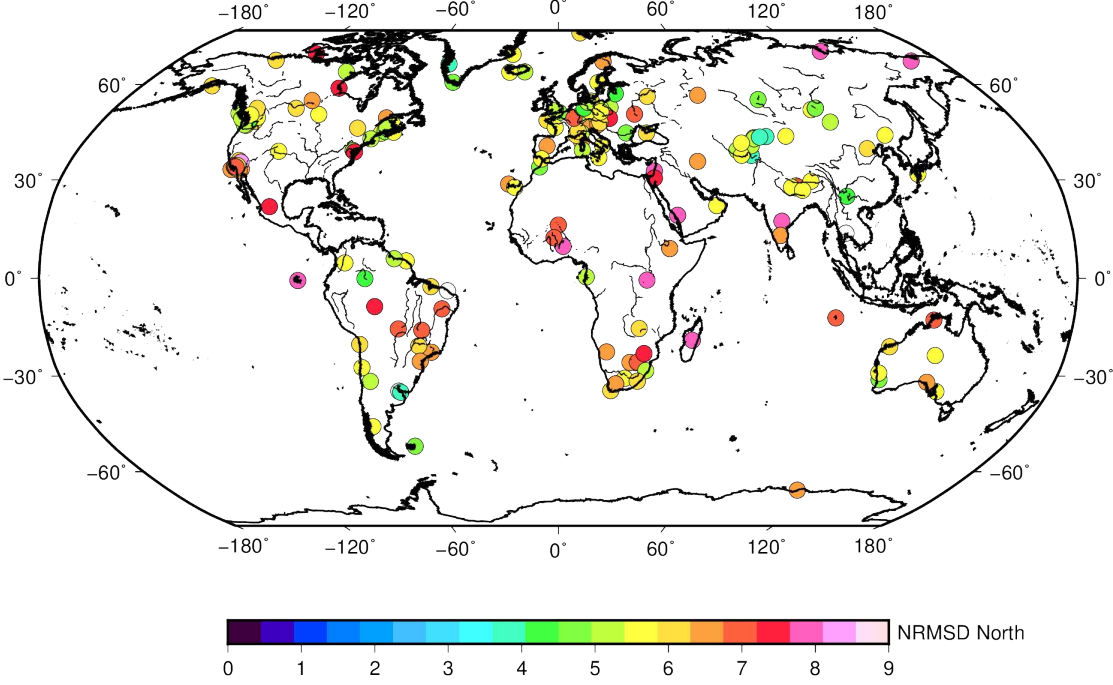
#### Amplitude and phase data-model comparison

In order to select only components with significant seasonal signals, we use a systematic method. Indeed, in some regions, annual variations in surface hydrology are negligible and

Chapter 3. Global seasonal deformation



(a) NRMSD East



(b) NRMSD North

### 3.3. Global elastic modeling of seasonal ground deformation induced by surface load variations

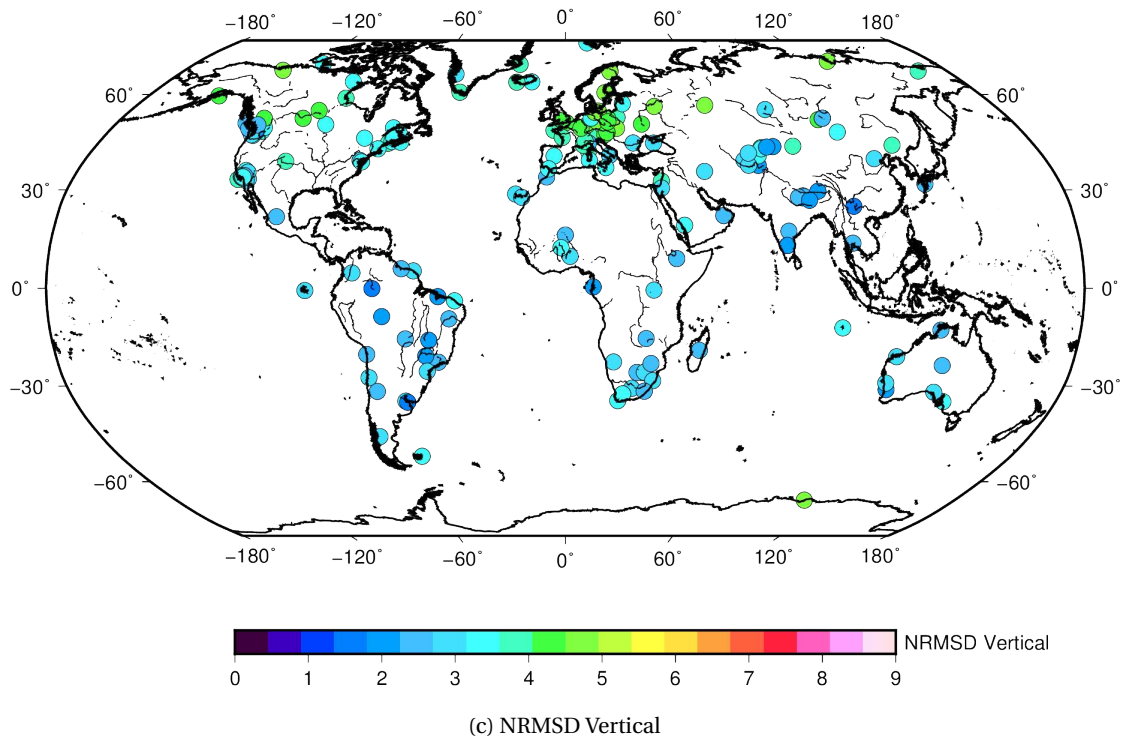


Figure 3.11 – Normalized root-mean-square deviation (NRMSD, see equation 3.3) by the mean amplitude of the signal between elastic displacement induced by GRACE seasonal signal predictions and observations for east (a), north (b) and vertical (c) components. Horizontal components are not reasonably predicted compared to the vertical component.

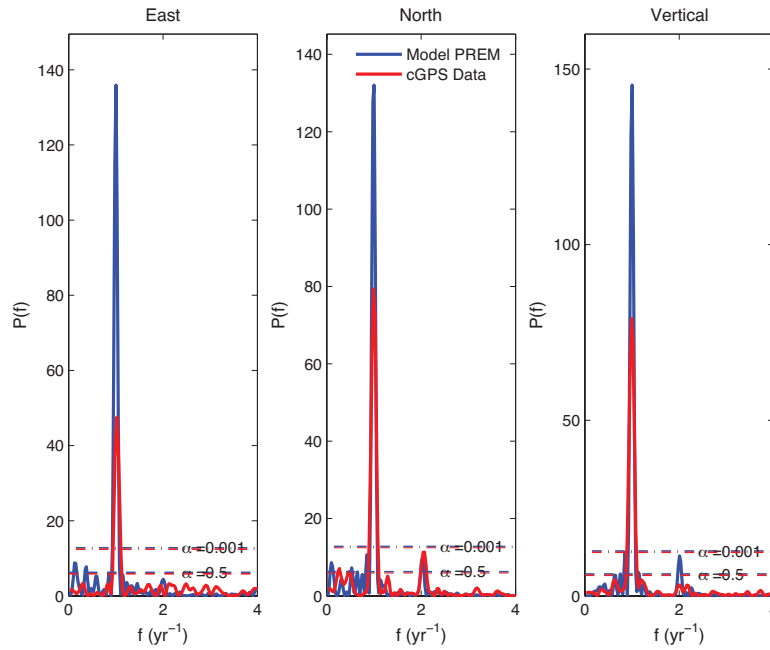
induced seasonal ground deformation that remain within measurement errors, thus possibly biasing our global data-model comparison.

Commonly, periodicities in time series are determined using a Fast Fourier Transform (FFT) algorithm. However, FFT is applicable only when data are evenly spaced and when no values are missing, which is not the case in our dataset. Since cGPS time series can present large data gaps due to material failure, interpolation is not a reliable method. We therefore detect periodic patterns in unevenly spaced cGPS time series and their associated statistic significance using the Lomb-Scargle periodogram (Scargle, 1982).

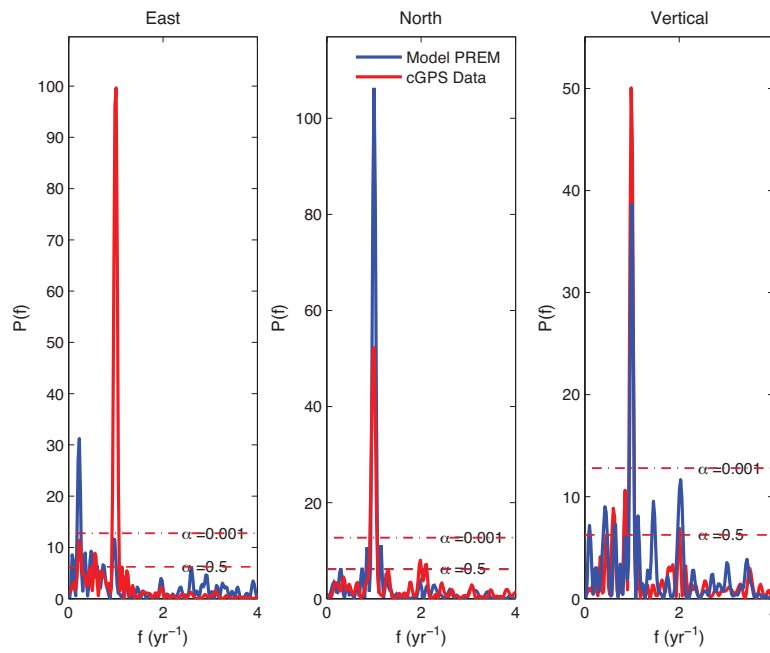
First introduced in astrophysics where controlling viewing times and telescope availability always leads to unevenly spaced datasets, Lomb (1976) proposed to use least-squares fits to sinusoidal curves and later, Scargle (1982) extended his work by defining the Lomb-Scargle

periodogram and by deriving the null distribution for it. The p-value of the Lomb–Scargle periodogram can be obtained using the periodogram results. Details on the method are given in [Press et al. \(1992\)](#). Figure 3.12 shows Lomb-Scargle periodograms for east, north and vertical components at stations (a) CHLM (Nepal), (b) HOFN (Iceland) and (c) SRNW (Suriname) for observations (red) and predictions using an elastic continental PREM model (blue). Dashed lines show significance levels, above which the null hypothesis is ruled out, i.e. above which the periodicity of the signal is significant. All the components of station CHLM (Figure 3.12 (a)) show a significant signal at an annual frequency for both our GRACE based model predictions and observations. However, sometimes, the model does not predict significant annual displacements while seen in observations, meaning that the station could be affected by local effects that the GRACE resolution cannot capture as illustrated by the eastern component of HOFN, located at 30 km of a glacier (Figure 3.12 (b)). Finally, at some stations, noise in the data does not allow detection of significant seasonal signals in the time series while predicted by the model (see Figure SRNW east component on 3.12 (c) for example). In order to avoid biasing global data-model comparisons at first to set out potential misfit patterns, we evaluate misfit functions only for components with a significant annual signal on both model (i.e. GRACE data) and GPS displacements.

### 3.3. Global elastic modeling of seasonal ground deformation induced by surface load variations



(a) CHLM, Nepal



(b) HOFN, Island

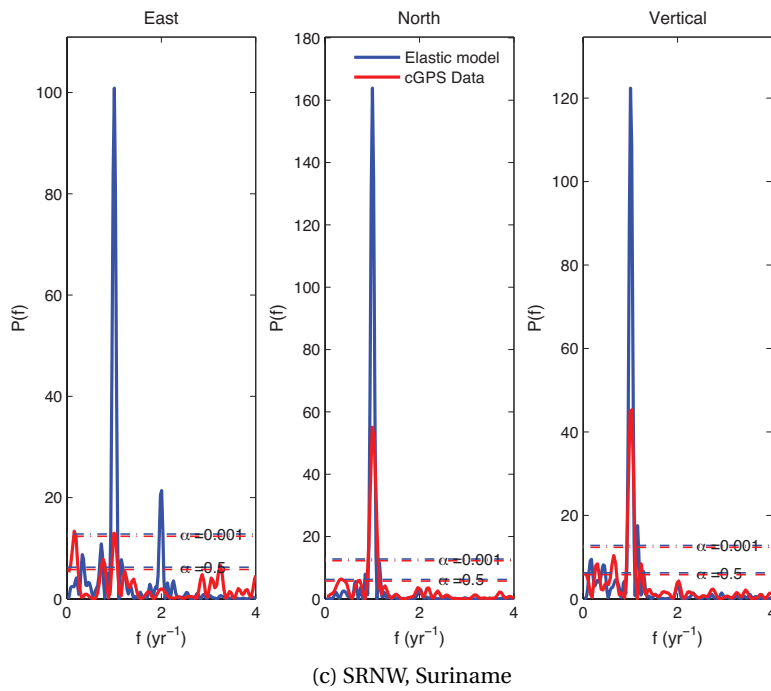


Figure 3.12 – Lomb-Scargle periodograms for east, north and vertical components at three continuous GPS stations: (a) CHLM, Nepal, (b) HOFN, Island and (c) SRNW, Suriname. Periodograms associated with geodetic observations and elastic modelling derived from GRACE data are respectively represented in red and blue. All components of (a) show a significant annual periodicity while the eastern component of respectively model and data of (b) and (c) do not, possibly because of noise in one of the geodetic dataset. Components that do not meet the significance level criterion of 0.001 are not considered in misfit functions evaluations.

Figures 3.13, 3.14 and 3.15 show maps of most significant frequencies in observed and modeled time series at stations referenced in table 3.4. Note that the seasonal signal at a small number of stations does not exhibit a clear seasonal signal (red dots), meaning that the seasonal in surface loading averaged by GRACE is not significant. Interestingly, the GPS stations, capture the signal. Using the 0.001 significance level criterion, we select subsets of 114 stations for the east, 125 for the North and 157 for the vertical components to compare our model with observations.

### 3.3. Global elastic modeling of seasonal ground deformation induced by surface load variations

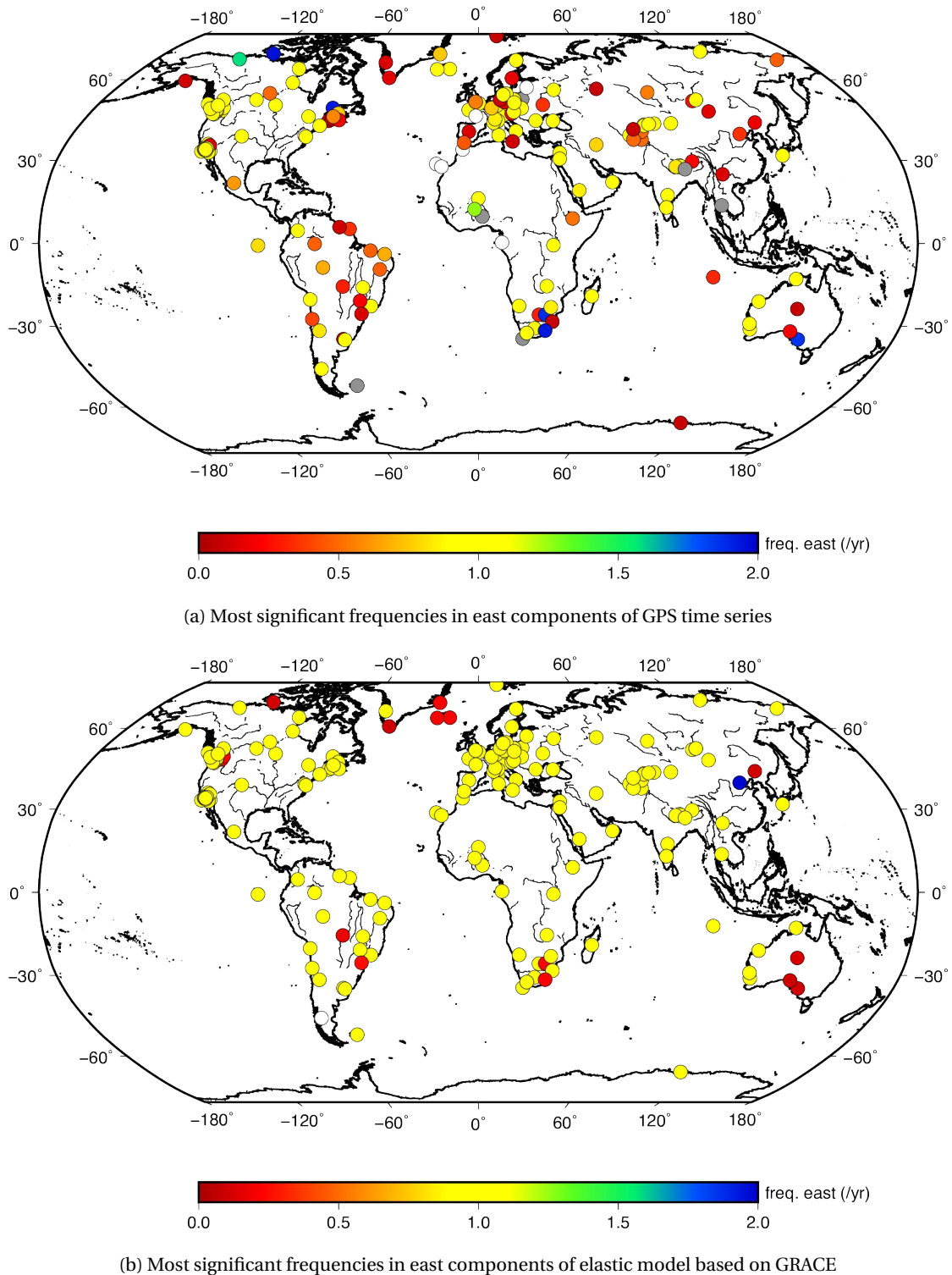


Figure 3.13 – Maps of most significant frequencies in (a) eastern GPS time series and (b) related displacements predicted by the response of an elastic continental PREM-like Earth model to seasonal surface loading variations derived from GRACE, determined using a Lomb-Scargle approach.

### Chapter 3. Global seasonal deformation

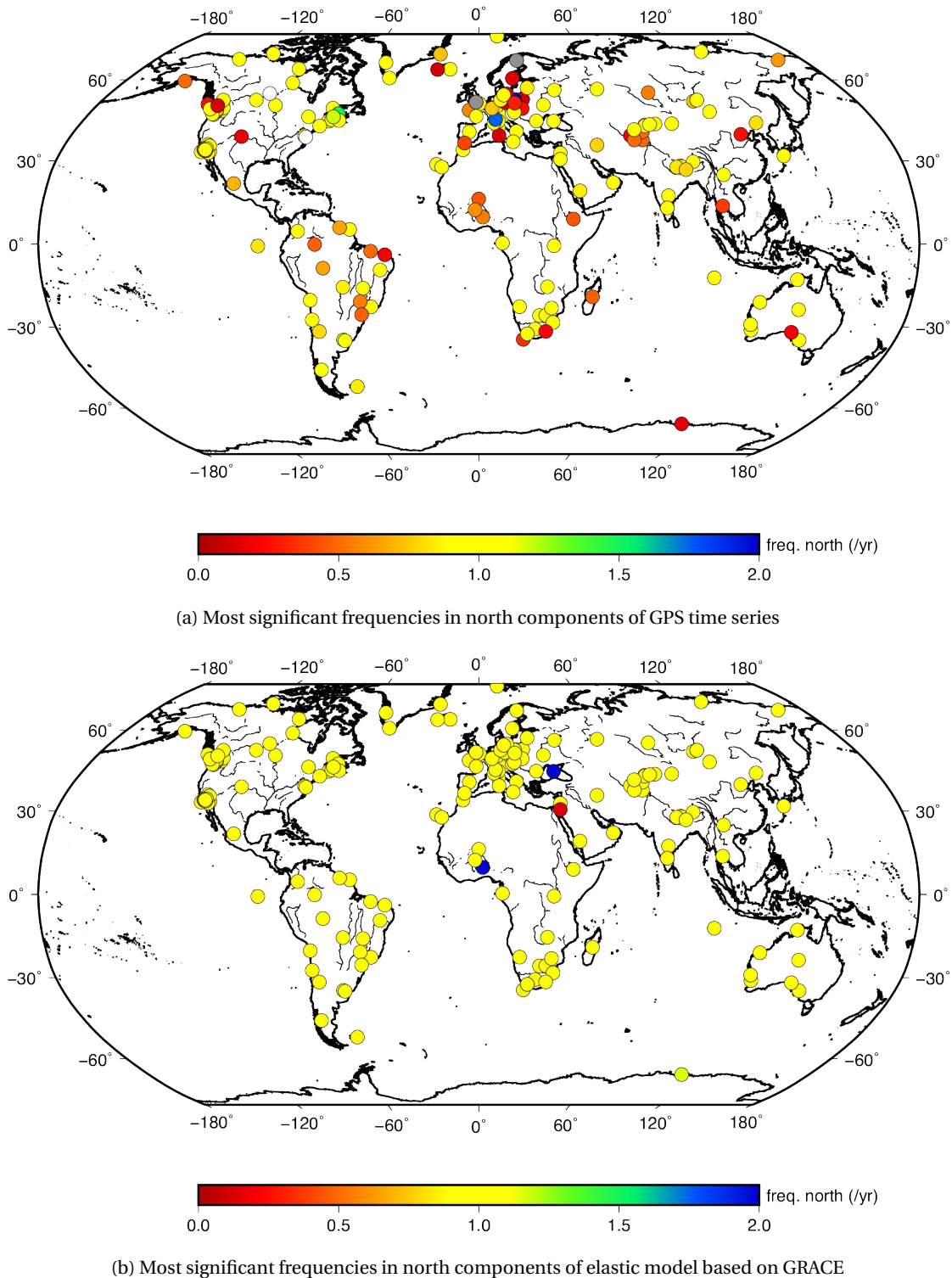


Figure 3.14 – Maps of most significant frequencies in (a) northern GPS time series and (b) related displacements predicted by the response of an elastic continental PREM-like Earth model to seasonal surface loading variations derived from GRACE, determined using a Lomb-Scargle approach.

### 3.3. Global elastic modeling of seasonal ground deformation induced by surface load variations

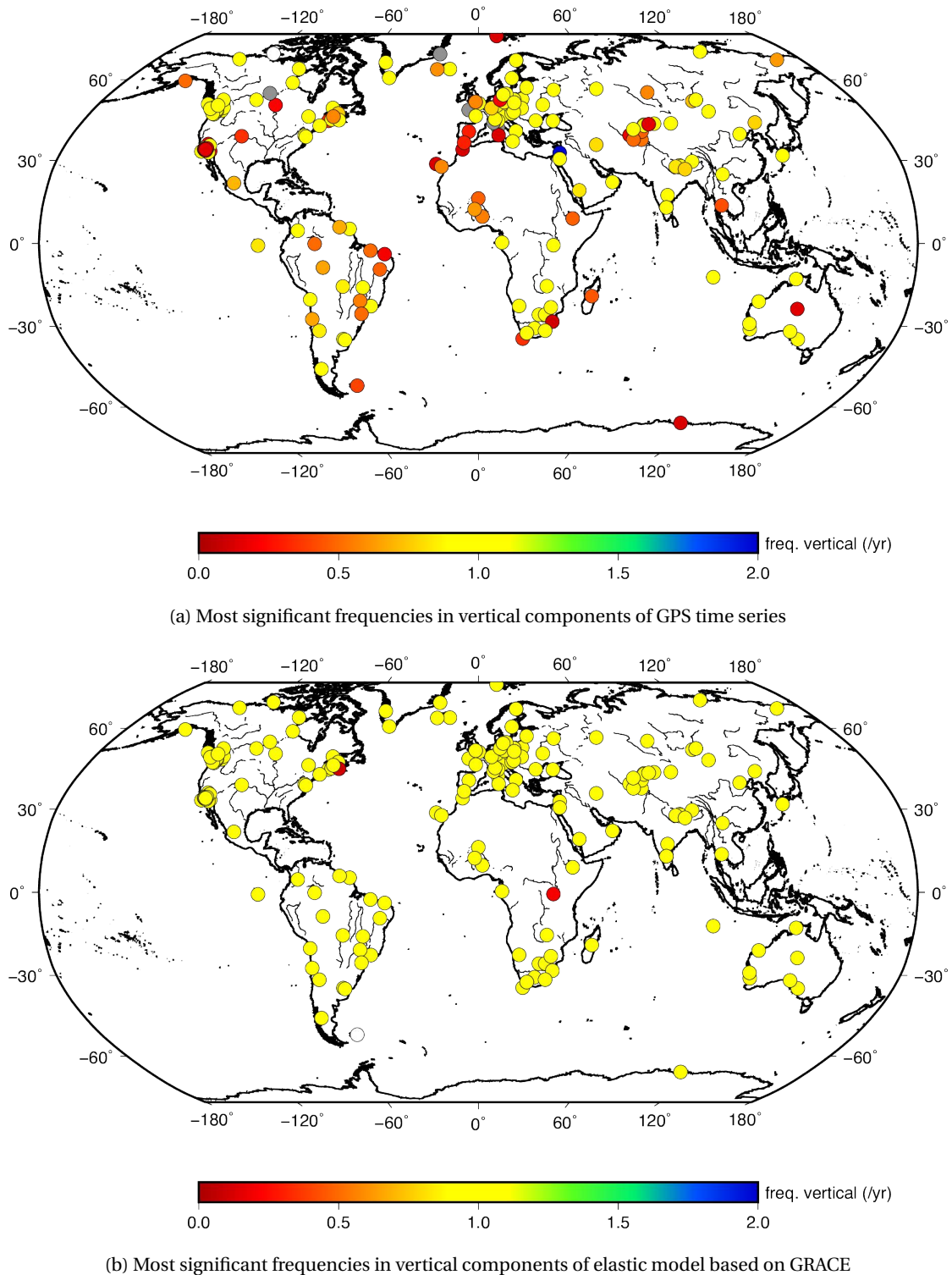


Figure 3.15 – Maps of most significant frequencies in (a) vertical GPS time series and (b) related displacements predicted by the response of an elastic continental PREM-like Earth model to seasonal surface loading variations derived from GRACE, determined using a Lomb-Scargle approach.

### Chapter 3. Global seasonal deformation

We now want to compare systematically elastic model predictions and observations, by evaluating separately amplitude and phase differences between our purely elastic model and geodetic displacements at the 195 cGPS stations described in section 3.2.2. Because our data and elastic model are not necessarily in phase, it is difficult to evaluate if a high normalized root mean square values are due to phase or amplitude prediction problems for each station. First, in order to reduce observational noise, we stack all years of geodetic time series and

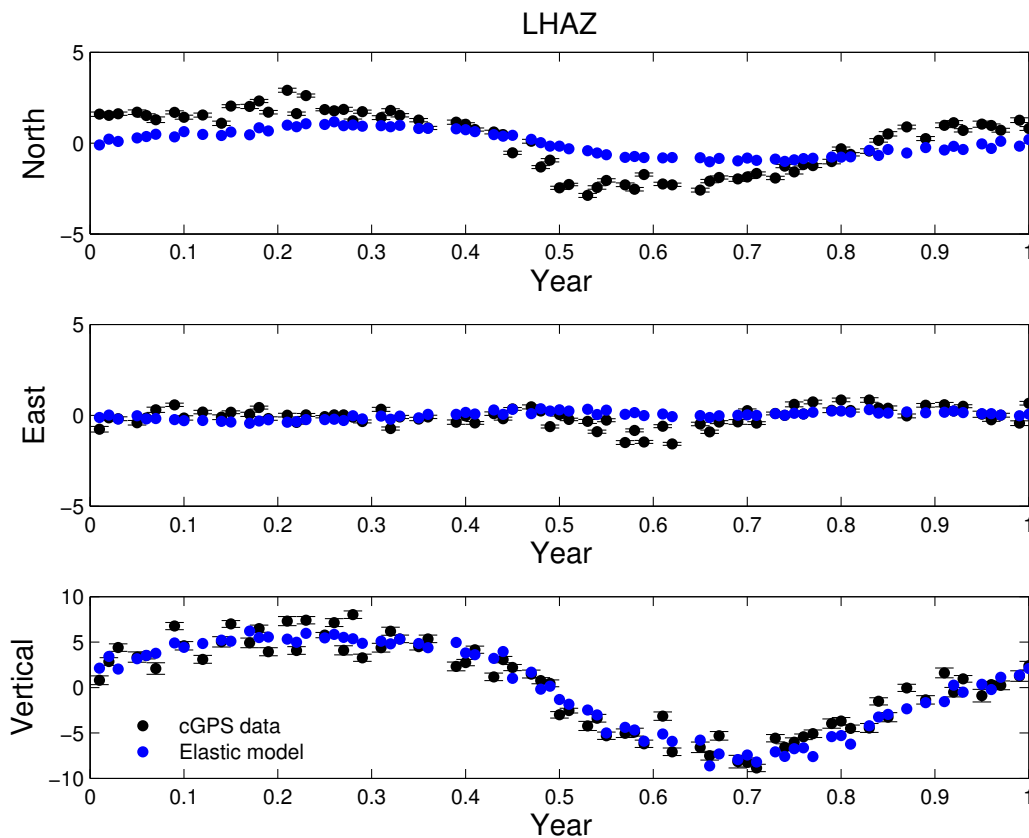


Figure 3.16 – Stacked east, north and vertical time series of all years of geodetic time series (black) and elastic displacements induced by seasonal hydrology (blue) into a single year

elastic displacements induced by seasonal hydrology into a single year. Note that there is a combination of inter-annual variations and noise in the time series. However we decide, as a first order approximation, to evaluate the fit of the model to the data stacked over a year. Figure 3.16 shows observed (black) and modeled (blue) seasonal displacements at station LHAZ, China (see Figure 3.1 for location), stacked over a year. The east component does not show a clear seasonal signal compared to the north and the vertical ones and is therefore

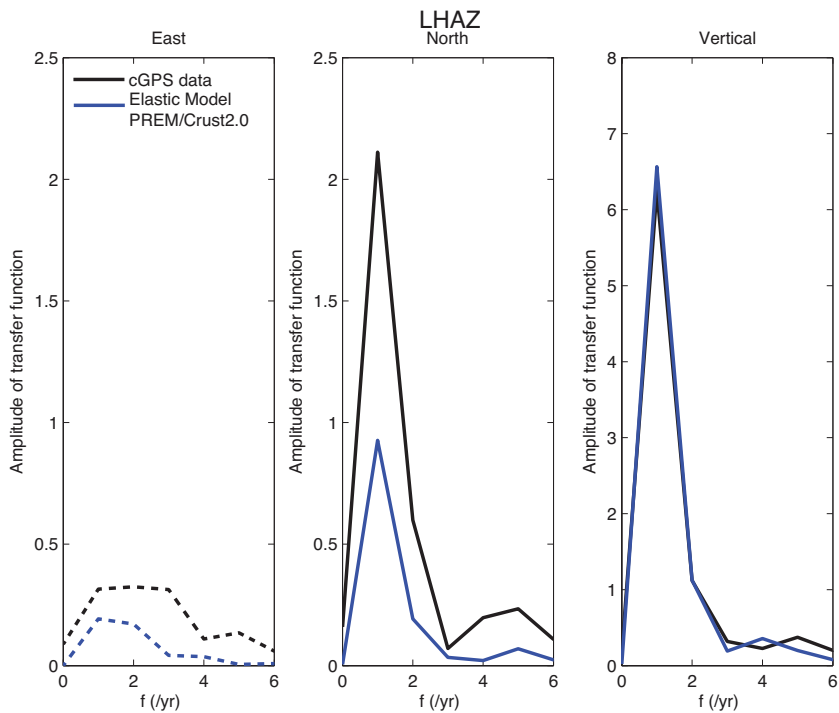
### 3.3. Global elastic modeling of seasonal ground deformation induced by surface load variations

---

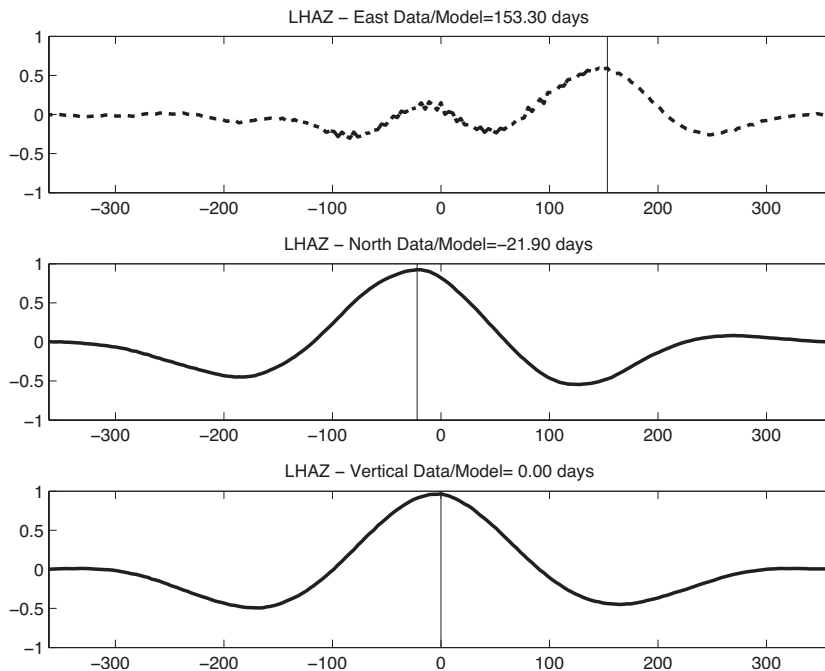
excluded in the data-model comparison. In addition, we note that the vertical component is fairly well predicted in amplitude and phase whereas the elastic northern displacements predicted by the elastic model lack amplitude and are slightly out of phase. Figure 3.17 shows the quantification of amplitude spectrum and time lag correlation between seasonal observations and model. While the vertical component at station LHAZ (China) is indeed well modeled by a purely elastic Earth model loaded by GRACE seasonal terms, the model only predicts half the amplitude of the north component. In addition, the model is in phase with vertical geodetic positions, whereas the north component of the model appears to be about 20 days delayed compared to the data.

At a global scale, figure 3.18 shows maps of the amplitude ratio of seasonal elastic model over seasonal data derived from the amplitude spectrum, for each component. A value of 1 means that the model predicts well the amplitude of seasonal signals observed. Under and over predictions of the model have respectively ratios inferior and superior to 1. It appears that horizontal seasonal geodetic positions are globally under-predicted by a purely elastic model, while the vertical component amplitudes are better fitted. The distribution of amplitude ratio shows no significant pattern for the horizontal components. However, the vertical amplitude of our model seems to be less well predicted for high and low latitudes.

Figure 3.19 illustrates time differences between data and model (negative values for model delayed compared to the data). The phase of horizontal components agree less with the elastic model than the vertical component. Note that GRACE and GPS data are averaged over 10 days, making the correlation function reliable  $\pm 10$  days. As for the amplitude, we do not notice a clear regional distribution pattern of the time shift between the elastic model and the data, suggesting a global misprediction of the horizontal components by our elastic model. In the next section, we describe and evaluate the importance of all potential contributors, to our knowledge, to the missing seasonal signal.



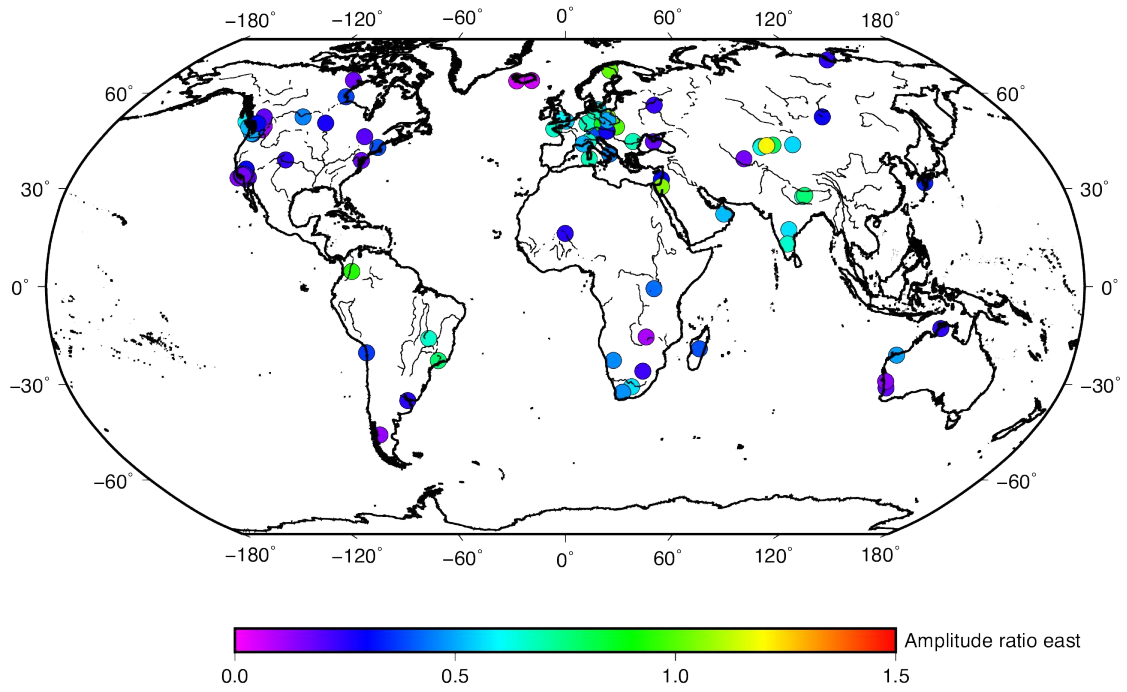
(a) Amplitude of the transfer function



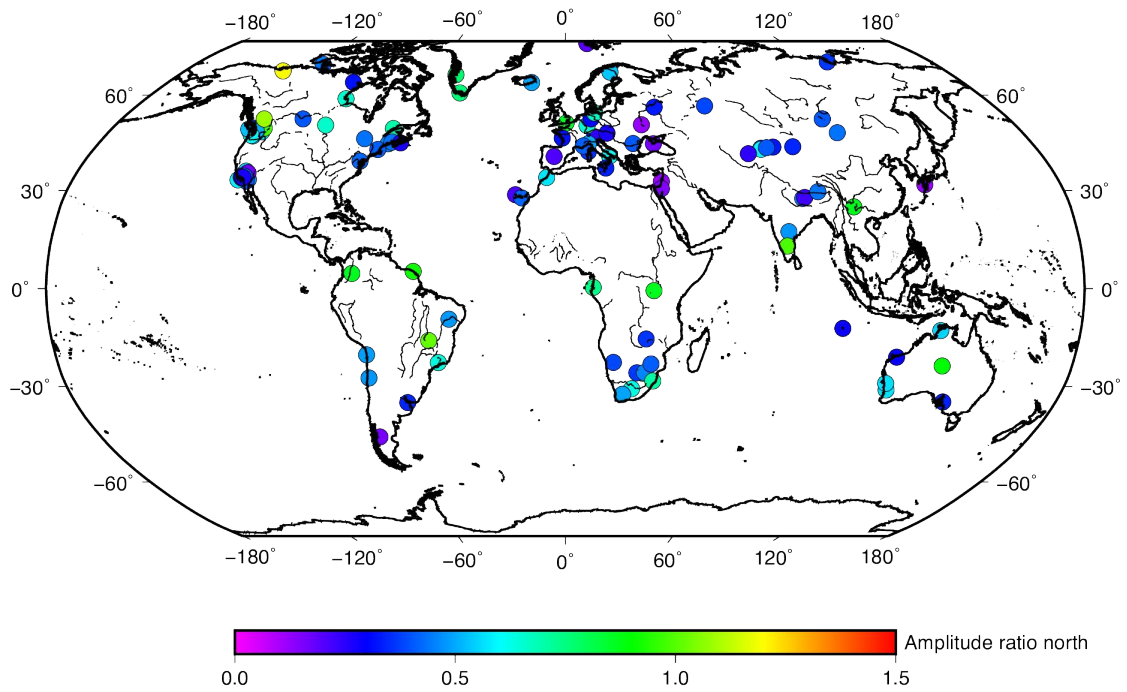
(b) Time lag between data and elastic model

Figure 3.17 – (a) shows amplitude spectrum of the stacked geodetic displacements (black) recorded at LHAZ and predicted displacements induced by variations in surface hydrology derived from GRACE (blue) over one year. (b) shows the time lag cross correlation functions between observations and predictions. Dashed lines point out non seasonally significant components.

### 3.3. Global elastic modeling of seasonal ground deformation induced by surface load variations

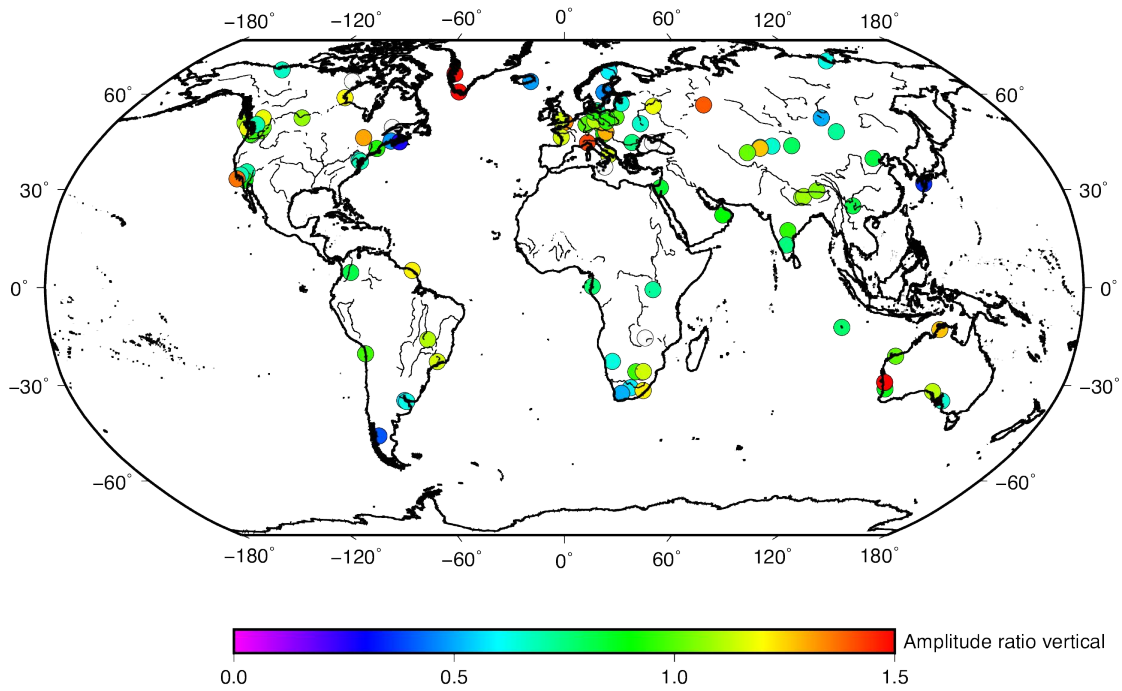


(a) Amplitude ratio between east displacements from elastic model and cGPS data



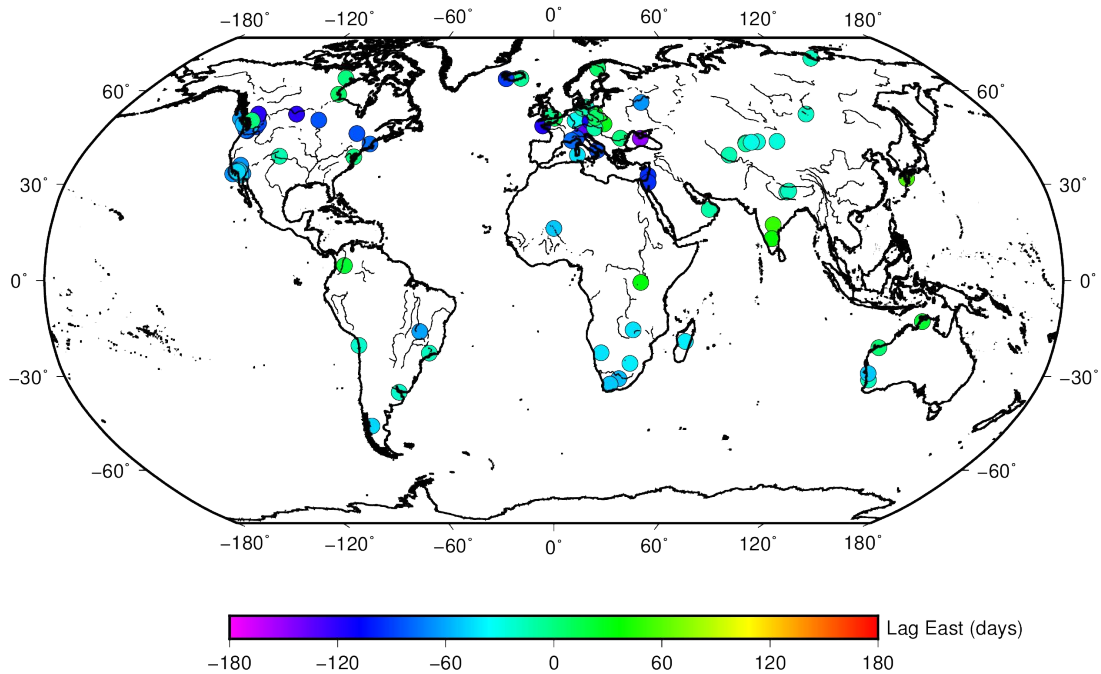
(b) Amplitude ratio between north displacements from elastic model and cGPS data

### Chapter 3. Global seasonal deformation



(c) Amplitude Ratio between vertical displacements from elastic model and cGPS data

Figure 3.18 – Maps of the amplitude ratio of seasonal elastic model over seasonal data derived from the amplitude spectrum, for each component. Under, exact and over predictions of the model have ratios inferior, equal and superior to 1, respectively.



(a) Phase between modified PREM and Data (mm) - East

### 3.3. Global elastic modeling of seasonal ground deformation induced by surface load variations

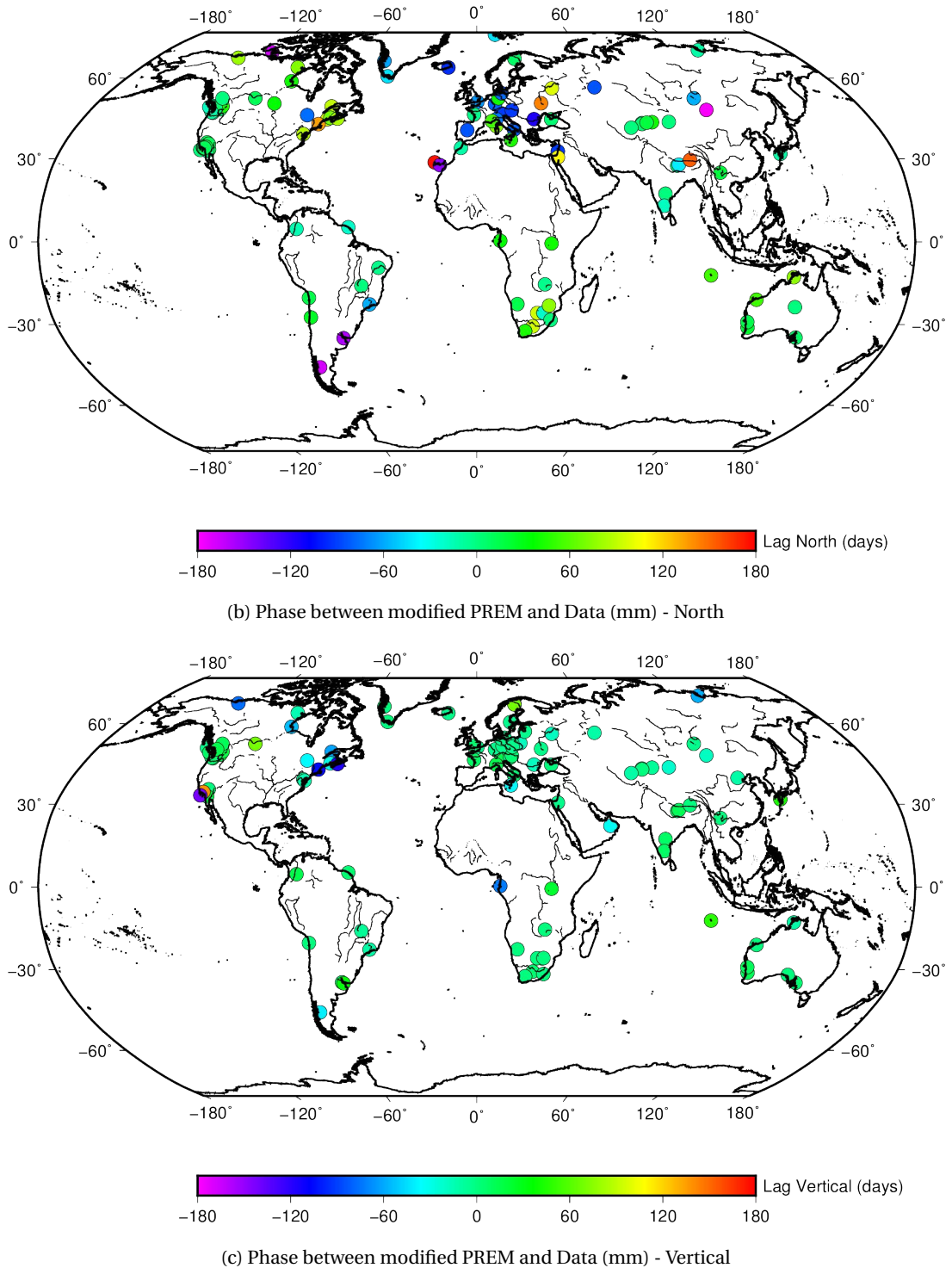


Figure 3.19 – Maps of time differences in days between seasonal elastic model and seasonal data estimated from a cross-correlation technique.

### 3.4 Potential contributors to missing seasonal signals

The contributions of continental hydrology, atmospheric and non-tidal mass variations when loading a spherical and layered elastic Earth explain, as demonstrated in the previous section, a portion of the observed seasonal vertical variations in the site coordinate time series. However, the horizontal geodetic displacements are considerably out of phase and under-predicted by the model. Understanding the remaining unmodeled seasonal effects possibly provides insights on (i) the nature of seasonal surface deformation, (ii) systematic errors in geodetic processing or (iii) valuable information on the anelastic structure of the Earth at an annual time scale. Figure 3.20 shows a diagram of the discussed possible candidates to explain the unmodeled seasonal signals by a purely elastic model, once pole tides, ocean tides, continental hydrology, atmospheric and non-tidal mass loading have been taken into account. However, the task is complicated as some sources cannot be separated directly from geodetic data analysis. We will discuss possible systematic errors arising from geodetic data and processing in this section and the possible anelastic behavior of the Earth at an annual time scale in section 3.5.

#### 3.4.1 Differences in GPS processing software

The systematic errors induced by differences in processing techniques and softwares can be important sources for seasonal residuals. Even if differences in horizontal geodetic positions estimates are unlikely to be more different than the vertical ones, we compare GPS time series processed by different groups, using completely different processing strategies, the Nevada Geodetic Laboratory, part of the University of Nevada Reno (UNR) and the Massachusetts Institute of Technology (MIT), at 150 IGS stations, for all components. We want to evaluate the impact of GPS processing techniques on the amplitude of seasonal signals.

In addition to the time series processed by the UNR, we use daily GPS observations from 150 stations of the IGS network were processed by the MIT using the GAMIT software (King & Bock, 2000). Daily position estimates of station positions were reduced in 24-hr sessions, choosing the ionosphere-free combination. Precise orbits from the International GNSS Service

### 3.4. Potential contributors to missing seasonal signals

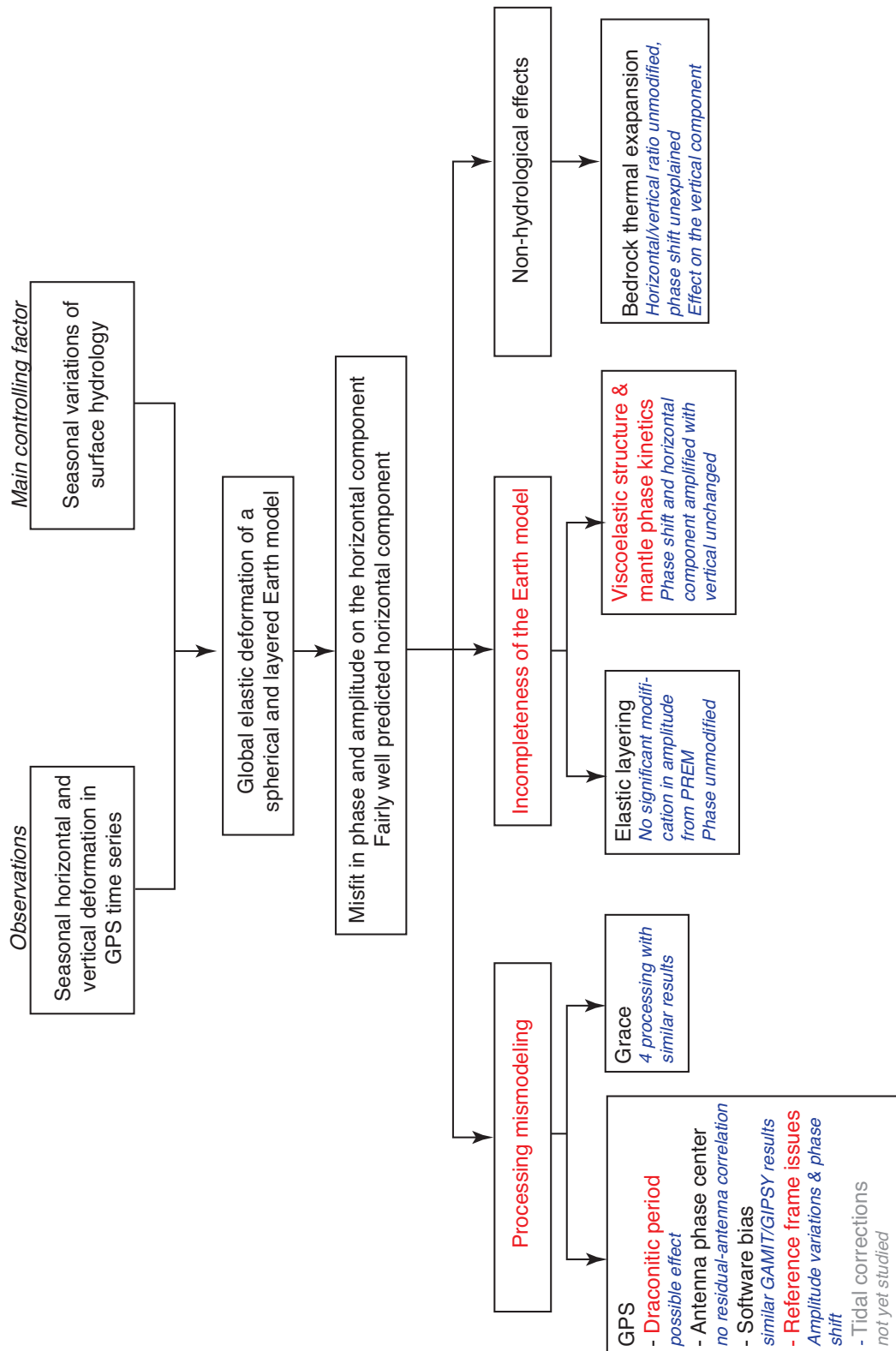


Figure 3.20 – Diagram of potential contributors to the unmodeled seasonal signals by a purely elastic model

for Geodynamics (Beutler et al., 1999) are used and IGS tables describe the phase centres of antenna. Tropospheric delays are adjusted per station every 2 hours, using the standard mapping function (Boehm et al., 2006).

Figure 3.21 shows an example of detrended and corrected for material jumps daily geodetic positions at station LHAZ, China processed by MIT (gray) and UNR (red) groups. Seasonal signals appear consistent between processing strategies. In order to compare systematically amplitudes of seasonal signals between GPS processing techniques, we compare the amplitude of the Lomb-Scargle periodogram of the residuals between the two processing strategies at a 1 year period for 150 cGPS stations. Figure 3.22 shows the annual Lomb-Scargle power of the residuals between the MIT and the UNR processings at the 150 cGPS stations, compared to the statistical significance level derived from the p-value of the Lomb-Scargle periodogram (see section 3.3.3). Most stations compared show no significant seasonal signals in the GPS processing residuals for horizontal components. However, one third of the stations have a remaining significant seasonal signal in the vertical time series. Yet, the vertical component is fairly well modeled by our elastic model loaded by surface load variations, ruling out the use of GPS software as a contributor to the horizontal missing seasonal amplitude but not a common error or unmodeled signal (redistribution of water mass as a consequence of pole tides for example).

#### 3.4.2 Phase center modeling

A GPS site position corresponds to the distance between the electromagnetic phase centers of the transmitting and the receiving antenna. Usually these phase centers are neither fixed nor identical with the points the observations refer to: the center of mass of the satellite and a mechanically well-defined antenna reference point of the receiver antenna. The phase center is then modeled and errors arising have been shown to enlarge seasonal amplitudes up to a few millimeters (Hatanaka et al., 2001) but the mechanism of the phenomenon is unclear (thermal noise, multipath model, etc.). Phase center models are related to the type of antenna. Among all stations, we have various types of antennas within a single region, but the misfit of the elastic model to observations does not correlate with the antenna type and is spatially

### 3.4. Potential contributors to missing seasonal signals

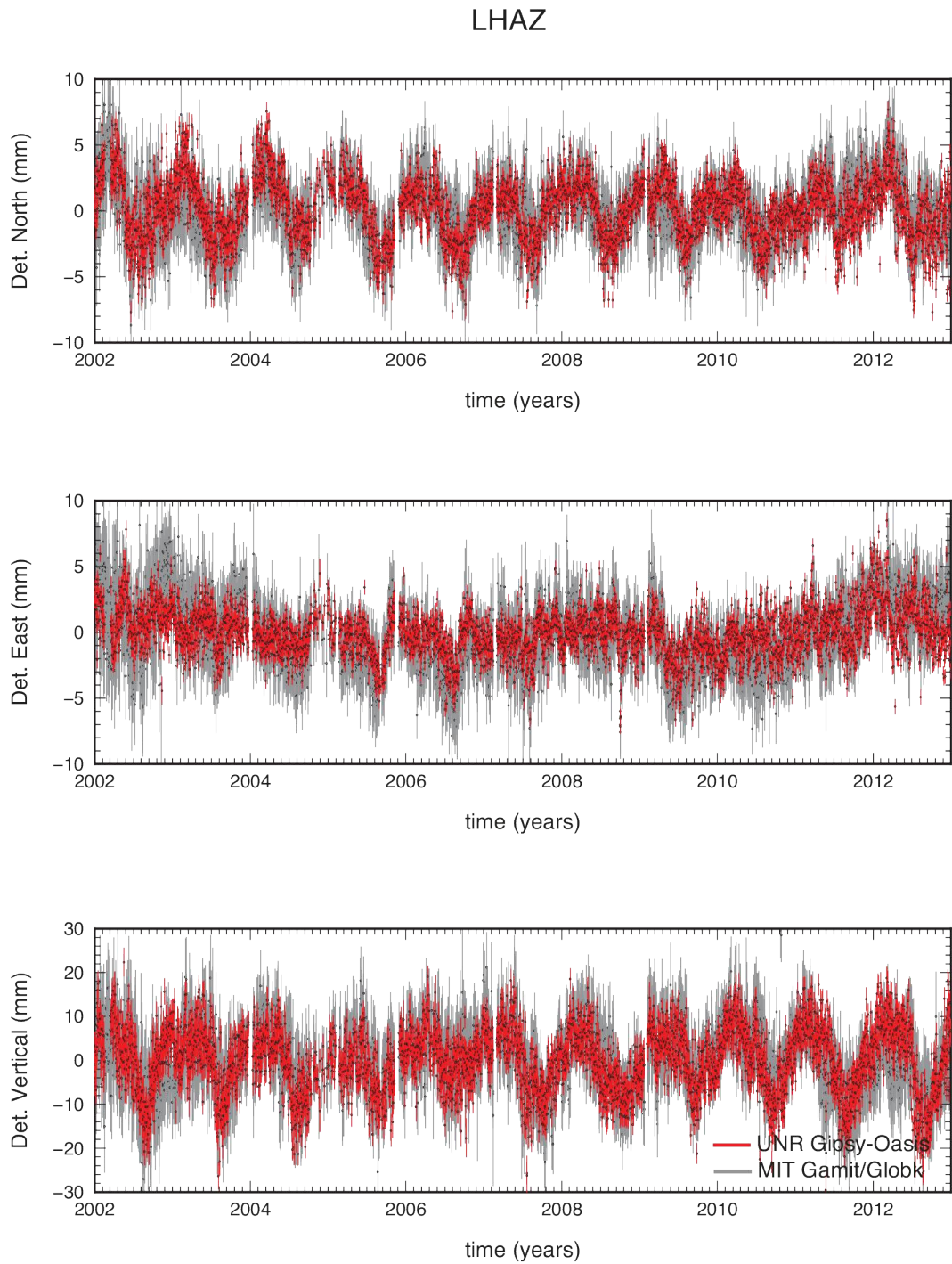
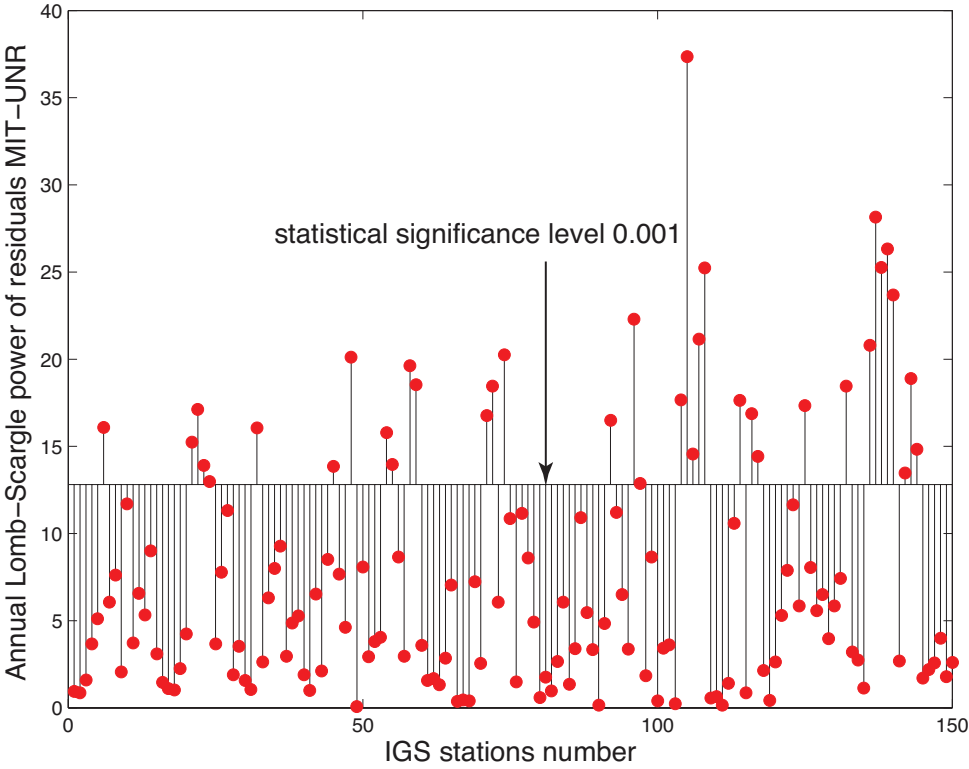
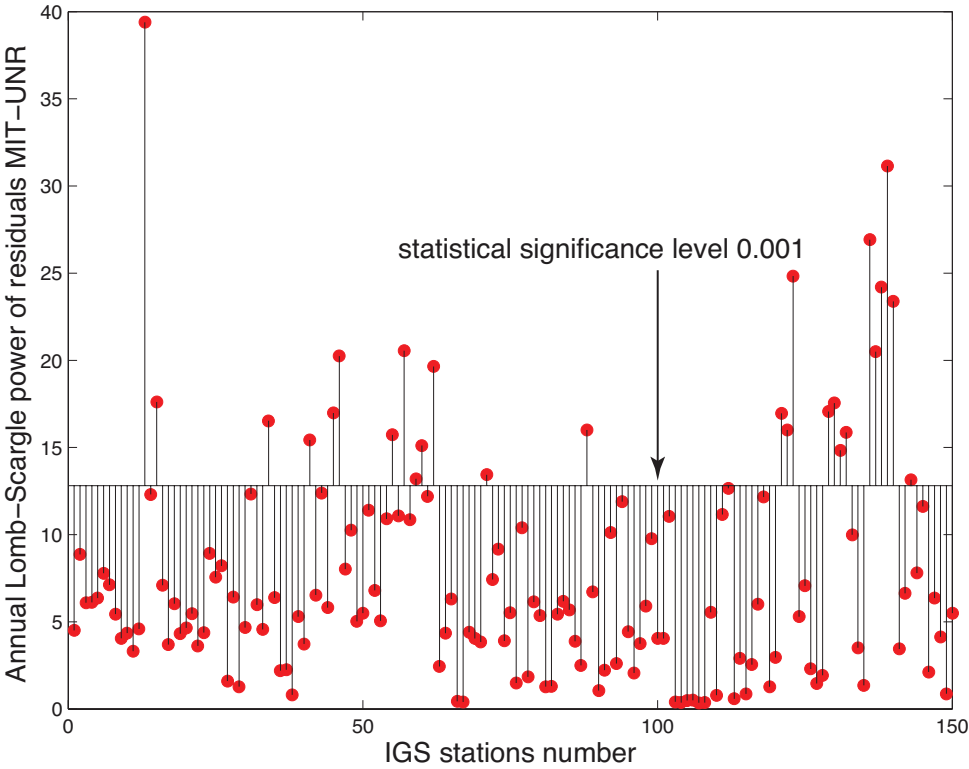


Figure 3.21 – Detrended and corrected for material jumps daily geodetic positions, determined at station LHAZ (see Figure 3.1 for location) processed by the Nevada Geodetic Laboratory, using Gipsy-Oasis software (red) and by the Massachusetts Institute of Technology, using Gamit/Globk software (gray) with error-bars showing  $1\text{-}\sigma$  uncertainties.



(a) East



(b) North

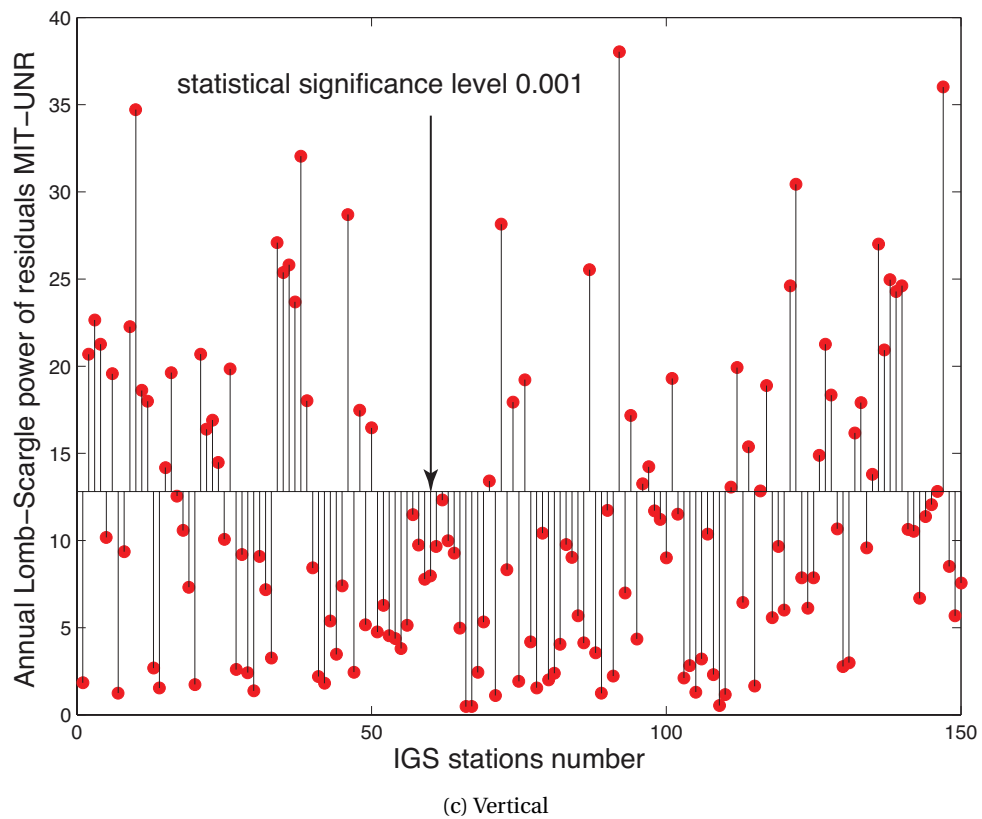


Figure 3.22 – Annual Lomb-Scargle power of the residuals between the MIT and the UNR processing at 150 globally distributed cGPS stations, compared to the statistical significance level derived from the p-value of the Lomb-Scargle periodogram. Most stations compared show no significant seasonal signals in the GPS processing residuals for horizontal components whereas there are significant differences between MIT and UNR processing for the vertical component.

coherent. We thus exclude this hypothesis as a possible candidate from the missing seasonal signal.

### 3.4.3 Environmental factors

The estimation of site position can be affected by multipath issues, when the signals reflect off surrounding terrains. These issues may vary seasonally, because of the vegetation for example, and cause measurement errors. However, these errors would be site specific and could not explain the global seasonal misfit observed. In addition, choke ring antennas are commonly used to reduce these effects.

### 3.4.4 GPS draconitic year

In a recent study, [Ray et al. \(2008\)](#) stacked spectra of 167 GPS sites, obtained from the weekly solutions of the IGS. They noticed a spectral peak at a period of 351.4 days. Since then, other studies found the same systematic periodic error and its harmonics in various GPS-derived geodetic products: in sites coordinates ([Ray et al., 2013](#), [Amiri-Simkooei, 2013](#), [Tregoning & Watson, 2009](#), [King & Watson, 2010](#), [Fu et al., 2015](#)) and orbits ([Griffiths & Ray, 2013](#)). This period coincided with the inertial orientation repeat period of the GPS constellation with respect to the Sun, commonly called "GPS draconitic year". Because this period approaches the solar year, it is likely that the imperfect GPS data processing strategy, including draconitic errors, could produce spurious signals and bias the estimate of seasonal variations of site positions induced by redistribution of surface loads.

Various sources have been proposed to explain these systematic errors in the GNSS data or models: orbit modelling deficiency, in particular due to the Sun-satellite interactions or during eclipse seasons ([Hugentobler et al., 2006](#), [Ray et al., 2008](#), [Rodriguez-Solano et al., 2014](#)), aliasing and/or propagation of site-dependent effects such as multipath or errors in the antenna or radome calibration ([Ray et al., 2008](#)), mismodeling of diurnal and semidiurnal ocean tides, neglecting of semidiurnal and diurnal atmospheric tides ([Tregoning & Watson, 2009, 2011](#)). An even more recent study by [Amiri-Simkooei \(2013\)](#) showed, using hundreds of geodetic positions time series, that the periodic draconitic error is correlated at spatial scales smaller than 3000 km but differs significantly for more distant stations. The draconitic error spatial correlation implies that it is not likely due to station related effects such as multipath or antenna miscalibration. The author also estimates a global range of variations for this periodic pattern of -2.9 to 3.0 mm, -3.3 to 3.0 mm and -6.3 to 6.7 mm for the north, east and vertical components respectively. Thus, the GPS draconitic year signal, with its spatially correlated errors and non-negligible amplitudes in GPS data at a period close to a year is a serious candidate to the global seasonal missing signal induced by hydrology, which globally extends from 11 to 15 months with a maximum around 12.5 months (Figure 3.23). Note that this 12.5 months periodicity may be due to time-averaged measurements.

### 3.4. Potential contributors to missing seasonal signals

In order to test the relevance of the draconitic error as potential contributor to explain

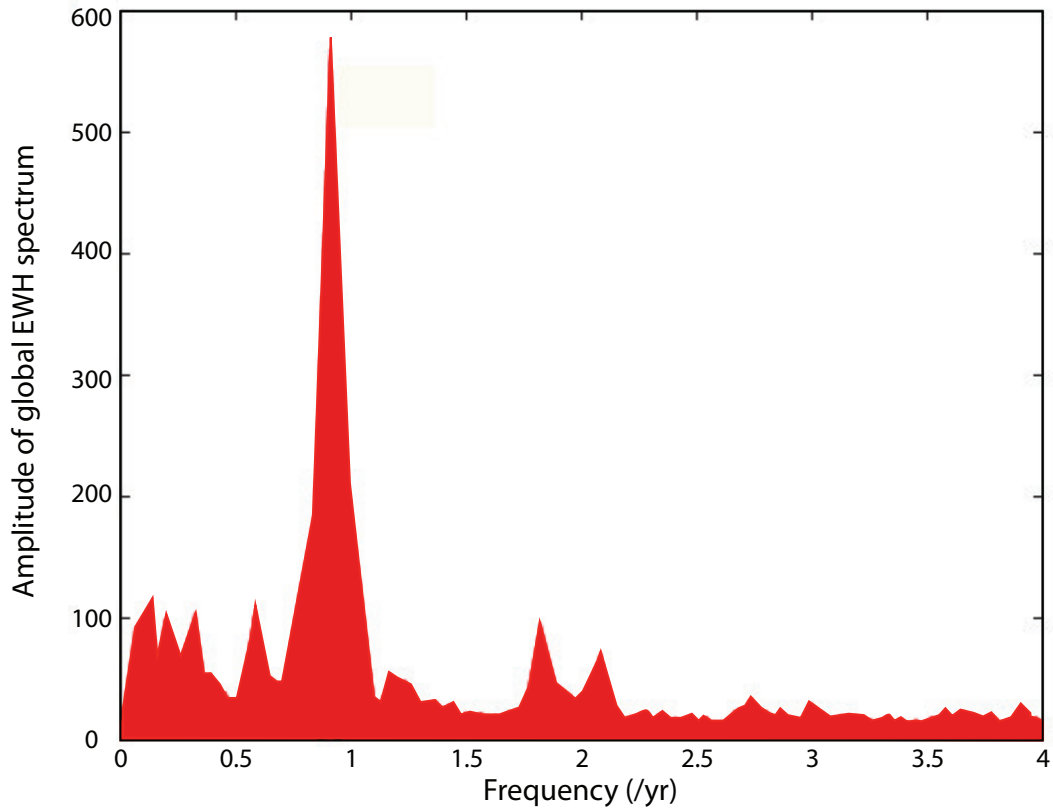


Figure 3.23 – Amplitude of the spectrum of seasonal Equivalent Water Height (EWH) time series derived from GRACE at all points of a 1x1 degree global grid. A clear annual peak with a period of  $\sim 12.5$  months appears, but extends from 11 to 15 months. Other frequencies show a non-negligible signal at numerous locations (semi-annual, bi-annual).

the residuals between seasonal observed displacements and predicted elastic displacements induced by hydrological variations, we further investigate the spatial correlation of these residuals. Indeed, if due to a draconitic effect, residuals have no reason to be directed towards the main regional loading area. We therefore estimate seasonal horizontal remaining signals in site positions (similar to the particle residual horizontal motion at a station) by best fitting a 90% confidence ellipse to the residuals between stacked data and elastic predictions over a year in the east/north plane. Figure 3.24 gives an example of ellipse estimate at station KUNM located in China. Even considering the scatter of the residuals due to noise in the data and model imperfections, the ellipse captures the main orientation of the residuals. At a

### Chapter 3. Global seasonal deformation

global scale, Figure 3.25 shows the estimated ellipses at all stations for which both horizontal components are seasonally significant (red), and for stations where only north (green) or east (orange) components are significant. Principal directions of horizontal residuals seem to be correlated to the surface loads derived from GRACE, at spatial scales smaller than 3000km (South Asia, South America for instance), that is not consistent with a potential draconitic effect. However, further investigation of the spatial correlation between the surface load and the geodetic displacement measurements is required to discard definitively this potential contributor to the missing modeled seasonal signal.

We think that the draconitic component is a potential systematic error in GPS time series that

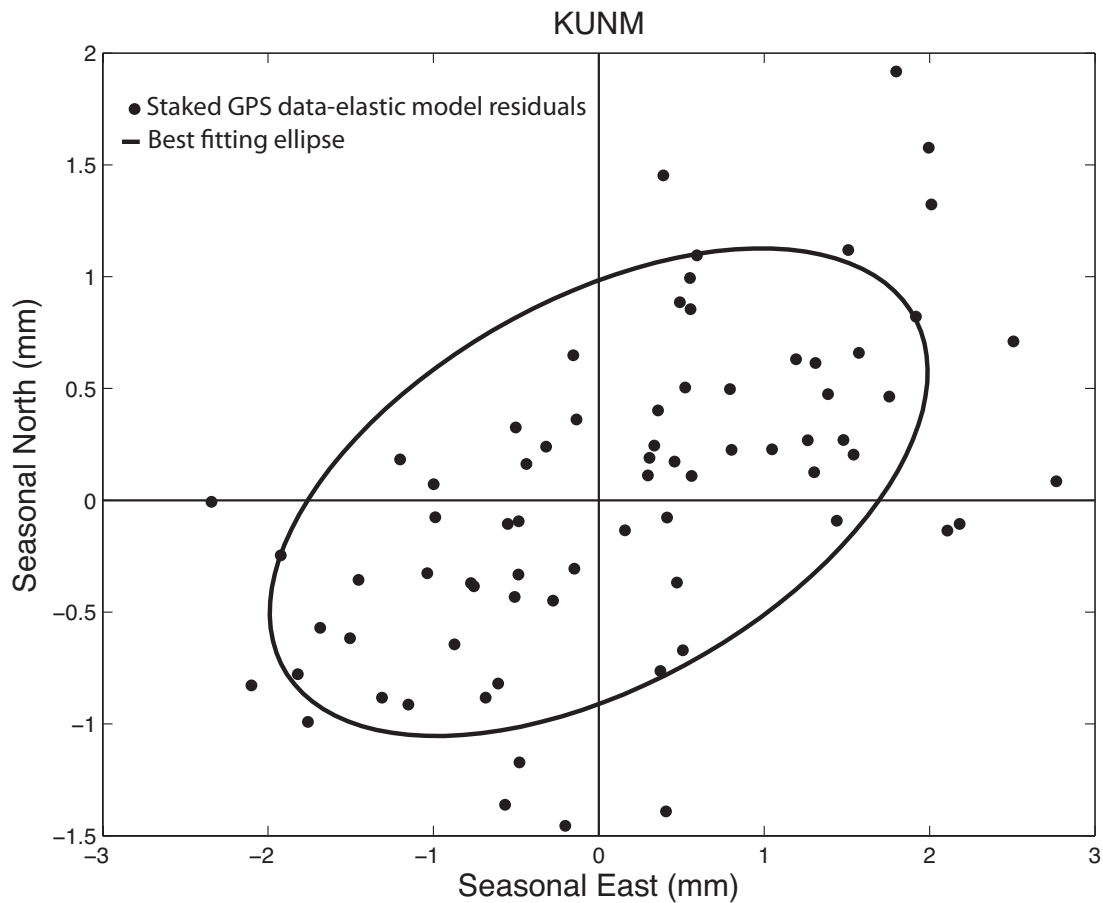


Figure 3.24 – Horizontal residuals between site position and elastic predicted displacements at station KUNM, China (dots), and best fitting 90% confidence ellipse.

could affect seasonal amplitudes of deformation induced by annual variations in continental loading, atmospheric and non-tidal mass. However, we see no reason why the draconitic

### 3.4. Potential contributors to missing seasonal signals

error, even if spatially correlated for adjacent stations, would be correlated to the surface load variations. We therefore discard this hypothesis as the principal contributor to the missing modeled seasonal signal but have no clear way of separating it from a seasonal deformation induced by surface loading.

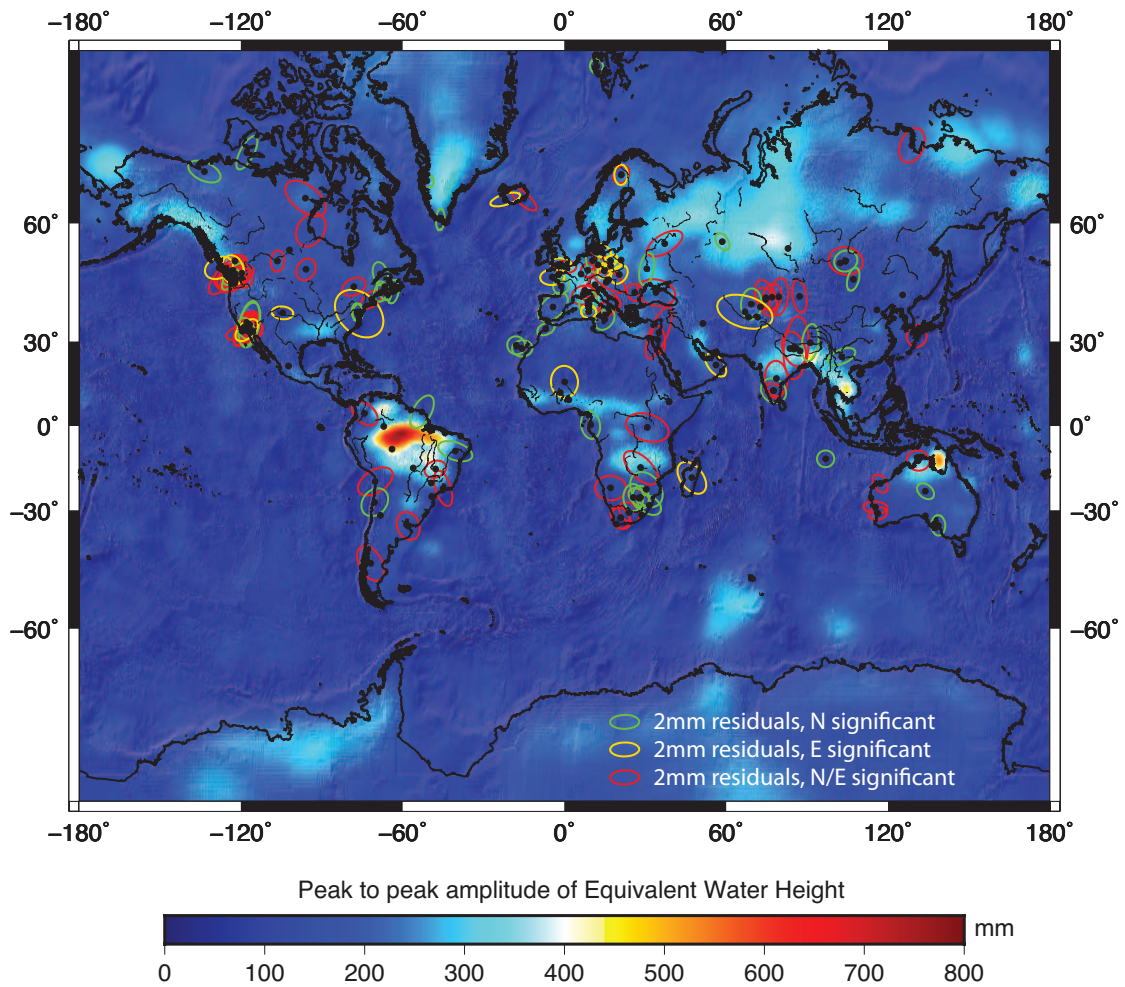


Figure 3.25 – Peak to peak amplitude of seasonal equivalent water height derived from GRACE (mm) and estimated horizontal displacements residuals ellipses between observations and elastic predictions at all stations for which both east and north components are seasonally significant (red), and for stations where only north (green) or east (orange) components are significant.

### 3.4.5 Bedrock thermal expansion

Bedrock thermal expansion is another possible contributor to the missing predicted seasonal signal. However, it would primarily affect the misfit between our elastic model and observations of the vertical component. In order to estimate roughly the contribution of bedrock thermal expansion on seasonal surface displacements, we describe an half-space ( $y \leq 0$ ) heat conduction model, as stated in (Dong et al., 2002) (Figure 3.26). The phenomena has also been investigated by Prawirodirdjo et al. (2006), Tsai (2011) in California. Tsai (2011) found the thermoelastic effects unlikely to explain the seasonal GPS site positions.

We assume the surface temperature is a periodic function of time so that  $T_s = T_0 + \Delta T \cos(\omega T)$ , where the circular frequency  $\omega$  is related to the frequency of temperature fluctuations  $f$  as  $\omega = 2\pi f$ . We also assume that  $T \rightarrow T_0$  as  $y \rightarrow \infty$ . The one dimensional heat equation writes:

$$\frac{\partial T}{\partial y} = \kappa \frac{\partial^2 T}{\partial^2 t} \tag{3.4}$$

with  $\kappa$  the thermal diffusivity. Using classical methods (Turcotte & Schubert, 2014) to solve

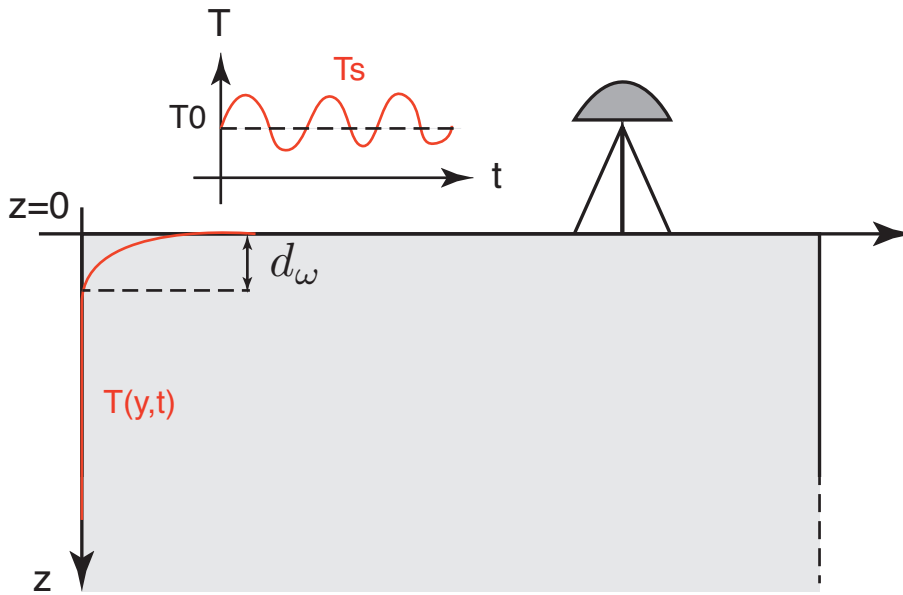


Figure 3.26 – Schematic of the thermal expansion model.

equation 3.4 using boundary conditions at  $y = 0$  and  $y \rightarrow \infty$ , we obtain:

$$T = T_0 + \Delta T \exp\left(-y\sqrt{\frac{\omega}{2\kappa}}\right) \cos\left(\omega t - y\sqrt{\frac{\omega}{2\kappa}}\right) \tag{3.5}$$

### 3.4. Potential contributors to missing seasonal signals

Equation (3.5) shows that the amplitude of the time dependent temperature fluctuations decreases exponentially with depth. For annual variations the skin depth  $d_\omega = \sqrt{\frac{2\kappa}{\omega}} = 3.2m$ , with  $\kappa = 1mm^2.s^{-1}$ , being the penetration depth of the annual temperature fluctuations.

We then need to take into account the stress related to thermal expansion of the half-space into the computation of the total strain as follows:

$$\epsilon_3 = \frac{1}{E}(-\nu\sigma_1 - \nu\sigma_2 + \sigma_3) - \alpha T \quad (3.6)$$

with  $E$  the Young's modulus,  $\nu$  the Poisson's ratio and  $\alpha$  the coefficient of linear expansion. Note that  $\epsilon_1, \epsilon_2 = 0, \sigma_3 = 0$  because the uniform elastic half-space is confined in horizontal directions.

The vertical strain is then:

$$\epsilon_3 = -\frac{1+\nu}{1-\nu}\alpha\Delta T \exp(-y\sqrt{\frac{\omega}{2\kappa}}) \cos(\omega t - y\sqrt{\frac{\omega}{2\kappa}}) \quad (3.7)$$

By integrating (3.7), we have the vertical variation at the surface:

$$\Delta h = \frac{1+\nu}{1-\nu}\alpha\Delta T \sqrt{\frac{\kappa}{\omega}} \cos(\omega t - \frac{\pi}{4}) \quad (3.8)$$

Using a temperature fluctuation  $\Delta T = 20^\circ$ , a coefficient of linear expansion  $\alpha = 10^{-5}$ , a standard Poisson's ration  $\nu = 0.25$  and a thermal diffusivity  $\kappa = 1mm^2.s^{-1}$ , the amplitude of the annual vertical surface displacement is  $\sim 0.6mm$ .

The effect of bedrock thermal expansion is therefore small compared to the misfit between our model and GPS data, and we conclude that this hypothesis cannot explain the missing modeled seasonal signals. However, as stated in section 3.3.3, vertical displacements are less well predicted for high and low latitudes. Accounting for thermal expansion may improve the fit of the model to the data but will not solve the horizontal misprediction. We decided to focus on improving horizontal predictions first.

#### 3.4.6 Differences in GRACE processing

Grace raw data are processed by three different centers which obtain a residual model using different techniques and release normalized Stokes coefficients for each time  $t$ , mean value of an observation period  $T$ . These centers are the Jet Propulsion Laboratory (JPL), the Geo-

### Chapter 3. Global seasonal deformation

---

ForschungsZentrum (GFZ) and the Center for Space Research at University of Texas (CSR), identified as the GRACE Science Data System (SDS) within the mission proposal.

These centers process the GRACE data to produce monthly estimates of the gravitational field and have recently published the Release 5 (RL05) gravity solutions. In addition, the Release-2 solutions produced by the Groupe de Recherche de Geodesie Spatiale at the Centre National d'Etudes Spatiales (CNES/GRGS) in France includes gravity field solutions that cover a shorter time-scale of 10 days. While all four centres employ similar techniques to convert the GRACE observations into models of the gravitational field, structural, tuning, and processing differences within the estimation scheme result in different solutions. These differences could conduct to large or systematic differences in seasonal variations between the four products and potentially bias our results. However, [Sakumura et al. \(2014\)](#) analysed the four gravity field solutions in the spatial and spectral domains and showed that the four individual fields were highly correlated especially in their identification of seasonal signals and that their differences ranged within the formal error bounds of the GRACE solution itself [Sakumura et al. \(2014\)](#). We therefore use only one of the GRACE solutions provided by the CNES/GRGS as a reliable estimate of seasonal hydrological signals (see 3.6 for examples of GRACE time series corrected for linear trends and large earthquake co-seismic contributions for five locations, and all four processing centers).

As discussed above, errors and mismodeling in GRACE and GPS data, as well as thermal expansion of the bedrock, do not seem to be responsible, alone, for the underpredicted horizontal signals by a purely elastic model. Another issue in modeling observed seasonal displacements at GPS stations as the response of the Earth to surface load variations is the difference in reference frames of GPS solutions and mass load solutions ([Dong et al., 2002](#)). Indeed, degree-one deformation, directly related to the reference frame, is not captured by GRACE but recorded by GPS.

#### 3.4.7 Degree-one deformation and reference frame issue

##### The degree-one deformation problem

Intuitively, when moving masses at the Earth surface from one hemisphere to the other, the Center of Mass (CM) of the total Earth system, that is the solid Earth and its fluid envelop, will remain the same in an inertial system (conservation of linear momentum) while the center of figure (CF) of the solid Earth surface will move and deform. From our observational point of view, CM will move with respect to CF, usually described as geocenter motion. Any datasets linking the solid part of the Earth to a space-based reference frame will therefore give valuable information on the geocenter motion.

Here, sources of degree-one deformation originate in redistribution of internal and surface loads such as variations in atmospheric, oceanic and continental water, without any mass loss. Loading theory includes a degree-one deformation caused by the movement of the load center of mass with respect to the solid Earth, associated with a CM-CF shift, of smaller amplitude. According to [Blewitt et al. \(2001\)](#), this would compress one hemisphere, and expands the opposite hemisphere without changing the Earth's shape, but would stretch its surface, affecting GPS site positions. The authors find that, in a CF frame, the poles would appear to be displaced downwards by 3.0 mm during their respective winters, and the equator would appear to move towards the winter pole by 1.5 mm. Figure 3.27 shows an illustration of the Earth seasonal deformation under surface loading and the associated CM motion with respect to CF.

The deformation and geocenter motion induced by degree-one harmonics is an issue when comparing seasonal GPS measurements and modeled seasonal deformation induced by surface mass variations derived from GRACE. Indeed, the case of degree-one surface or internal loading involves a specific deformation compared to higher harmonics ([Farrell, 1972](#), [Greff-Lefitz & Legros, 1997](#)) and is important to understand global redistribution processes, for example continental water, atmospheric and oceanic mass transfer, tides, glacial isostatic adjustment, etc. ([Stolz, 1976](#), [Dong et al., 1997](#), [Blewitt & Clarke, 2003](#), [Wu et al., 2002, 2012](#)). However, GRACE does not measure degree-one harmonic components and our model is there-

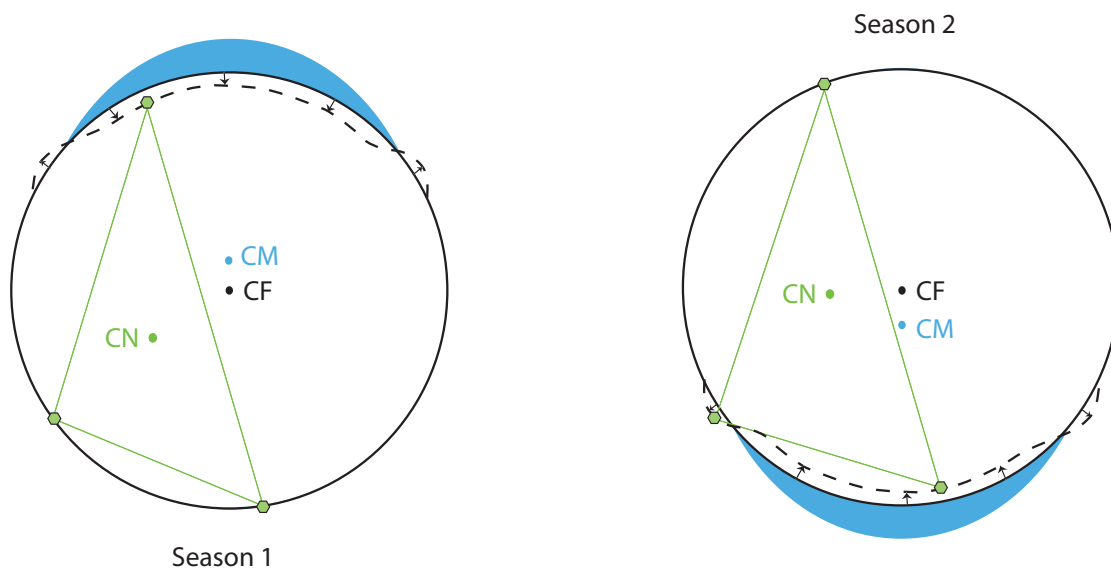


Figure 3.27 – Scheme of degree-one deformation and induced center of mass (CM) motion upon the season, with respect to the center of figure of the solid Earth (CF). The center of network (CN) for the extreme case of three stations is different from both CF and CM and will therefore absorb part of the degree one seasonal signal. CN would be identical to CF if GPS stations used to define the network origin were evenly spaced over the Earth's surface.

fore expressed in a reference frame with origin CM. For GPS measurements, the convention, as in the IERS Conventions (Petit & Luzum, 2010), is that the origin of the ITRF (Altamimi et al., 2011) is a long term average of CM, observed from a set of points at the Earth's surface via geodetic satellite data. This is unfortunately not possible for seasonal GPS measurements, which are expressed in a CF related reference frame because the motion of the tracking sites is not fully modeled, and only secular motions are taken into account. We use the term "CF related reference frame" because tracking sites are not uniformly distributed on the globe, the actual origin for daily position in ITRF is the Center of Network (CN), a representation of CF (Figure 3.27). Note that differences between CF and its representation CN can absorb part of the true seasonal deformation (Dong et al., 2002).

To our knowledge, only a few studies modeling horizontal seasonal deformation of the Earth induced by mass variations derived from GRACE addressed the degree-one problem even though the omission of degree-one information can have significant impact on the modeled time series. Tregoning et al. (2009) inserted degree-one terms into the GRACE spherical harmonic fields using results from Munekane (2007) (using GRACE and GPS data to estimate

### 3.4. Potential contributors to missing seasonal signals

---

degree-one contributions, to solve the reference frame issue with GPS data. [Fu et al. \(2013\)](#) replaced the degree-one components using the results obtained by [Swenson et al. \(2008\)](#) who used the GRACE Stokes coefficients and ocean model output to estimate degree one mass coefficients and geocenter motion. However both studies find unsatisfying correlations between model and GPS observations, particularly for horizontal components.

Geocenter motion estimates vary depending on the dataset and techniques used. A number of authors have estimated the annual and semiannual components of geocenter motion induced by different models of surface mass redistribution ([Bouille et al., 2000](#), [Chen et al., 1999](#), [Crétaux et al., 2002](#), [Dong et al., 1997](#)). While the geocenter motions from different atmospheric mass models tend to agree for all components, significant differences (up to 50%) are observed in annual and semiannual geocenter motion from ocean bottom pressure and, more importantly, from continental water mass. In their review, [Wu et al. \(2012\)](#) summarize in Table 2 measured and predicted annual geocenter motion from 17 studies, including GPS and Satellite Laser Ranging (SLR) data, climate models and various approaches (kinematics, network shift, inverse and unified approaches). The amplitude of geocenter motion shows non-negligible variations from one study to the other. If the geocenter motion is expressed in a geocentric frame ( $X, Y, Z$ ),  $Z$  pointing to the North pole and  $X$  in the equatorial plan, pointing East, then measured and predicted geocenter motion vary in translation as:

- $T_X \in [0.1; 4.2] mm$ , with  $\bar{T}_X = 2.5 mm$
- $T_Y \in [1.8; 4.3] mm$ , with  $\bar{T}_Y = 2.7 mm$
- $T_Z \in [1.5; 7.6] mm$ , with  $\bar{T}_Z = 3.7 mm$

Note that the model proposed by [Swenson et al. \(2008\)](#) and used to replace degree-one coefficients in GRACE dataset in several studies, and in particular in seasonal deformation models ([Fu et al., 2013](#)) estimates annual translations of relatively small amplitude compared to other studies with  $T_X = 1.5 mm$ ,  $T_Y = 2.6 mm$ ,  $T_Z = 1.5 mm$ . This may explain why the replacement of degree-one components in GRACE by the studies mentioned above gives unsatisfying results, comparable to a model with no degree-one components, i.e. centered in CM and not CF.

Due to the variations in geocenter motion and therefore in degree-one coefficients to include in GRACE, we decide to apply an a posteriori geometrical Helmert transformation

### Chapter 3. Global seasonal deformation

between GPS detrended time series and modeled displacements induced by GRACE, with no degree-one (3 translations, 3 rotations and an optional scaling parameter). Doing so, we add the CM-CF shift component to our model, modeled as a 6 parameters Helmert transformation and compare data and model in the same reference frame as explained in the following. Note that the transformation models a solid transformation but not fully the geocenter motion. This is not ideal and would need further investigation but was beyond the scope of my thesis.

#### Aligning CN (GPS) and CM (GRACE-derived model) solutions to minimize degree-1 effects

The Helmert transform is a classical geometrical similarity in geodesy that we use here to reconcile reference frames and insure that model and data are comparable. For two terrestrial

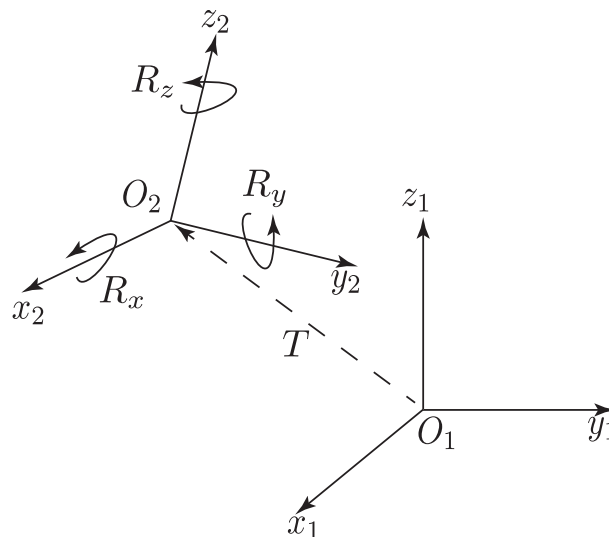


Figure 3.28 – Scheme of an Helmert transform between frame  $(O_1, x_1, y_1, z_1)$  and frame  $(O_2, x_2, y_2, z_2)$  with  $T$  the translation from  $O_1$  to  $O_2$  and  $(R_x, R_y, R_z)$  the three rotations along the  $(X, Y, Z)$

reference frames,  $R_1$  and  $R_2$ , a point  $M$  of coordinates  $M_1 = (x_1, y_1, z_1)^T$  and  $M_2 = (x_2, y_2, z_2)^T$  in  $R_1$  and  $R_2$  respectively (see Figure 3.28), the transformation writes:

$$M_2 = T + \lambda R M_1 \tag{3.9}$$

### 3.4. Potential contributors to missing seasonal signals

with  $T = (T_x, T_y, T_z)^T$  is the translation vector between the two origins  $O_1$  and  $O_2$ ,  $\lambda$  is a scaling factor and  $R$  is a rotation matrix such that  $R = R_x R_y R_z$ , with:

$$R_x = \begin{pmatrix} 1 & 0 & 0 \\ 0 & \cos R_x & -\sin R_x \\ 0 & \sin R_x & \cos R_x \end{pmatrix}, R_y = \begin{pmatrix} \cos R_y & 0 & -\sin R_y \\ 0 & 1 & 0 \\ \sin R_y & 0 & \cos R_y \end{pmatrix}, R_z = \begin{pmatrix} \cos R_z & \sin R_z & 0 \\ -\sin R_z & \cos R_z & 0 \\ 0 & 0 & 1 \end{pmatrix} \quad (3.10)$$

Because scaling and orientation differences between the two frames remain small, we can linearize the circular functions of the rotation matrix in equation 3.9 using an order 1 Taylor development and have:

$$R = I + R' = \begin{pmatrix} 1 & 0 & 0 \\ 0 & 1 & 0 \\ 0 & 0 & 1 \end{pmatrix} + \begin{pmatrix} 0 & R_z & -R_y \\ -R_z & 0 & R_x \\ R_y & -R_x & 0 \end{pmatrix} \quad (3.11)$$

We consider  $\lambda = 1$  and not estimate a scaling parameter as it would affect the vertical component mostly and therefore be close to 1.

Equation 3.9 in a linearized form writes:

$$M_2 = M_1 + T + R' M_1 \quad (3.12)$$

or,

$$D = Gm \quad (3.13)$$

with:

$$D = M_2 - M_1 \quad (3.14)$$

$$G = \begin{pmatrix} 1 & 0 & 0 & 0 & z_1 & -y_1 \\ 0 & 1 & 0 & -z_1 & 0 & x_1 \\ 0 & 0 & 1 & y_1 & -x_1 & 0 \end{pmatrix}, \quad (3.15)$$

and

$$m = (T_x \ T_y \ T_z \ R_x \ R_y \ R_z)^T \quad (3.16)$$

We also need to transform global geocentric coordinates  $M_{XYZ}$  into local topocentric coordinates  $M_{ENU}$  (East, North, Vertical) applying a another translation  $T = (x', y', z')^T$  and a

rotation using the rotation matrix:

$$R_{XYZ \rightarrow ENU} = \begin{pmatrix} -\sin \lambda & \cos \lambda & 0 \\ -\sin \phi \cos \lambda & -\sin \phi \sin \lambda & \cos \phi \\ \cos \phi \cos \lambda & \cos \phi \sin \lambda & \sin \phi \end{pmatrix}, \quad (3.17)$$

with  $\phi$  and  $\lambda$  the latitude and longitude of the station of interest.

The transformation from global to local coordinates is given by the equation:

$$M_{ENU} = R_{XYZ \rightarrow ENU} M_{XYZ} + T \quad (3.18)$$

Let  $C_{XYZ}$  be the variance-covariance matrix in global coordinates, then the local variance-covariance matrix  $C_{ENU}$  is:

$$C_{ENU} = R_{XYZ \rightarrow ENU} C_{XYZ} R_{ENU \rightarrow XYZ}^T \quad (3.19)$$

The equation 3.13, including the global-local transformation is:

$$R_{XYZ \rightarrow ENU} G_{XYZ} = R_{XYZ \rightarrow ENU} D_{XYZ} \quad (3.20)$$

which leads to:

$$D_{ENU} = G_{ENU} m \quad (3.21)$$

with  $G_{ENU} = R_{XYZ \rightarrow ENU} G_{XYZ}$  and  $D_{ENU} = R_{XYZ \rightarrow ENU} D_{XYZ}$ . In the following, we will use the local formulation of the preceding equations as it is more convenient when using GPS data.

Now that we have established the working frame, we need to find the best parameters of the transformation to circumvent the differences between model and observations due to degree-one deformation and geocenter motion. We do a least square inversion, which is a standard inversion used in reference frame transformations.

For each station  $i$ , we obtain a system of equations at each time step such that  $G_i m = D_i, C_i$  with  $C_i = (C_i^1 + C_i^2)^{-1}$ , where  $(C_i^1, C_i^2)$  are the variance-covariance matrices of the station in each reference frame. We consider that each point is independent and thus,  $C$  is diagonal.

We invert equation 3.21 and find the best-fitting 6 parameter of the Helmert transform between our model and data by solving:

$$m = (G^T C G)^{-1} G^T C D \quad (3.22)$$

and minimizing the residual vector  $R$

$$R = Gm - D \tag{3.23}$$

We perform the inversion for all available stations of our set of 195 cGPS sites at each time step. Figure 3.29 gives the number of stations used at each time step for the inversion. Because degree-one deformation and associated geocenter motion affect horizontal and vertical displacements in a significantly different way, we treat the components separately. As we are trying to improve the fit of our model to the horizontal positions, we use only the horizontal displacements as a misfit function and insure that the vertical fit is not affected significantly. Results are given on Figure 3.30 for the best-fitting translations and on Figure 3.31 for the best fitting rotations associated with degree-one deformation and geocenter motion. Geocenter motion and degree-one deformation modeled as a geometrical transformation mostly show a seasonal translation and rotation along  $Z$ .

Note that there is no reason to include the vertical component in our inversion as the degree-one deformation does not follow the same pattern. Figures 3.33 and 3.32 show respectively the best-fitting three rotations and translations of an inversion minimizing only the vertical component. Time series of Helmert parameters derived from the vertical data are significantly different than the ones derived from the horizontal positions, with a larger amplitude, a shift in phase, and with a less clear seasonality. Since most geocenter motion estimates are derived from vertical, or a combination of vertical and horizontal geodetic displacements, degree-one coefficients derived to replace GRACE missing coefficients may not be accurate to predict seasonal horizontal observations.

Interestingly, the deformation contribution of geocenter motion can be found using the separate horizontal and vertical inversions and remains to do ([Blewitt et al., 2001](#)).

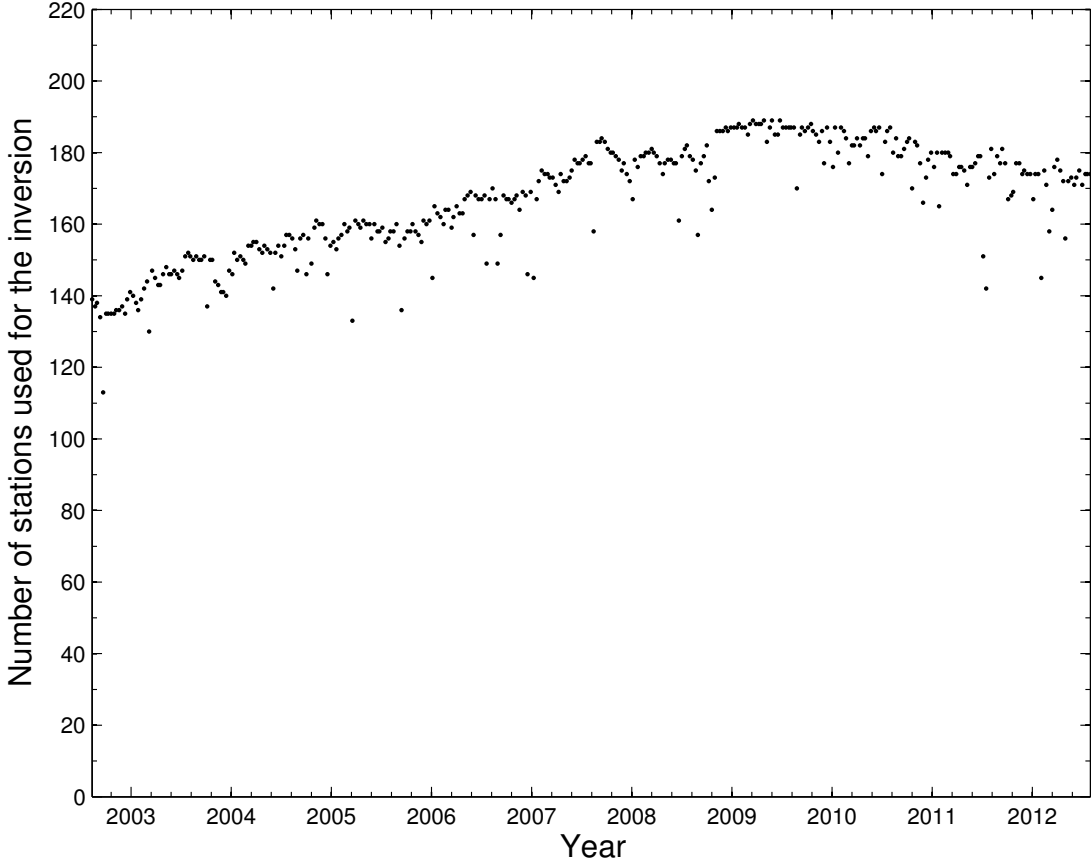


Figure 3.29 – Number of cGPS sites used in the least-square inversion of horizontal positions as a function of time.

### 3.4. Potential contributors to missing seasonal signals

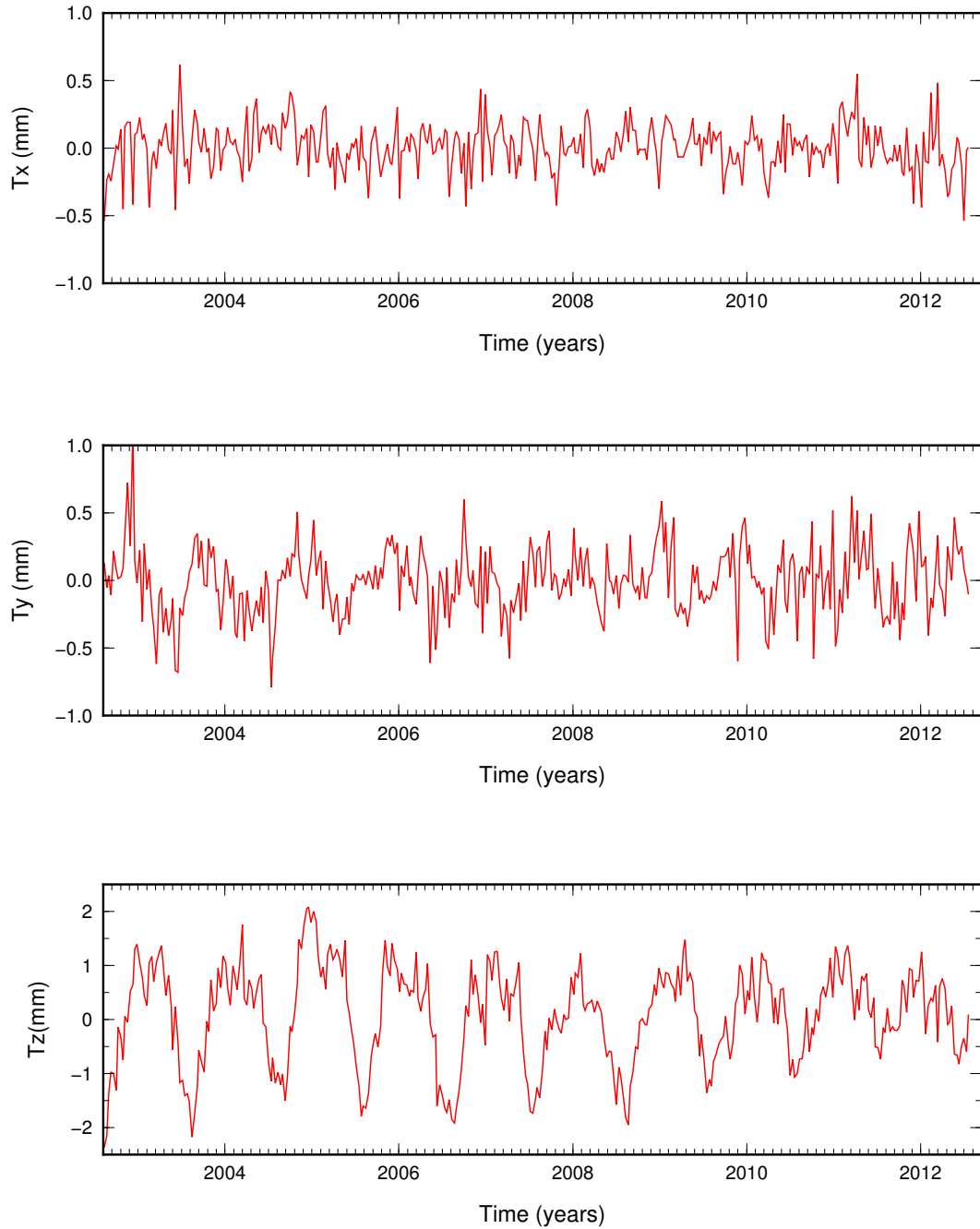


Figure 3.30 – Best-fitting translations  $T_x$ ,  $T_y$ ,  $T_z$  derived from a global least square inversion of the horizontal time series of the 195 cGPS sites of our study.

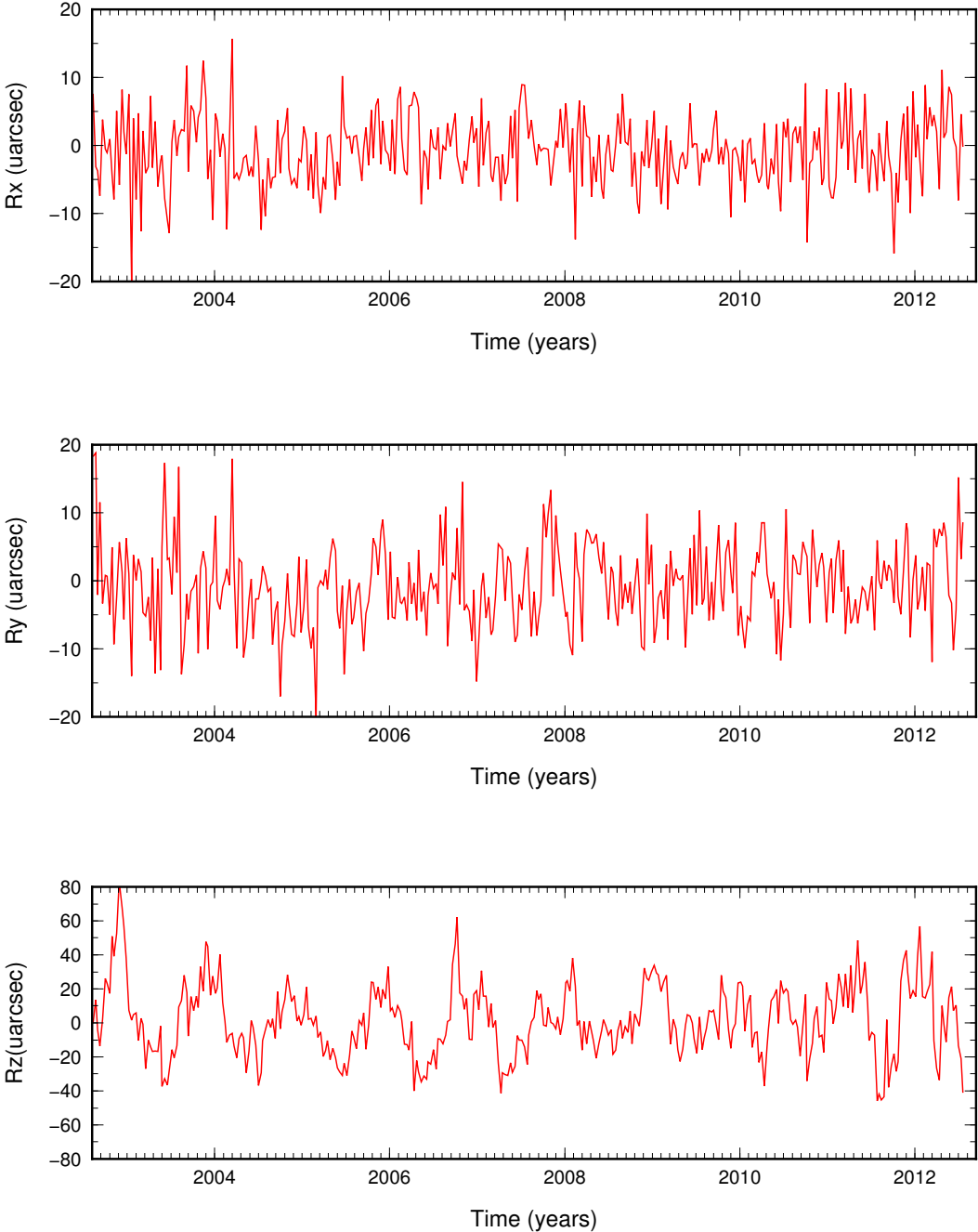


Figure 3.31 – Best-fitting rotations  $R_x, R_y, R_z$  derived from a global least square inversion of the horizontal time series of the 195 cGPS sites of our study.

### 3.4. Potential contributors to missing seasonal signals

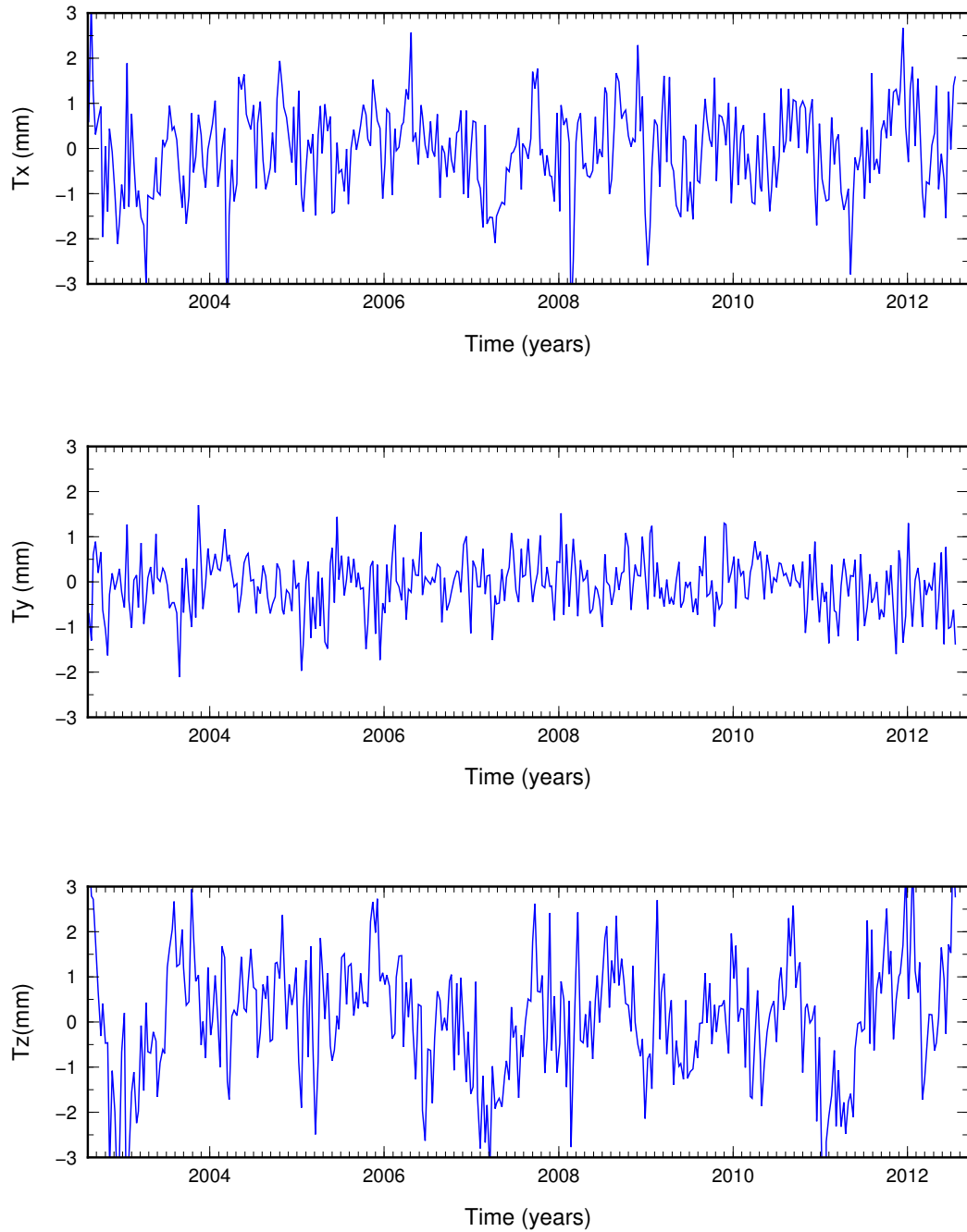


Figure 3.32 – Best-fitting translations  $T_x$ ,  $T_y$ ,  $T_z$  derived from a global least square inversion of the vertical time series of the 195 cGPS sites of our study.

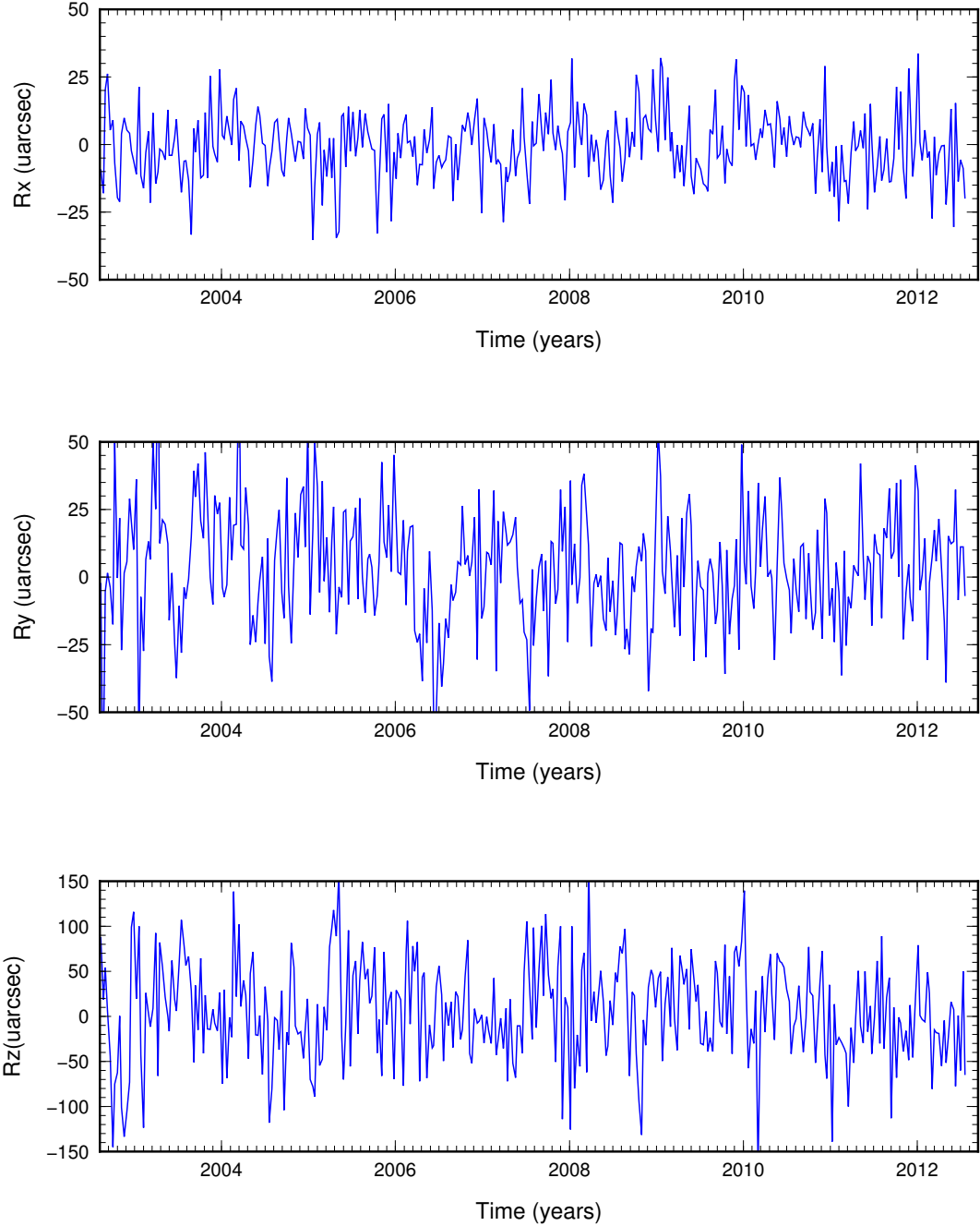


Figure 3.33 – Best-fitting rotations  $R_x, R_y, R_z$  derived from a global least square inversion of the vertical time series of the 195 cGPS sites of our study.

### 3.4. Potential contributors to missing seasonal signals

Using the best-fitting 6 Helmert transformation parameters to the horizontal site positions, we compute the transformed model for all components at each station. Figure 3.34 shows detrended geodetic positions (gray), and their 10-days average (black crosses) at stations (a) LHAZ, (b) CHPI and (c) GOLD GPS stations with error-bars for  $1-\sigma$  uncertainties (gray symbols). Blue and green lines show predicted displacements induced by seasonal surface hydrology variations using a purely elastic continental PREM Earth model in a frame with origin a representation of the center of figure (CF) of the Earth derived using results from Swenson et al. (2008) and in the best fitting frame with origin the center of our GPS network (CN). The first model (Swenson et al., 2008) predicts fairly well vertical components while horizontal signals are under-predicted and, in the GOLD case, out of phase. Our transformed model is better on the horizontal components, both in amplitude and phase and does not degrade the vertical predictions. However, there is still a smaller under-prediction of the amplitude of north and east components.

Figure 3.35 shows the spatial distribution of the NRMSD for the transformer elastic model, to be compared to Figure 3.11. The fit to the horizontal components is globally improved, especially for northern displacements. We computed  $\chi^2$  for our 195 cGPS stations between the data, the null model, the elastic model and the elastic transformed model. Global results are given in Table 3.2 Our transformed model reduces the  $\chi^2$  values at 155 sites for the north, 129

	North	East	Vertical	H & V
Data-Null	9831	12299	9210	10571
Data-Elastic	8887	12015	7752	9636
Data-Elastic transformed	7174	11645	7814	8997

Table 3.2 –  $\chi^2$  values for each components and all components for all stations of our study.

for the east but only 95 for the vertical components over the 195 sites of our study. However, the fit of the improved model to the vertical component remains acceptable. As mentioned in section 3.4.5, the vertical prediction may be missing a thermal expansion term.

Even if improved, our model is not ideal. Particularly, the horizontal amplitude is still under-predicted. On Figure 3.36, we plot the  $\chi^2$  by component as a function of the station latitude in

### Chapter 3. Global seasonal deformation

---

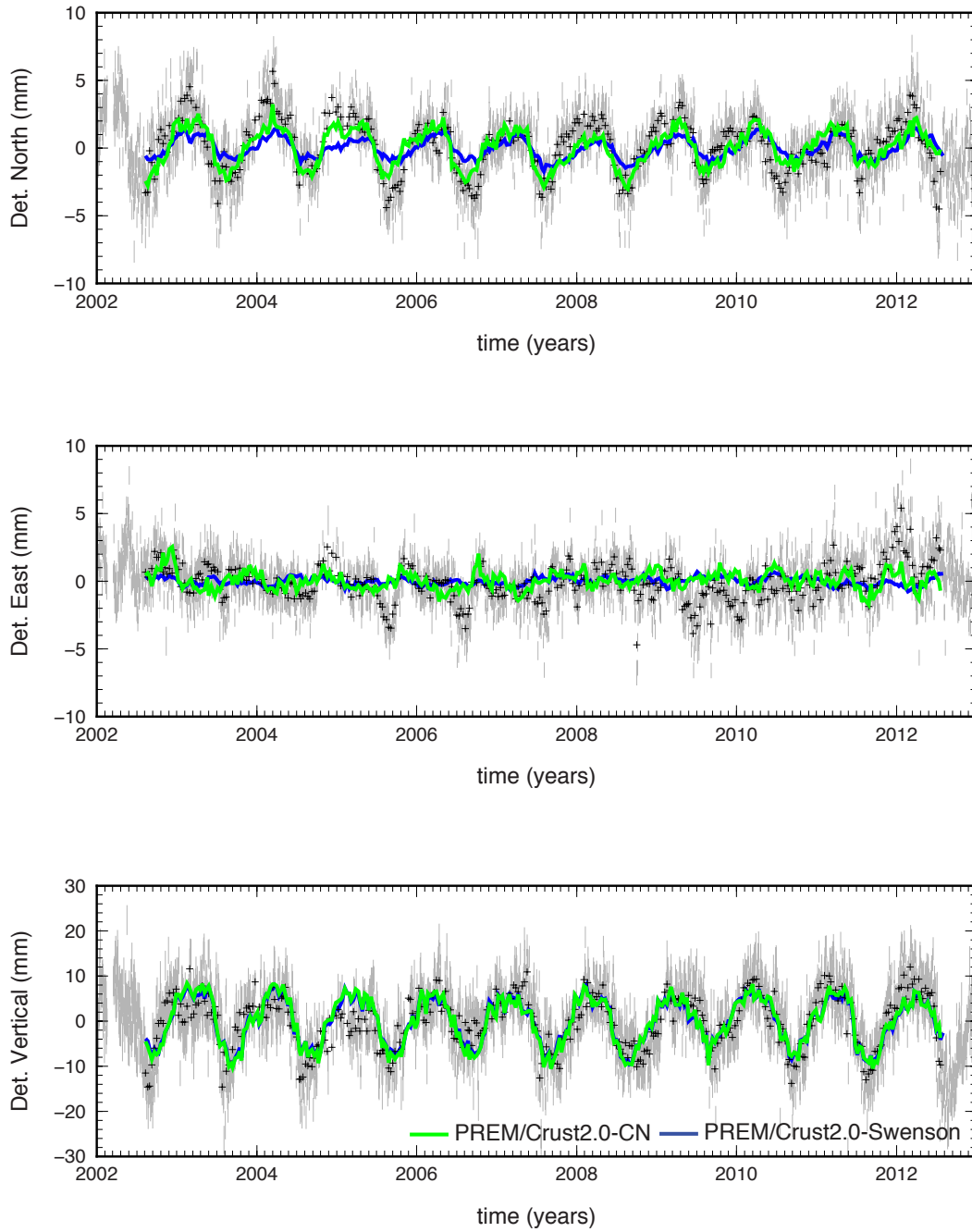
blue for the elastic model and in green for the elastic transformed one. While the  $\chi^2$  values are higher for the vertical component at high latitudes, no clear correlation appears for the horizontal component. Therefore, we decide to look for another potential missing signal at a global scale. In the following section, we will question the validity of the PREM model at an annual time scale and test the influence of elastic parameters, viscoelastic asthenospheres and mantle phase transitions on the modeling of seasonal deformation.

---

Figure 3.34 (*following page*) – Daily detrended geodetic positions, determined at station (a) LHAZ, (b) CHPI and (c) GOLD GPS stations with error-bars for 1- $\sigma$  uncertainties (gray symbols). See Figure 3.1 for location. Black crosses are 10-days moving-average of the daily geodetic observations. Blue and green lines show predicted displacements induced by seasonal surface hydrology variations using a purely elastic continental PREM Earth model where degree-1 contributions are given by [Swenson et al. \(2008\)](#) or by estimating a best fitting Helmert transform a posteriori. The original model predicts fairly well vertical components while horizontal signals are under-predicted and, in the GOLD case, out of phase. The transformed model is better on the horizontal components, both in amplitude and phase even if the amplitude is still under-predicted.

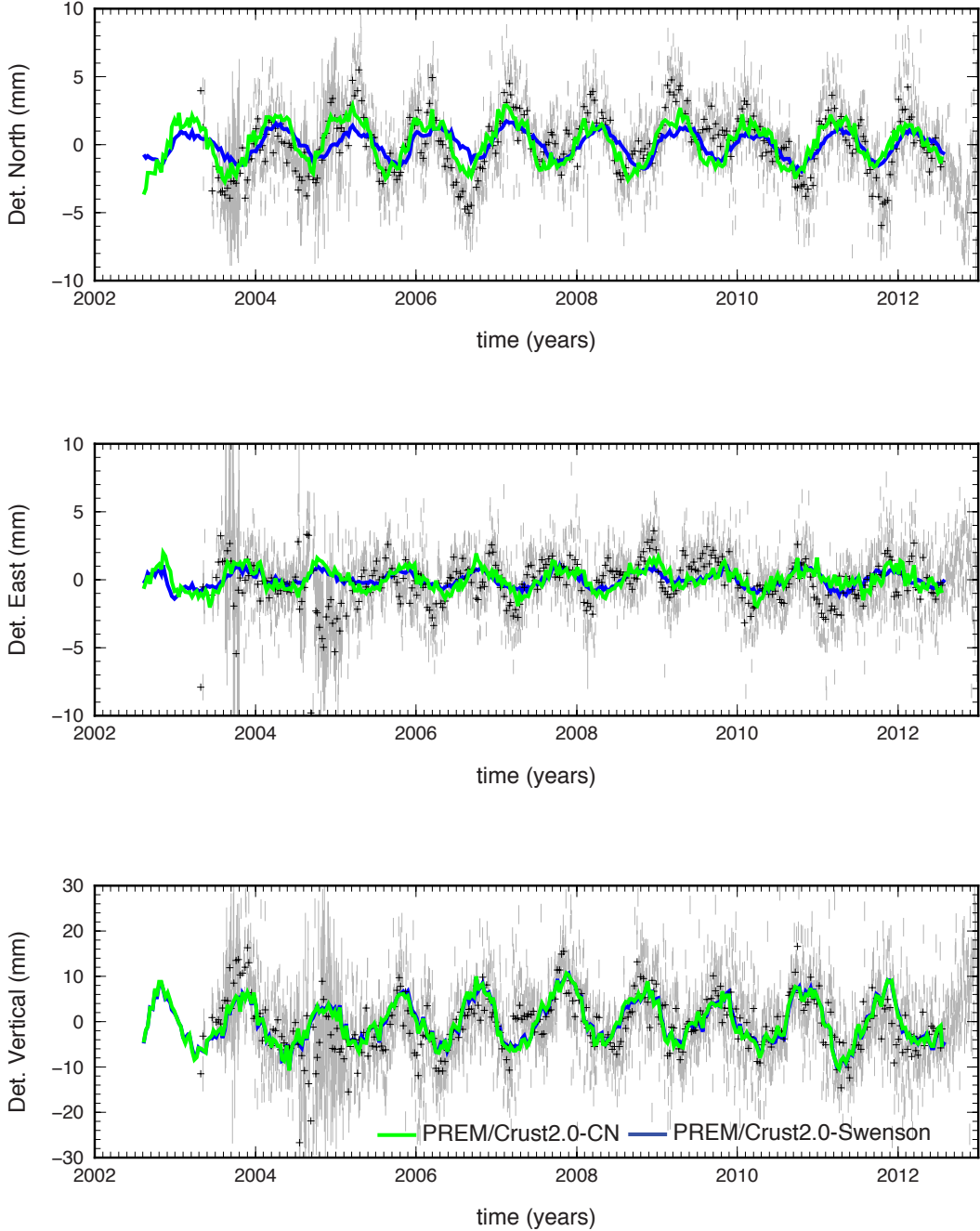
### 3.4. Potential contributors to missing seasonal signals

#### LHAZ



(a) LHAZ, China

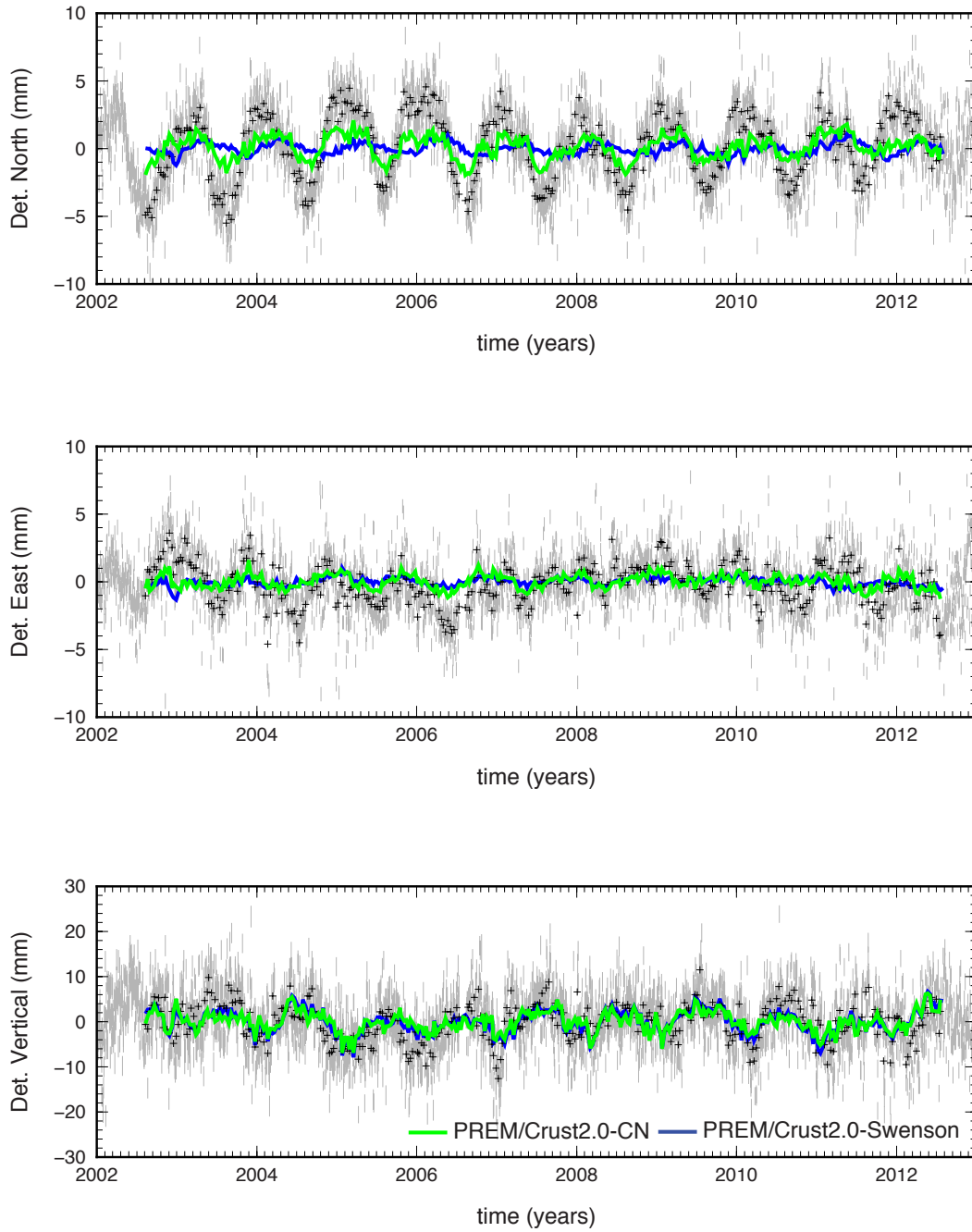
CHPI



(b) CHPI, Brazil

### 3.4. Potential contributors to missing seasonal signals

#### GOLD



(c) GOLD, United States (California)

### Chapter 3. Global seasonal deformation

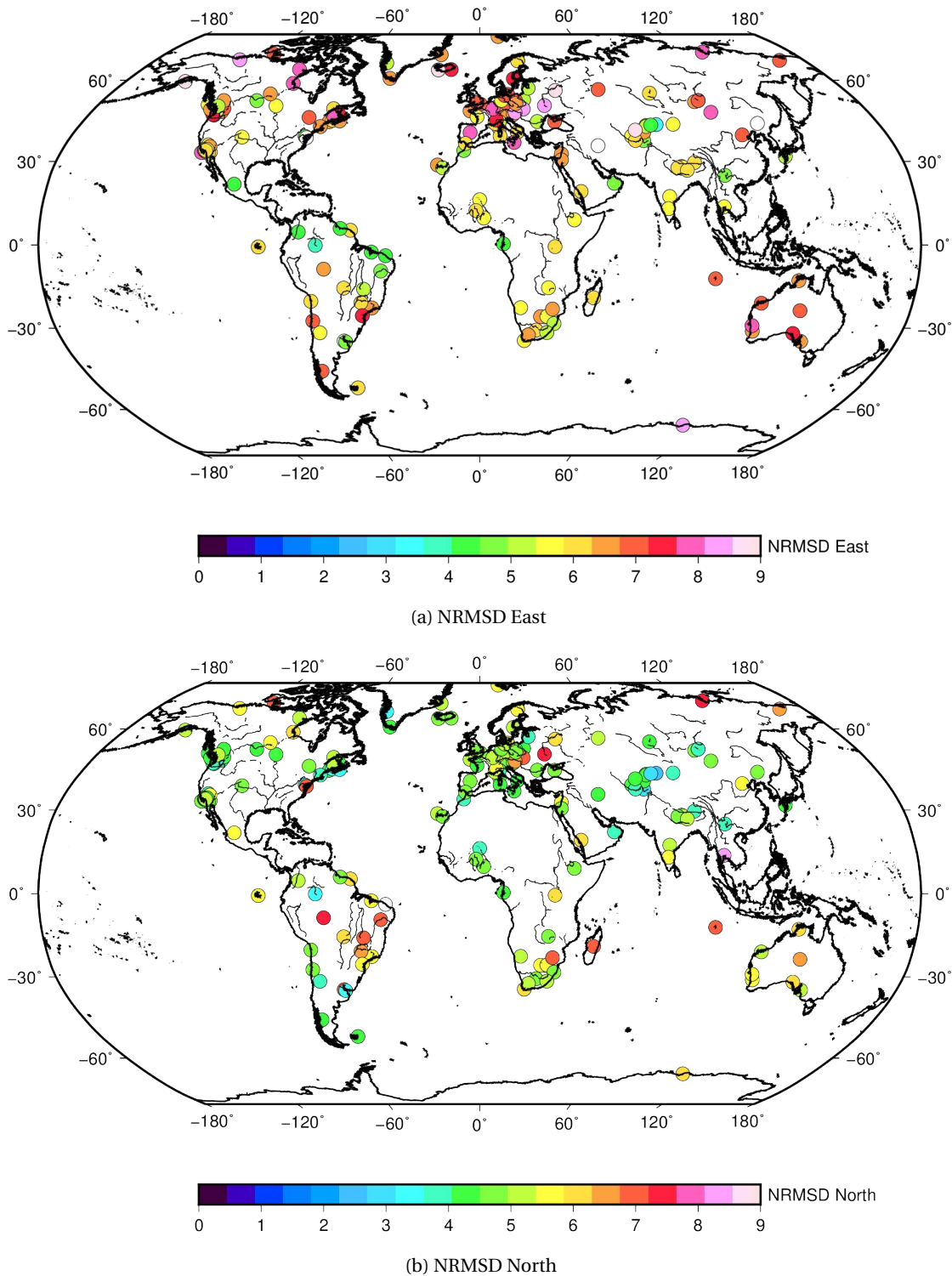


Figure 3.35 – Normalized root-mean-square deviation (NRMSD, see equation 3.3) by the mean amplitude of the signal between elastic seasonal displacement predictions transformed using the horizontal best-fitting 6 parameters of the Helmert transform and observations for east (a), north (b) and vertical (c).

### 3.4. Potential contributors to missing seasonal signals

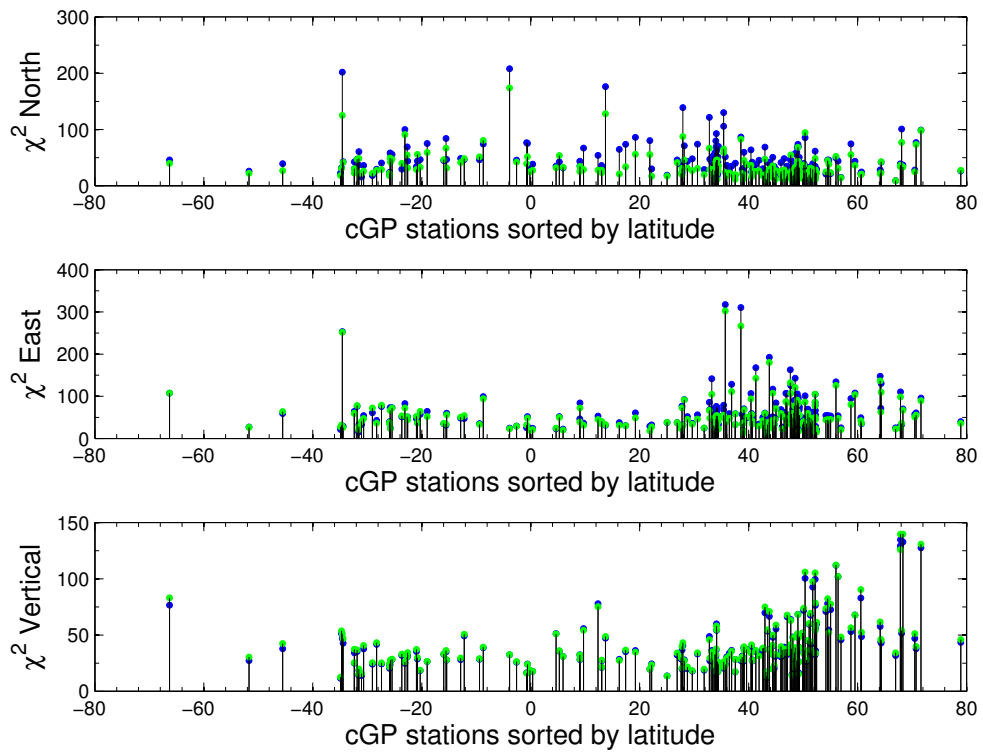
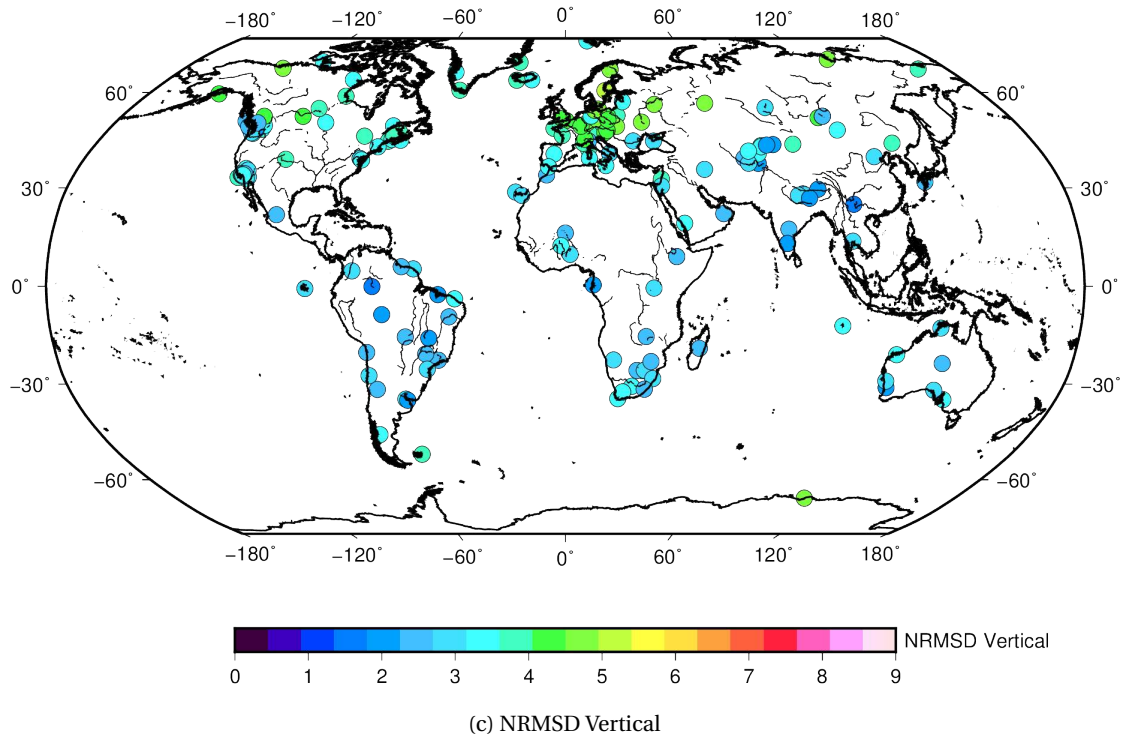


Figure 3.36 –  $\chi^2$  as a function of latitude of the site between data and elastic model (blue dots) and elastic transformed model (green dots) by component.

### 3.5 Seasonal variations and implications for the Earth mechanical properties

As PREM is derived from seismic estimates, and therefore valid at time scales smaller than an hour, we question in this section the validity of using a global 1D purely elastic PREM based model to predict seasonal deformation. To our knowledge, all published studies of seasonal hydrological or atmospheric loading comparing GRACE-derived predictions with space geodetic observations assume a purely elastic Earth model, with a half-space of spherical geometry. In the following, we investigate the influence of variations in elastic properties, viscoelastic structures and volume variations due to mantle phase transformations on surface displacements induced by seasonal surface load variations.

#### 3.5.1 Influence of shallow elastic properties

As shown by (Ito & Simons, 2011), oceanic tidal loading can be exploited to provide new insights into the Earth's interior elastic structure. The authors inverse the ocean tidal loads (OTLs) to infer depth-dependent profiles of material elastic properties, i.e. the bulk modulus, density and shear modulus ( $K, \rho, \mu$ ) down to  $\sim 350$ km, significantly improving the fit to displacements induced by OTLs from PREM. Their best fitting models has parameters varying within  $\pm 10\%$  from PREM.

Our interest is in annual loading. Figure 3.37 shows the amplitude of horizontal and vertical displacements induced by unit loading for spherical non-rotating elastic and isotropic models: PREM (magenta), and 10% variations from PREM in the 0-350km depth of parameters  $\mu$  (red),  $K$  (green) and  $\rho$  (blue). We conclude that, for an annual periodic loading, variations of shallow depth elastic parameters from PREM within 10% will not influence vertical displacements induced by annual surface loading and only change the amplitude of horizontal displacements by, at the maximum, 5% for loads of wavelength smaller than 4000 km (spherical harmonic order  $\sim 10$ ). Reasonable elastic parameter variations in the first 350 km are therefore not sufficient to model the  $\sim 50\%$  missing seasonal horizontal amplitude at a global scale even if it was a regional candidate for the Himalaya, where the horizontal signals were already reasonably well predicted by a PREM based model. In addition, since the model is still purely

elastic, the remaining phase misfit would be identical to the PREM-based results with no inter-layering variations.

#### 3.5.2 Influence of low viscosity in the asthenosphere

In the past decades, numerous studies of post-seismic relaxation used a time-dependent rheology in the asthenosphere to model transient deformation observed in GPS time series, usually 1 to 3 years after the earthquake. For instance, [Pollitz \(2003\)](#) used a bi-viscous Burger rheology to model the rapid early deformation seen in GPS time series, and the longer term relaxation of the upper mantle following the M7.1 Hector Mine, California, earthquake. The author's best fitting model requires a transient viscosity of  $1.6 \cdot 10^{17} Pa \cdot s$ . Such low transient viscosity has a relaxation time that would affect annual periodic surface loading. Since then, various studies proposed models with a range of low transient viscosities in the asthenosphere, following large earthquakes, raising the question of the compatibility of such viscosities with annual loading ([Ryder et al., 2011](#), [Pollitz & Thatcher, 2010](#), [Pollitz, 2005](#), [Chandrasekhar et al., 2009](#), [Pollitz et al., 2006](#), [Trubienko et al., 2013](#)). Note that low transient viscosities could be explained by other physical phenomena (afterslip for example).

In order to test the influence of viscoelastic rheologies in the asthenosphere on seasonal surface deformation, we first describe the realistic viscoelastic bodies commonly used to model the time dependent response of the Earth to loading (surface or seismic) and then discuss their influence on the prediction of surface displacements.

We consider a visco-elastic material to which stress is applied. In response, the material deforms with a time-dependent behaviour. Similarly, if a strain change is imposed to the material, stress will not be transmitted through the material instantaneously: the material undergoes relaxation. In our model, we consider different types of visco-elastic behaviour which can be illustrated by elementary mechanical elements (Figure 3.38).

The spring represents the instantaneous reversible deformation where stress and strain are related with Hooke's law  $\sigma = \mu \epsilon$ . The dash-pot represents the Newtonian viscous deformation, where stress and strain are related by  $\sigma = \eta \dot{\epsilon}$ , with  $\eta$  the viscosity in Pa.s. These two

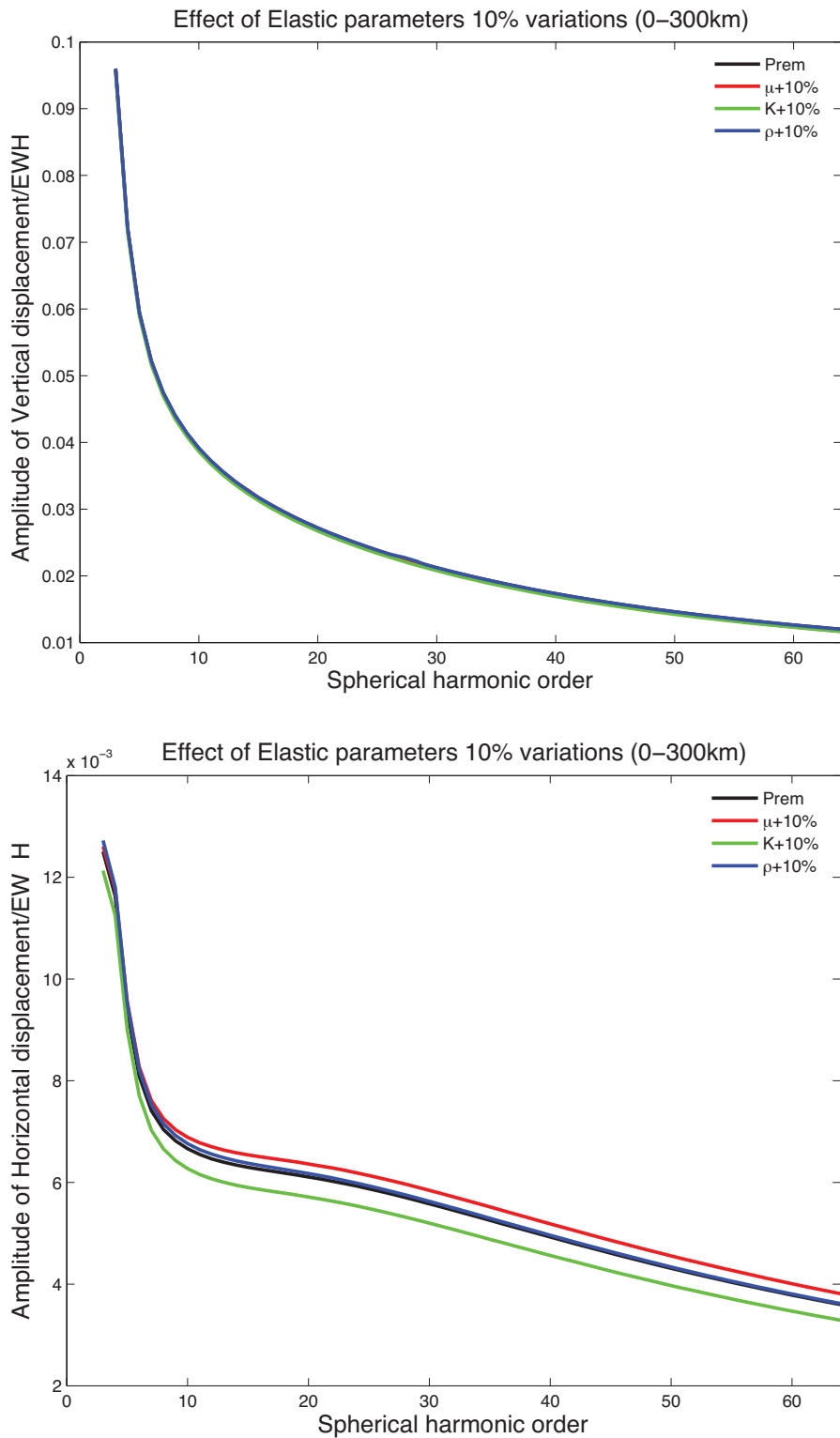


Figure 3.37 – Amplitude of vertical and horizontal displacements induced by unit annual loading for SNREI models: PREM (magenta), and variations from PREM in the 0-350km detph range with  $\mu = \mu_{prem} + 10\%$  (red),  $K = K_{prem} + 10\%$  (green) and  $\rho = \rho_{prem} + 10\%$  (blue)

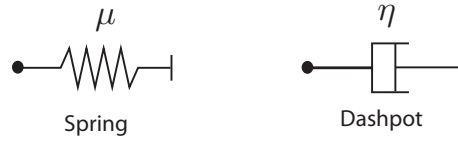


Figure 3.38 – Elementary mechanical elements

elements can be combined to model various rheology for the Earth. In our models, we use two types of viscoelastic rheologies, Burger and Maxwell, shown on figure 3.39. The Kelvin-Voigt intermediate model is also shown.

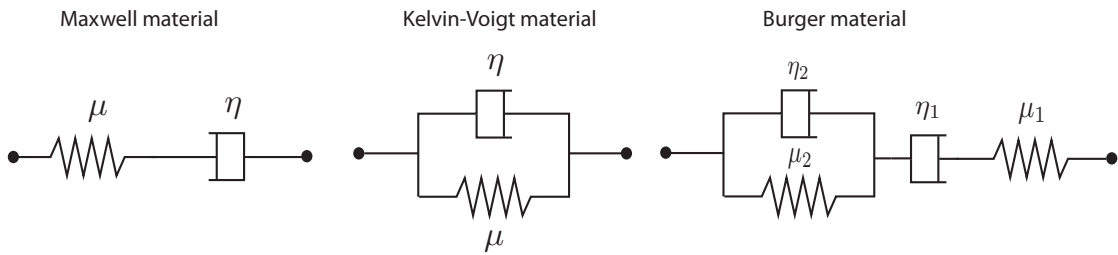


Figure 3.39 – Maxwell, Kelvin-Voigt and Burger materials

### Maxwell rheology

The most commonly used rheology to describe the visco-elastic rheology of the Earth is the Maxwell material. A Maxwell material is the serial association of a spring and a dashpot (Figure 3.39). A stress applied to a Maxwell system is equal in both elements but the deformations will add up, i.e.  $\epsilon_{maxwell} = \epsilon_{spring} + \epsilon_{dashpot}$ .

The associated constitutive equation is then:

$$\dot{\epsilon} = \frac{1}{\mu} \dot{\sigma} + \frac{1}{\eta} \sigma \quad (3.24)$$

If a stress  $\sigma_0$  is applied to the system at  $t = 0$ , the Maxwell system will instantaneously respond elastically with a strain equal to  $\frac{\sigma_0}{\mu}$  and then evolve with a constant strain rate equal to  $\frac{\sigma_0}{\eta}$  due to its viscous relaxation as shown on Figure 3.40. Note that for  $\eta \rightarrow \infty$ , the Maxwell body is equivalent to an elastic solid. This rheology is widely used to model the response of the Earth's mantle to glacial loading (Peltier, 1974). We are interested in seasonal hydrological loading of the Earth's surface. For a periodic load,  $\sigma(t) = \sigma_0 \cos(\omega t)$ , with  $\omega$  the pulsation of the system, the response of the Maxwell material is given by the transfer function  $H_m = \frac{\epsilon}{\sigma}$ . Using equation

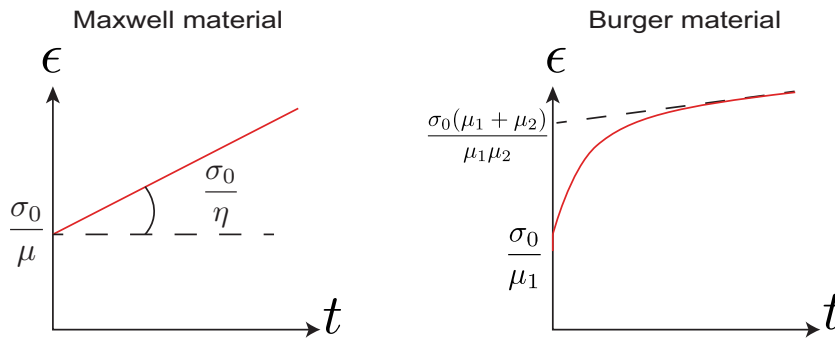


Figure 3.40 – Deformation of Maxwell and Burger materials to a stress  $\sigma_0$  suddenly applied at  $t = 0$ .

(3.24), the amplitude and phase of the resulting deformation are:

$$|H_m| = \sqrt{\frac{1}{\mu^2} + \frac{1}{\eta^2 \omega^2}} \quad (3.25)$$

$$\Phi_m = \arctan\left(\frac{\mu}{\eta \omega}\right) \quad (3.26)$$

Figure 3.41 shows the deformation (bottom part, blue curve) of a Maxwell body to an annual periodic load (top part), with parameters  $\eta = 5.10^{17} Pa.s$ ,  $\mu = 100 GPa$ . Compared to the elastic deformation (bottom part, black curve), the Maxwell system has a delayed response in time ( $\sim 60$  days) and is amplified.

For a viscosity of order  $3.10^{18} Pa.s$  and realistic shear modulus values, the relaxation time is larger than a year, i.e. the observational time, and the system will respond elastically.

### Kelvin-Voigt rheology

The Kelvin-Voigt model combines a spring and a dash-pot in parallel (figure 3.39). When a stress  $\sigma_0$  is applied to this system at  $t = 0$ , the elastic response of the spring is delayed by the dash-pot's viscous response. The stress in the system is the sum of the elastic and viscous stresses, i.e.  $\sigma = \sigma_{spring} + \sigma_{dashpot} = \mu \epsilon + \eta \dot{\epsilon}$ .

### Burger rheology

We describe another type of rheology, the Burger material, commonly used in postseismic studies, which is the serial association of a Maxwell and a Kelvin-Voigt elements (figure

### 3.5. Seasonal variations and implications for the Earth mechanical properties

3.39). The stress-strain relation is therefore controlled by two shear modulus  $\mu_1, \mu_2$  and two viscosities  $\eta_1, \eta_2$ . The constitutive equation is then:

$$\eta_2 \dot{\epsilon} + \mu_2 \dot{\epsilon} = \frac{\eta_2}{\mu_1} \dot{\sigma} + \left( \frac{\eta_2}{\eta_1} + \frac{\mu_2}{\mu_1} + 1 \right) \dot{\sigma} + \frac{\eta_2}{\mu_1} \sigma \quad (3.27)$$

If a stress  $\sigma_0$  is applied to a Burger body at  $t = 0$ , the system will instantaneously exhibit an elastic behaviour with a strain of  $\frac{\sigma_0}{\mu_1}$ , followed by transient creep on a short time scale related to  $(\eta_2, \mu_2)$  and a viscous behaviour over a longer time scale  $(\eta_1, \mu_1)$ , as shown on figure 3.40. For  $\eta_2 \rightarrow \infty$ , the Burger body is equivalent to a Maxwell material with a viscosity of  $\eta_1$ . For  $\eta_1, \eta_2 \rightarrow \infty$ , the response is equivalent to an elastic one. This rheology is commonly used to model the upper crust or the upper mantle postseismic response (Ryder et al., 2011, Pollitz & Thatcher, 2010, Pollitz, 2005, Chandrasekhar et al., 2009, Pollitz et al., 2006, Trubienko et al., 2013) .

For a periodic load,  $\sigma(t) = \sigma_0 \cos(\omega t)$ , with  $\omega$  the pulsation of the system, the Burger material will deform with an amplitude and phase derived from the transfer function  $H_b$  as follows:

$$H_b = \frac{\frac{\eta_2}{\mu_1} - \frac{\eta_2 \omega^2}{\mu_1} + \left( \frac{\eta_2}{\eta_1} + \frac{\mu_2}{\mu_1} + 1 \right) i \omega}{i \mu_2 \omega - \eta_2 \omega^2} \quad (3.28)$$

Figure 3.41 shows the deformation (bottom part, green curve) of a Burger body to an annual periodic load (top part), with parameters  $\eta_1 = 1.10^{20}$  Pa.s,  $\eta_2 = 5.10^{17}$  Pa.s,  $\mu_1 = 100$  GPa,  $\mu_2 = \mu_1$ . Compared to the elastic deformation (bottom part, black curve), the Burger system has a delayed amplified response, with a different phase and amplitude than the Maxwell model.

Using phase and amplitude differences between different rheological models could be useful. For example, several studies of the postseismic response of the Earth to the 2004 Sumatra-Andaman earthquake, proposed various Burger models to explain GPS and GRACE observations. The seasonal variations in the region, mostly in phase with the load derive from GRACE could provide a lower bound to the transient viscosity of such models. Figure 3.42 shows the phase shift in days between a periodic annual load and the deformation of a viscoelastic Burger half-space with long term viscosity  $\eta_1$  and transient viscosity  $\eta_2$ . Best fitting models of several studies are indicated. If seasonal deformation are in phase, say within 30 days, with the load, in this very simple model, transient viscosity cannot be lower than  $1.10^{18}$  Pa.s.

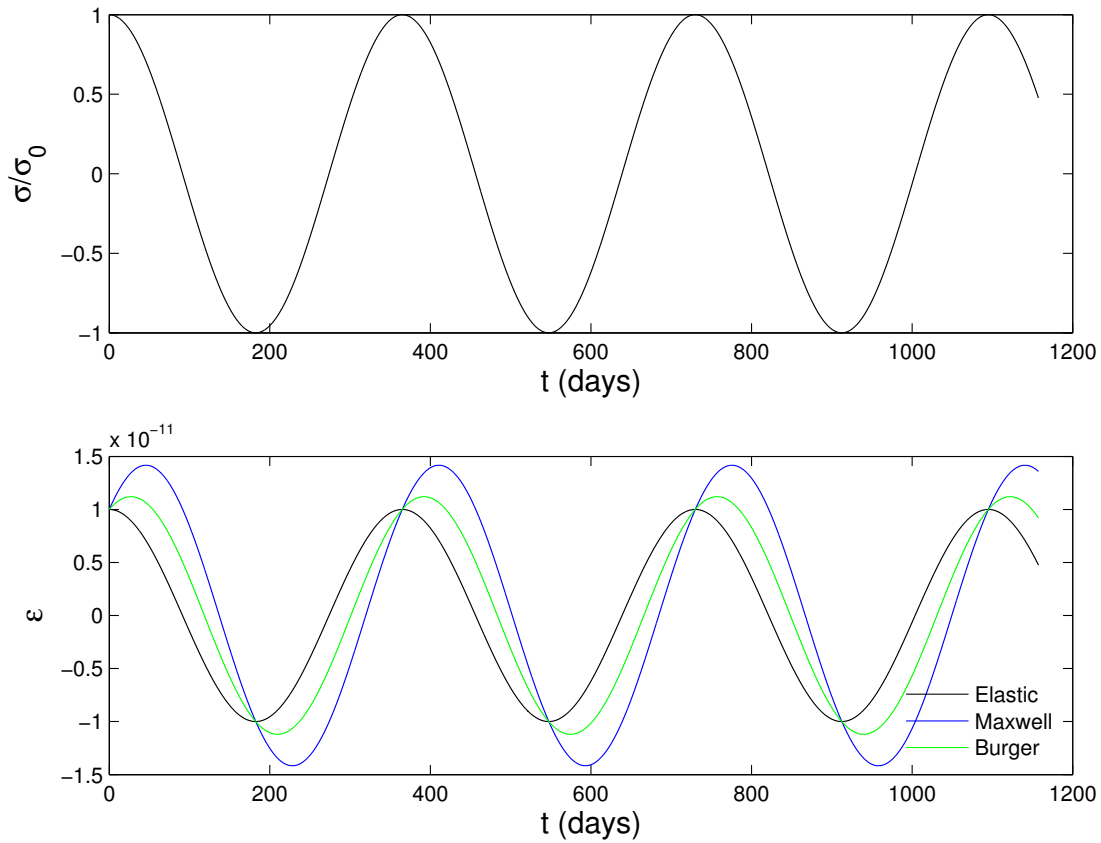


Figure 3.41 – Deformation of elastic, Maxwell ( $\eta = 5.10^{17}$  Pa.s,  $\mu = 100$  GPa) and Burger ( $\eta_1 = 1.10^{20}$  Pa.s,  $\eta_2 = 5.10^{17}$  Pa.s,  $\mu_1 = 100$  GPa,  $\mu_2 = \mu_1$ ) systems induced by a sinusoidal stress.

### Generalization to appropriate stress tensor

Before continuing, we have to consider the appropriate tensor extensions of the simple spring and dash-pot models. Indeed, models are not only subjected to shear but also to compressional stress.

For an elastic isotropic solid, the constitutive equation becomes:

$$\sigma_{ij} = \lambda_e \epsilon_{kk} \delta_{ij} + 2\mu_e \epsilon_{ij} \quad (3.29)$$

with  $\delta_{ij}$  the Kronecker symbol.

For a Newtonian fluid, we have:

$$\sigma_{ij} = \frac{1}{3} \sigma_{kk} \delta_{ij} + 2\eta \dot{\epsilon}_{ij} \quad (3.30)$$

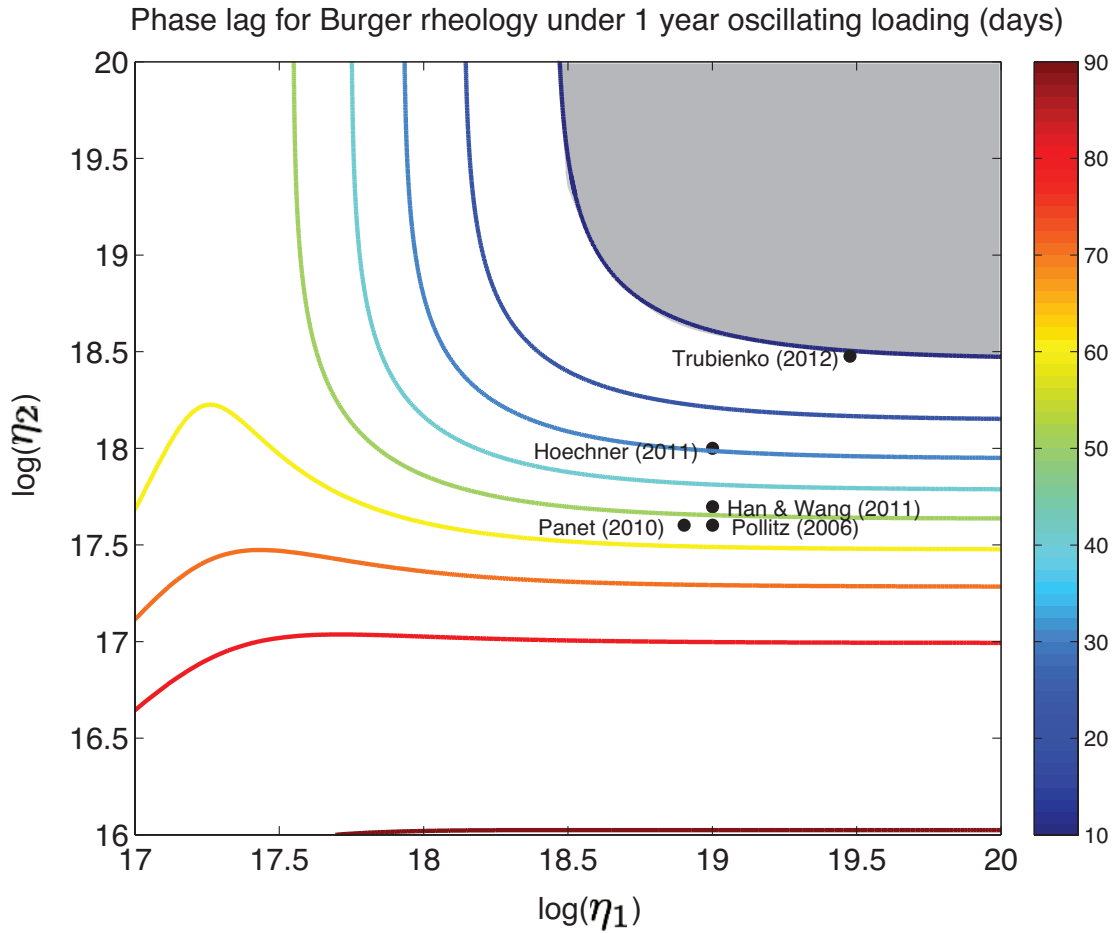


Figure 3.42 – Phase shift in days between a periodic annual load and the deformation of a viscoelastic Burger half-space with long term viscosity  $\eta_1$  and transient viscosity  $\eta_2$ . Best fitting models of several studies are indicated.

Then, for a Maxwell material for instance, by differentiating Hooke's law with respect to time, we have the governing equation:

$$\dot{\sigma}_{ij} + \frac{\mu_e}{\eta} (\sigma_{ij} - \frac{\sigma_{kk}}{3} \delta_{ij}) = 2\mu_e \dot{\epsilon}_{ij} + \lambda_e \dot{\epsilon}_{kk} \delta_{ij} \quad (3.31)$$

### Effect of a Maxwell rheology in the asthenosphere on seasonal deformation

With this working frame, we now test the effect of a viscoelastic Maxwell rheology in the asthenosphere. We compute the ratios Green's functions for horizontal and vertical surface displacements associated to the deformation of various viscoelastic models including Maxwell rheologies to the spherical non-rotating elastic and isotropic model for Earth under unit sea-

### Chapter 3. Global seasonal deformation

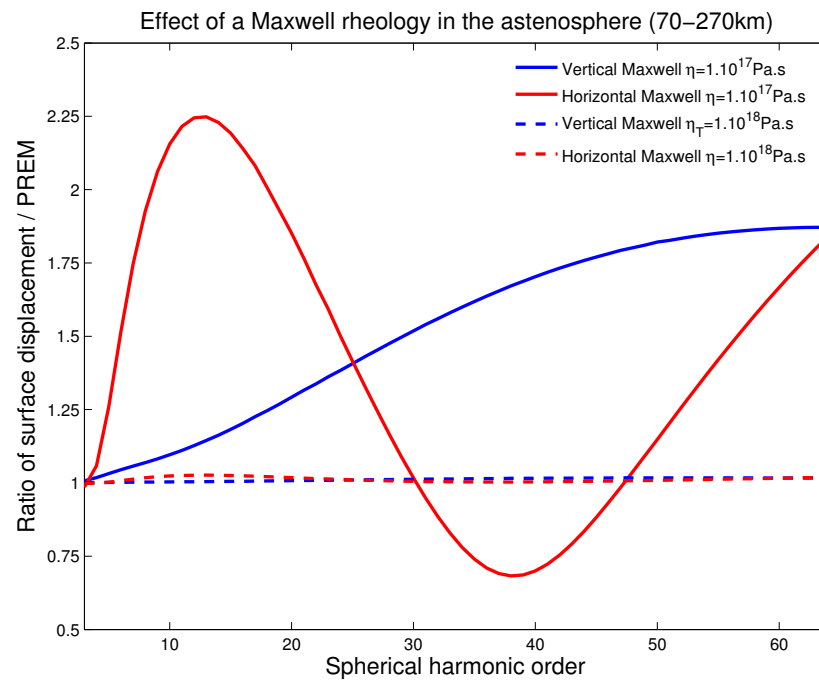
---

sonal loads. First, Figure 3.43 shows (a) the ratio of the Green's functions for surface horizontal (red), and vertical (blue) displacements in response to a seasonal unit load as a function of the spherical harmonic number  $n$ , or the wavelength  $\lambda$  of the load defined as  $\lambda = \frac{2\pi R}{n}$ , with  $R$  the radius of the Earth and (b) the phase lag in days between models. Of course, a viscosity as low as  $1.10^{17} Pa.s$  for a Maxwell rheology in the asthenosphere is unrealistic but, Figure 3.43 emphasizes that, for a 200 km thick asthenosphere between 70 and 270 km, Maxwell rheologies higher than  $1.10^{18} Pa.s$  would have no effect on the amplitude of seasonal ground deformation whereas a value of  $1.10^{17} Pa.s$  would double the amplitude GRACE loading wavelengths. Predicted displacement would also be out of phase by as much as 90 days.

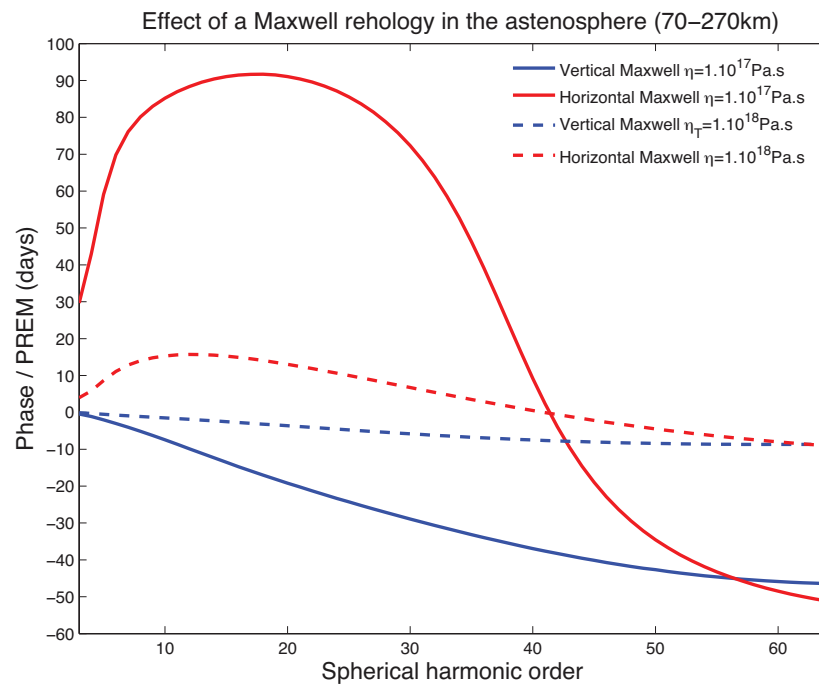
Figure 3.44 shows the influence of the thickness of a  $1.10^{17} Pa.s$  Maxwell asthenosphere on seasonal deformation. For a 100 km thick layer, vertical and horizontal displacements will have amplitudes comparable to a purely elastic model. However the phase shift between elastic and a  $1.10^{17} Pa.s$  Maxwell body between 70 and 170 km would still be observable. For layers thinner than 20km, the difference between elastic and viscoelastic models would not be measurable.

Finally, we test the influence of the elastic thickness overlaying a 200 km thick Maxwell asthenosphere with a viscosity of  $1.10^{17} Pa.s$ . Figure 3.45 shows that for thin elastic thicknesses, as low as 20 km, differences between elastic and viscoelastic models will affect much lower loading wavelengths for the horizontal components, and be similar for the vertical component. In addition, the horizontal component will be amplified for all spherical harmonic orders, which is not the case for thicker elastic thicknesses.

### 3.5. Seasonal variations and implications for the Earth mechanical properties

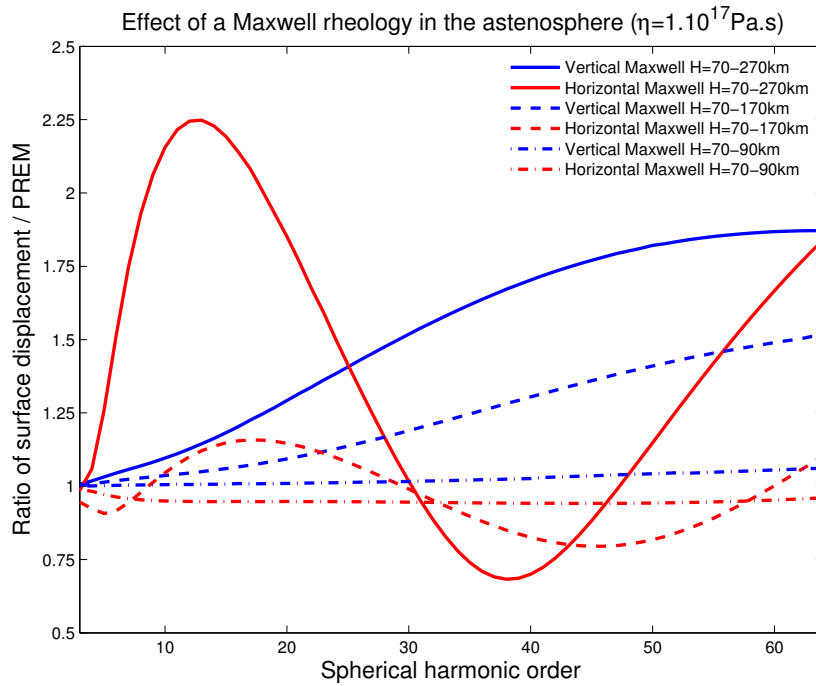


(a) Horizontal and Vertical displacements ratios

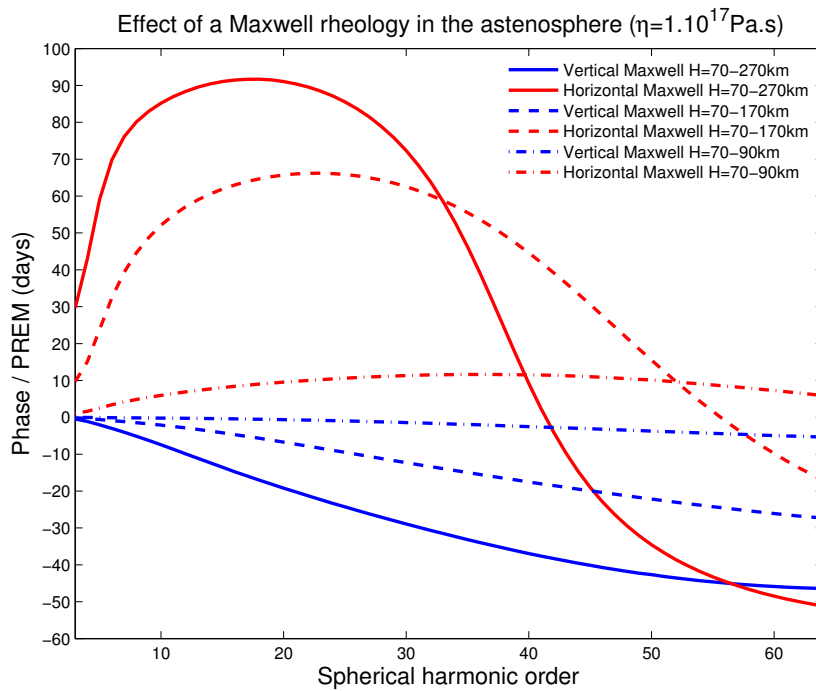


(b) Horizontal and vertical time lags

Figure 3.43 – (a) Ratio of horizontal and vertical surface displacements induced by a unit annual loading and (b) time difference in days for models with a Maxwell rheology with different viscosities in the asthenosphere (70-270km) to PREM.



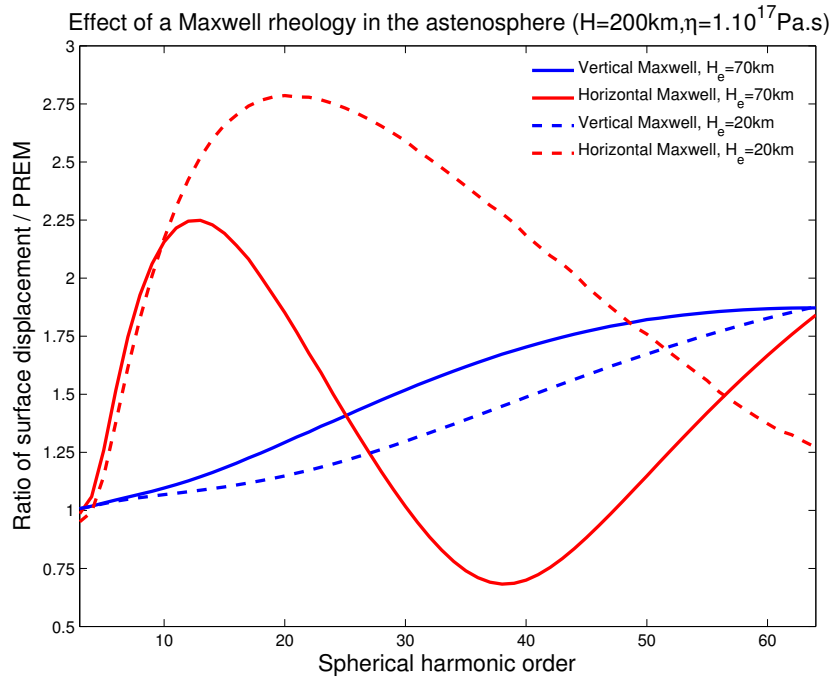
(a) Horizontal and Vertical displacements ratios



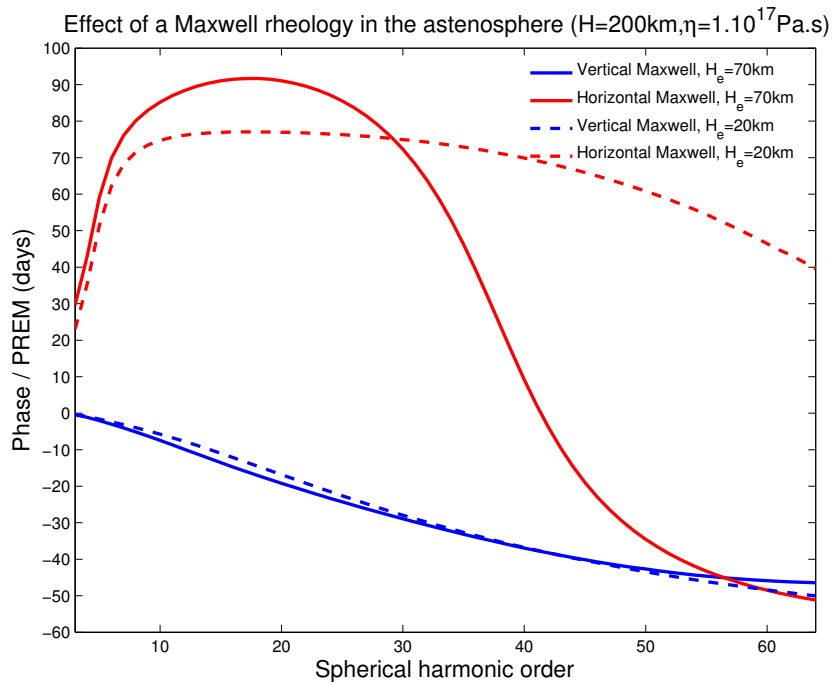
(b) Horizontal and vertical time lags

Figure 3.44 – (a) Ratio of horizontal and vertical surface displacements induced by a unit annual loading and (b) time difference in days for models with a Maxwell rheology for a  $1.10^{17} Pa.s$  viscosity and various asthenospheric thicknesses to PREM.

### 3.5. Seasonal variations and implications for the Earth mechanical properties



(a) Horizontal and Vertical displacements ratios



(b) Horizontal and vertical time lags

Figure 3.45 – (a) Ratio of horizontal and vertical surface displacements induced by a unit annual loading and (b) time difference in days for models with a Maxwell rheology for a  $1.10^{17}\text{Pa.s}$  located in a thin shallow channel to PREM.

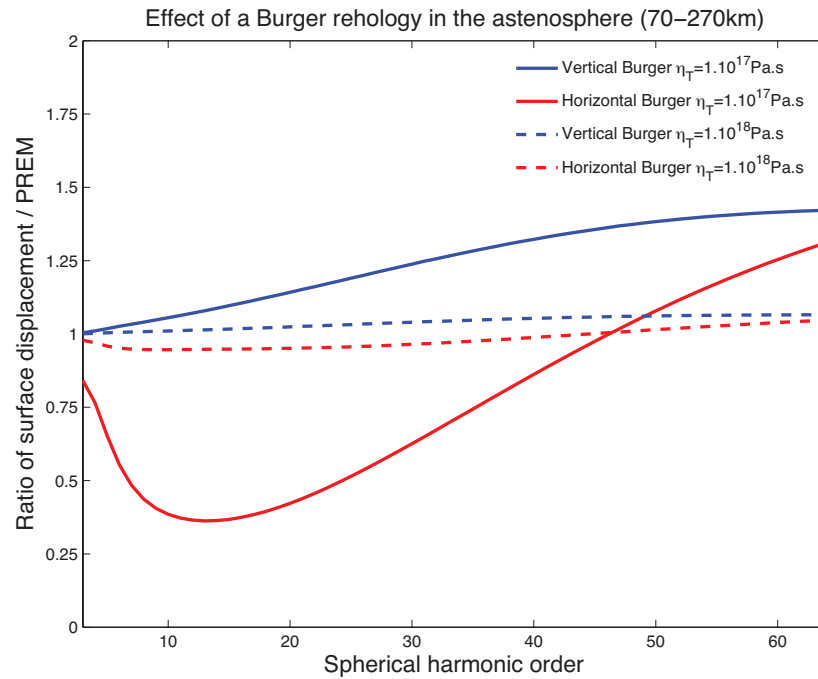
#### Effect of a Burger rheology in the asthenosphere on seasonal deformation

We now focus on the effect of a Burger rheology in the asthenosphere with an annual loading function. Figure 3.46 shows the ratio of horizontal and vertical surface displacements and phase difference for models with a Burger rheology in the asthenosphere (70-270km) relative to PREM. A  $1.10^{17} Pa.s$  transient viscosity of a Burger rheology in the asthenosphere, with transient and long term shear modulus equal, will divide the amplitude of horizontal displacements by two for harmonic orders affected by GRACE and amplifies the vertical signal. In addition, horizontal displacements would be in advance compare to the elastic response by  $\sim 30$  days while vertical displacements should remain in phase with the elastic model. This is unexpected and occurs because the amplitude of the signal decreases significantly when using this rheology compared to the elastic model. Effects would be much attenuated for a  $1.10^{18} Pa.s$  transient viscosity.

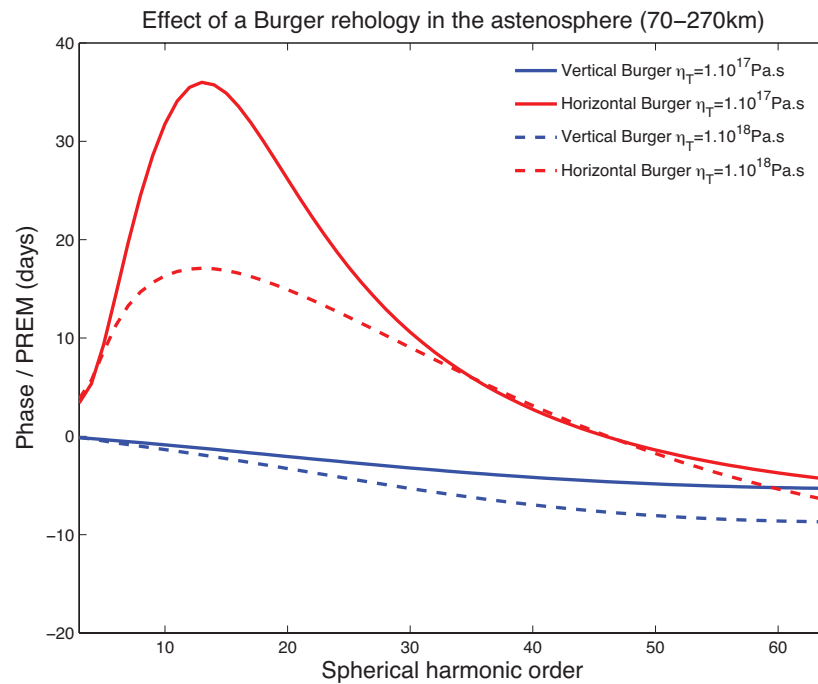
Figure 3.47 shows the influence of the thickness of an asthenosphere with a Burger rheology. Note that, a 100 km thick Burger asthenosphere with a transient viscosity  $1.10^{17} Pa.s$  is similar to a 200 km layer with a transient viscosity  $1.10^{18} Pa.s$ . However, even though there would be a trade off between models, seasonal ground deformation may provide a lower bound on transient viscosities used in postseismic relaxation models.

Finally, Figure 3.48 shows the influence of the elastic thickness when using a Burger rheology for the asthenosphere, with a transient viscosity of  $1.10^{17} Pa.s$ . Displacements and phase would evolve similarly for a thin or a thick elastic thicknesses with the wavelength of the load. However, thinner elastic thicknesses would affect much lower loading wavelengths.

### 3.5. Seasonal variations and implications for the Earth mechanical properties

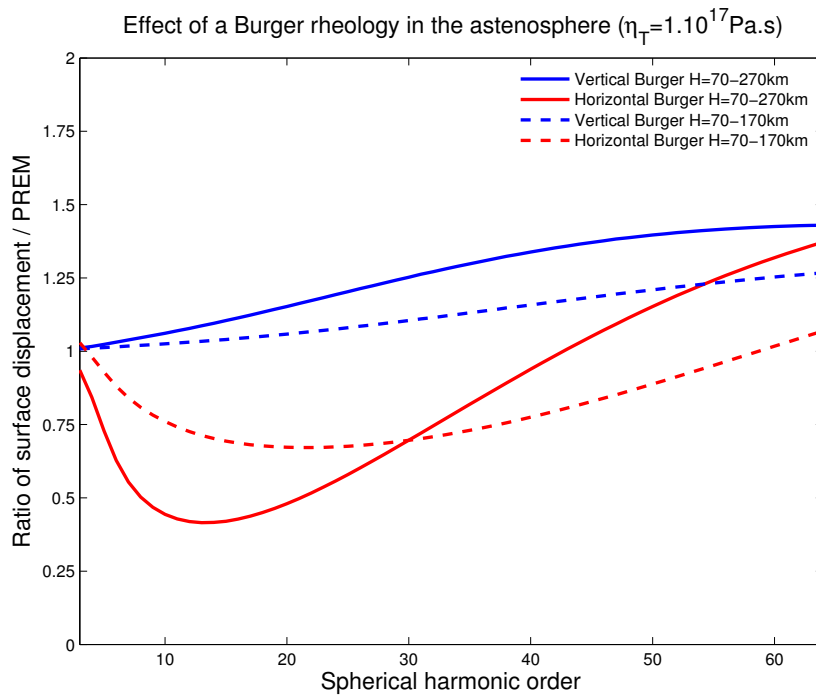


(a) Horizontal and Vertical displacements ratios

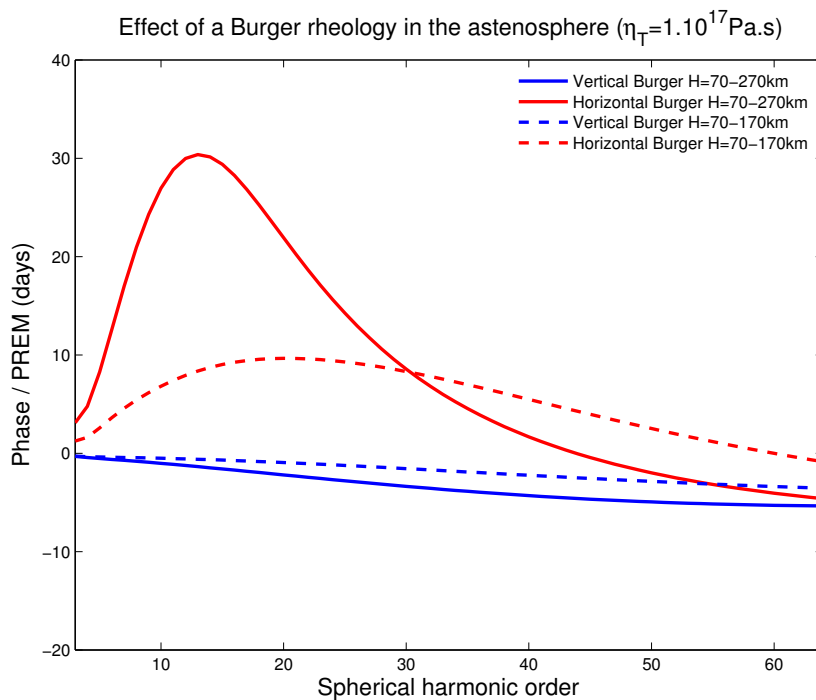


(b) Horizontal and vertical time lags

Figure 3.46 – (a) Ratio of horizontal and vertical surface displacements induced by a unit annual loading and (b) time difference in days for models with a Burger rheology in the asthenosphere (70-270km) to PREM.



(a) Horizontal and Vertical displacements ratios



(b) Horizontal and vertical time lags

Figure 3.47 – (a) Ratio of horizontal and vertical surface displacements induced by a unit annual loading and (b) time difference in days for models with a Burger rheology for a  $1.10^{17} Pa.s$  viscosity and various astenospheric thicknesses to PREM.

### 3.5. Seasonal variations and implications for the Earth mechanical properties

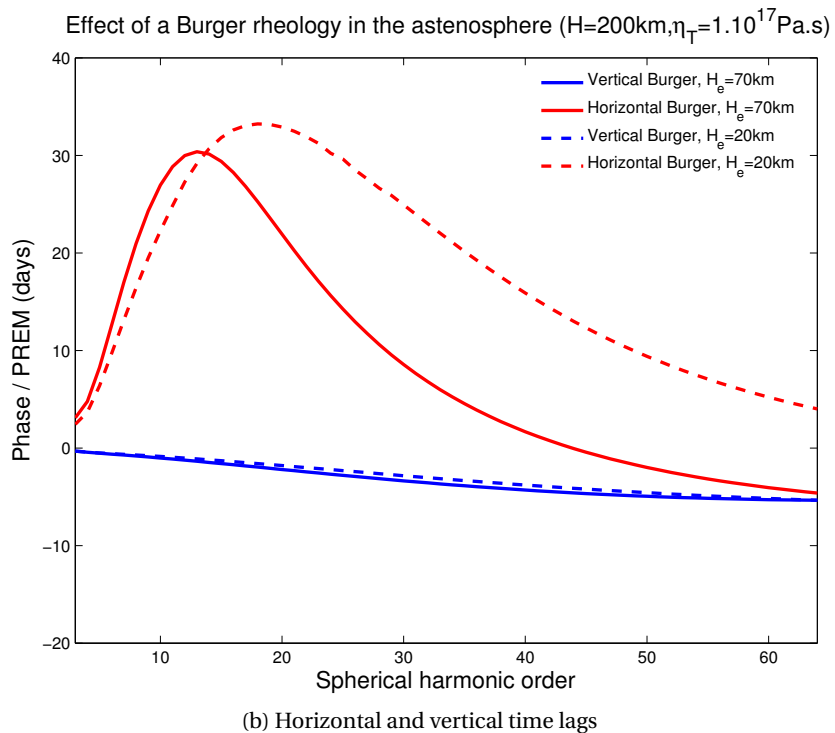
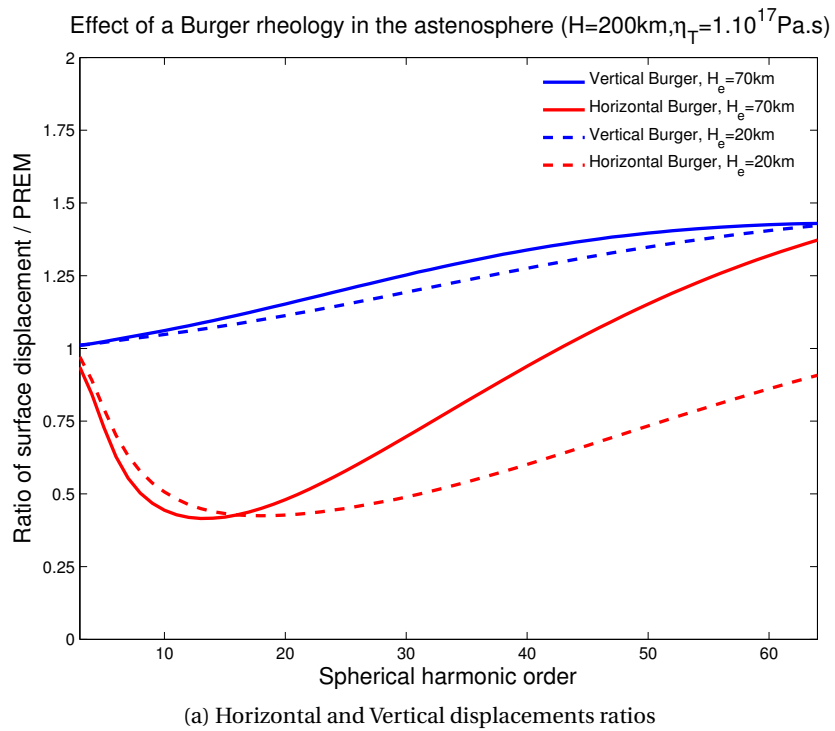


Figure 3.48 – (a) Ratio of horizontal and vertical surface displacements induced by a unit annual loading and (b) time difference in days for models with a Burger rheology for a  $1.10^{17}\text{Pa.s}$  viscosity and various elastic thicknesses to PREM.

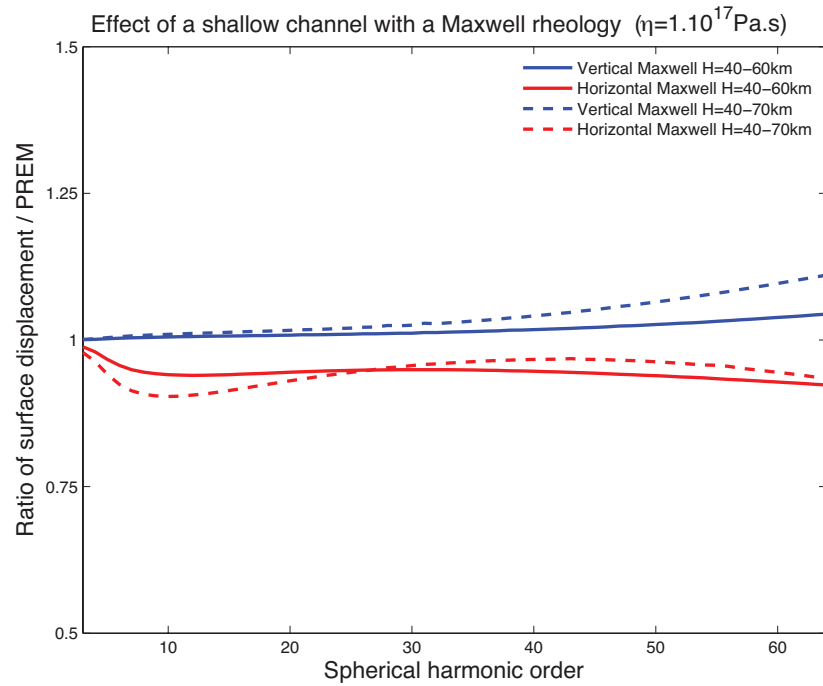
#### Effect of a shallow low viscosity channel on seasonal deformation

In the *Chapter 2*, we focused on the Himalayan region. In this region, an interesting and opened question, that has been debated over the past decades, is the viscoelastic structure underneath the Tibetan Plateau and especially the low viscosity shallow channel under the Plateau hypothesis to explain its topography (Zhao & Morgan, 1987, Beaumont et al., 2001, 2004, Jamieson et al., 2004). This question is usually addressed using historic changes in lake levels resulting in significant elastic stress fields and producing viscous flow at depth, such as for Lake Meade, Lake Bonneville and Lahontan, Lake Silling Co (Bills et al., 2007, Bills & May, 1987, Doin et al., 2015). The fluctuations in volume and surface area of closed paleo-lakes are recorded by shorelines left behind as the lake level dropped. As a result of changes in lake level, the crust and upper mantle visco-elastic response to hydrological loading and unloading deforms the paleo-shorelines. By measuring this deformation and estimating the lake history, it is possible to constrain local visco-elastic Earth models. Several other studies, based on high-resolution seismic data (Brown et al., 1996, Zhao et al., 2001) or post-seismic relaxation studies (Hilley et al., 2005, DeVries & Meade, 2013), have been proposed to investigate whether or not the hypothesis of a low viscosity channel is a possible explanation to the Tibetan Plateau topography and formation of the high Himalaya.

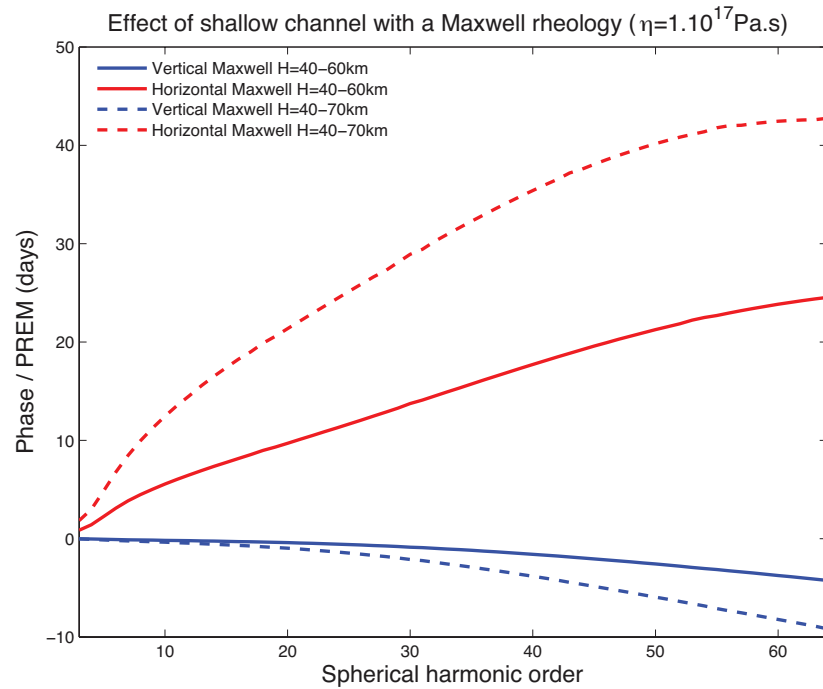
The Earth response to seasonal variations of hydrological surface loading, recorded in the last decade by geodetic techniques may also play a role in the understanding of subsurface rheology. Figure 3.49 shows the ratio of amplitudes of vertical and horizontal displacements of a viscoelastic model with a thin low viscosity  $1.10^{17} Pa.s$  channel of varying thickness to our elastic model (a) and the phase shift between models in days (b). Even though a shallow low viscosity channel will have very comparable amplitudes to a purely elastic model, the horizontal phase shift for short wavelengths loads will be significant. Therefore, looking at annual fluctuations of lake water level or rivers, at a regional scale, and at the seasonal geodetic displacements recorded by close by GPS stations, or even by InSAR as suggested by Doin et al. (2015), may provide useful insights of the shallow local viscoelastic structure.

Up to this point, we have described the vertical and horizontal displacements ratio and

### 3.5. Seasonal variations and implications for the Earth mechanical properties



(a) Horizontal and Vertical displacements ratios



(b) Horizontal and vertical time lags

Figure 3.49 – (a) Ratio of horizontal and vertical surface displacements induced by a unit annual loading and (b) time difference in days for models with a Maxwell rheology for a  $1.10^{17}$  Pa.s viscosity and various elastic thicknesses to PREM.

phase shift of viscoelastic models including Maxwell or Burger layers compared to a purely elastic model. We conclude that, while seasonal deformation may be used place constraints on the viscoelastic Earth structure at depth shallower than 300 km depth, such structures would not solve the original horizontal misfit of the purely elastic model. Only unrealistic Maxwell rheologies in the asthenosphere would amplify the horizontal signal. We thus focus on deeper rheologies, describe and test the hypothesis of partial mantle volume changes due to mineral transformations in the transition zone in the next section.

### 3.5.3 Mantle phase transitions

To explain the discrepancy between predictions and observations, unlikely due to the asthenosphere rheology, one can also invoke the validity of the PREM elastic Earth model in the mantle. Indeed, considering the wavelength of seasonal loading, the Earth's mantle might play a role in the surface deformation associated with seasonal hydrology.

As a matter of fact, we know from post-glacial rebound studies that the rheology of the mantle is not simply elastic but viscoelastic. In addition, the Earth's mantle mineral aggregates undergo various phase changes that are induced by the increase of pressure with depth. The current view of the radial seismic structure of the mantle consists of smooth velocity variations, most likely caused by the pyroxene-garnet-perovskite phase transitions, punctuated by discontinuities at 410, 520 and 660 km, caused by the sharp olivine-wadsleyite-ringwoodite-perovskite phase transformations (Bina & Helffrich, 1994, Ringwood, 1970).

Up to now, the response of these mineralogical transformations to small strain induced by surface periodic loading remains unknown. However, in regions with a two-phase equilibrium, i.e. where high and low-pressure phases coexist, we expect even small stress oscillations to disrupt the equilibrium, inducing re-equilibration processes. Because of the reactions kinetics, readjustments are not necessarily instantaneous. Yet, the kinetics of these reactions is not well constrained. Bounds on the characteristic equilibration time have been placed by seismic attenuation studies and global mantle circulation between 7000 s (Krien & Fleitout, 2010, Durand et al., 2012, Resovsky et al., 2005) and  $10^5$  years (Čadek & Fleitout, 2003). Complex-

### 3.5. Seasonal variations and implications for the Earth mechanical properties

ities arise from the possible relaxation of the bulk modulus due to mantle phase transition (Anderson, 1989). A more appropriate description of the elastic properties of materials subject to stress variations over these time scales should account for transient elastic moduli over a characteristic kinetic time or a distribution of characteristic times. Specifically, a distinction should be made between an unrelaxed  $\kappa_\infty$  and a relaxed  $\kappa_0$  bulk modulus defined respectively as:

$$\delta P = \kappa_\infty \frac{\delta \rho}{\rho} \quad (3.32)$$

and,

$$\frac{dP}{dr} = \kappa_0 \frac{d\rho}{\rho dr} \quad (3.33)$$

The two bulk modulus represent changes in material properties linked to the progress of the phase transition (Krien & Fleitout, 2010, Durand et al., 2012, Ricard et al., 2009, Weidner & Li, 2010). Figure 3.50 gives a depth profile of the unrelaxed ( $\kappa_\infty$ ) and relaxed bulk modulus ( $\kappa_0$ ) in the transition zone. Note that some points of the estimated  $\kappa_0$  are larger than  $\kappa_\infty$ . This points have no physical meaning as  $\kappa$  obtained from seismic data is our upper limit frequency and  $\kappa$  can only be more relaxed (outliers are most likely due to inaccuracies in PREM).

Behaviour of the bulk modulus in the Earth under seasonal surface loading has not yet been investigated to our knowledge. The problem has been treated mostly for large forcing periods ( $\sim 10^4$  years) in post-glacial rebound context for example (Christensen, 1985, Tamisiea & Wahr, 2002).

The olivine transitions, with  $\kappa_0 \sim \kappa_\infty/100$ , have finite sharp widths (4 to 10 km) due to the partitioning of iron and magnesium between coexisting phases (Katsura & Ito, 1989, Irifune, 1993). Even if the difference between  $\kappa_0$  and  $\kappa_\infty$  is significant within these layers, they are extremely small compared to the loading wavelength and therefore, will have a negligible effect on surface displacements. The pyroxene-garnet-perovskite transition however, with  $\kappa_0 \sim \kappa_\infty/2$ , tends to have broad two-phase zones that is controlled by the partitioning of aluminium between coexisting phases (Akaogi et al., 2002). Figure 3.51, taken from Ita & Stixrude (1992), shows an example of the difference between sharp olivine transitions, appearing as seismic discontinuities and larger smooth pyroxene transitions, on a Pressure-Temperature diagram obtained from mineral composition of pyrolites.

At an annual time scale, we expect the bulk modulus of the pyroxene-garnet-perovskite

### Chapter 3. Global seasonal deformation

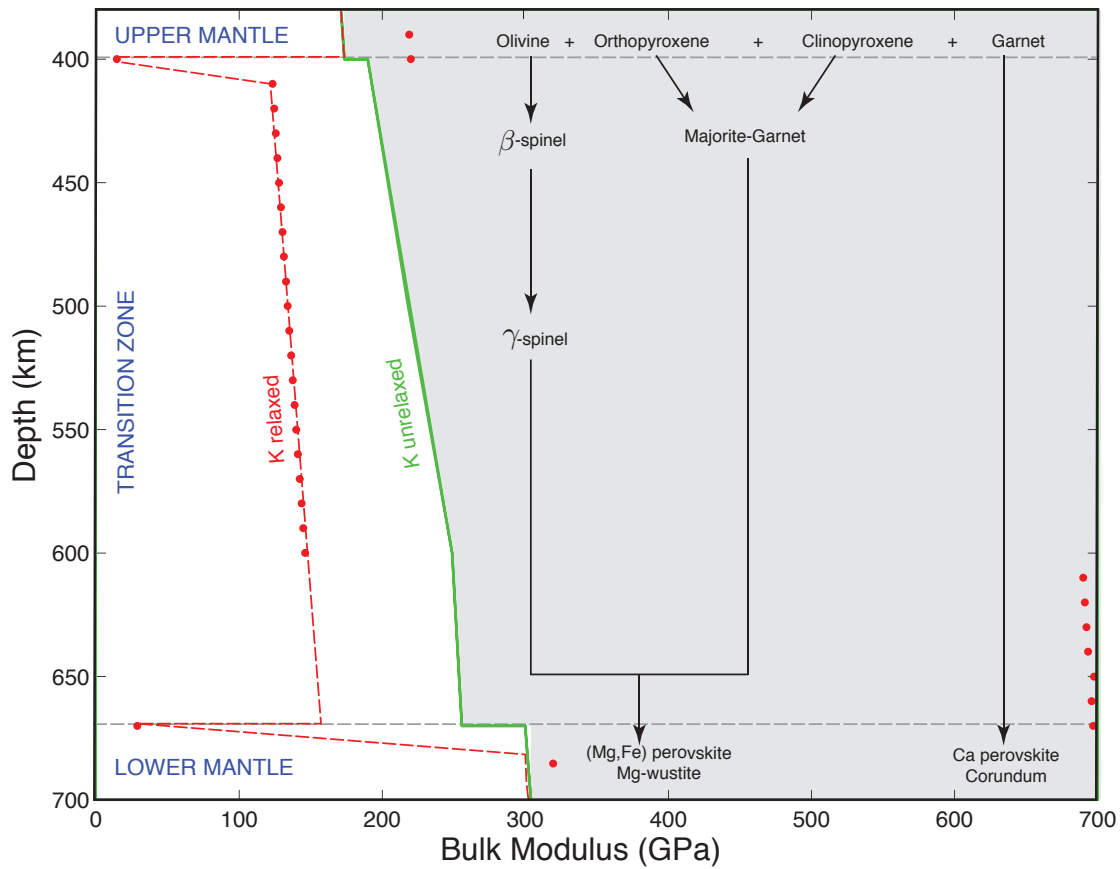


Figure 3.50 – Unrelaxed and relaxed bulk modulus profiles in the mantle transition zone and associated mineral phase transitions.

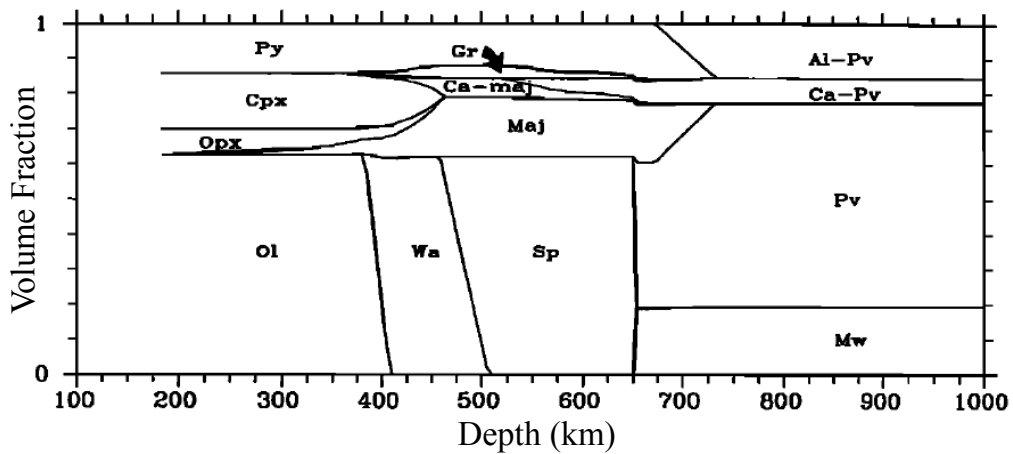


Figure 3.51 – Volume percentage of mineral present pyrolites at a function of depth, from [Ita & Stixrude \(1992\)](#)

### 3.5. Seasonal variations and implications for the Earth mechanical properties

transition to be intermediate between the unrelaxed and the relaxed bulk modulus, depending on the phase transformation kinetics, likely due to aluminum diffusion between the coexisting phase. Note that latent heat and interface controlled kinetic mechanisms are here assumed to be inefficient to retard mantle phase transformation (Fleitout, personal communication).

Here, for simplicity we consider only the broad pyroxene-garnet-perovskite phase transition. The associated bulk modulus between 410 and 660 km is modeled as the association of a purely elastic element with short term bulk modulus  $\kappa_\infty$ , and a Kelvin-Voight element with long-term bulk modulus  $\kappa_0$  and  $\eta_\kappa$  parameter representing the kinetics of the phase transition as a pseudo-viscosity that delays the mineralogical reactions, likely controlled by diffusion of aluminium, but describing any retarding processes. Figure 3.52 shows the association of elementary mechanical elements used to describe the behaviour of our complex bulk modulus. We then derive the stress-strain relation associated with this bulk modulus rheology, similarly to a Burger body.

Figure 3.53 shows amplitudes of vertical and horizontal displacements induced by a unit

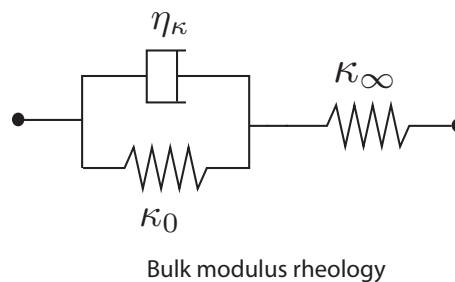
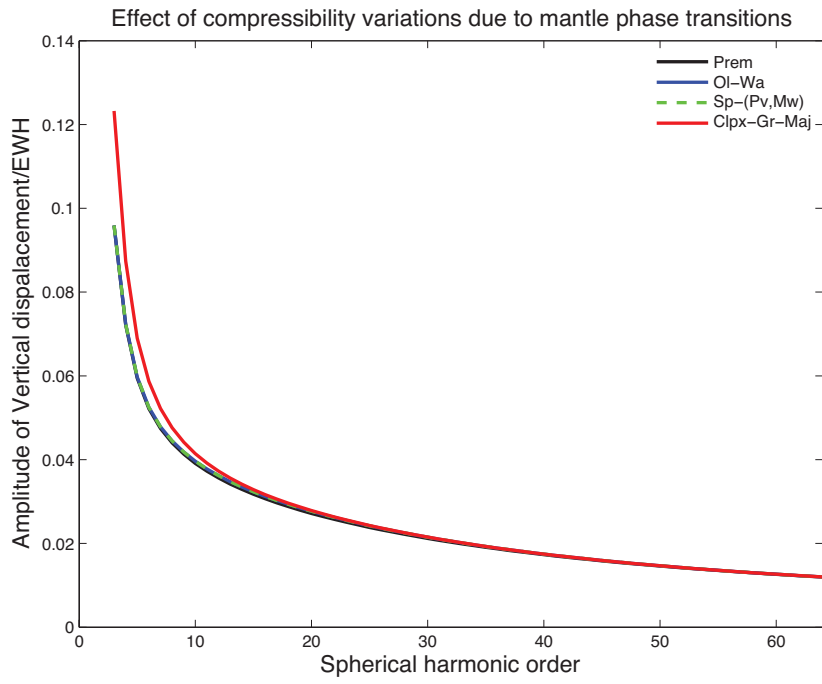
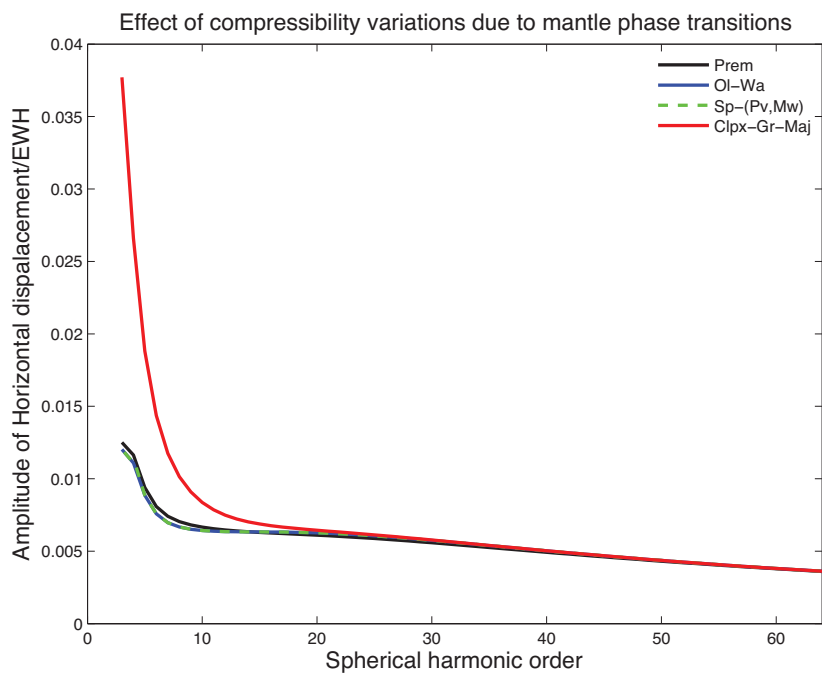


Figure 3.52 – Bulk modulus rheology for variations due to phase mantle transformations.

load as a function of the spherical harmonic order for a purely elastic continental PREM model (black), a model including relaxed bulk modulus for the olivine-wadsleyite (blue), the ringwoodite–perovskite (red) and the pyroxene-garnet-perovskite transformations (dashed green). Sharp phase transitions of the olivine have indeed a negligible effect on amplitudes of surface displacements induced by surface loading. However, the broad transition of pyroxenes, with a fully relaxed bulk modulus, can amplify up to vertical displacements by  $\sim 10\%$  and horizontal displacements by  $\sim 10$  to  $60\%$  for harmonic orders influencing large scale surface loads. Figure 3.54 shows the time lag between a purely elastic model and models with including the broad pyroxene phase transition with various kinetics characteristic times. For



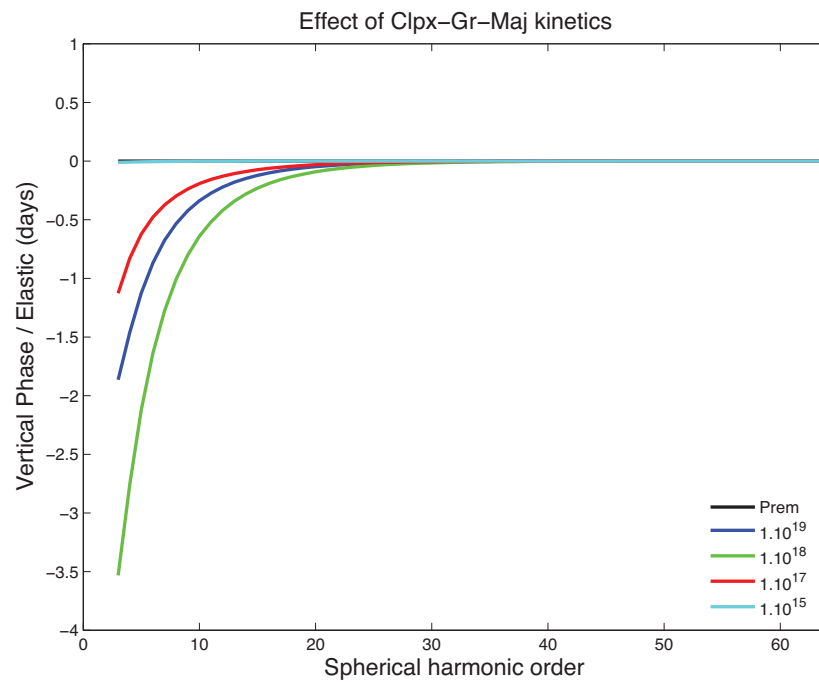
(a) Vertical displacements



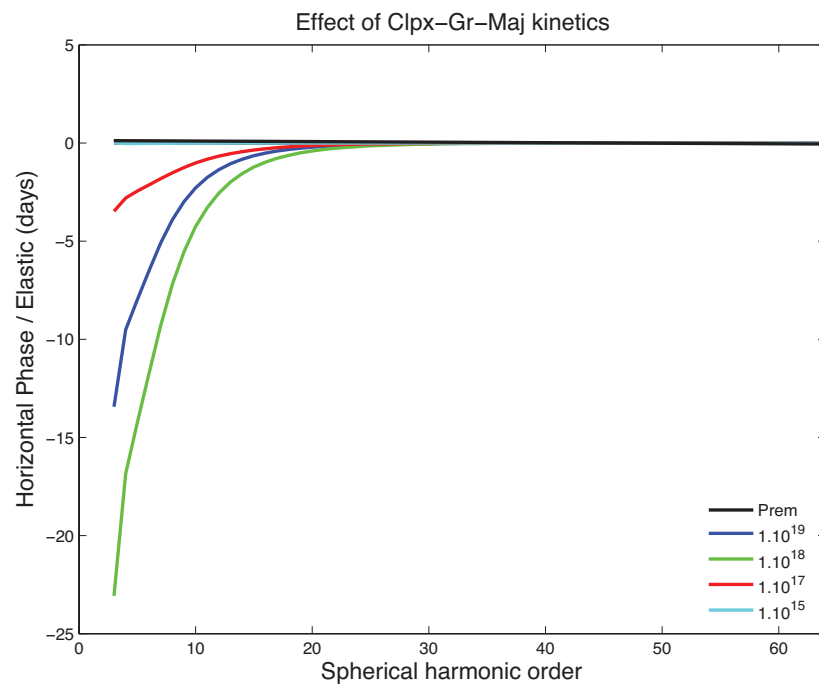
(b) Horizontal displacements

Figure 3.53 – Vertical (a) and horizontal (b) amplitudes of surface displacement as a function of spherical harmonic number, in response to a unit seasonal load for a purely elastic continental PREM model (black), a model including relaxed bulk modulus for the olivine-wadsleyite (blue), the ringwoodite–perovskite (red) and the pyroxene-garnet-majorite transformations (dashed green).

### 3.5. Seasonal variations and implications for the Earth mechanical properties



(a) Vertical time lag



(b) Horizontal time lag

Figure 3.54 – Time lag between a purely elastic continental PREM model and models including the broad pyroxene phase transition with various kinetics characteristic times.

large wavelengths loads, the anelastic model can create time lags up to 20 days from the elastic one for the horizontal components. Vertical time lags remain negligible.

We show here that an Earth structure including fully relaxed bulk modulus values in the mantle transition zone due to volume variations induced by the broad phase transition of pyroxene-garnet-perovskite can amplify considerably horizontal seasonal displacements induced by annual surface loading, while vertical displacements remain similar to those predicted by a purely elastic Earth model. This hypothesis, or at least a partial occurrence of broad mantle phase transitions, appears to be an appropriate candidate to model the missing horizontal amplitude seasonal signal highlighted in the previous section.

Our hypothesis is supported by several recent papers that have used either geodetic observations to retrieve the deformation of the Earth induced by tides using Satellite Laser Ranging (Benjamin et al., 2006), Very Long Baseline Interferometry (Krásná et al., 2013) or Global Positioning System (Yuan et al., 2013, Kang et al., 2015) measurements. Elastic Earth models provide accurate predictions of surface displacements or induced gravity perturbations for periods up to a month but not for longer periods (Benjamin et al., 2006, Krásná et al., 2013). At these longer periods, it is now accepted that the mantle must be considered as viscoelastic: for example, the 2010 IERS conventions (Petit & Luzum, 2010) introduces viscoelasticity through complex, frequency dependent, Love numbers. Both Benjamin et al. (2006), Krásná et al. (2013) however point out that the viscoelastic correction in the conventions is insufficient and proposed new values for the complex degree 2 tidal Love numbers. The degree 2 tidal Love number is mainly sensitive to the mechanical properties of the lower mantle while the load Love numbers of higher degree, which plays a major role in the Earth's response to non-tidal periodic loads, are mainly sensitive to the rheology of the upper mantle.

We constrain the broad pyroxene-garnet-perovskite to occur between 410 and 660 km and run a set of 100 forward models of seasonal surface displacements at the 195 cGPS stations induced by seasonal loading derived from GRACE for two varying parameters. The first one is the bulk modulus ratio  $\kappa_\infty/\kappa_1$ , where  $\kappa_\infty$  is the unrelaxed bulk modulus and  $\kappa_1$  is the bulk modulus for an annual loading function. The second one is the pseudo-viscosity  $\eta_\kappa$ , representing the

### 3.5. Seasonal variations and implications for the Earth mechanical properties

kinetics of the reaction. We then perform a 6 parameters Helmert transform to avoid the geocenter motion and degree-one deformation issue. We focus on the best fitting parameters to match to reduce the  $\chi^2$  of both horizontal and vertical displacements for our subset of 195 cGPS stations. Best fitting models feature a transient annual bulk modulus that divides the one derived from seismic estimates by 1.21 and a kinetics lower than  $10^{17}$ , that allows the reaction to occur partially at an annual time scale at least. A summary of  $\chi^2$  for all models is given in Table 3.3. Table 3.3 suggests that the model allowing for mantle volume variations to

	North	East	Vertical	H & V
Data-Null	9831	12299	9210	10571
Data-Elastic	8887	12015	7752	9636
Data-Elastic transformed	7174	11645	7814	8997
Data-Phase transition & transformed	7045	11512	7801	8762

Table 3.3 –  $\chi^2$  values for each components and all components for all stations of our study.

occur, at least partially, at an annual time scale, improves the seasonal deformation prediction. In fact, over the 195 cGPS sites used in our study, this model reduces  $\chi^2$  values at 153 sites for the north component, 119 for the east component and 41 for the vertical.

Using this model, we plot on Figure 3.55 time series at three cGPS stations, LHAZ, Tibet (a), CHPI, Brazil (b) and GOLD, Ca-USA (c) (see Figure 3.1 for location). Predictions of seasonal positions derived using an elastic PREM based model, the transformed elastic PREM based model and a model including phase transformations and transformed are respectively shown in blue and green, and red. The model including phase transformations predicts more reasonable amplitudes than the transformed elastic model for horizontal seasonal displacements without over-predicting the vertical components. Figure 3.56 shows the spatial distribution of the NRMSD for the transformed elastic model including mantle phase transformation, to be compared to Figure 3.35. The fit to the horizontal components is globally improved, especially for northern displacements.

Although much remains to be done to confirm this hypothesis and refine the model, the bulk modulus of the mantle appears to be an appropriate candidate to explain the missing

### Chapter 3. Global seasonal deformation

---

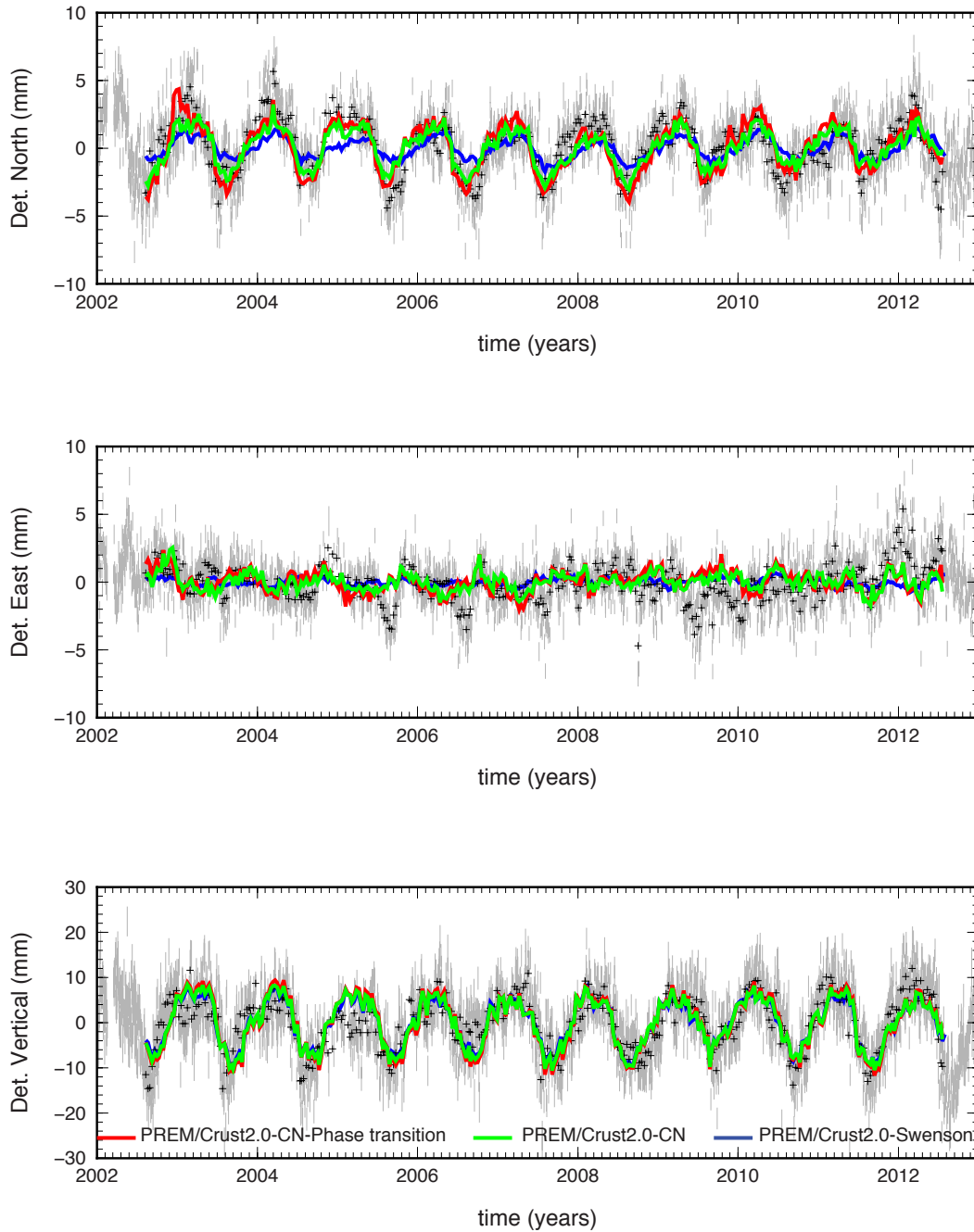
seasonal horizontal amplitude of the signal without perturbing the fit to the vertical. Mantle volume variations induced by phase transitions might thus be visible at an annual time scale.

---

Figure 3.55 (*following page*) – Daily detrended geodetic positions, determined at station (a) LHAZ, (b) CHPI and (c) GOLD GPS stations (see Figure 3.1 for location) with error-bars for  $1-\sigma$  uncertainties (gray symbols). Black crosses are 10-days moving-average of the daily geodetic observations. Blue, green and red line shows respectively predicted displacements induced by seasonal surface hydrology variations using a purely elastic continental PREM, its transformed using a best fitting 6-Helmert transformation to circumvent degree one and geocenter motion discrepancy with GPS positions and a PREM-based model including the mantle relaxed bulk modulus due to the pyroxene-garnet-perovskite, transformed as well.

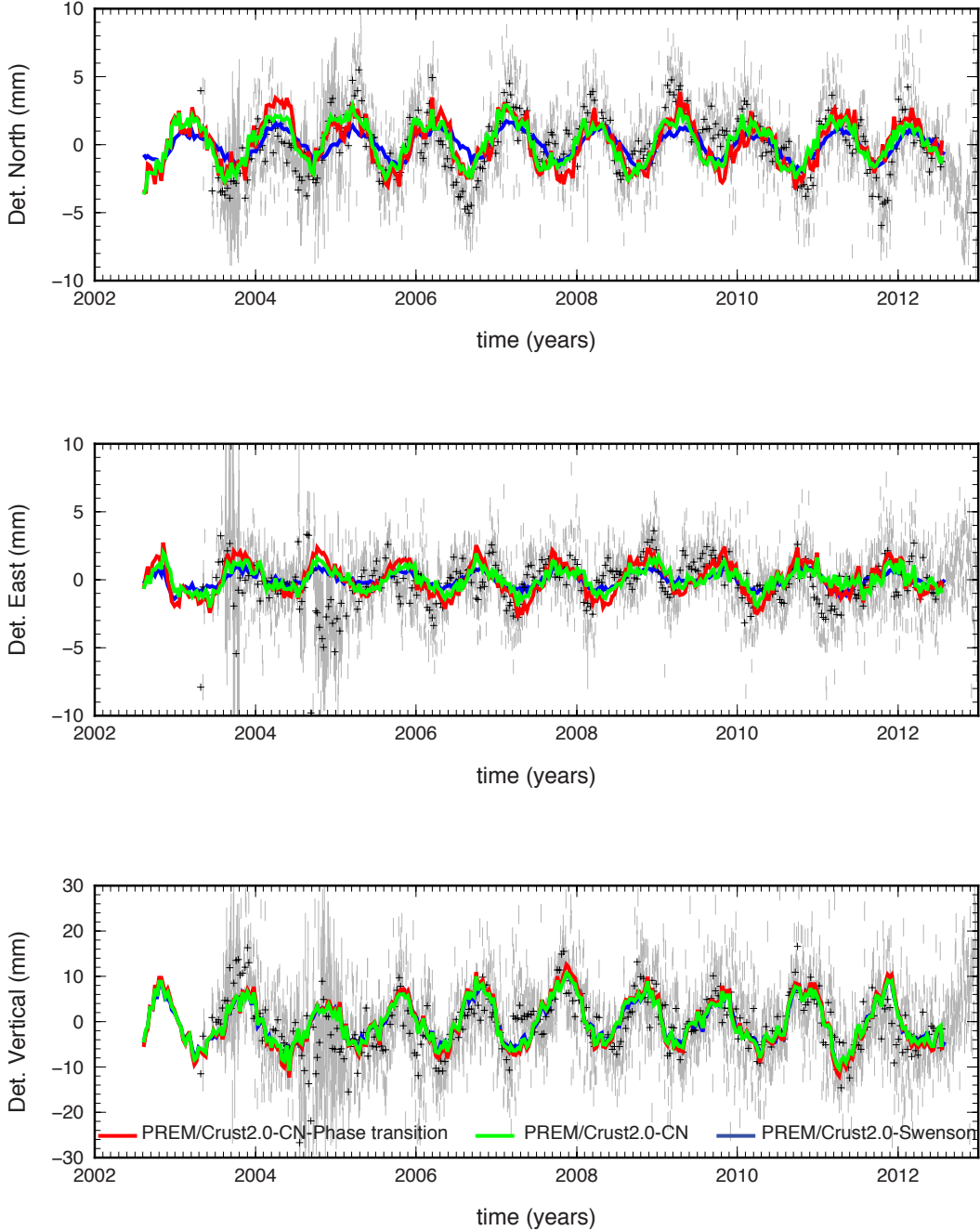
### 3.5. Seasonal variations and implications for the Earth mechanical properties

LHAZ



(a) LHAZ, China

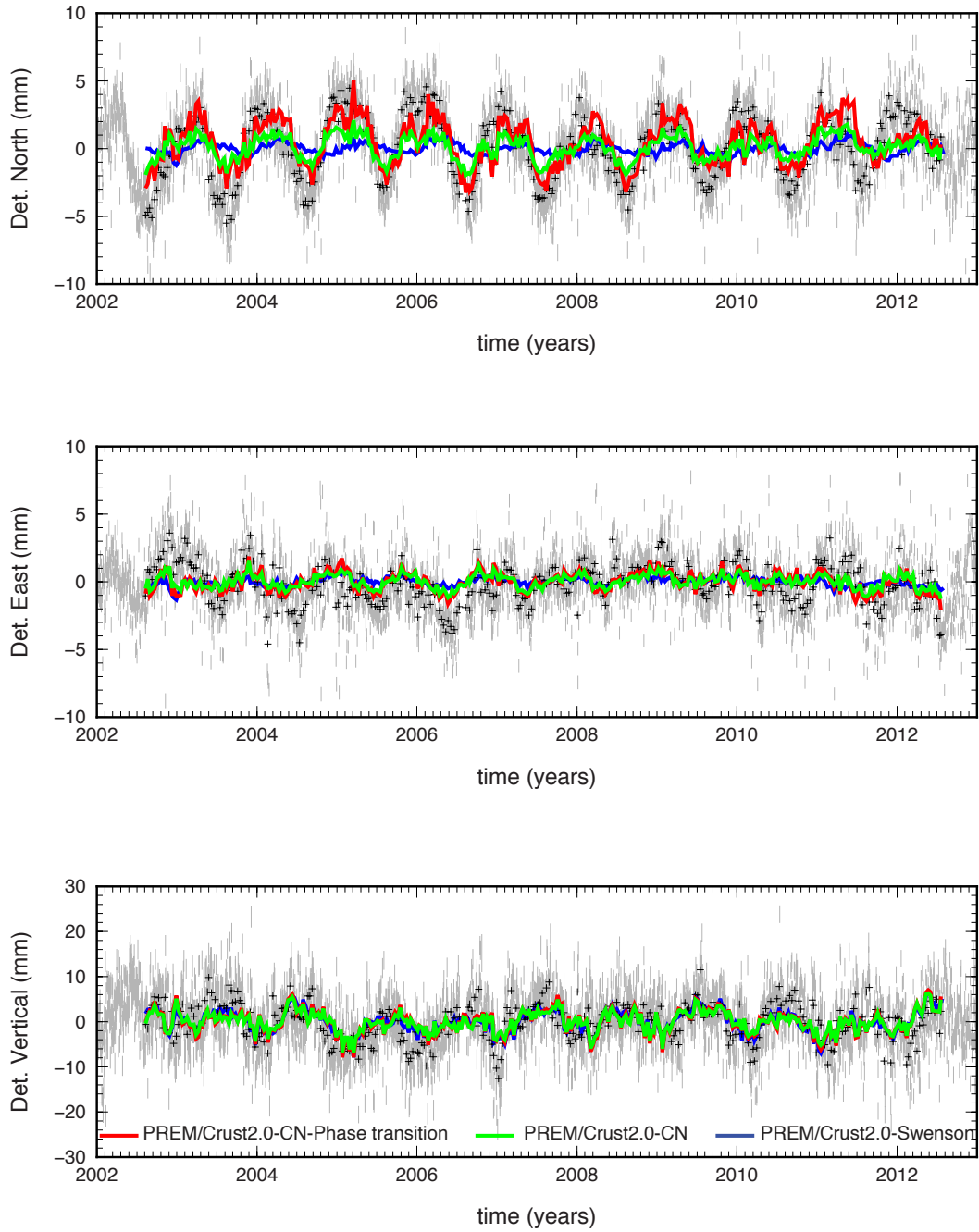
CHPI



(b) CHPI, Brazil

### 3.5. Seasonal variations and implications for the Earth mechanical properties

#### GOLD



(c) GOLD, United States (California)

### Chapter 3. Global seasonal deformation

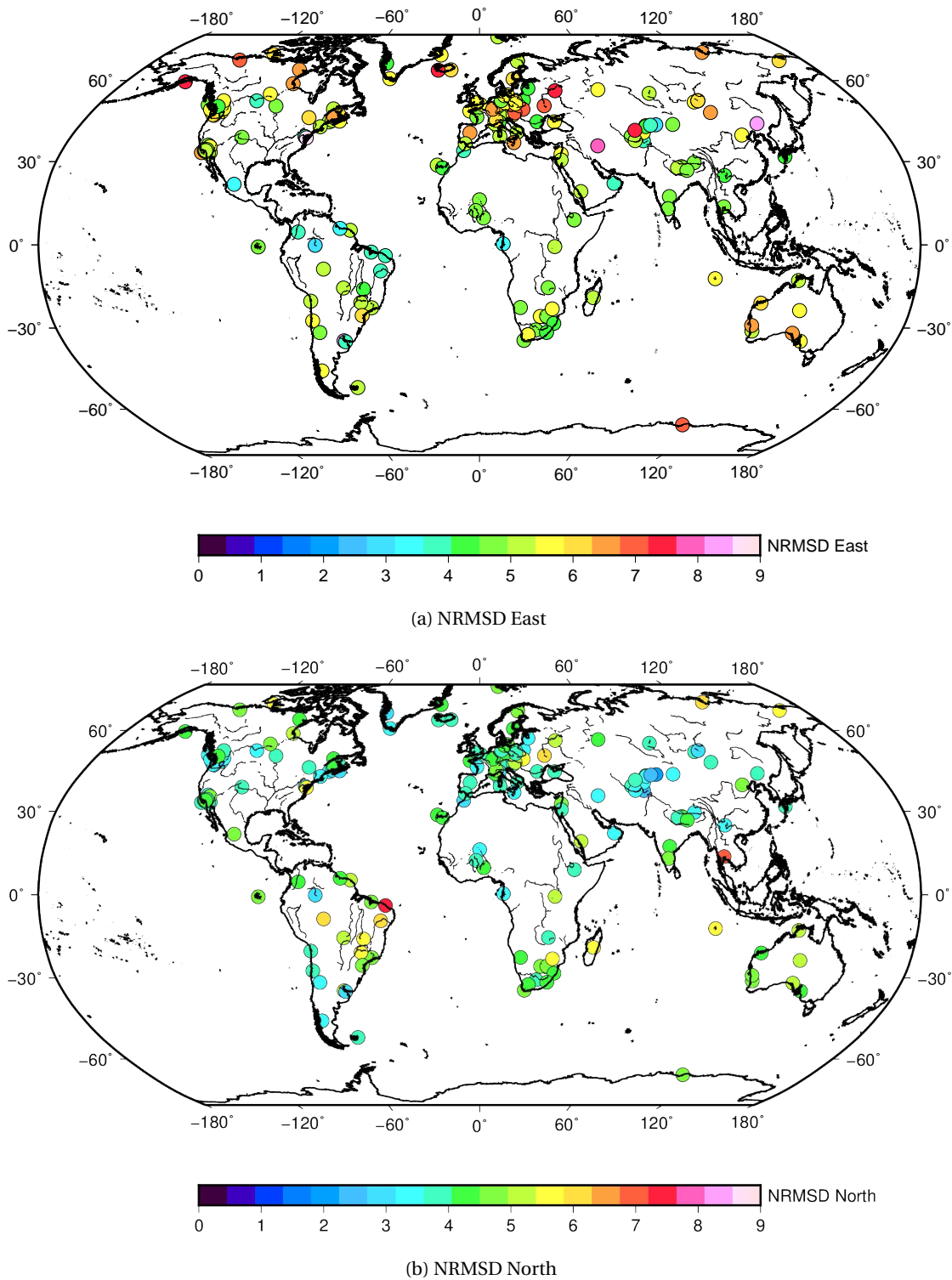
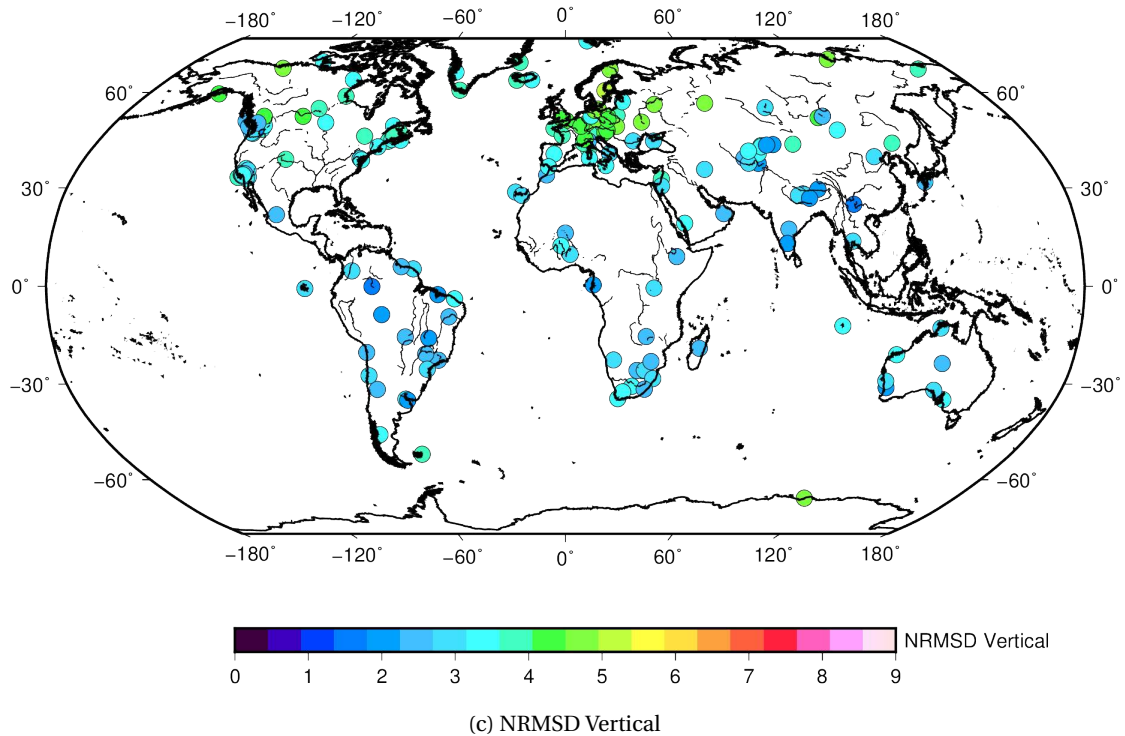


Figure 3.56 – Normalized root-mean-square deviation (NRMSD, see equation 3.3)) by the mean amplitude of the signal between elastic seasonal displacement predictions transformed using the horizontal best-fitting 6 parameters of the Helmert transform and including mantle phase transitions and observations for east (a), north (b) and vertical (c).



### 3.6 Implications and Conclusions

We have implemented first a global elastic model to reproduce horizontal and vertical geodetic displacements induced by seasonal variations of continental water, atmospheric pressure, and oceanic circulation derived from gravity variations recorded by the GRACE satellite mission. We then compared predicted displacements with observations from 195 cGPS stations globally distributed. While the agreement between model and observations is fairly good for the vertical component, it is often quite poor for the horizontal, with significant disagreements both in phase and amplitude.

We reviewed and discuss potential contributors to a missing amplitude in the seasonal signals and concluded that, the referential shift and associated geocenter motion, uncaptured by GRACE is responsible for a large part of the misfit in phase and amplitude of our model to the data. Referential shift and potentially part of the degree one deformation can be modeled as a geometrical transformation and we performed a least square inversion using separately the horizontal and vertical components are they are not affected in the same way by degree one deformation. We showed that the best fitting 6-parameters Helmert transformation to the

horizontal data reduced significantly the  $\chi^2$  values between model and data.

However, because the model is still underpredicting the horizontal displacements, we investigated the validity of a purely elastic Earth model derived from seismic data, at an annual time scale. After excluding potential contributions from a viscoelastic asthenosphere, we showed that partial volume variations in a viscoelastic mantle induced by the broad phase transformation of pyroxene-garnet-perovskite may be a reasonable candidate to better explain the amplitude of observed seasonal signals at the surface. It has been shown that for periods characteristic of normal modes, i.e. under 7000 s, these phase transformations do not have the time to occur (Durand et al., 2012). This constraint is obtained from the observed high values of the bulk attenuation  $Q_\kappa \sim 5000$  in the mantle, suggesting that only a limited fraction of the phase transformations occur at seismic time scales. Note however that other mechanisms could be responsible for bulk attenuation at these time scales (Heinz et al., 1982). The other end of the spectrum is unclear and the kinetics of the mantle phase transitions is poorly known. The possibility for mantle phase transitions to partially occur at time scales of the order of a year is therefore valid but must not compromise other constraints provided by different datasets. For example, our model does not change significantly the tidal Love numbers largely used in the elastic case.

However, in order to better understand the remaining misfit to the horizontal signals, one would need a deeper understanding of corrections, and particularly tidal corrections, applied in GPS processing. Unfortunately, this was beyond the scope of my thesis and would need further investigation.

In the end, we improved the usual seasonal model for horizontal components. Such physics-based models for seasonal deformation will, in turn, help improve the accuracy and precision of international terrestrial reference frame. In addition, the possible use of deformation of the Earth under forcing from seasonal changes in surface mass loading to place constraints on the Earth rheology may help understand other geophysical processes occurring at comparable time scales. Strain and stress variations associated with seasonal loading are also of interest. Indeed, small perturbations of stresses on a fault may trigger earthquakes, such as in dynamic

### 3.6. Implications and Conclusions

---

triggering, or even modulate background seismicity. In the *Chapter 4*, we will try to better understand the interactions between periodic loading and faulting, using an experimental approach.

## Supplements

### Supplement 1: Comparison of GRACE processing techniques

As an example of consistency of GRACE seasonal signals from the processing techniques, we show here GRACE time series corrected for linear trends and large earthquake co-seismic contributions for five locations, and all four processing centers.

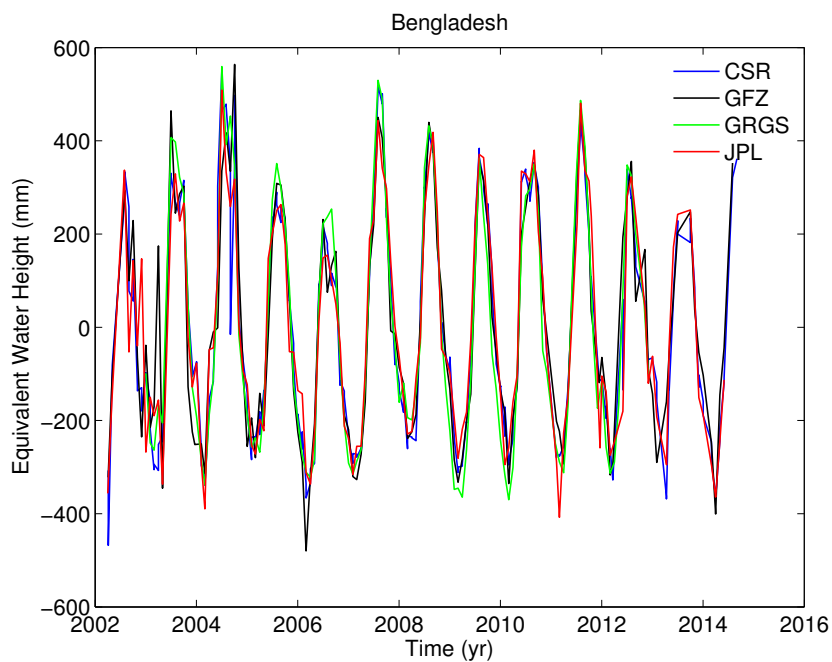
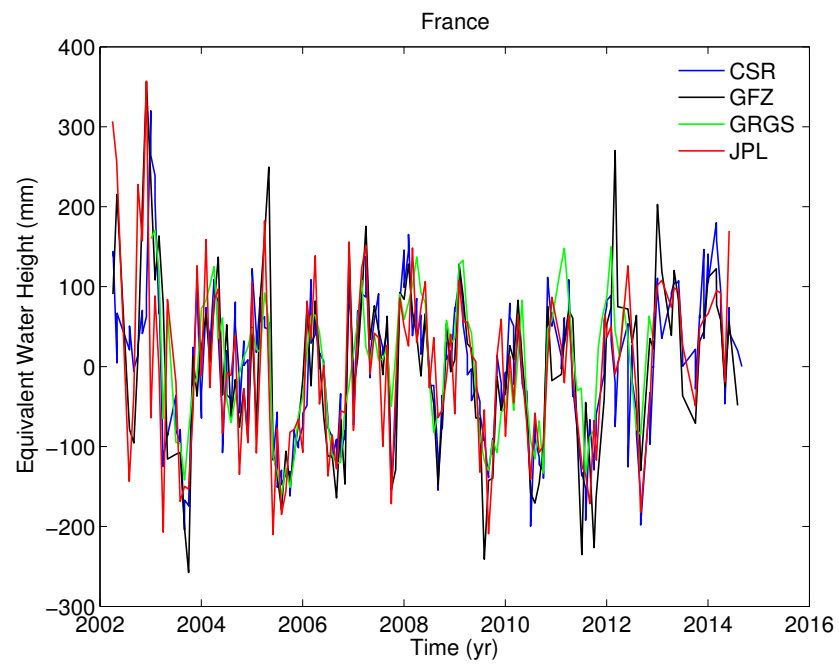
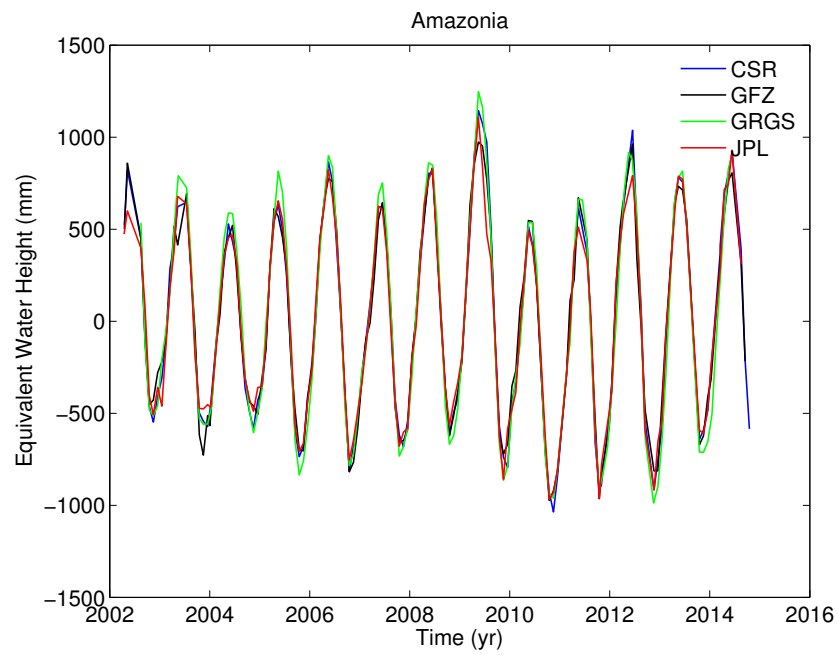
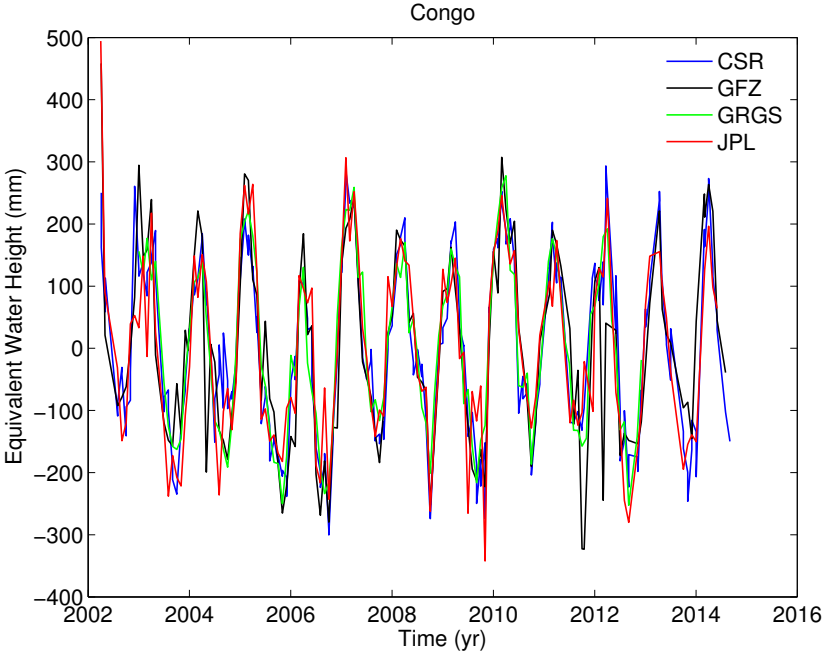
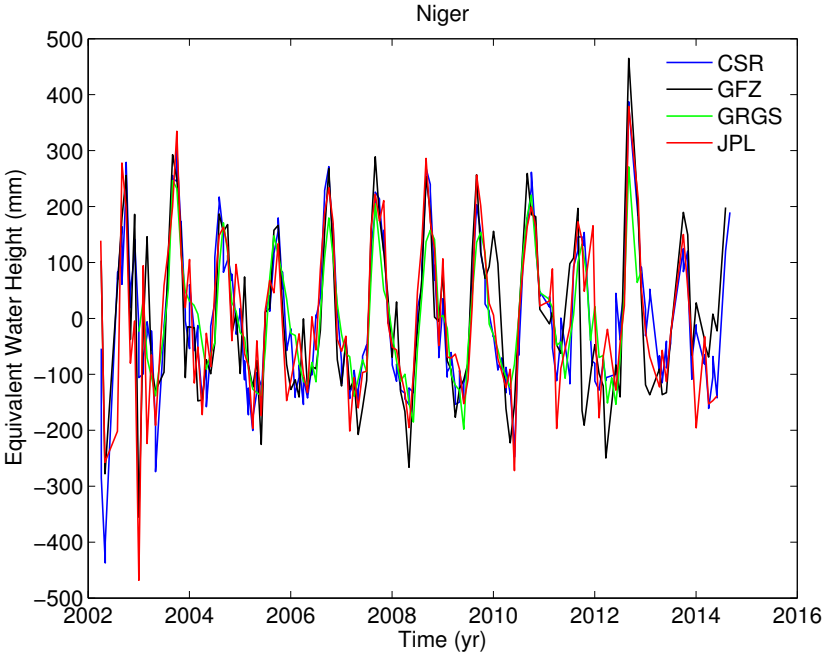


Figure S.1 –Detrended and corrected from large earthquake contributions times series of equivalent water height derived from GRACE by the four processing centers: Jet Propulsion Laboratory (JPL), the GeoForschungsZentrum (GFZ), the Center for Space Research at University of Texas (CSR), and the Groupe de Recherche de Geodesie spatiale (GRGS) at four locations. Differences between processing techniques in the seasonal signals remain fairly small.

### 3.6. Implications and Conclusions





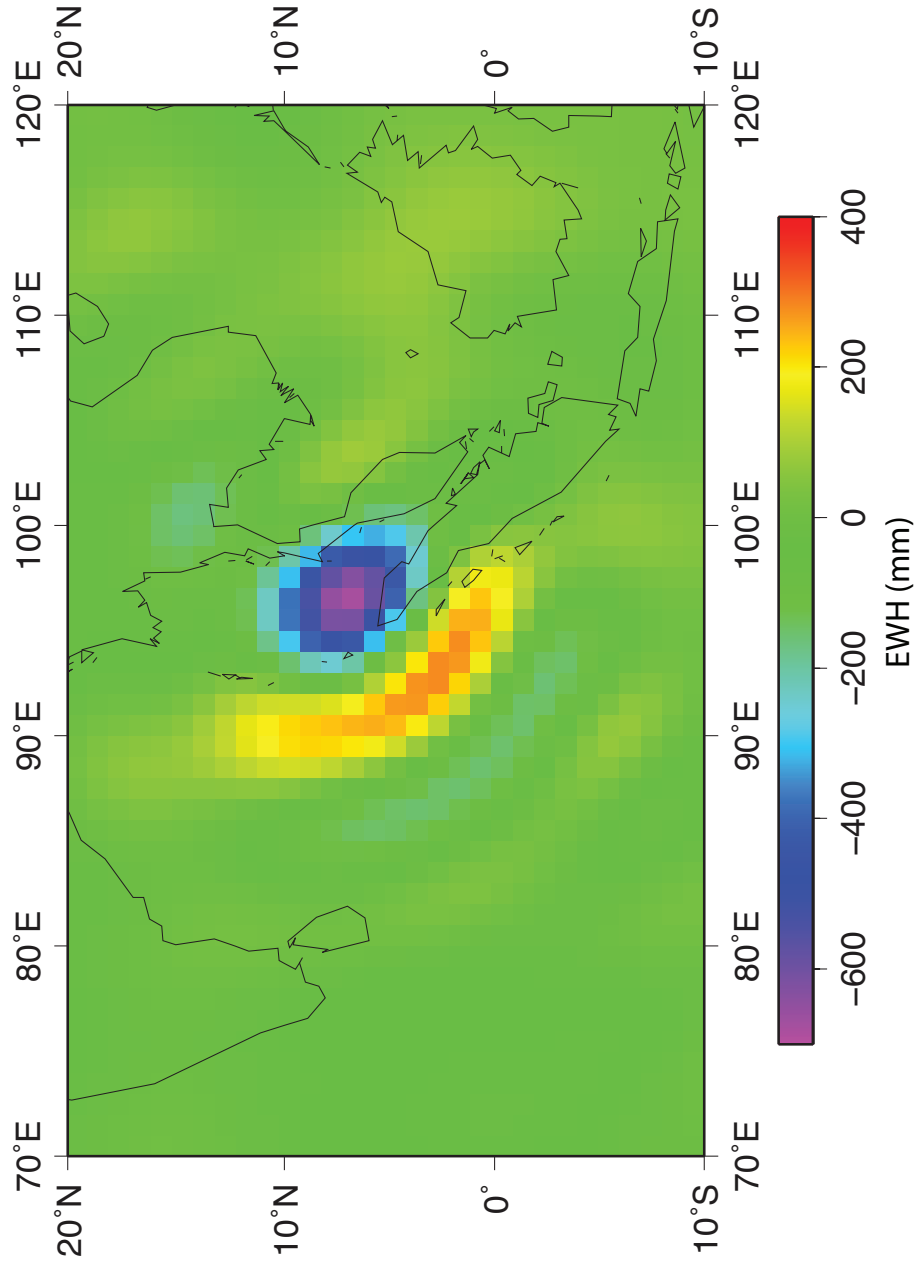
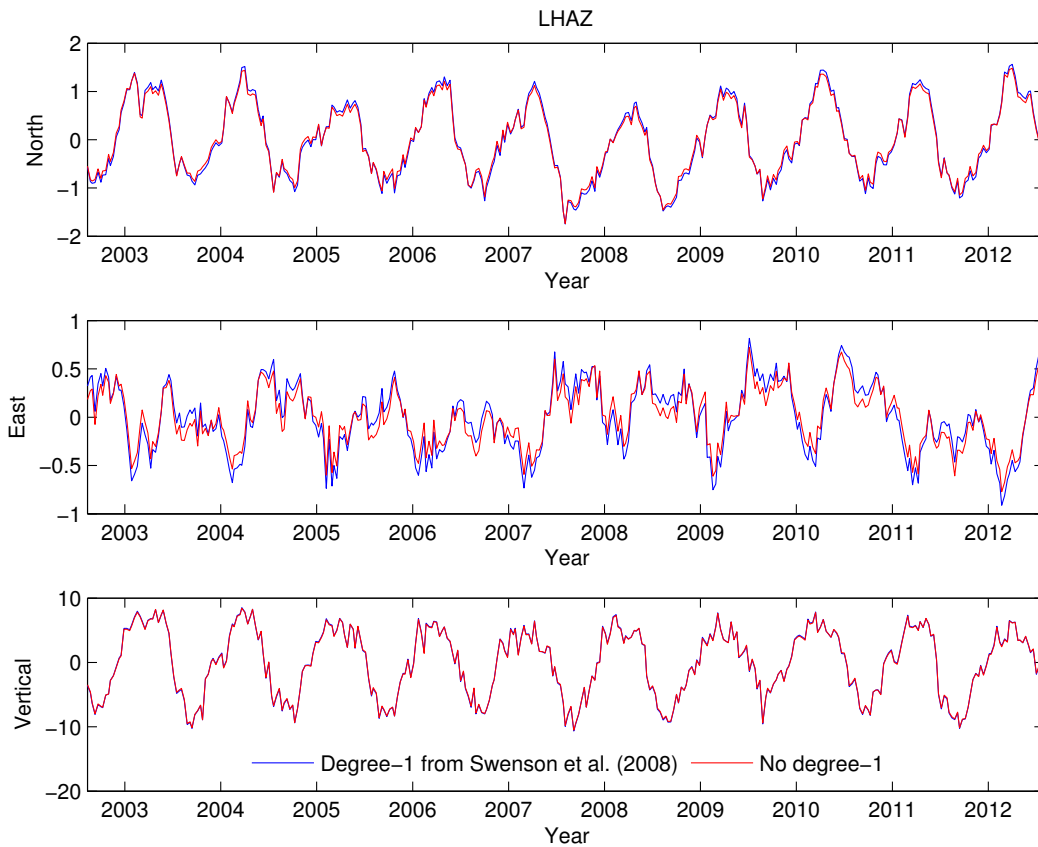
**Supplement 2: Co-seismic Equivalent Water Height offset induced by the 2004 Sumatra-Andaman earthquake**

Figure S.2 – Amplitude of the M9.1 December 2004 Sumatra-Andaman earthquake coseismic contribution to the gravity field expressed in mm of equivalent water height (between 24-12-2004 and 03-01-2005)

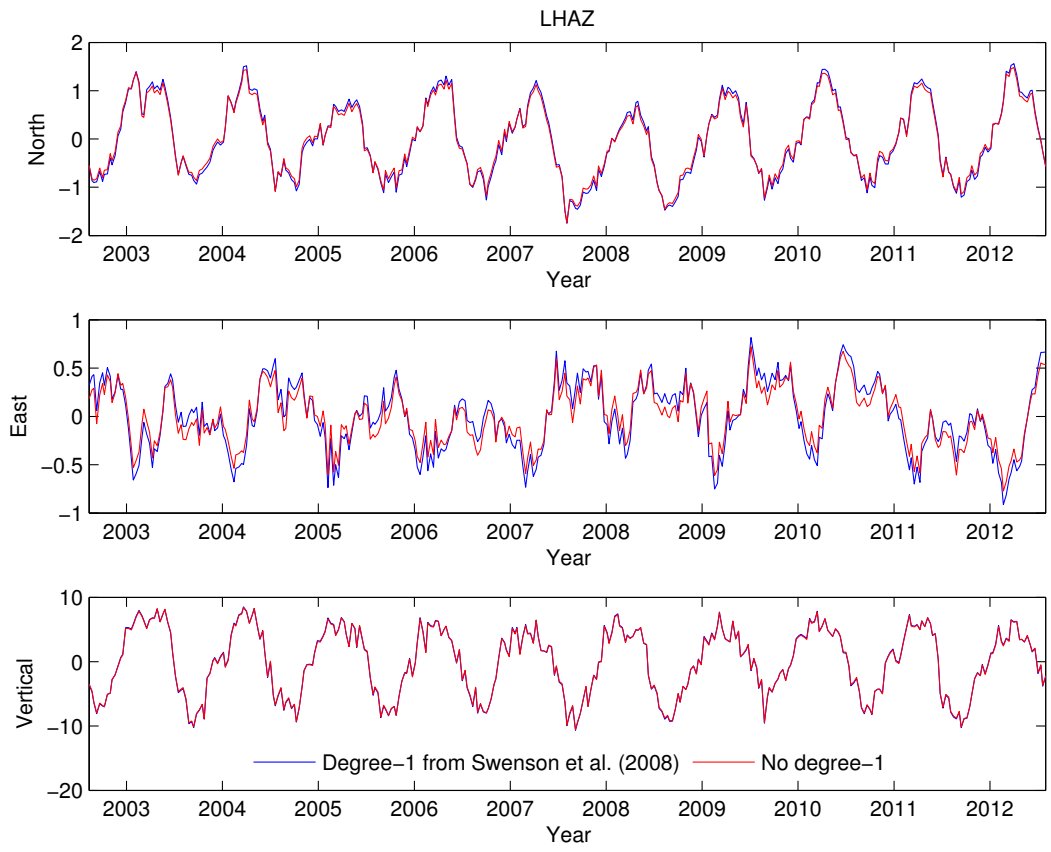
Supplement 3: Comparison of displacement estimates using GRACE with no degree-one loads of including estimates from Swenson et al. (2008)



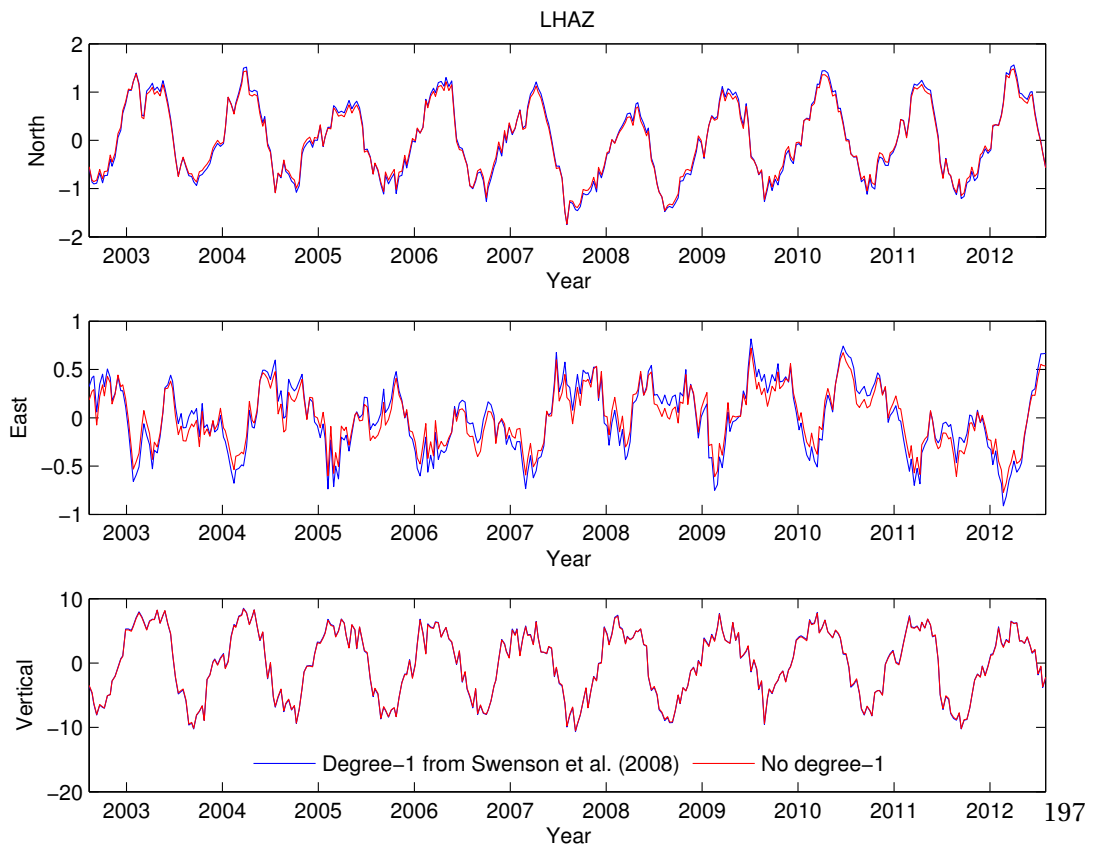
(a) LHAZ, China

Figure S.3 –Blue line shows predicted displacements induced by seasonal surface hydrology variations derived from GRACE where degree-1 components have been omitted and red line where they have been accounted for for following results from Swenson et al. (2008), using a purely elastic continental PREM Earth model.

### 3.6. Implications and Conclusions



(b) CHPI, Brazil



(c) GOLD, United States (California)

### Chapter 3. Global seasonal deformation

#### Supplement 4: GPS stations list

Site	Latitude	Longitude	Material Changes	Jumps added	Earthquakes
IGS stations					
ABPO	-19.02	47.23	1999.73, 2007.16, 2013.7, 2014.12, 2014.76	2008.75 (east)	/
ADE1	-34.73	138.65	1995	/	/
ADIS	9.04	38.77	2007.49, 2008.19, 2014.76	/	/
AIRA	31.82	130.6	2000.5, 2003.14, 2011.28, 2012.59	/	Japan
AJAC	41.93	8.76	2000.06, 2008.91, 2012.93, 2014.76	/	/
ALBH	48.39	-123.49	1992.34, 1992.4, 1994.28, 1995.03, 2003.67, 2003.68, 2003.69, 2014.76	/	/
ALGO	45.96	-78.07	1991.05, 199.413, 1997.04, 2012.97, 2014.76	/	/
ALIC	-23.67	133.89	1994.37, 2003.45, 2011.55, 2014.76	/	/
AMC2	38.8	-104.52	1998.23, 2002.45, 2007.75, 2014.76	/	/
ARTU	56.43	58.56	1999.6, 2014.76	/	/
AZU1	34.13	-117.9	2004.6, 2008.2, 2014.76	2010.2 (material- UNR)	California
BADG	51.77	102.23	2005.25, 2005.87, 2006.65, 2007.25, 2010.2	/	/
BAIE	49.19	-68.26	2001.84	/	/
BAKE	64.32	-96	2009.95	/	/
BAMF	48.84	-125.14	2005.66	/	/
BAN2	13.03	77.51	2008.18	/	Indian ocean
BARH	44.39	-68.22	2007.24	/	/
BILI	68.08	166.44	/	/	/
BJFS	39.61	115.89	2010.39	/	China
BOGI	52.47	21.04	2001.75	/	/
BOGT	4.64	-74.08	1994.84, 2003.48, 2005.53, 2007.62, 2007.95, 2008.44, 2009.69	poly3	/
BOR1	52.1	17.07	1999.41	/	/

### 3.6. Implications and Conclusions

BRAZ	-15.95	-47.88	1995.17, 1996.66, 1998.32, 2007.2, 2012.72, 2012.91, 2013.32, 2014.76, 1995.17, 1996.66, 1998.32, 2007.2, 2012.72, 2012.91, 2013.32, 2014.76, 1995.17, 1996.66, 1998.32, 2007.2, 2012.72, 2012.91, 2013.32	/	/
BREW	48.13	-119.68	2001.85, 2007.95	/	/
BRFT	-3.88	-38.43	2005.68	/	/
BRST	48.38	-4.5	2006.57, 2007.3, 2008.45, 2011.82, 2012.3	/	/
BSHM	32.78	35.02	/	poly 3 east	/
BUCU	44.46	26.13	1999.12, 2000.2, 2008.84	poly 3 vertical	/
BUE1	-34.57	-58.52	/	/	Maule
BZRG	46.5	11.34	2000.92, 2002.4, 2002.52, 2007.95, 2012.13	/	/
CAGZ	39.14	8.97	2001.75	/	/
CASI	-66.28	110.52	2004.9, 2013.95	/	/
CEDU	-31.87	133.81	1994.37, 1997.69, 2006.49, 2006.54	/	/
CFAG	-31.6	-68.23	/	/	Chile all
CHAN	43.79	125.44	1998.37, 2007.87	2007.9, 2011.3	/
CHIL	34.33	-118.03	1995.26, 1995.41, 2012.35	poly 3 east, vertical	/
CHPI	-22.69	-44.98	2003.35, 2013.58	/	/
CHUM	43	74.75	1998.61, 2003.71	/	/
CHUR	58.76	-94.09	1994.28, 2000.55, 2004.74, 2004.74, 2005.09, 2008.24, 2009.25, 2010.67	/	/
CHWK	49.16	-122.01	1999.59, 2008.07, 2010.85	/	/
CIT1	34.14	-118.13	2012.85, 2013.9, 2013.96	/	California
CLAR	34.11	-117.71	1995.38, 2012.13	/	California
CMP9	34.35	-118.41	1995.59, 2008.73, 2008.74, 2011.25	2004.3, 2006.6	California
COCO	-12.19	96.83	/	poly3	India Ocean, Sumatra
COPO	-27.38	-70.34	/	/	Chile
COSO	35.98	-117.81	1996.33	2001.55	/
COYQ	-45.51	-71.89	/	poly3	Chile
CRAO	44.41	33.99	/	/	/
CRFP	34.04	-117.1	/	poly3	California
CUSV	13.74	100.53	/	poly3, 2012.3	/

### Chapter 3. Global seasonal deformation

---

DARW	-12.84	131.13	1996.5, 2001.8, 2001.95, / 2003.26	/	/
DEAR	-30.66	23.99	/	/	/
DHLG	33.39	-115.79	2000.27, 2010.78, 2012.47	/	California
DRAO	49.32	-119.63	1995.28, 1996.03, 1999.42, / 2004.53, 2013.19	/	/
DUBO	50.26	-95.87	1997.02, 1999.76, 2009.65	/	/
EPRT	44.91	-66.99	1999.73, 2004.53, 2014.49	/	/
ESCU	47.07	-64.8	2013.81	/	/
FALK	-51.69	-57.87	/	/	/
FFMJ	50.09	8.66	2005.38, 2008.14	/	/
FLIN	54.73	-101.98	1997.02, 1999.72, 2009.36, / 2010.97	/	/
GANP	49.03	20.32	2006.65	/	/
GENO	44.42	8.92	/	/	/
GLPS	-0.74	-90.3	2012.87, 2012.93	/	/
GLSV	50.36	30.5	2007.87	/	/
GODE	39.02	-76.83	2001.42, 2012.52, 2012.56, / 2012.6, 2012.88, 2012.95, 2013.08, 2013.08	/	/
GODZ	39.02	-76.83	2012.52, 2012.56, 2012.6, / 2012.88, 2012.95, 2013.08, 2013.08	/	/
GOL2	35.42	-116.89	2011.7	/	California
GOLD	35.42	-116.89	1995.83, 2011.7, 2014.76	/	California
GOPE	49.91	14.79	1999.84, 2000.56, 2000.76, / 2006.07, 2006.53, 2009.95	/	/
GRAS	43.75	6.92	1996.76, 2003.31, 2004.81	/	/
GRAZ	47.07	15.49	1996.48, 2001.35, 2005.22, / 2005.84, 2010.38	/	/
GUAO	43.47	87.18	2010	/	/
HARB	-25.89	27.71	1999.42, 2000.61, 2004.2, 2004.2 2007.91, 2011.92	/	/
HERT	50.87	0.33	2007.93	/	/
HLFX	44.68	-63.61	2002.22, 2013.61	/	/
HNPT	38.59	-76.13	1999.07, 2000.39, 2007.45	poly 3	/
HNUS	-34.42	19.22	/	/	/
HOFN	64.27	-15.19	2000.4, 2001.72, 2007.73	poly3	/
HOLB	50.64	-128.13	1996.24, 1999.02, 1999.38, / 2002.06, 2007.03, 2008.59, 2012.34	poly3	/
HOLM	70.74	-117.76	2002.61	/	/

### 3.6. Implications and Conclusions

HRAO	-25.89	27.69	1998.04, 1999.14, 1999.53, 2003.79, 2004.89, 2005.34, 2006.12, 2006.15, 2007.32, 2008.12, 2012.85, 2013.14	2008;2009	
HRM1	51.45	-1.28	/	/	/
HRM2	51.45	-1.28	/	/	/
HYDE	17.42	78.55	1995.74, 1997.28, 2001.53, 2012.3, 2007.9	2012.3 (gap)	Sumatra
IENG	45.02	7.64	/	/	/
IISC	13.02	77.57	1995.75, 2008.53	/	Sumatra, Indian Ocean
INEG	21.86	-102.28	1993.14, 1999.73, 2000.1	/	/
INVK	68.31	-133.53	2003.64	/	/
IQQE	-20.27	-70.13	/	/	Iquique
IRKJ	52.22	104.32	/	/	/
IRKM	52.22	104.32	/	2010, 2011	/
IRKT	52.22	104.32	/	2011	/
JPLM	34.2	-118.17	1990	/	hector mine, baja
KARR	-20.98	117.1	1994.53, 2010.38, 2013.7	/	/
KELY	66.99	-50.94	1996.26,2001.7	poly3	/
KIRO	67.88	21.06	/	/	/
KIRU	67.86	20.97	1995.39, 2000.75, 2003.19, 2013.14	/	/
KIT3	39.14	66.88	1994.75, 1999.95, 2012.8	/	/
KOUR	5.25	-52.81	1992.8, 1997.76, 1998.01, 2002.08, 2006.78, 2007.47, 2008.04, 2012.89	/	/
KUNM	25.03	102.8	1998.46	/	Sumatra
LEIJ	51.35	12.37	2000.38, 2010.5	/	/
LHAZ	29.66	91.1	1999.73, 2007.16, 2008.75, 2013.7, 2014.12	/	/
LPAL	28.76	-17.89	2008.52	/	/
LPGS	-34.91	-57.93	2000.16, 2012.21, 2012.76	/	Chile
LROC	46.16	-1.22	/	/	/
MAD2	40.43	-4.25	1996.74, 2003.69, 2003.83, 2003.86	2002, 2011, 2004.6, 2012.2	/
6-Mar	60.59	17.26	/	/	/
MAS1	27.76	-15.63	1996.3, 2008.52, 2012.47	poly3	/
MAT1	40.65	16.7	2009.42	/	/
MATE	40.65	16.7	1996.52, 1999.46, 2004.11, 2008.9, 2009.79	poly3	/

### Chapter 3. Global seasonal deformation

---

MBAR	-0.6	30.74	nothing in the log but clearly, gaps	2001.22, 2002, 2003, 2004,2008.3, 2011.2, 2012	/
MDVJ	56.02	37.21	/	/	/
METZ	60.22	24.4	/	/	/
MFKG	-25.8	25.54	nothing in the log but clearly, gaps	poly3, 2008.9	/
MONP	32.89	-116.42	1994.55, 1994.76, 1995.46, 1995.58, 2000.22	2011.5, 2010.2, 2012.6	/
MTBG	47.74	16.4	2008.86	2007.6	/
NAMA	19.21	42.04	/	/	/
NANO	49.29	-124.09	1999.6, 2003.02, 2009.73		
NKLG	0.35	9.67	2010.34, 2013.24	/	/
NNOR	-31.05	116.19	2002.46, 2012.76	/	/
NOT1	36.88	14.99	/	/	/
NOVM	55.03	82.91	2006.85	2012.3 (gap in data)	/
NYA1	78.93	11.87	1997.42, 1999.42	/	/
POL2	42.68	74.69	1997.35, 1999.39, 1999.48, 2002.18, 2009.81	/	/
POVE	-8.71	-63.9	/	/	/
PRE1	-25.75	28.22	/	2007, 2007.4	/
PTBB	52.3	10.46	2000.24, 2002.21	/	/
QAQ1	60.72	-46.05	2001.79, 2003.68, 2003.75, 2004	/	/
RABT	34	-6.85	/	/	/
RAMO	30.6	34.76	2000.55, 2004.21	/	/
REYK	64.14	-21.96	1995.84, 1998.7, 1999.19, 2003.45, 2007.72, 2007.72, 2008.2, 2013.33, 2014.76	/	2008.3
RIGA	56.95	24.06	1996.24, 2005.04, 2006.39, 2007.96, 2013.95	/	/
ROAP	36.46	-6.21	2003.09, 2011.82	poly3	/
ROCK	34.24	-118.68	1995.34, 1995.39, 2012.26	/	/
SALU	-2.59	-44.21	2007.39, 2013.44	/	/
SASK	52.2	-106.4	2003.35, 2013.67	/	/
SASS	54.51	13.64	2003.81, 2004.65	/	/
SCOR	70.49	-21.95	/	/	/
SELE	43.18	77.02	1998.94, 2008.52	/	/
SFDM	34.46	-118.75	/	2005	/
SNI1	33.25	-119.52	1998.63, 2000.97	2011.1	California
SPK1	34.06	-118.65	1995.65, 2011.58	/	/
SUTH	-32.38	20.81	2002.16, 2004.42	/	/

### 3.6. Implications and Conclusions

SUTM	-32.38	20.81	2000.2, 2013.35	/	/
TABL	34.38	-117.68	1995.8, 2012.13, 2013.68, 2013.89	poly3	California
TASH	41.33	69.3	2003.42, 2010.7	/	/
TDOU	-23.08	30.38	2006.3	2008.12	/
TEHN	35.7	51.33	2004.5	poly3	
TIXI	71.63	128.87	1998.77, 2002.2, 2002.79, 2010.8	/	/
TORP	33.8	-118.33	2011.2	/	California
TRAK	33.62	-117.8	1994.86, 1995.59, 2009.25, 2011.4	poly3	California
UCLP	34.07	-118.44	1995.15, 2012.73	/	California
UCLU	48.93	-125.54	1995.61, 1996.12, 1996.14, 2000.42, 2001.93, 2007.34	/	/
UFPR	-25.45	-49.23	/	/	/
ULAB	47.67	107.05	/	/	/
ULDI	-28.29	31.42	/	2003.1,poly3	/
UMTA	-31.55	28.67	/	/	/
UNBJ	45.95	-66.64	/	/	/
WARN	54.17	12.1	2003.81, 2004.62, 2005.16, 2010.71	/	/
WES2	42.61	-71.49	1993.11, 1994.52, 1994.59, 1995.6, 1995.68, 1996.24, 1996.43, 1996.45, 1996.5, 1997.39, 1997.5, 1998.42, 2000.57, 2000.64, 2001.57, 2014.48	/	/
WHC1	33.98	-118.03	2012.2	/	/
WILL	52.24	-122.17	1994.47, 1995.52,1 999.42, 2004.02,2004.46, 2013.81	/	/
WIND	-22.57	17.09	2011.16	2007, 2012	/
WROC	51.11	17.06	2000.37, 2001.07, 2007.28, 2012.81	2006.58	/
WSLR	50.13	-122.92	1999.42, 2000.24	poly3	/
YAR2	-29.05	115.35	2002.37, 2012.39, 2012.75, 2013.47	/	/
YIBL	22.19	56.11	/	poly3	/
ZAMB	-15.43	28.31	/	/	/
<hr/>					
Other stations					
GUMB	27.9	-274.12	2000, 2006	/	/
DAMA	27.6	-274.89	1999.8, 2006.5	/	/
CHLM	28.2	-274.68	2006, 2008.5	/	/
KLDN	27.76	-276.39	/	poly3	/
ODRE	26.86	-272.6	/	poly3	/

### Chapter 3. Global seasonal deformation

---

SHTZ	37.56	-291.87	/	/	/
MANM	37.54	-288.31	2010.1	poly3	/
OSHK	40.52	-287.22	2009	/	/
CHUM	42.99	-285.24	2003.6	/	/
PODG	43.32	-280.51	2010.4	poly3	/
SRNW	5.945	-56.99	/	/	/
SAGA	-0.143	-67.05	/	/	/
PEPE	-9.384	-40.5	/	/	/
CUIB	-15.55	-56.06	2004, 2013	poly3	/
SJRP	-20.78	-49.35	/	poly3	/
AC43	59.52	-149.6	/	/	/
SC04	48.92	-123.7	/	/	/
SC02	48.54	-123	/	/	/
SEDR	48.52	-122.2	/	/	/
NEAH	48.29	-124.62	2003.9	/	/
LKCP	47.94	-121.83	/	/	/
SEAT	47.65	-122.3	2004.3	/	/
TWHL	47.01	-122.92	2010.4, 2002	/	/
CPXF	46.84	-122.25	2007.8	/	/
DJOU	9.692	-358.33	/	/	/
ETAD	9.019	-321.23	2010.5	/	/
GAO1	16.25	-0.006	/	/	/
OUAG	12.35	-1.512	/	/	/

Table S.1 – GPS stations used in this study with location

## Supplement 5: List of earthquakes corrected for in GPS time series

Decimal year	Location	Magnitude
<b>Japan</b>		
2001.22	Geiyo	6.7
2003.73	Hokkaido	8.3
2004.81	Chuetsu	6.9
2005.22	Fukuoka	6.6
2005.62	Miyagi	7.2
2006.87	Kuril Islands	8.3
2007.03	Kuril Islands	8.1
2007.23	Noto	6.9
2007.54	Chuetsu	6.6
2008.53	Iwate-Miyagi	6.9
2009.61	Izu Islands	7.1
2009.61	Tokai	6.6
2010.16	Ryukyu Islands	7
2010.97	Bonin Islands	7.4
2011.18	Tohoku foresh.	7.2
2011.19	Tohoku Oki	9
2011.19	Tohoku aftersh.	7.1
2011.26	Miyagi aftersh.	7.1
2011.28	Fukushima	7.1
2011.52	Fukushima aft.	7
2012	Izu Islands	6.8
<b>Turkey</b>		
1999.63	Izmit	7.6
1999.86	Duzce	7.2
<b>Chile</b>		
2002.46	Chile-Argentina Borde	6.6
2003.47	Coast of Central Chile	6.8
2004.34	Bio-Bio	6.6
2005.45	Tarapaca	7.8
2007.87	Antofagasta	7.7
2007.96	Antofagasta	6.7
2008.01	Tarapaca	6.3
2009.86	Offshore Tarapaca	6.5
2010.16	Offshore Bio-Bio	8.8
<b>Samoa</b>		
2009.76	Samoa	8.1
<b>California</b>		
1999.79	Hector Mine	7.1
2010.03	Offsh. NCa	6.5
2003.95	San Simeon	6

### Chapter 3. Global seasonal deformation

---

2004.74	Central Ca	6
2005.44	South LA	5.2
<b>Mexico</b>		
2010.26	Baja	7.3
<b>Indian Ocean</b>		
2003.54	Carlsberg Ridge	7.6
2004.99	Sumatra-Andaman Is- land	9.1
2012.28	off the Wcoast of NSuma- tra	8.6
2012.28	off the Wcoast of NSuma- tra	8.2
<b>China</b>		
2002.49	Priamurye-Northeastern China border region	7.3
2002.98	Kyrgyzstan-Xinjiang bor- der region	5.7
2003.15	Southern Xinjiang	6.3
2003.55	Yunnan	6
2008.21	Xinjiang-Xizang border region	7.2
2008.36	Eastern Sichuan	7.9
2008.76	Eastern Xizang	6.3
2009.52	Yunnan	5.7
2010.25	Southern Qinghai	6.9

Table S.2 – List of earthquakes corrected for in GPS time series

### 4.1 Introduction

Earthquakes occur when the elastic stress in plates driven by long-term motion overcomes the failure stress of faults (Scholz, 2002). In this frame work, one could think that earthquakes are somehow periodic and predictable if the mechanical parameters of a fault were constant (Figure 4.1, top). However, natural examples indicate that fault systems are more complex, as schematically represented on Figure 4.1 (bottom), most likely because the regional loading rate, strength of the fault and friction depend on other geological parameters evolving with time (lithology, geometry of faults, sliding history etc). Therefore, the initiation of slip on a given fault remains an open question in earthquake seismology.

The role of short-term processes in earthquake triggering has been particularly investigated in the past decades. While regional stresses may remain incrementally below the frictional strength of faults for periods of decades to centuries as they accumulate slowly, transient perturbations may cause significant earthquakes (usually magnitudes  $\leq 6$ ). Earthquake triggering by small perturbations may also be an indicator of the critical state of a fault (Brodsky & van der Elst, 2014, van der Elst et al., 2013).

Short-term stress perturbations in the crust at seismogenic depths can be caused by various sources and numbers of studies have shown robustly their link to earthquake triggering. Among them, dynamic triggering from other earthquakes (Das & Scholz, 1981, Brodsky et al., 2000, Brodsky & Prejean, 2005, Fischer et al., 2008, Gomberg & Johnson, 2005, Gomberg et al.,

1997, Hill & Prejean, 2007, Hill et al., 1993, Husker & Brodsky, 2004, Peng et al., 2010, Pol-litz et al., 2012, Prejean et al., 2004, Rubinstein et al., 2011), magmatic intrusions (Savage & Cockerham, 1984, Hill et al., 2002, Manga & Brodsky, 2006), anthropogenic activities such as reservoir-filling, mining, and fluid injection or withdrawal (McGarr et al., 2002, van der Elst et al., 2013, Amos et al., 2014, Talwani, 1998), solid earth tides and ocean loading (Métivier et al., 2009, Cochran et al., 2004, Thomas et al., 2012, Tanaka et al., 2002, 2004, Ide & Tanaka, 2014), deglaciation unloading (Sauber & Molnia, 2004, Dahl-Jensen et al., 2010) and seasonal variations in continental water (Bollinger et al., 2007, Heki, 2003, Saar & Manga, 2003, Bettinelli et al., 2008, Christiansen et al., 2005, Ader & Avouac, 2013, Costain & Bollinger, 1996, Braun-miller et al., 2014). However, mechanisms involved in slip initiation on faults by short-term small stress variations and the time evolution of a fault strength under such conditions are not well understood.

We are interested here in stress perturbations induced by seasonal loading. First, at a global scale, we compute the strain and stress response of the Earth to seasonal loading derived from the Gravity and Recovery and Climate Experiment (GRACE), loading a spherical, layered and elastic model based of the Preliminary Reference Earth Model (PREM). In discussions of earth-quake triggering, the change of Coulomb Failure Function (CFF) is often used, which consists of shear stress change resolved on the fault plane added to the change in the fault-normal stress multiplied by friction coefficient. We take the example of the Nepal Himalaya, where the seismicity rate is twice as high in the winter as in the summer (Bollinger et al., 2007, Bettinelli et al., 2008, Ader & Avouac, 2013), and find a correlation between the CFF rate induced by seasonal loading and the regional seismicity.

However, the role of periodic stress perturbations (tidal loading, seasonal continental water variations) in triggering or modulating seismicity is not well established (Vidale et al., 1998). In a rate and state frame work, largely used to model faults behavior, the critical threshold is determined by a competition between loading and healing (Dieterich, 1994, 1979). It has been proposed that short-period stress transients are not effective at triggering earthquakes if they occur faster than nucleation times (Dieterich, 1992). Lockner & Beeler (1999) esti-mated a nucleation time of  $\sim$  one year from stick slip laboratory experiments in a triaxial

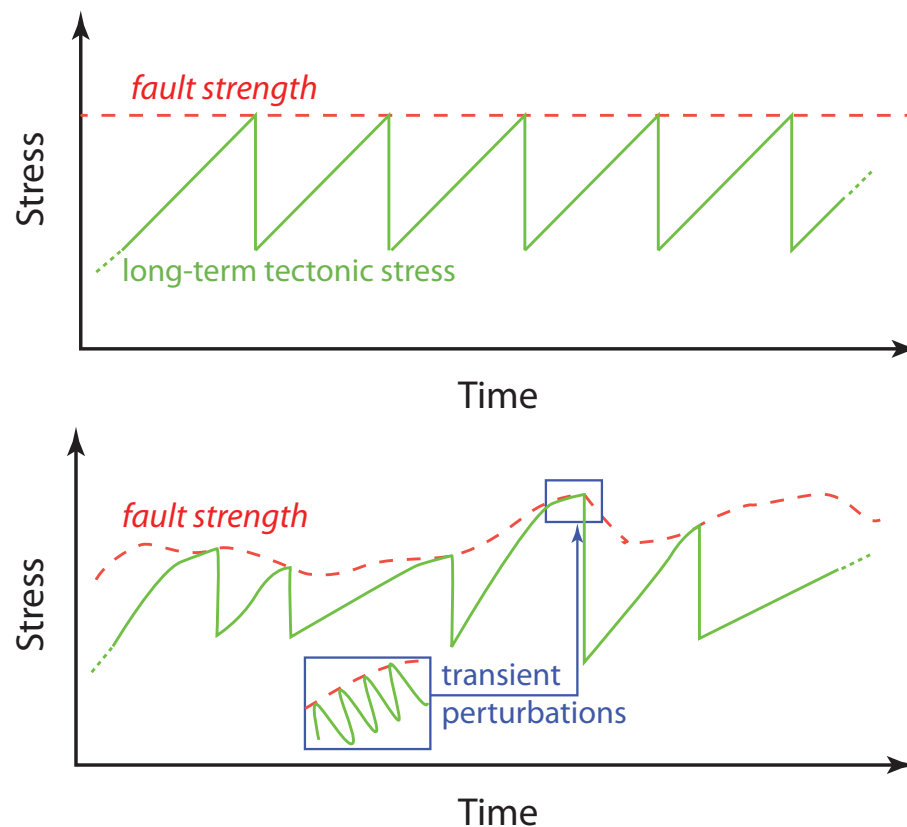


Figure 4.1 – Scheme of the state of stress and strength on a fault with a constant loading rate, stress drop, and strength from which perfectly periodic failure results (top) and with variable loading rate, stress drop, and strength (bottom). In a realistic system, a fault is loaded by transient perturbations, such as periodic surface loading (tides, continental water) in addition to long-term tectonic stress. Transient stress, even small, may initiate a major failure of a fault in a critical state of stress or provide an information on its state of stress by triggering smaller earthquakes.

apparatus on granite samples, with a periodic loading function varying in frequency and amplitude. Later on, they used this estimate to explain the poor correlation between tidal loading and earthquakes (Beeler & Lockner, 2003). However, some robust studies suggest a strong correlation between Earth tides and earthquakes, and even at higher frequencies between dynamic triggering from seismic waves and earthquakes (Brodsky et al., 2000, Fischer et al., 2008, Gomberg & Johnson, 2005, Hill & Prejean, 2007, Hill et al., 1993, Husker & Brodsky, 2004, Peng et al., 2010, Prejean et al., 2004, Rubinstein et al., 2011), .

In addition to the loading frequency and amplitude of a transient periodic perturbations, we suspect the state of stress of a fault to play an important role in its sensitivity to short-term

small stress variations. This idea is supported by the observation of an increase in correlation between tidal loading and seismicity localized in nucleation zones of large earthquakes: the Sumatra megathrust earthquakes of 26 December 2004 (Mw 9.0), 28 March 2005 (Mw 8.6), and 12 September 2007 (Mw 8.5) (Tanaka, 2010), and the 2011 Tohoku-Oki earthquake (Mw 9.1) (Tanaka, 2012). Intuitively, faults in a critical state should be sensitive to small stress perturbations that may contribute, when added to a high pre-existing stress, to failure (Figure 4.1). On the contrary, faults far from failure would be insensitive to small periodic loading.

In order to address this issue, we deform Fontainebleau sandstone sample in the laboratory, under steps of constant applied differential stress over extended periods of time, a phenomenon known as brittle creep (or static fatigue in the engineering literature), and under periodic pore pressure variations of different amplitudes. Our experiments aim at better understanding the influence of small periodic stress perturbations on shear fracture nucleation at in-situ pressure conditions. In particular, we monitor the triggering of acoustic emissions (AEs) which precedes shear failure of brittle rock samples, as a function of the amplitude of cycling-stressing and the general stress state of the rock under brittle creep deformation. We will first review brittle creep introduce the experiment setup and sample preparation. Then, we will present and discuss the mechanical data from both constant strain rate and pore pressure stress-cycling experiments with various amplitudes and the associated acoustic emissions records.

## 4.2 Seasonal stress and seismicity

### 4.2.1 Global stress and strain induced by seasonal hydrology

We first compute the absolute global stress and strain changes induced by the seasonal surface loading variations. Figure 4.2 and Figure 4.3 show a map of the peak square root of the second invariant of the strain and deviatoric stress tensors respectively at 20 km depth. Large strains and stresses are located under and around areas with significant surface load variations. Large stress and strain variations may affect areas such as the Himalayas, the Cascadia, coast of Peru etc. In the following, we will focus on the Nepal Himalaya example.

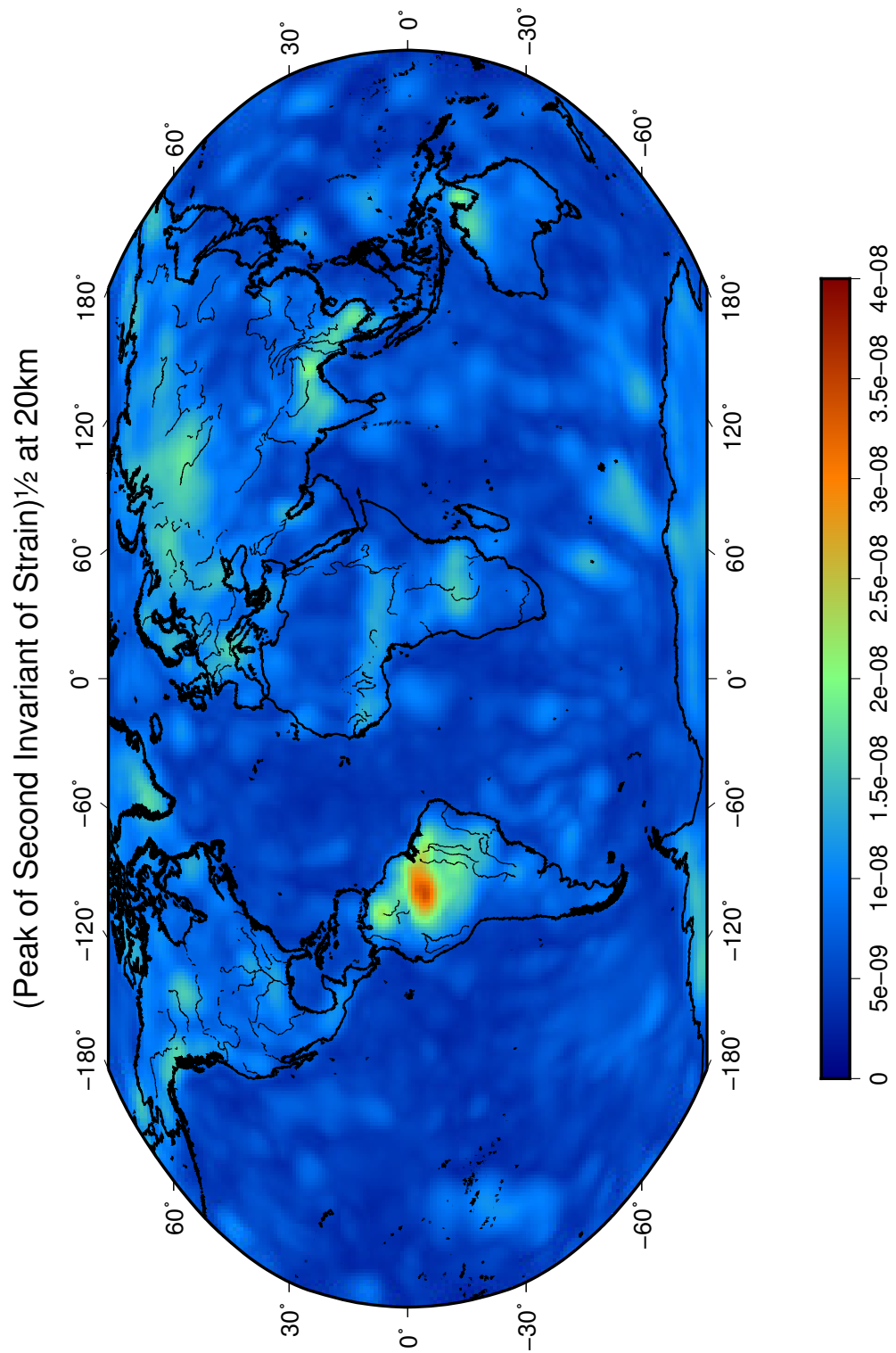


Figure 4.2 – Map of the peak square root of the second invariant of the strain tensor derived from GRACE (2002-2012) at 20 km depth.

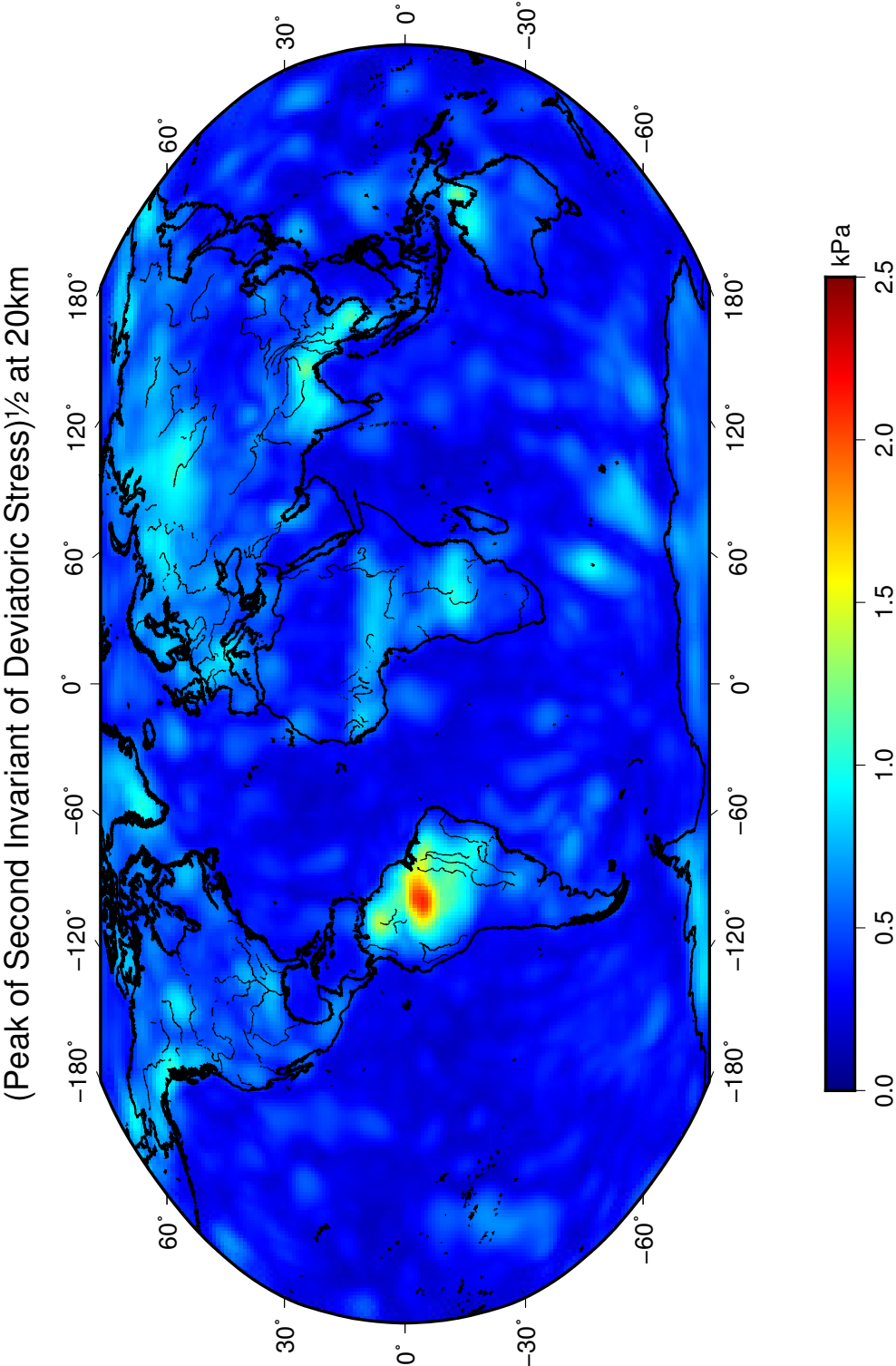


Figure 4.3 – Map of the peak square root of the second invariant of the deviatoric stress tensor derived from GRACE (2002-2012) at 20 km depth

### 4.2.2 Seismicity in Nepal & seasonal Coulomb stress variations

Micro-seismicity in Nepal is shown on Figure 4.8, as the evolution of cumulative number of events in time, from 1994 to 2009. Numbers of earthquakes in the region cluster at the downdip end of the locked part of the Main Himalayan Thrust (MHT) (Ader et al., 2012a, Cattin & Avouac, 2000), and is well recorded by the National Seismological Center (NSC), Nepal. It has been shown that seismic events from this midcrustal cluster from 1995 to 2009 (Figure 4.5) exhibit significant higher seismicity rates over the winter than during the summer, attributed to stress variations on the MHT induced by the hydrological loading variations, driven by the Monsoon cycle (Bollinger et al., 2007, Bettinelli et al., 2008, Ader & Avouac, 2013).

Using our estimate of seasonal stress variations derived from the GRACE dataset, we propose

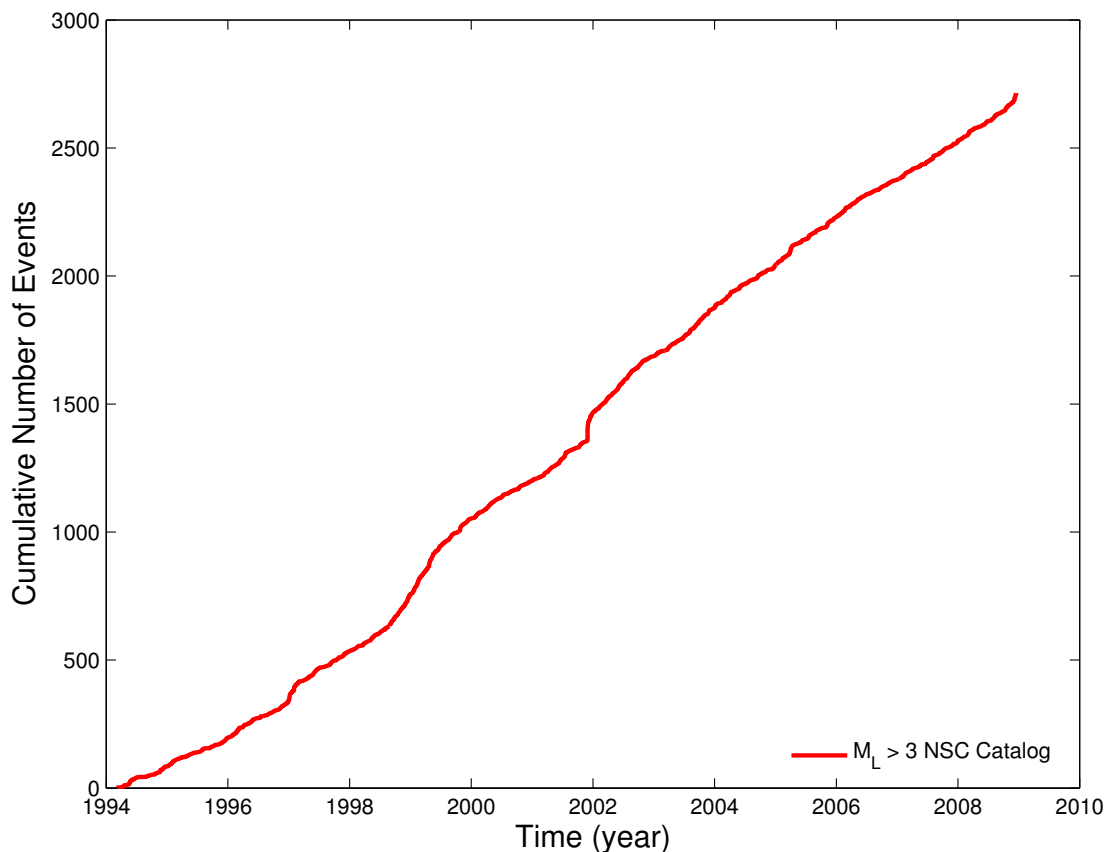


Figure 4.4 – Time distribution of the  $M_L \leq 3$  NSC seismicity showing the cumulative number of events from 1994 to 2009 for the raw catalog (red curve)

to investigate a possible correlation between seismicity rate and stress rate in the region as

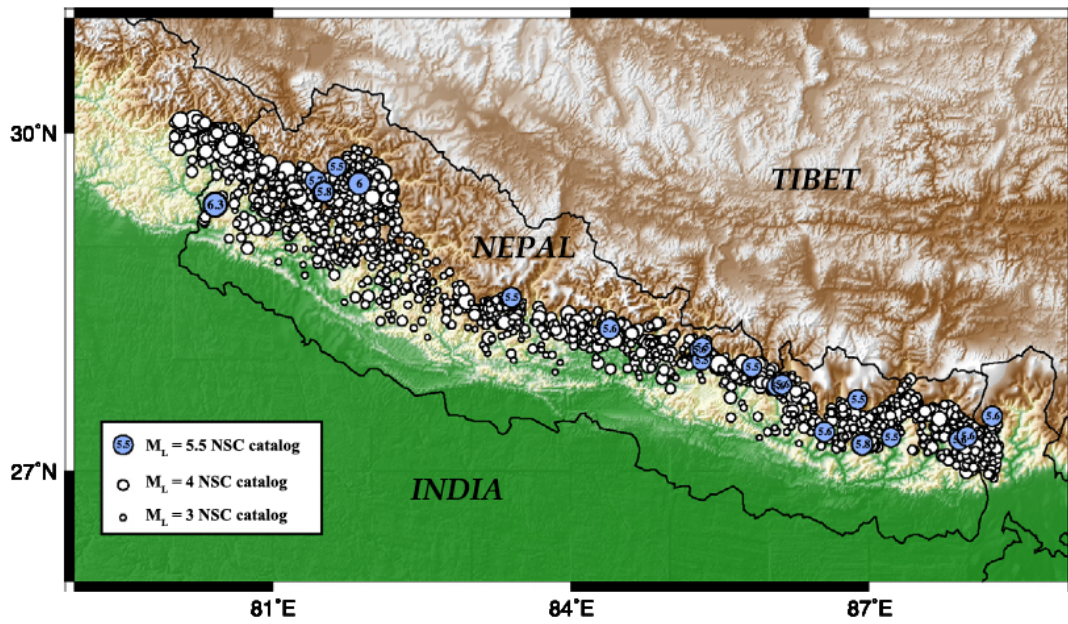


Figure 4.5 – Figure from (Ader & Avouac, 2013). Map showing mid crustal events from the raw NSC catalog, selected according to their localization, using the same selection contour as in Bollinger et al. (2007). Circle sizes are proportional to event magnitudes.

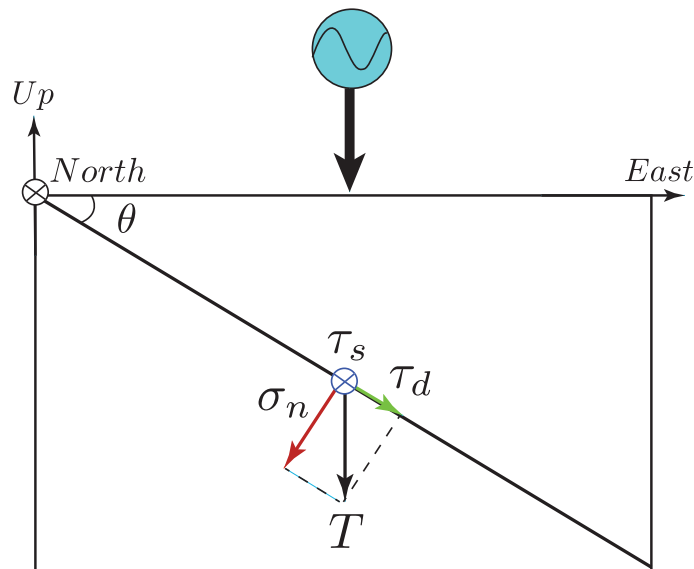


Figure 4.6 – Scheme of shear and normal stress induced by periodic surface loading.

proposed by previous studies (Bettinelli et al., 2008). Thus, we quantify the fault susceptibility to failure under annual surface loading. Using Coulomb failure assumptions, the Coulomb failure stress is given by:

$$\sigma_c = |\tau| + \mu(\sigma_n - p) + C \quad (4.1)$$

where  $\tau$  is the shear stress on the fault (along strike  $\tau_s$  and dip  $\tau_d$ ),  $\sigma_n$  is the normal stress on the fault,  $\mu$  is the friction coefficient,  $C$  the cohesion and  $p$  the pore-fluid pressure (see Figure 4.6). Assuming that  $p$ ,  $S$ ,  $C$  and  $\mu$  are constant in time, the change of Coulomb stress is given by:

$$\Delta\sigma_c = \Delta|\tau| + \mu\sigma_n \quad (4.2)$$

Our convention is that  $\Delta\sigma_n$  is positive in tension. Accordingly, a Coulomb stress increase should enhance seismicity. As pointed out previous studies, a periodic loading, with period  $T$ , superimposed over a secular loading rate  $\Delta\dot{\sigma}_0$ , will have substantial effect on seismicity only if the amplitude of periodic stress variation,  $\Delta\sigma$ , is of the order of magnitude of the secular increase over a cycle equation  $\Delta\dot{\sigma}_0 T$  (Vidale et al., 1998, Lockner & Beeler, 1999, Beeler & Lockner, 2003, Heki, 2003). If the amplitude of the seasonal term is smaller than the limit for stress rate reversal,  $\frac{1}{2\pi}\Delta\dot{\sigma}_0 T$  seismicity is expected to correlate with the stress rate, while in the case of stress reversal the seismicity will tend to correlate more with the peak coulomb stress. The annual stress increase due to interseismic loading is estimated to  $\sim 6$  kPa within 5 km of the centroid of microseismic activity beneath the Greater Himalaya (Bollinger et al., 2004), providing an estimate of the order of magnitude of the stress variations needed to explain the observed fluctuations of seismicity.

We compute the time evolution of the Coulomb stress at a 20 km depth in Nepal (27.5,85.5), as shown on Figure 4.7, on two faults dipping at  $8^\circ$  (red) and  $20^\circ$  (blue) and a friction coefficient of 0.3. We find that the seasonal load will increase the chance of failure over the winter, when the MHT is unclamped, independently of the dipping angle. We now compare CFF and CFF rate to the regional seismicity. Because the seismic catalog and the GRACE data acquisition periods do not exactly overlap, we stack both datasets over a year. Figure 4.8 shows the  $M_L \leq 3$  events from the 1994-2009 NSC catalog stacked over a year (gray) and Coulomb Failure Function rate derived from GRACE loading a spherical and layered elastic model based on PREM (red). Events occur significantly more over the winter months than between June and September, when the Monsoon loads the Ganges Basin. We find a correlation between seismicity and CFF rate, as proposed by other studies (Bollinger et al., 2007). However, the amplitude of stress variations induced by seasonal loading,  $\sim 1$  kPa, in the Himalayas is much

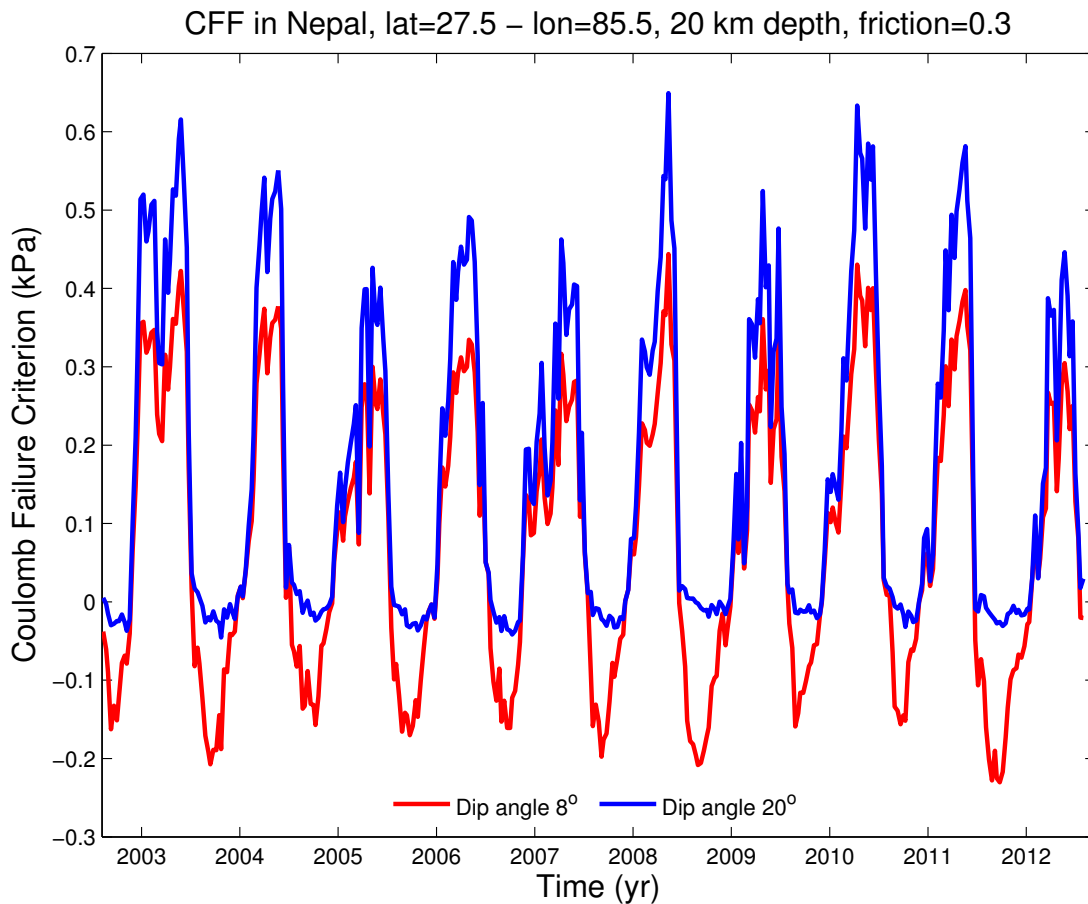


Figure 4.7 – Coulomb Failure Function (CFF) derived from seasonal loading of the hydrosphere (GRACE) in Nepal, at 20km depth, on two faults dipping at  $8^\circ$  (red) and  $20^\circ$  (blue). Positive values of the CFF indicate that the load is increasing the chance of failure.

lower than the estimate of interseismic loading,  $\sim 6$  kPa, given by [Bollinger et al. \(2004\)](#), suggesting that other parameters (erosional unloading, atmospheric pressure fluctuations, snow load and temperature variations) than the competition between interseismic stress rate and seasonal stress rate driven by the Monsoon Cycle may play a role in the winter triggering of micro-seismicity in the Himalayas.

As proposed by [Tanaka \(2012, 2010\)](#), the state of stress of the fault may be an important parameter in the observation of correlation between seasonal, or periodic loading, and seismicity. In the following, we investigate the question using an experimental rock mechanics approach.

### 4.3. Dynamic acoustic emission triggering by small periodic pore pressure variations during brittle creep experiments

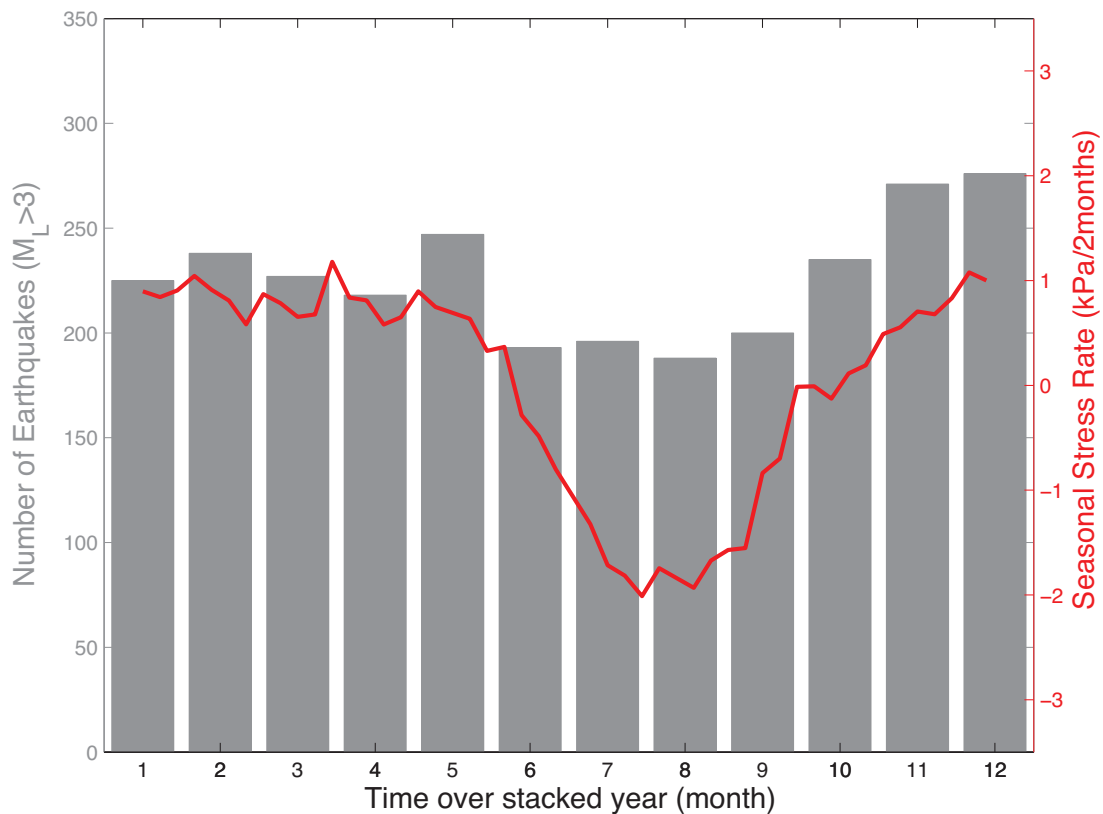


Figure 4.8 – Stack of  $M_L \leq 3$  events from the 1994-2009 NSC catalog over a year (gray) and Coulomb Failure Function rate derived from GRACE loading a spherical and layered elastic model based on PREM (red).

### 4.3 Dynamic acoustic emission triggering by small periodic pore pressure variations during brittle creep experiments

Fluid induced stress perturbations in the crust at seismogenic depths can be caused by various sources, as explained previously. Numbers of studies have robustly shown their link to earthquake triggering. However, the role of small periodic stress variations induced by solid earth and oceanic tides or seasonal hydrology in the seismic cycle, of the order of a few kPa, remains unclear. Indeed, the existence or absence of correlation between these loading phenomena and earthquakes has been equally proposed in the literature.

As proposed by [Tanaka \(2010, 2012\)](#), an increase in correlation between tidal loading and seismicity localized in nucleation zones of large earthquakes may occur before rupture, during

the long nucleation phase. To investigate the importance of the state of stress of a fault on triggering or modulation of seismic events, we performed a set of triaxial deformation experiments on water-saturated Fontainebleau sandstones, 7% porous. Rock samples were loaded by the combined action of steps of constant stress (creep), intended to simulate tectonic loading and small sinusoidal pore pressure variations with a range of amplitudes, analogous to tides or seasonal loading. Previous studies investigated the possible influence of cyclic loading on pre-cut samples and showed the importance of duration of failure nucleation compared to the loading frequency (Beeler & Lockner, 2003, Lockner & Beeler, 1999). To our knowledge, the behavior of rock samples under periodic pore pressure variations during brittle creep experiments has not yet been investigated.

### 4.3.1 Brittle creep deformation

Brittle creep is a classical term used to describe the inelastic deformation of a solid material under a long-term constant stress, below the short term failure stress of the material. It has been shown experimentally that, for bulk rock deforming under such conditions, the brittle creep deformation is a non-linear function of the time (Main et al., 1993, Main, 2000). The deformation actually exhibits a trimodal behavior in a time-axial strain plan (Figure 4.9), known as a creep curve and largely experimentally observed (Lockner, 1993, Main, 2000, Baud & Meredith, 1997). Brantut et al. (2013) gives a review of brittle creep experiments in rocks. The three stages of the creep curve are usually described as (i) primary creep, (ii) secondary steady-state creep, and (iii) tertiary accelerating creep.

It is likely however that this does not represent three distinct mechanisms, but the product of a decelerating and accelerating mechanism. The primary creep phase is characterized by an initially high strain rate that decreases with time to reach a quasi-linear secondary phase that is often interpreted as steady-state creep. After an extended period of time, a tertiary phase is entered, characterized by accelerating strain. This eventually results in macroscopic failure of the samples by propagation of a shear fault. Creep strain rates are calculated from the quasi-linear portions of the creep curves.

### 4.3. Dynamic acoustic emission triggering by small periodic pore pressure variations during brittle creep experiments

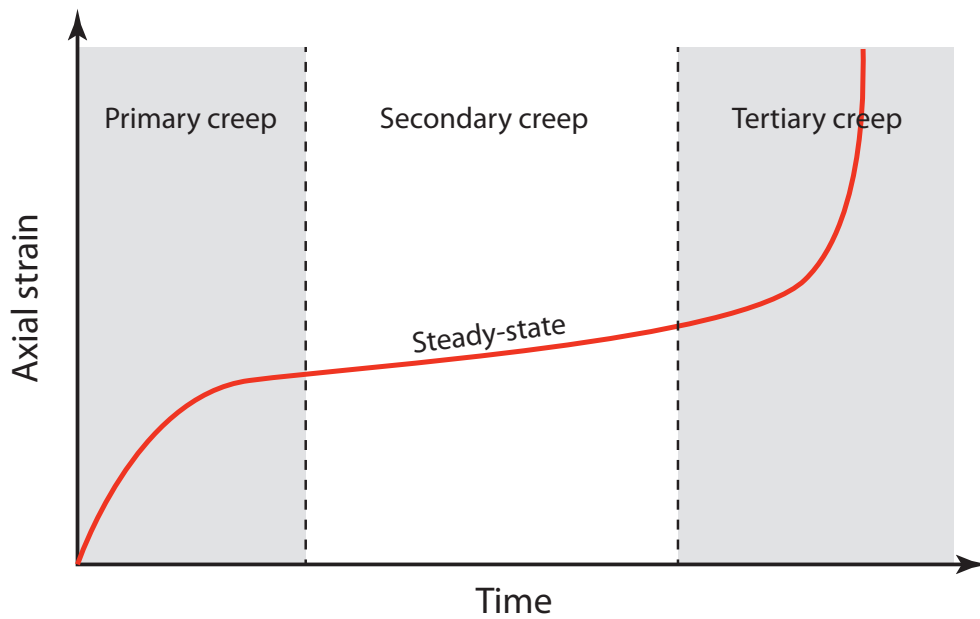


Figure 4.9 – Trimodal creep curve with (i) primary creep, (ii) secondary steady-state creep, and (iii) tertiary accelerating creep.

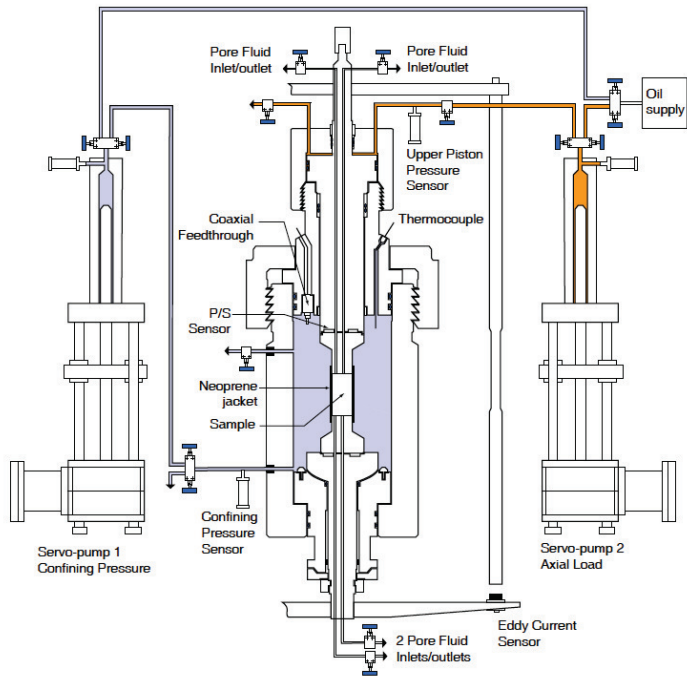
#### 4.3.2 Experimental setup and sample preparation

##### Triaxial apparatus

We run our experiments in a triaxial oil cell installed at the École Normale Supérieure (Figure 4.10). Volumetric servo-pumps control both the confining pressure (up to 100 MPa) and the axial piston responsible for axial stress (up to 680 MPa on a 40 mm diameter sample). Confining pressure is measured directly by a pressure sensor while the axial stress is derived from a pressure measurement. If the axial stress is higher than the confining pressure, the sample is under compressive shear stress and will deform under strain rates controlled by the axial stress or deform under constant stress. Axial deformation of rock samples is measured by averaging three eddy current sensors corrected for the deformation of the apparatus itself. Both axial and radial deformation are recorded by four strain gauges glued on the samples (Figure 4.12). All our experiments were run at an homogeneous temperature of 35°C using the external heating system surrounding the vessel. The system also includes 16 coaxial cables to position 16 acoustic sensors and 18 single cables for 9 strain gauges.



(a) Photo of the triaxial cell



(b) Schematic diagram of the triaxial apparatus

Figure 4.10 – Photo (a) and schematic diagram (b) of the experimental apparatus, after (Brantut et al., 2011).

### Pore pressure

We use a double micro-volumetric pump, Quizix, to impose a pore pressure within the sample. The pump is made of two separate pistons, running together or independently. During our experiments, the two pumps are connected to the two entrance points of the pore fluid pressure network. The pumps alternate, either receiving fluid is discharged by the system or injecting fluid into the sample if the pore pressure decreases. We record the pore pressure within the sample using a sensor at the bottom of the sample. Quizix also controls oscillations of pore pressure using an automated schedule of injecting and receiving fluid of the two pumps. Figure 4.11 shows a sample of the pore pressure records for the first 30 minutes of each experiments. Our three experiments presented here were run at (1) constant pore pressure of 5 MPa (blue), (2) oscillating pore pressure at  $5 \pm 2.5$  MPa with a period of 4 minutes (red) and (3) oscillating pore pressure at  $5 \pm 0.5$  MPa with a period of 4 minutes (green).

### 4.3. Dynamic acoustic emission triggering by small periodic pore pressure variations during brittle creep experiments

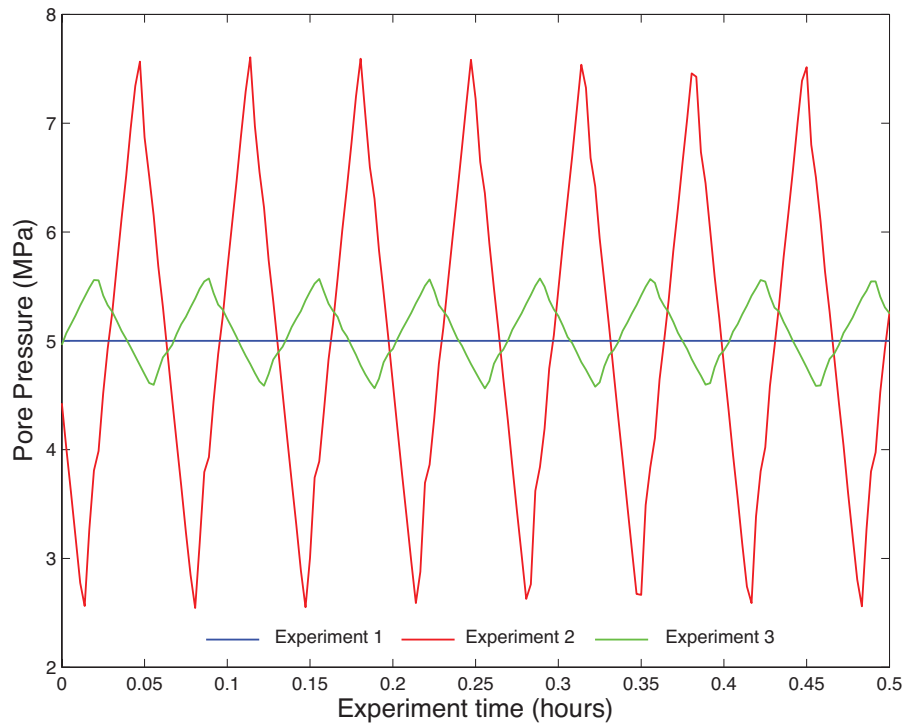
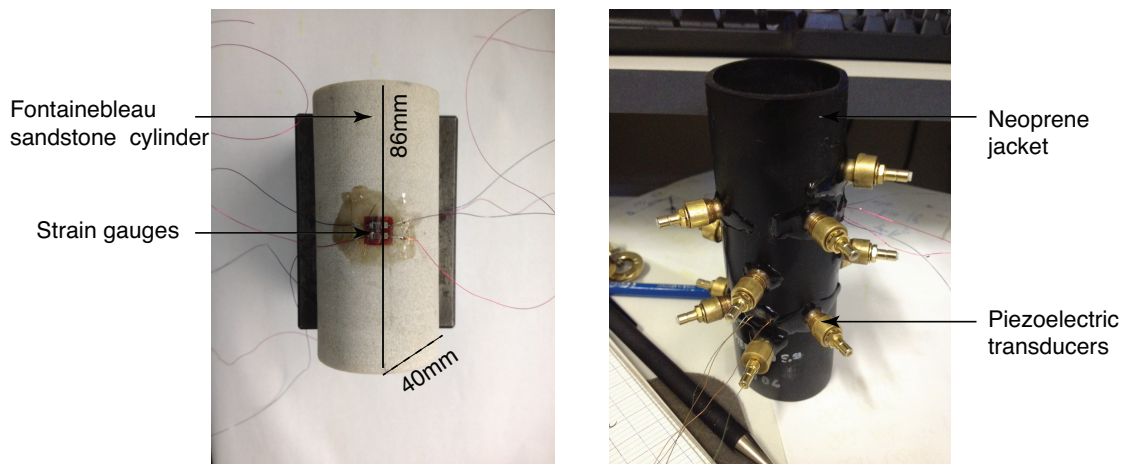


Figure 4.11 – Pore pressure setup in our three experiments: (1) constant pore pressure of 5 MPa (blue), (2) oscillating pore pressure at  $5 \pm 2.5$  MPa with a period of 4 minutes (red) and (3) oscillating pore pressure at  $5 \pm 0.5$  MPa with a period of 4 minutes (green). Pore pressure within the sample is controlled by a dual pumps setup (Quizix).

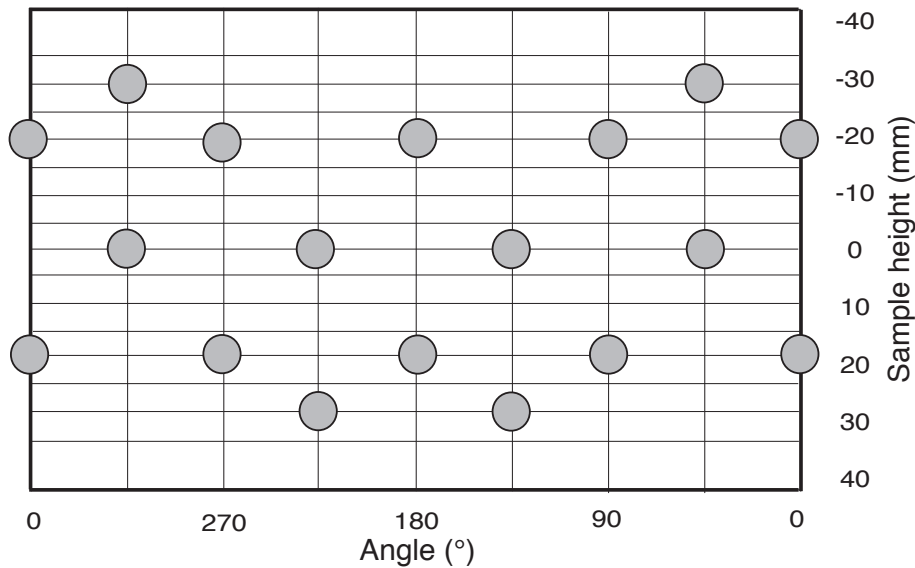
#### Material and sample preparation

The material used in our experiments is sandstone from Fontainebleau (France), formed of pure quartz grains that are well sorted and have a nearly uniform grain size of around  $250 \mu\text{m}$  (Bourbie & Zinszner, 1985). It is isotropic and presents a wide variation of porosities, ranging between 2% and 30%. We use a low porosity 7% block for our experiments.

All samples are cored in the same Fontainebleau sandstone block, with a diameter of 40 mm and a mean length of 86 mm, rectified with a  $5 \mu\text{m}$  precision to assure parallel cuts, and dried. We then place the rock samples in a neoprene jacketed to assure their impermeability to confining oil. The jacket has 16 holes so we can glue the acoustic sensors directly on the sample's surface.



(a) Sample preparation



(b) Acoustic sensors positions

Figure 4.12 – (a) Photos of a Fontainebleau sandstone sample with a double strain gauge (left) and the fully prepared sample with acoustic sensors on their mounts (right). (b) Acoustic sensors map: 16  $V_p$  distributed around the sample.

A network of 16 piezoceramic transducers (PZT) was used in order to measure P wave velocities along several directions and locate acoustic emissions during the experiment (further discussed in the following section). Each PZT is made of a piezoelectric crystal, sensitive to P waves, is mounted on a stand. Once the sensors glued, a soft glue around the PZTs insures the

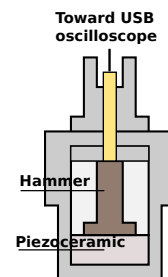


Figure 4.13 – PZT Stand

### **4.3. Dynamic acoustic emission triggering by small periodic pore pressure variations during brittle creep experiments**

---

jacket impermeability. The acoustic sensor map used in all experiments is given on Figure 4.12 (b). The sensors are distributed on five lines, with two to five sensors, to insure a good coverage of the rock. We also glue two double strain gages (radial and axial) at opposite sides of the sample (Figure 4.12 (a)). Then, the sample was placed inside the pressure vessel. For our experiments, samples are prepared dry and then saturated in the apparatus.

#### **Data acquisition: acoustic emissions**

Acoustic sensors in the vessel are connected to the outside by 16 high voltage coaxial wires, plugged into high frequency 40 dB amplifiers with two distinct outputs. Continuous records of the acoustic emissions (AEs) are written directly on hard drives. A trigger logic insures that signals above a certain threshold amplitude on a given number of channels are recorded on the oscilloscopes at 50 MHz sampling rate. In addition to passive AEs records, wave velocity are actively measure by pulsing a high frequency voltage of 200 V signal on each channel while the other channels record. This results in the emission of a P wave and since the origin time of the pulse and the sensors positions are known, the measurement of the travel times allows us to calculate the average velocity along each ray path. Note that, during active velocity surveys it is not possible to record passively AEs.

#### **4.3.3 Experimental Results**

We present results from three experiments in which rock samples were loaded by the combined action of steps of constant stress (creep), intended to simulate tectonic loading and small sinusoidal pore pressure variations with a range of amplitudes, analogous to tides or seasonal loading. All tests were conducted at a regulated temperature of 35°C and a constant 35 MPa confining pressure.

#### **Mechanical Data**

Figure 4.12 shows the evolution of stress (differential stress), axial strain and acoustic activity (number of detected AEs) for three experiments, where the only varying parameter is the Pore pressure ( $P_p$ ). For (a) Experiment 1,  $P_p$  is set to 5 MPa. Brittle failure was attained at a

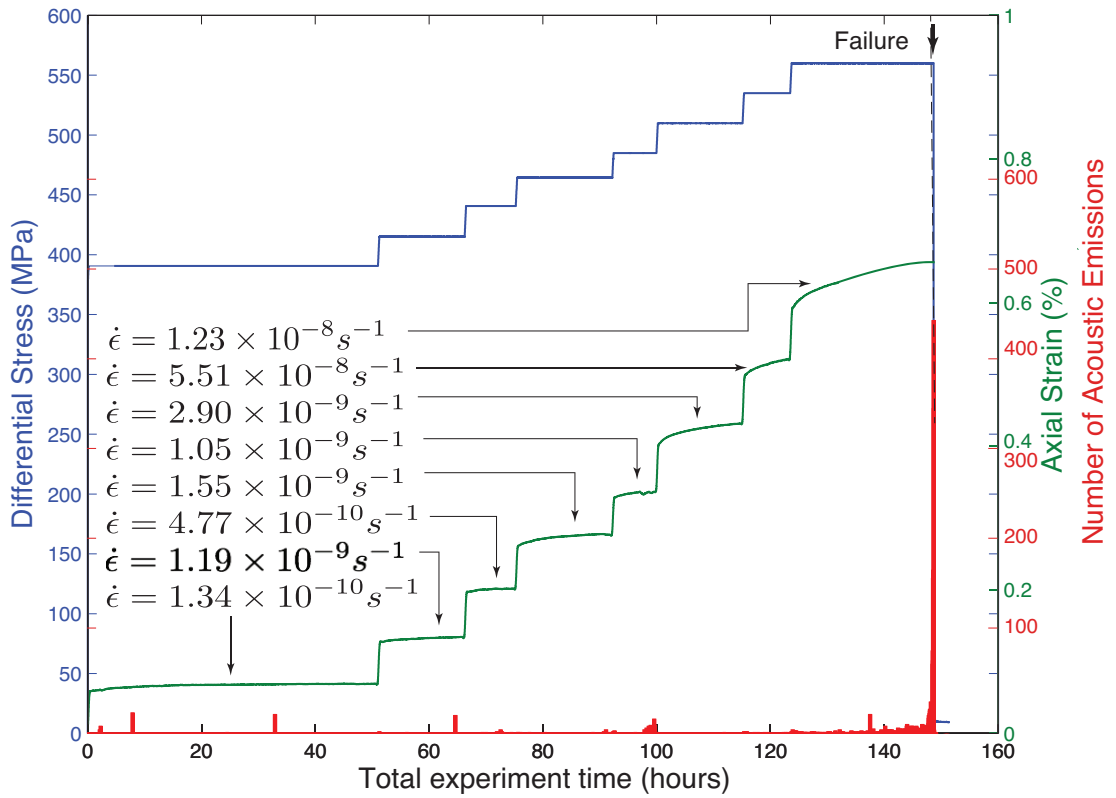
550 MPa differential stress. Deformation is measured using strain gages glued on the rock sample. The rock deformed with an increasing strain rate at each differential stress step and failure occurred after  $\sim 30$  hours of deformation at  $1.23 \cdot 10^{-8} \text{s}^{-1}$ , with a progressive increase of acoustic activity reaching up to 400 per second for a few seconds. For (b) Experiment 2,  $P_p$  was a periodic function, with period 244 seconds, and amplitude variations of  $5 \pm 2.5$  MPa. Brittle failure occurred at a differential stress of 500 MPa, after 20 hours of deformation at a rate of  $1.02 \cdot 10^{-8} \text{s}^{-1}$  over which acoustic emissions increased progressively. However, the acoustic content of the rest of the experiment is more complex and significant AEs occurred during the increase of differential stress for the first 80 hours of the experiment, probably due to heterogeneity in the sample. Finally, (c) shows results for Experiment 3 where  $P_p$  was a periodic function, with period 244 seconds, and amplitude variations of  $5 \pm 0.5$  MPa. Failure occurred at 600 MPa, after a short differential stress step of 6 hours, during which the rock was deforming at a rate of  $1.09 \cdot 10^{-8} \text{s}^{-1}$ , with a progressive increase of AEs. We conclude that the pore pressure oscillations did not influence the deformation rate at which the rock breaks. Differences in differential stress values at which brittle failure occurs is most likely due to heterogeneities within the Fontainebleau sandstone block where samples were drilled.

### Acoustic Emissions

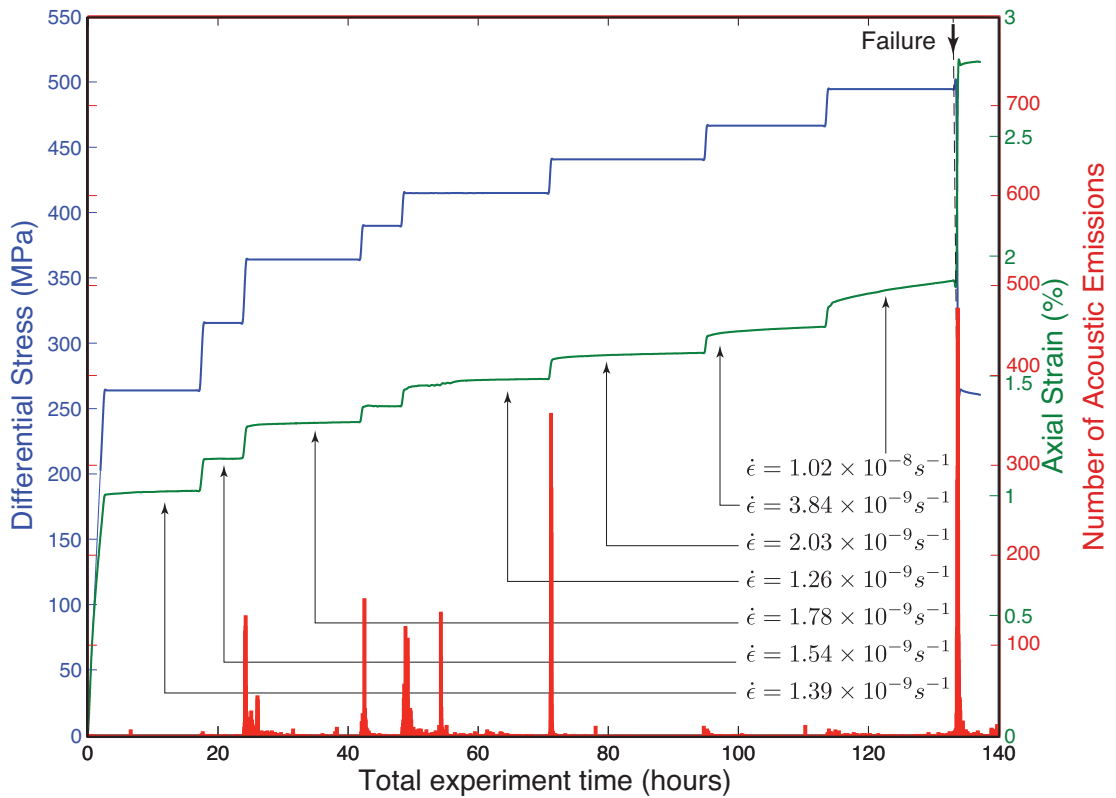
For each experiment, we record a catalog of AEs in order to investigate the correlation of pore pressure oscillations with acoustic activity and its temporal evolution.

First, we examine the response of acoustic emissions to a 244 s periodic stressing. This type of investigation is regularly carried out under the assistance of the Schuster test ([Tanaka, 2010, 2012](#), [Schuster, 1897](#)). Note that [Lockner & Beeler \(1999\)](#), [Beeler & Lockner \(2003\)](#) also used the Schuster test to quantify the response of a fault submitted to periodic load variations during laboratory experiments. We take advantage of [Ader & Avouac \(2013\)](#) and compute the Schuster spectrum for the two last differential stress steps of each experiments. The Schuster spectrum applied to AE catalogs allows placing constraints on the amplitude of variations of acoustic emissions at a 244 seconds period, the pore pressure oscillation period. Figure 4.13 shows Schuster spectrum computed for catalogs of acoustic emissions events occurring

### 4.3. Dynamic acoustic emission triggering by small periodic pore pressure variations during brittle creep experiments



(a) Experiment 1



(b) Experiment 2

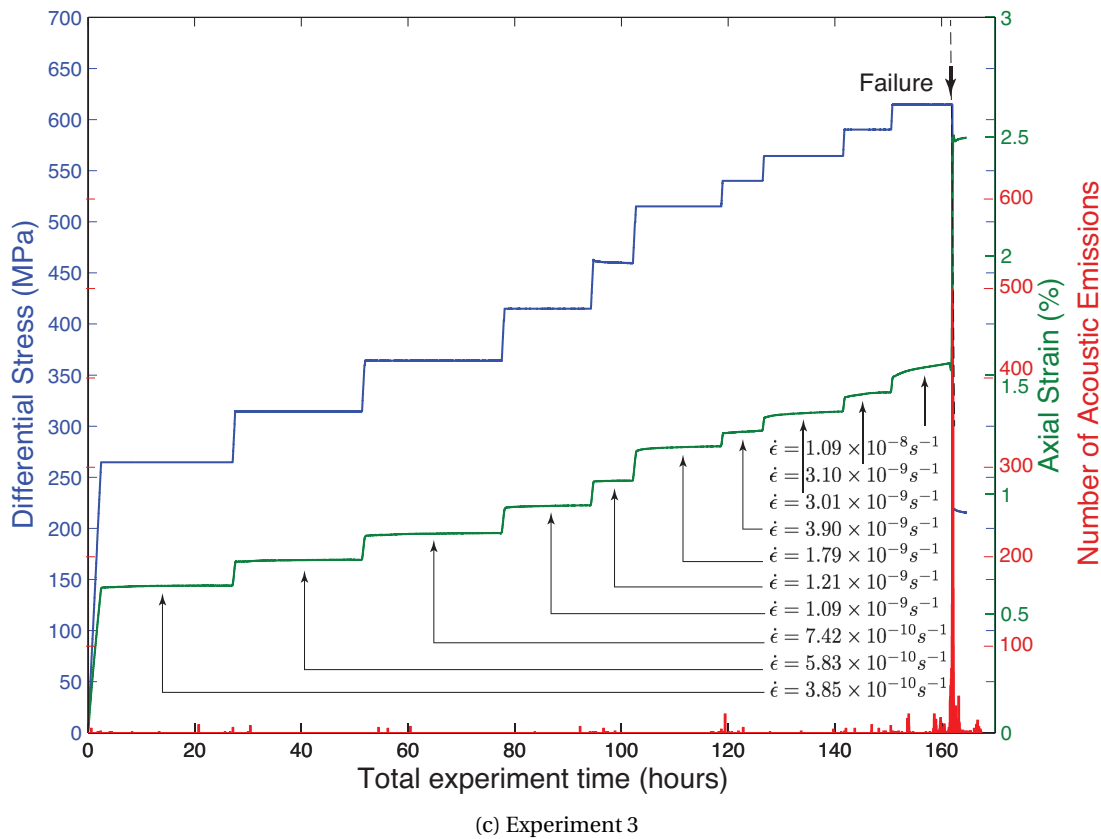


Figure 4.12 – Differential stress, axial strain, and acoustic activity (number of AE) versus elapsed time during the experiment for (a) Experiment 1, (b) Experiment 2 and (c) Experiment 3 with respectively constant pore pressure of 5 MPa, oscillating pore pressures with a 244 seconds period, with amplitude  $5 \pm 2.5$  MPa and  $5 \pm 0.5$  MPa. Strain rates are estimated for each differential stress step during the secondary steady-state creep.

during the differential stress step prior to failure and during the step of failure for Experiment 1 (a,b), Experiment 2 (c,d) and Experiment 3 (e,f). For Experiment 1, no significant periodicity is detected as expected. More interestingly, in Experiment 2 and 3, the period of Pore pressure oscillations is detected in the AEs catalog only during the failure step, suggesting that the state of stress is a factor of the correlation between small stress perturbations and AEs (note that in steps prior to failure, a non-negligible number of AEs occurs, and the absence of periodicity detection is not caused by the absence of acoustic events). Several correlations are found around the 244 seconds period, most likely because the period of pore pressure oscillations varied a little in time.

In order to follow the time evolution of AEs and pore pressure oscillations over the failure

### 4.3. Dynamic acoustic emission triggering by small periodic pore pressure variations during brittle creep experiments

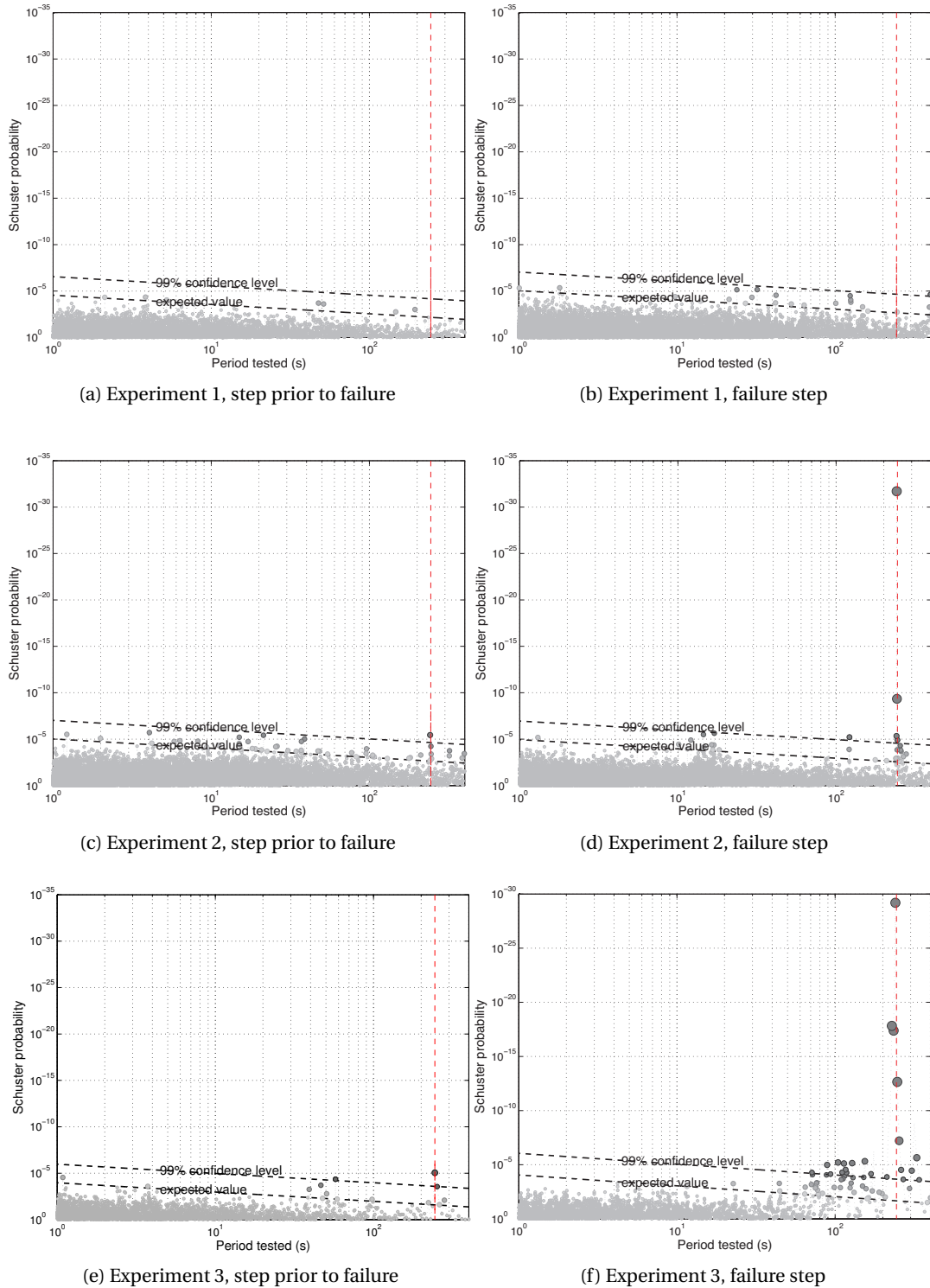


Figure 4.13 – Schuster spectrum computed for catalogs of acoustic emissions events occurring during the differential stress step prior to failure and during the step of failure for Experiment 1 (a,b), Experiment 2 (c,d) and Experiment 3 (e,f). Red dashed line represents a 244 seconds period. The period-dependent “expected value” dashed line represents the expected minimum Schuster p-value, while “99% confidence level” corresponds to 1% of minimum expected values.

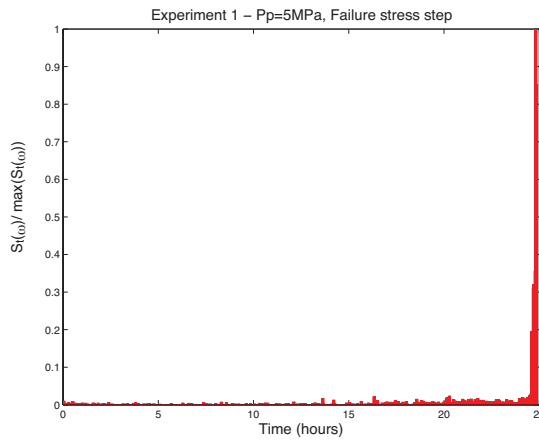
step, we describe the time evolution of Fourier components at the pore pressure oscillation frequency. For a cumulative number of events  $n$  over a time step  $t$ , the correlation coefficient between pore pressure oscillations at a pulsation  $\omega = \frac{2\pi}{T}$ , where  $T$  is the cyclic loading period and AEs is given by:

$$S_t(\omega) = \sqrt{\frac{(\sum_{j=1}^N \frac{dn}{dt} \cos(\omega t_j))^2 + (\sum_{j=1}^N \frac{dn}{dt} \sin(\omega t_j))^2}{\langle \frac{dn}{dt} \rangle}} \quad (4.3)$$

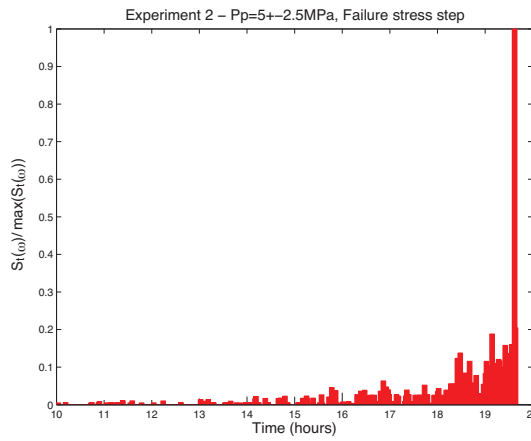
Figure 4.14 shows the time evolution of  $S_t$  during the differential stress step of failure for (a) Experiment 1 where  $P_p=5$  MPa, (b) Experiment 2 where  $P_p= 5\pm 2.5$  MPa and (c) Experiment 3 where  $P_p=5\pm 0.5$  MPa. There is no significant increase in the correlation coefficient in the hours prior to rupture for Experiment 1. Note that  $S_t$  increases dramatically at rupture since a large number of AEs occur within a very short time period. For Experiment 2 and 3,  $S_t$  increases progressively during the 10 and 2 hours prior to rupture respectively. This suggest that during the nucleation phase, small stress perturbations caused by the oscillations of pore pressure may trigger AEs.

We are now interested by the phase of pore pressure oscillations and AEs to investigate whether or not dynamic triggering of AEs by cyclic stress perturbations is a direct or delayed effect. We first compute a coherent mean over the differential stress step of brittle failure for each experiment and compare the number of AEs in time, over a stacked cycle of pore pressure oscillation. Figure 4.15 shows the results of the coherent mean for each experiment, during the differential stress step of failure. As expected, no correlation is observed for Experiment 1. However, AEs occur significantly more when the pore pressure is at its lowest. This suggests that AEs, close to failure, occur more likely when micro-cracks within the rock undergo less pore pressure, and are relatively "unclamped". Finally, we investigate the time evolution of phase correlation between AEs and pore pressure oscillation during the experiments. For a given differential stress step, we determine the angular phase  $\theta$  between the occurrence of each AE and the forcing pore pressure function. By convention, an angle  $\theta = 0$  corresponds to an AE occurring in phase with the forcing function. The AE catalog can be treated as a random walk problem, in which each AE result in a unit length step in the direction defined by its phase angle. If the sequence is random, it will wander. As for the Schuster spectrum in Figure 4.13, the probability  $P$  that a walk is not random above a distance  $D$  can be defined. We use

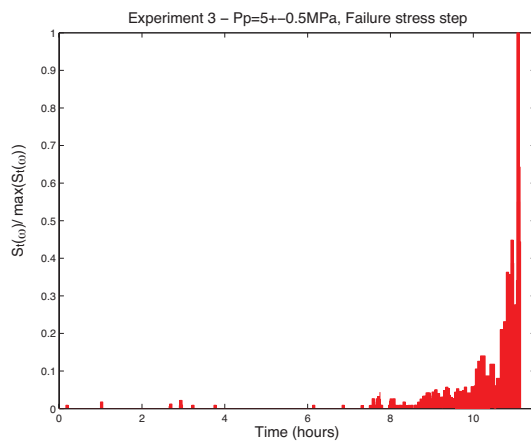
### 4.3. Dynamic acoustic emission triggering by small periodic pore pressure variations during brittle creep experiments



(a) Experiment 1, failure step

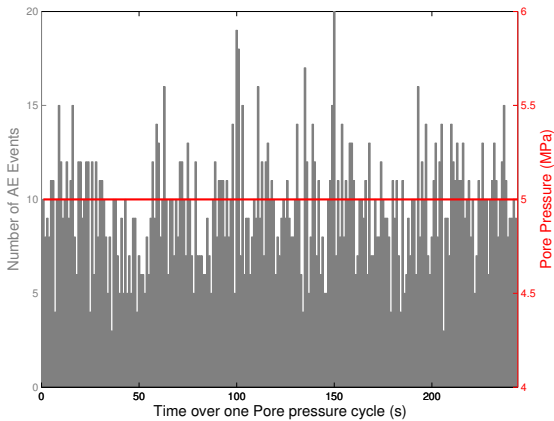


(b) Experiment 1, failure step

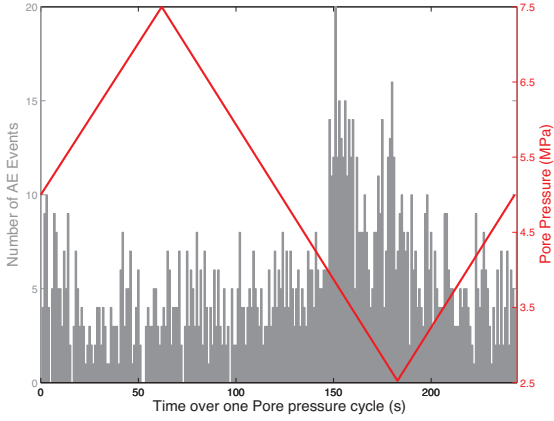


(c) Experiment 2, failure step

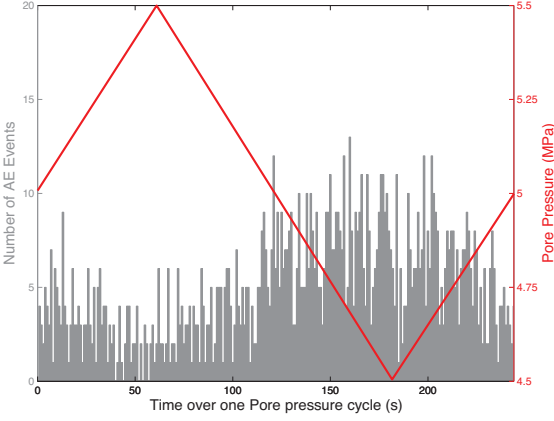
Figure 4.14 – Time evolution of the correlation between acoustic emissions events occurring during the differential stress step of failure and the pore pressure oscillations of pulsation  $\omega = \frac{2\pi}{T}$ ,  $T=244s$ , for Experiment 1 (a), Experiment 2 (b) and Experiment 3 (c). For both Experiments with Pore pressure oscillations, the correlation coefficient increases progressively during a few hours before rupture.



(a) Experiment 1, failure step



(b) Experiment 1, failure step



(c) Experiment 2, failure step

Figure 4.15 – Coherent mean over the differential stress step of brittle failure for (a) Experiment 1, (b) Experiment 2 and (c) Experiment 3 between AEs (gray) and pore pressure oscillations (red), over a stacked cycle of pore pressure oscillation

### 4.3. Dynamic acoustic emission triggering by small periodic pore pressure variations during brittle creep experiments

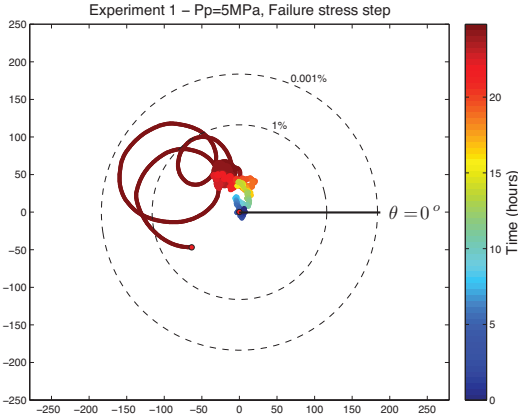
---

the simple expression given by [Schuster \(1897\)](#):

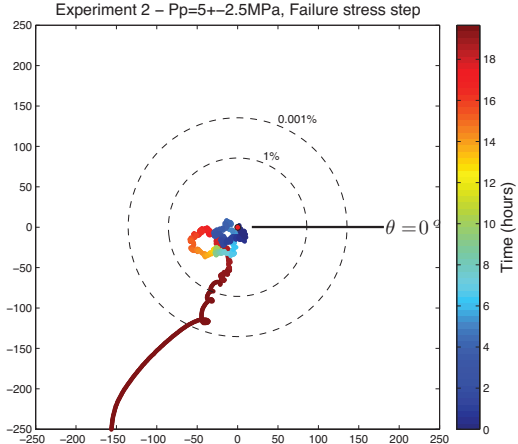
$$P = \exp\left(\frac{-D^2}{N}\right) \quad (4.4)$$

where  $N$  is the number of AEs. Figure 4.16 shows the random walks of AEs occurring during the last differential stress step of each experiments. For Experiment 1, the walk is random at the 99.9% confidence level as expected. The random walk of Experiment 2 and 3 show steady drifts with a phase angle of  $-100^\circ$  and  $-90^\circ$  respectively, within the last hours before brittle failure, with a confidence level above 99.9%. This corresponds, to the approach to and the lowest pore pressure value. We conclude that, there is no significant change in the phase correlation of AEs and pore pressure oscillations for Experiments 2 and 3 and that, correlations observed in figure 4.15 are steady in time.

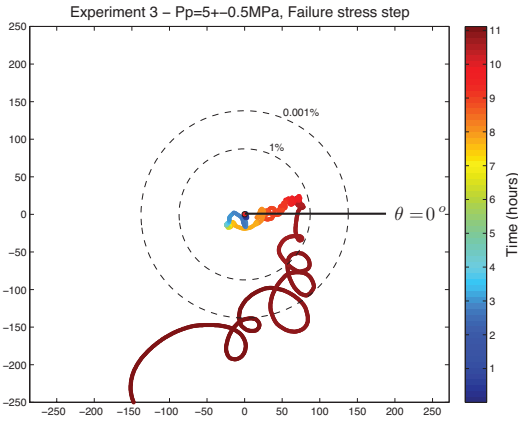
Our experiments, even if only preliminary, show that dynamic triggering of acoustic emissions by small cyclic pore pressure variations during brittle creep experiments on Fontainebleau rock samples, is possible and increase as the rock approaches failure. The phase correlation between AEs and pore pressure variations is steady within the few hours prior to failure and AEs occur most likely when the pore pressure is lower.



(a) Experiment 1, failure step



(b) Experiment 1, failure step



(c) Experiment 2, failure step

Figure 4.16 – Random walks of AEs occurring during the last differential stress step for (a) Experiment 1, (b) Experiment 2 and (c) Experiment 3 and probability confidence levels derived from equation 4.4.

## 4.4 Conclusions

In this *Chapter 4*, we focused on the link between seasonal loading from surface hydrology and seismic activity. We first provided a useful global estimate of spatio-temporal stress and strain evolution induced by variations of mass within the hydrosphere derived from GRACE. Using the example of the Nepal Himalaya, we discussed the influence of seasonal loading on the Main Himalayan Thrust and found a correlation between seasonal stress rate and micro-seismicity in the region, as proposed by other authors ([Bettinelli et al., 2008](#), [Bollinger et al., 2007](#)). Because number of studies in other regions found no significant correlation between seismic rate and seasonal or tidal loading, we investigated the effect of the stress state of the fault on this correlation experimentally. This idea is supported by the work of ([Tanaka, 2010, 2012](#)), who showed that the correlation between tidal loading and earthquakes increases in the nucleation zone prior to large seismic event such as the Sumatra or Tohoku megathrust earthquakes. We conducted laboratory experiments on Fontainebleau sandstone under constant stress, with superimposed sinusoidal pore pressure functions. Our preliminary experimental results show that (1) pore pressure oscillations do not seem to influence the deformation rate at which the rock fails, (2) they correlate with acoustic emissions. Even more interestingly, we observe a progressive increase of the correlation coefficient in time as the rock approaches failure. Finally, we show that, in the last hours of creep before failure, acoustic emissions occur significantly more when the pore pressure is at its lowest. This suggests that the correlation of small stress perturbations and acoustic emissions depends on the state stress of a rock and the amplitude of the perturbations and that emissions occur more likely when cracks are unclamped. In other words, our observations suggests that triggering from periodic loading, whether it is tidal or seasonal, might occur favorably during the long nucleation phase of earthquakes.



## CONCLUSIONS

Modeling accurately seasonal deformation of the Earth induced by mass redistributions within the hydrosphere has become possible thanks to the recent advances in global geodesy. Indeed, even if the theoretical framework had been available for a long time, the access to large scale variations of surface hydrology and the precise measure of ground deformation is only recent. First, the Gravity Recovery and Climate Experiment (GRACE) has now provided over 10 years of high spatial and temporal resolution measurement of the gravity field variations. Secondly, the globally distributed continuous stations of the Global Positioning System (GPS) record accurately the daily ground deformation. One of the motivations of this thesis was to bring these two datasets together and provide a precise model of deformation of the Earth by seasonal hydrology, for both horizontal and vertical components. Comparable to tides, once properly modeled, physics-based seasonal deformation models have far reaching implications in global geodesy. First, seasonal motion is one of the current factors limiting the accuracy and precision of the definition of international terrestrial reference frame. Then, unless accounted for, they can bias estimations of GNSS site velocities intended for high accuracy purposes such as plate tectonics and reference frames. Accurate seasonal deformation models are also crucial for the detection of transient deformation of similar amplitude and close periodicity. Understanding the Earth's deformation under loads of multiple wavelengths at an annual time scale can also provide useful constraints on its rheology.

In this manuscript, we first focused on modeling seasonal variations recorded by the GPS stations in across the Himalaya range. Our study confirmed that these signals are primarily due to surface load variations induced by continental hydrology. The comparison between the homogeneous elastic half-space and a PREM type model highlighted the importance of using realistic Earth models when predicting vertical and horizontal displacements induced by surface loading, and suggest that simple half-space models should not be used to derive

## Conclusions

---

elastic properties of the Earth.

We then extend the model to a global scale and show that there was a systematic under-prediction and phase lag of the horizontal observations while the vertical displacements are fairly well predicted. After excluding several potential contributors, we show that, degree-one deformation and associated geocenter motion are of importance when modeling seasonal ground deformation and that existing models to replace GRACE uncaptured degree-one components are not necessarily appropriate for modeling seasonal horizontal displacements and derived our own estimate of this contribution, using a 6-parameters Helmert transform, best fitting the horizontal. The model improved considerably the horizontal predictions without degrading the fit to the vertical observations. Because of a remaining small global under-prediction of the horizontal components, we then question the validity of a purely elastic model derived from seismic measurements at an annual time scale. We show that including mantle volume variations due to phase transformations may be of importance, even at an annual time scale and improves the accuracy of our model. As a by-product, we showed that seasonal deformation could be used to place constraints of viscoelastic rheologies of the Earth at a temporal scale comparable to post-seismic studies.

Finally, we investigated the effect of seasonal variations of surface loading on faults by giving first and estimate of stress and strain evolution induced by variations within the hydrosphere. We then derive the Coulomb Failure Function (CFF) induced by seasonal loading on the Main Himalaya Thrust and show that seismic activity in the region correlates with the CFF rate, as suggested by previous studies. We then conducted laboratory experiments on Fontainebleau sandstone under constant stress, with superimposed sinusoidal pore pressure functions. Our preliminary experimental results suggest that the correlation of small stress perturbations and acoustic emissions depends primarily on the state stress of the rock and that emissions occur more likely when cracks are unclamped. In other words, our observations suggests that tidal triggering might occur favorably during the long nucleation phase of earthquake.

Our seasonal global deformation and stress model derived from variations within the hydrosphere measured by GRACE is now satisfyingly, even if still improvable, and opens the

way to other interesting studies. First, the re-analysis of GPS time series exhibiting transient deformation such as the observed slow slip events in the Cascadia area. Indeed, because the amplitude and timing of these slow slip events is comparable to seasonal signals, accurately modeling non-tectonic signals and removing them from geodetic time series is crucial. All studies in the Cascadia area treat the seasonal signals as a common annual mode to all stations as they are relatively close (Szeliga et al., 2008, Dragert et al., 2001, Rogers & Dragert, 2003). However, one need to be careful when removing empirical seasonal displacements as the signal contains a spatio-temporal evolution and inter-annual variations and using predictions from a global seasonal model rather than an empirical estimate becomes possible, even for horizontal components. In addition, as proposed by Lowry (2006) and confirmed by Ader et al. (2012b), periodic slow slip events may be a resonant response to climate-driven stress perturbations and further investigation in some regions, using an accurate seasonal deformation model may be of interest. Another interesting application would be the investigation of deep seismicity seasonality. Indeed, as shown by Schubnel et al. (2013), phase transformations of metastable olivine might trigger deep-focus earthquakes (400 to 700 km) in cold subducting lithosphere. If the importance of phase transformation in modeling the seasonal surface deformation is verified, annual hydrological forcing may be related to the occurrence of deep-focus earthquakes.



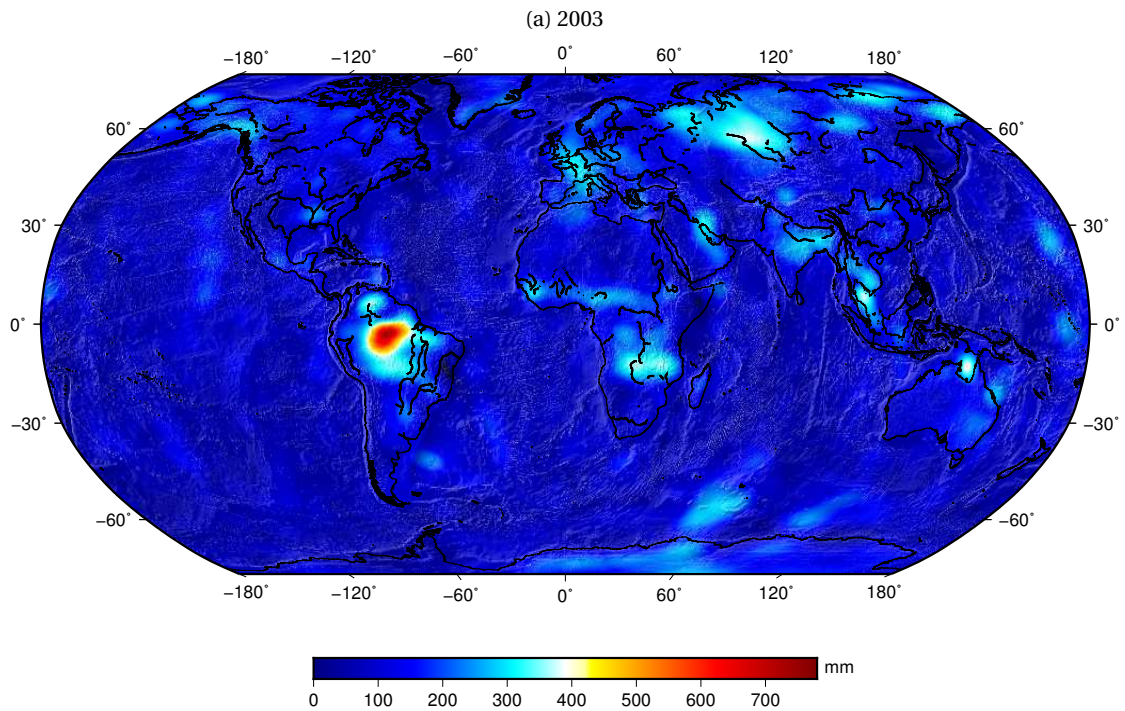
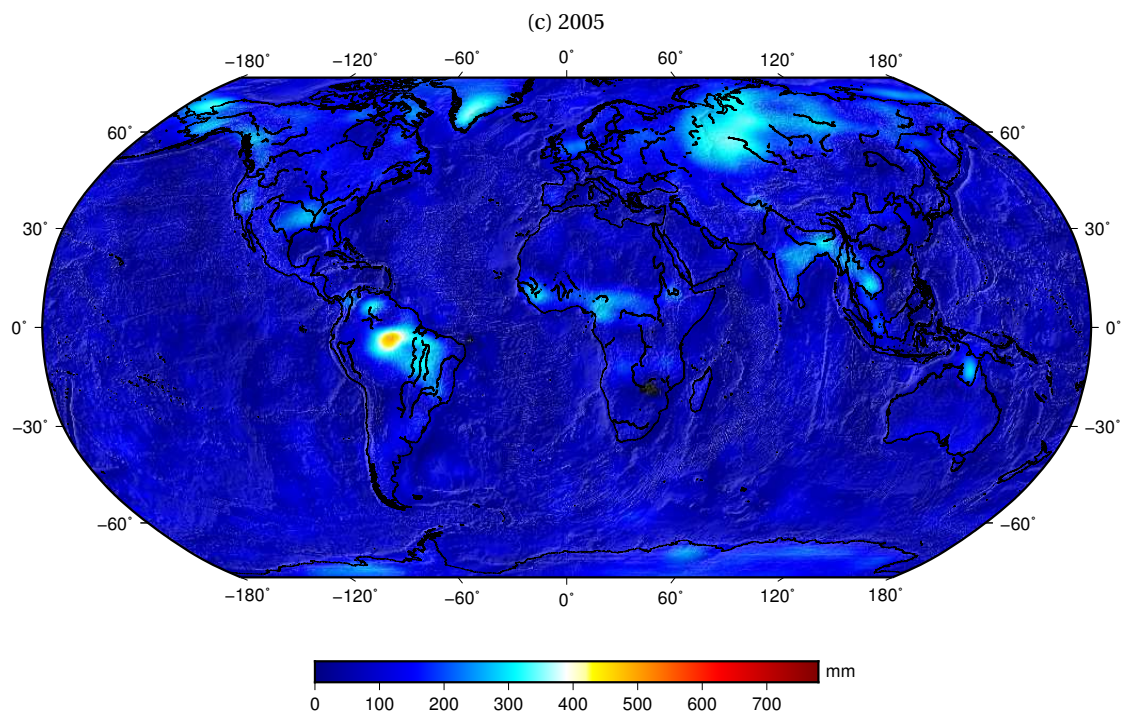
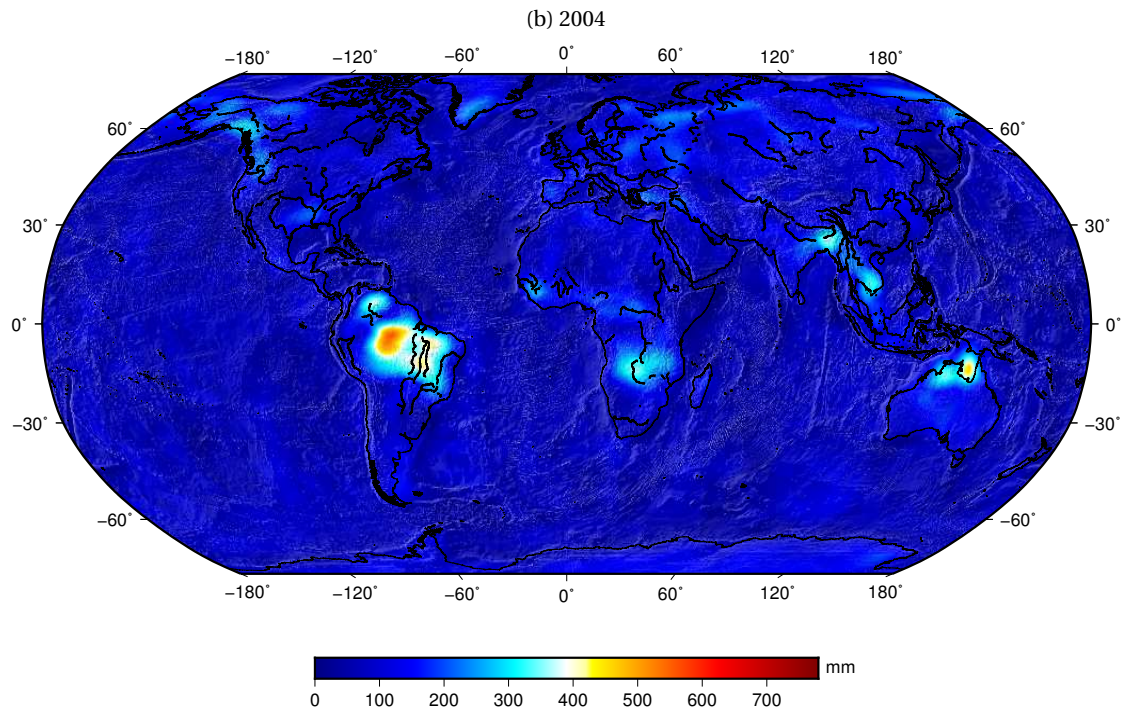
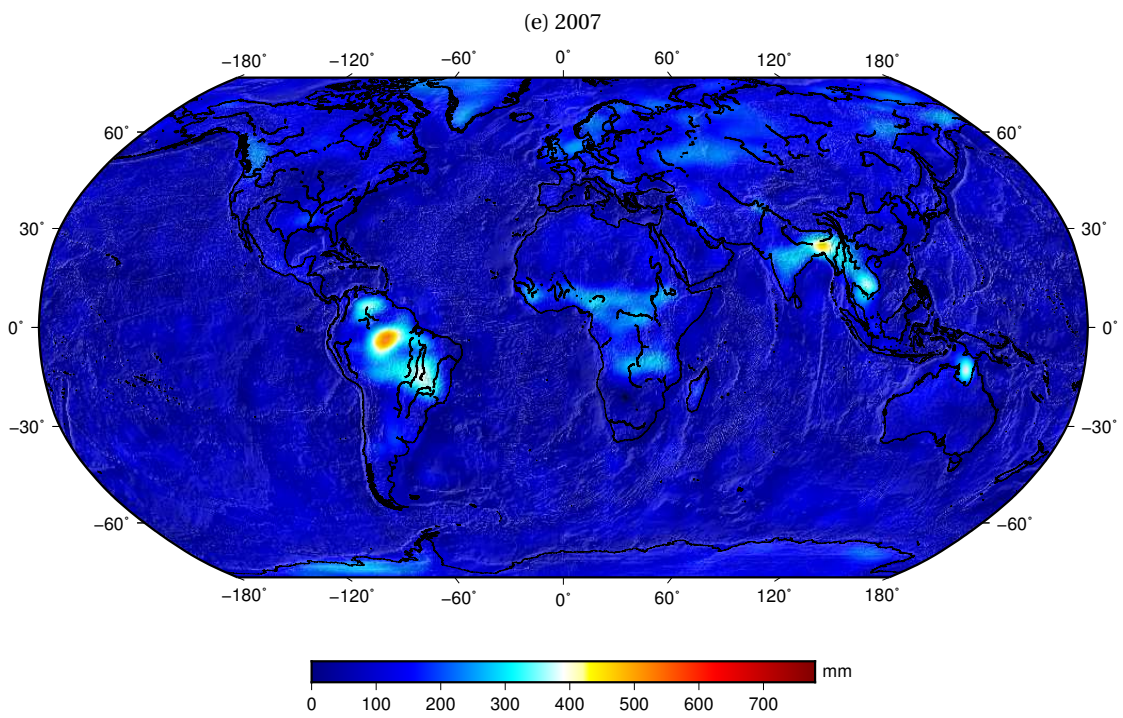
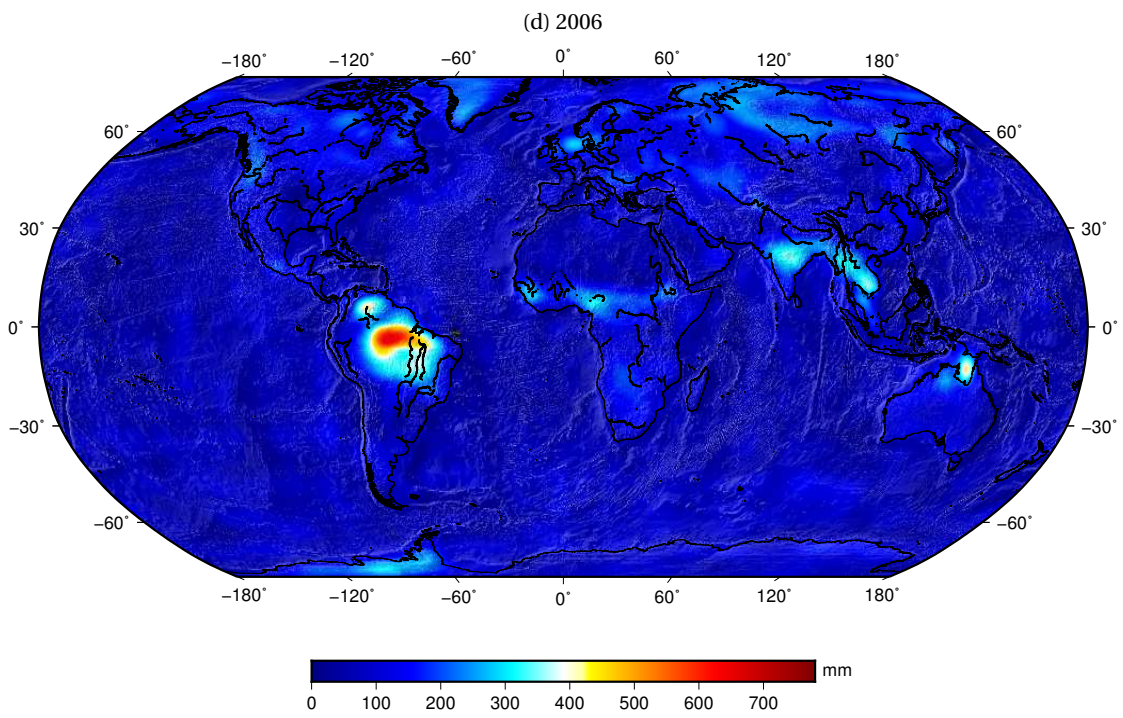


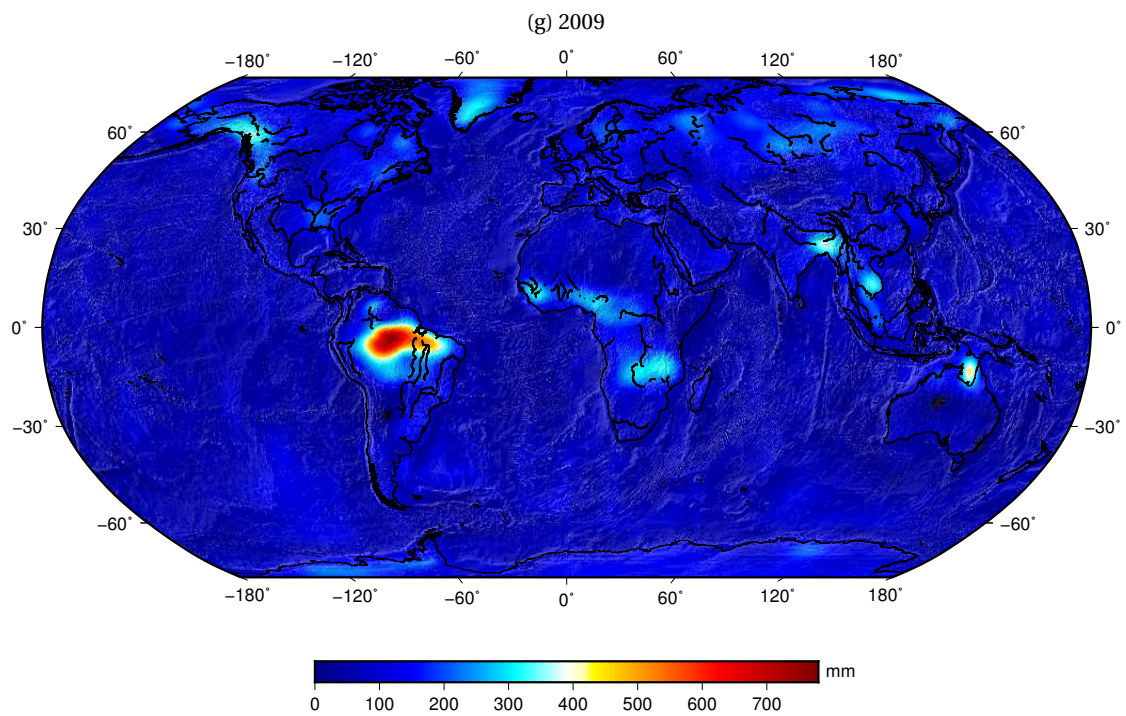
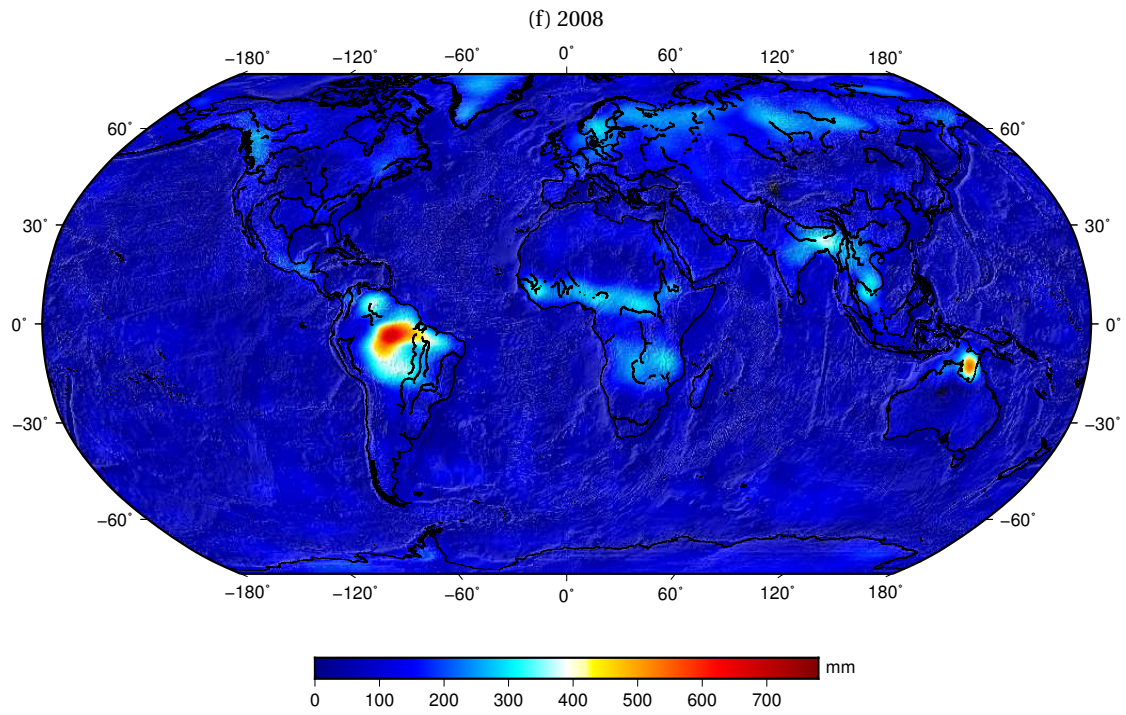
Figure A.2 – Peak to peak surface load variations, expressed in equivalent water height (in mm), derived from GRACE for years 2003 to 2011 period and corrected from detectable earthquakes coseismic contributions, for inter-annual comparison

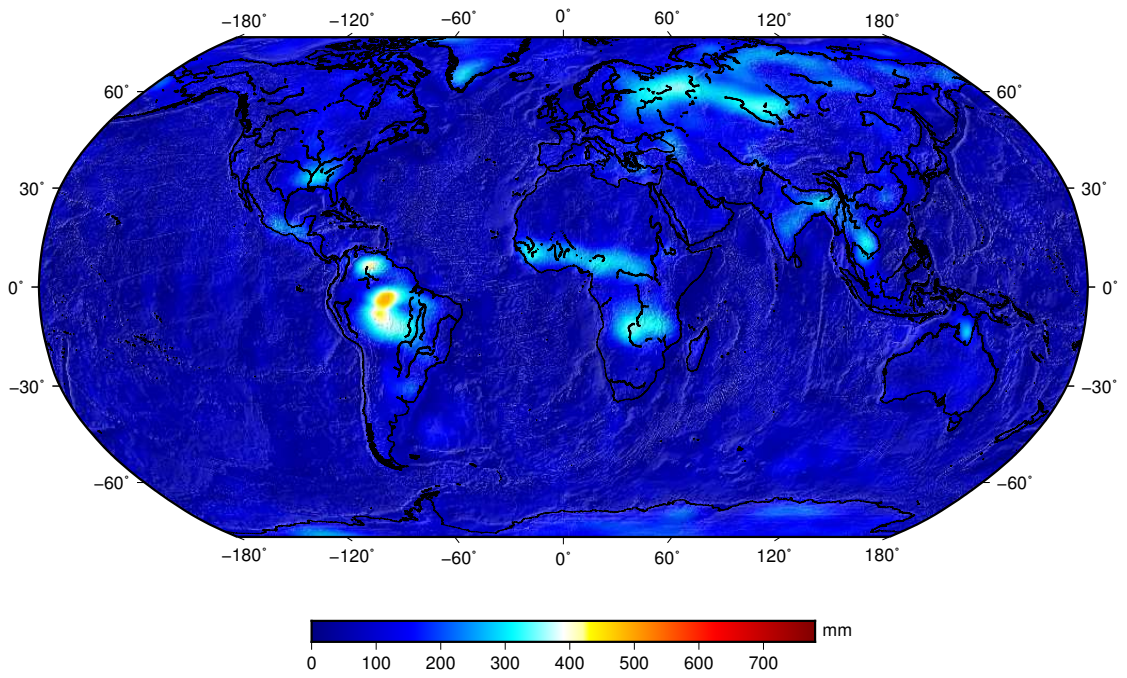
## Appendix A. GRACE seasonal amplitude



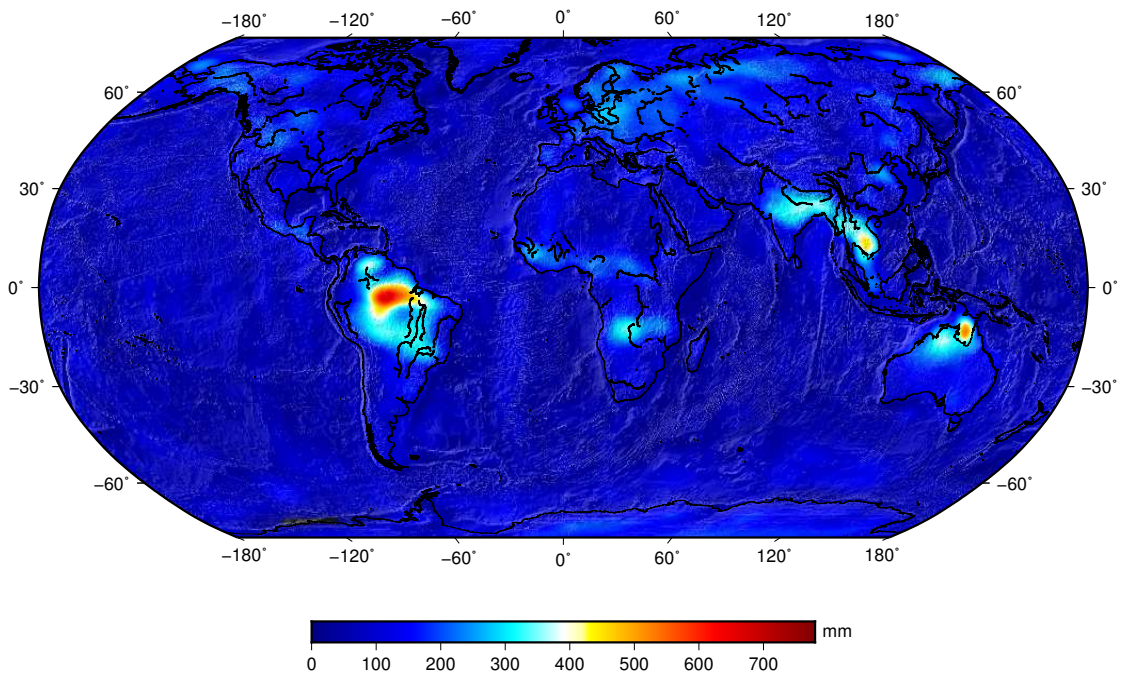


## Appendix A. GRACE seasonal amplitude





(h) 2010



(i) 2011



Geodetic horizontal and vertical seasonal displacements recorded by continuous stations of the Global Positioning System (cGPS) can be fairly well predicted as the response of a spherical and layered elastic Earth to annual variations of continental water storage. For this purpose, we use satellite data from the Gravity Recovery and Climate Experiment (GRACE) to determine the seasonal time evolution of surface loading. We then compute the surface displacements induced by loading a layered non-rotating spherical Earth model (Farrell, 1972, Guo et al., 2004) based on the Preliminary Reference Earth Model and a local seismic velocity model (Dziewonski & Anderson, 1981, Monsalve et al., 2006).

## B.1 Contents

To get started, download the "Matlab script-Chanard et al, JGR-2014" folder, containing the following files:

- `main.m`, main function of the code,
- `calendar.txt`, time vector of loading files
- `grace_global`, folder containing GRACE global loading grids for seasonal hydrology by date,
- `extraction_grace_area.m`, extracts loading zone form global GRACE data in `grace_global`
- `model_seasonal_var.m`, models displacements induced by seasonal variations of surface hydrology derived from GRACE,
- `cgps_sites.txt`, GPS stations location file,
- `prem.data`, input code table specific to the modified PREM Earth structure,

## Appendix B. Code associated with Chapter 2

---

- `plot_disp_ts.m`, plots East/North/Vertical displacement time series at all locations specified in `cgps_sites.txt` file or at specific location using station name,
- `plot_grace_ts.m`, plots Equivalent Water Height time series derived from GRACE at a specific points given as inputs,
- `plot_tmaps.m`, plots GRACE loading map and East/North/Vertical displacement maps for extracted zone at specific date.

Note: if you want to use other loading datasets, replace the loading files and the time vector `calendar.txt`.

### B.2 Set up & Computation

1. You must have Matlab installed on your computer.
2. In Matlab environment, go to Matlab script-`Chanard et al, JGR-2014/code`.
3. Modify the continuous gps stations coordinates `cgps_sites.txt` to compute seasonal displacements at wished locations. The file must have 3 columns : station name - longitude (degree) - latitude (degree). Here, longitudes are expressed in  $[-180^{\circ};180^{\circ}]$ .
4. Run the main function with inputs longitude and latitude vectors of the chosen loading area and the name of your stations locations file. If you want to compute seasonal displacements at stations located in the Himalayas, run for example:

```
main(70.5:110.5,10.5:40.5,'cgps_sites.txt')
```

Note that stations in `cgps_sites.txt` must be in the loading area to avoid NaN values of the seasonal displacements.

5. The `extraction_grace_area.m` function will automatically create a `grace_extract` folder containing loading files in the chosen area.
6. You will then be asked:

```
Do you want to compute Green function? y/n
```

Compute the Green functions by answering `y` only once for a specific loading area. Note that the larger the area, the longer the computation. If you answer `y`, the code will create two files `green_functions_horizontal.mat` and `green_functions_vertical.mat`, surface displacements of the area induced by unit loads.

7. Finally, the code will create two output folders. The first one, `disp_zone`, contains `.mat`

files of east,north and vertical displacements for all points in loading zone, by date (in `calendar.txt`). The second one, `disp_gps`, contains ascii files of t/east/north/vertical displacements at each location referenced in your `gps` location file.

### B.3 Plotting tools

1. `plot_disp_ts` plots East/North/Vertical displacement time series at all locations specified in the `gps` location file or at a specific location using station name. The function does not require arguments. Figures will be saved as `.eps` files in the created folder `disp_gps/figures`.
2. `plot_grace_ts(lon,lat)` plots Equivalent Water Height (EWH) time series derived from GRACE at a specific lon/lat vectors given as inputs. Figures will be saved as `.eps` files in the created folder `grace_extract/figures`.
3. `plot_tmaps(lon,lat,fdate)` plots GRACE loading map and East/North/Vertical displacement maps for extracted (lon,lat) zone at specific date (fdate). Figures will be saved as `.eps` files in the created folder `disp_zone/figures`.

## Appendix B. Code associated with Chapter 2

---

```
1 function main(lon,lat,cgps_location)
2
3 % Compute surface displacements induced by seasonal variations of
4 % continental water, non-tidal and atmospheric surface loading
5 %
6 % Loading data:
7 % from GRACE, processed by CNRS-GRGS (http://grgs.obs-mip.fr/grace)
8 %
9 % Input: - lat: latitude vector of loading zone
10 %        - lon: longitude vector of loading zone
11 % (note that the GRACE loading grid has a 1x1 degree spacing)
12 %        - 'cgps_location': text file in between quotes with
13 %                               station_name/longitude/latitude where you wish to
14 %                               compute displacements induced by surface loads
15 %
16 % Output: - grace_extract folder with equivalent water height files for
17 %           loading zone / date
18 %          - green_functions_horizontal.mat
19 %          - green_functions_vertical.mat
20 %          - disp_zone folder with .mat files of east,north and
21 %            vertical displacements for all points in loading zone, by
22 %            date
23 %          - disp_gps folder with ascii files of t/east/north/vertical
24 %            displacements at each location referenced in 'cgps_location'
25 %            file
26 %
27 % Calls: - extraction_grace_area.m to extract loading zone from GRACE data
28 %         - model_seasonal_var.m to compute displacements induced by surface
29 %           loads in the loading zone and at locations referenced in
30 %           'cgps_location' file
31 %
32 % Called by: none
33 %
34 % Associated plotting functions:
35 %          - plot_disp_ts.m: displacement time series at gps stations
36 %          - plot_grace_ts.m: equivalent water height (EWH) time series
37 %            derived from GRACE
38 %          - plot_tmaps.m: maps of EWH, East/North/Vertical displacements in
39 %            extracted loading zone / time
40 %
41 % K. Chanard, last modified 20-03-14, from M. Barre 31-07-14
42
43
44
```

```
45 %%          ***** Load GRACE data *****
46
47 % Create 'grace_extract' folder containing loading files in the zone of
48 % interest, from GRACE global dataset
49
50 extraction_grace_area(lon,lat);
51
52 % Note to change input loading data
53 % If you wish to use another loading dataset, create your own lon/lat/h
54 % files by date in a grace_extract folder and modify calendar.txt
55
56 %%          ***** Compute displacements *****
57
58 model_seasonal_var(lon,lat,cgps_location);
59
60 end

1
2 function extraction_grace_area(lon,lat)
3
4 % Extracts loading zone form global GRACE data in grace_global
5 %
6 % Note:
7 % we empirically model and remove secular trends and earthquake-induced
8 % mass redistribution observable in the gravity field measurements of M>7.5
9 % within the 2002-2012 GRACE time span.
10 %
11 % Loading data:
12 % from GRACE, processed by CNRS-GRGS (http://grgs.obs-mip.fr/grace)
13 %
14 % Input: - lat: latitude vector of loading zone
15 %         - lon: longitude vector of loading zone
16 % (note that the GRACE loading grid has a 1x1 degree spacing)
17 %
18 % Output: - grace_extract folder with equivalent water height files for
19 %           loading zone / date
20 %
21 % Calls: none
22 % Called by: main.m
23 %
24 % K. Chanard, last modified 20-03-14, from M. Barre 31-07-14
25
26
```

## Appendix B. Code associated with Chapter 2

---

```
27 nlat = length(lat); nlon = length(lon);
28 lon1 = lon(1); lon2 = lon(nlon);
29 lat1 = lat(1); lat2 = lat(nlat);
30
31 grace_directory_g = dir(fullfile('./grace_global/20*'));
32 grace_global = {grace_directory_g.name}';
33 ngrace_g = length(grace_global);
34
35 if ~exist('grace_extract', 'dir')
36     mkdir('grace_extract');
37 end
38
39     for j=1 : ngrace_g;                                % Analysis of each GRACE
40         data
41         disp(sprintf('Extracting zone lon=[%3.1f,%3.1f], lat=[%3.1f,%3.1f] from
42             GRACE file # %d out of 365',lon1,lon2,lat1,lat2,j))
43         name_j = grace_global{j};                      % Conserve current file's
44             name
45
46         grace_j = fullfile('./grace_global',grace_global{j});
47         [lon_m,lat_m,loads_m] = textread(grace_j,'%f%f%f');
48
49         ind1 = find(lat_m <= lat2 & lat_m >= lat1); % Keep only latitudes
50             belonging to the study area
51         ind2 = find(lon_m <= lon2 & lon_m >= lon1); % Keep only longitudes
52             belonging to the study area
53
54         ind = intersect(ind1, ind2);                  % Junction of the 2
55             conditions
56         grace_j = zeros(length(ind),3);
57
58         for i = 1 : length(ind);
59             grace_j(i,:) = [lon_m(ind(i)),lat_m(ind(i)),loads_m(ind(i))];
60
61             % Creation of a new GRACE
62             data containing
63             informations of
64             % points of the study area
65             only
66
67         end
68
69         cd ./grace_extract
70
71         dlmwrite([num2str(name_j)], grace_j,'delimiter','\t','precision',9);
```

```
61                                     % All theses GRACE data
                                     files keep the same name
                                     and are stocked
62                                     % in the 'grace_extract' file
63     cd ../
64
65     end
66
67 end

1
2 function model_seasonal_var(lon,lat,cgps_location)
3
4 % Modeling deformation induced by seasonal variations of continental
5 % water in the Himalaya region : Sensitivity to Earth elastic structure
6 %
7 % Input: - lat: latitude vector of loading zone
8 %         - lon: longitude vector of loading zone
9 % (note that the GRACE loading grid has a 1x1 degree spacing)
10 %         - 'cgps_location': text file in between quotes with
11 %                                     station_name/longitude/latitude where you wish to
12 %                                     compute displacements induced by surface loads
13 %
14 % Output: - grace_extract folder with equivalent water height files for
15 %          loading zone / date
16 %          - green_functions_horizontal.mat if required (only once for a specific
17 %             zone)
18 %          - green_functions_vertical.mat if required (only once for a specific
19 %             zone)
20 %          - disp_zone folder with .mat files of east,north and
21 %             vertical displacements for all points in loading zone, by
22 %             date
23 %          - disp_gps folder with ascii files of t/east/north/vertical
24 %             displacements at each location referenced in 'cgps_location'
25 %             file
26 % Calls: subfunctions within file
27 % Called by: main.m
28 %
29 % K. Chanard, last modified 20-03-14
30 %% load GRACE data
31 grace_directory = dir(fullfile('./grace_extract/20*'));
```

## Appendix B. Code associated with Chapter 2

---

```
32 grace_files = {grace_directory.name};
33 ngrace=length(grace_files);
34
35 time = textread('./calendar.txt','%f');
36
37 %% GPS coordinates
38 [rname,rlon,rlat] = textread(cgps_location,'%s%f%f');
39 ngps = length(rname);
40
41 %% BUILD THE MESH
42 [iclone,iclat,~] = textread('./grace_extract/2002_08_08_2002_08_17','%f%f%f');
43 deg2rad = pi/180;
44 nlat = length(lat);
45 nlon = length(lon);
46 nall = nlat*nlon;
47 iclon = reshape(iclon,nlon,nlat);           % return a nlon-by-nlat matrix whose
      elements are taken column-wise from iclon
48 iclat = reshape(iclat,nlon,nlat);
49 iwlon = ones(size(iclat(:)));
50 iwlat = ones(size(iclat(:)));
51
52 [oolon,oolat] = meshgrid(lon,lat);         % replicates the grid vector lon and lat
      to produce a full grid
53
54 %% COMPUTE THE GREEN FUNCTIONS
55
56 prompt = 'Do you want to compute Greens function? y/n : ';
57 str = input(prompt,'s');
58
59 if str=='y'
60 %   Vertical component
61
62     for n=1 : size(oolat(:))
63         disp(sprintf('Computing vertical Green functions at grid point # %d out
64             of %d',n,nall))
65         olat = oolat(n).*deg2rad;
66         olon = oolon(n).*deg2rad;
67         [udisp] = load_disp_u(iclat.*deg2rad,iclone.*deg2rad,iwlat.*deg2rad,iwlon
68             .*deg2rad,olat,olon,1);
69         greenf_u(n,:) = udisp(:);
70     end
71
72     save green_functions_vertical greenf_u
73
```

```

72 % Horizontal components
73
74 for n=1 : size(oolat(:))
75     disp(sprintf('Computing horizontal Green functions at grid point # %d out
76                 of %d',n,nall))
77     olat = oolat(n).*deg2rad;
78     olon = oolon(n).*deg2rad;
79     [edisp,ndisp] = load_disp(iclat.*deg2rad,iclou.*deg2rad,iwlat.*deg2rad,
80                             iwlon.*deg2rad,olat,olon,2);
81     greenf_e(n,:) = edisp(:);
82     greenf_n(n,:) = ndisp(:);
83 end
84
85 save green_functions_horizontal greenf_e greenf_n
86
87 end
88
89 load green_functions_horizontal
90 load green_functions_vertical
91
92 if ~exist('disp_zone', 'dir')
93     mkdir('disp_zone');
94 end
95
96 for ii=1:ngrace
97
98     file = fullfile('./grace_extract',grace_files{ii});
99     [iclou,iclat,loads] = textread(file,'%f%f%f');
100     tloads(ii,:)=loads;
101     loads=loads./1e3; % mm to m of equivalent water height
102     iclou = reshape(iclou,nlon,nlat);
103     iclat = reshape(iclat,nlon,nlat);
104
105     name_grace_file = grace_files(ii);
106
107     for n=1 : size(oolat(:))
108         ccn(ii,n) = nansum(greenf_n(n,:).*loads(:)'); % (ii,n) ii and n mean
109                 temporal and spatial, respectively.
110         cce(ii,n) = nansum(greenf_e(n,:).*loads(:)');
111         ccu(ii,n) = nansum(greenf_u(n,:).*loads(:)');
112     end
113
114     tmpn = reshape(squeeze(ccn(ii,:)),nlat,nlon); % return the nlat-by-
115                 nlon matrix tmpn whose elements are taken column-wise from squeeze(ccn(

```

## Appendix B. Code associated with Chapter 2

---

```
    ii,:))
112     tmpe = reshape(squeeze(cce(ii,:)),nlat,nlon);
113     tmpu = reshape(squeeze(ccu(ii,:)),nlat,nlon);
114
115     alln(ii,:,:)= tmpn;           % alln alle allu are
    all displacements on the grid
116     alle(ii,:,:)= tmpe;
117     allu(ii,:,:)= tmpu;
118
119
120     file_du = sprintf('disp_zone/%s_du.mat',grace_files{ii});
121     save(file_du,'tmpu');
122     file_dn = sprintf('disp_zone/%s_dn.mat',grace_files{ii});
123     save(file_dn,'tmpn');
124     file_de = sprintf('disp_zone/%s_de.mat',grace_files{ii});
125     save(file_de,'tmpe');
126
127
128
129     for jj=1 : ngps
130         ein = interp2(oolon,oolat,tmpn,rlon(jj),rlat(jj));
131         eie = interp2(oolon,oolat,tmpe,rlon(jj),rlat(jj));
132         eiu = interp2(oolon,oolat,tmpu,rlon(jj),rlat(jj));
133         nn(ii,jj) = ein;
134         ee(ii,jj) = eie;
135         uu(ii,jj) = eiu;
136
137
138
139
140
141
142     end
143
144     save('grace_extract/grace_ts','time','tloads','iclone','iclat'); % save
    displacements at cgps stations in .mat file
145
146         % displacements (time,gps_station)
147
```

```

148     if ~exist('disp_gps', 'dir')
149         mkdir('disp_gps');
150     end
151
152     save('disp_gps/displacements_cgps','time','uu','nn','ee','rname','ngps'); %
153         save displacements at cgps stations in .mat file
154         for i=1:ngps
155             tmp=[time,nn(:,i),ee(:,i),uu(:,i)];
156             file_ts=sprintf('disp_gps/%s.txt',rname{i}); % save time series of
157                 displacements at each cgps station in text file
158             save(file_ts,'-ascii','tmp')
159         end
160     end
161
162     function [udisp] = load_disp_u(iclat,iclcn,iwlat,iwlcn,olat,olon,indx)
163     % green functions for prem with continental crust based on Guo et al.(2004)
164     % indx 1:ur 2:utheta 3:G^E 4:t^E 5:err 6:ethetatheta 7:elamdalamda
165     % indx 3 and x by 1E5.
166
167     readf('prem.data');
168     nlen = length(iwlat);
169     disp_u = zeros(nlen,1);
170
171     for n=1 : nlen
172         wlat = iwlat(n);
173         wlcn = iwlcn(n);
174         clat = iclat(n);
175         clcn = iclcn(n);
176
177         if indx == 1
178             udisp(n) = gdisp2(clat,clcn,wlat,wlcn,olat,olon,indx);
179         end
180
181         if indx == 2
182             [displ(n)] = gdisp2(clat,clcn,wlat,wlcn,olat,olon,indx);
183             [az] = azrad(olat,olon,clat,clcn);
184             ndisp(n) = displ(n).*cos(az);
185             edisp(n) = displ(n).*sin(az);
186         end
187     end
188 end
189

```

## Appendix B. Code associated with Chapter 2

---

```
190 function [edisp, ndisp] = load_disp(iclat, iclon, iwlat, iwlon, olat, olon, indx)
191 % green functions for prem with continental crust based on Guo et al.(2004)
192 % indx 1:ur 2:utheta 3:G^E 4:t^E 5:err 6:ethetatheta 7:elamdalamda
193 % indx 3 and x by 1E5.
194
195 readf('prem.data');
196 nlen = length(iwlat);
197 disp_u = zeros(nlen,1);
198
199 for n=1 : nlen
200     wlat = iwlat(n);
201     wlon = iwlon(n);
202     clat = iclat(n);
203     clon = iclon(n);
204
205     if indx == 1
206         udisp(n) = gdisp2(clat, clon, wlat, wlon, olat, olon, indx);
207     end
208
209     if indx == 2
210         [disp(n)] = gdisp2(clat, clon, wlat, wlon, olat, olon, indx);
211         [az] = azrad(olat, olon, clat, clon);
212         ndisp(n) = disp(n).*cos(az);
213         edisp(n) = disp(n).*sin(az);
214     end
215
216 end
217 end
218
219
220 function [gauss] = gdisp2(clat, clon, wlat, wlon, olat, olon, indx)
221 % Gauss-Legendre Quadrature
222
223 earthr = 6.371e6;
224 gausst = 9999;
225 [area] = areasph(clat, clon, wlat, wlon);
226
227 for dim=1 : 6;
228     r = [];
229     w = [];
230
231     if (dim==1);
232         r(1: 2) = [-0.577350269189626; 0.577350269189626];
233         w(1: 2) = [ 1.000000000000000; 1.000000000000000];
```

```

234     elseif (dim==2);
235         r(1: 3) = [-0.774596669241483; 0.000000000000000; 0.774596669241483];
236         w(1: 3) = [ 0.5555555555555556; 0.888888888888889; 0.555555555555556];
237     elseif (dim==3);
238         r(1: 4) = [-0.861136311594053;-0.339981043584856; 0.339981043584856;
                0.861136311594053];
239         w(1: 4) = [ 0.347854845137454; 0.652145154862546; 0.652145154862546;
                0.347854845137454];
240     elseif (dim==4);
241         r(1: 5) = [-0.906179845938664;-0.538469310105683; 0.000000000000000;
                0.538469310105683; 0.906179845938664];
242         w(1: 5) = [ 0.236926885056189; 0.478628670499367; 0.568888888888889;
                0.478628670499367; 0.236926885056189];
243     elseif (dim==5);
244         r(1: 5) =
                [-0.973906528517;-0.865063366689;-0.679409568299;-0.433395394129;-0.14887433898];
                r(6:10)=-fliplr(r(1:5));
245         w(1: 5) = [ 0.066671344309; 0.149451349151; 0.219086362516;
                0.269266719310; 0.29552422472]; w(6:10)= fliplr(w(1:5));
246     elseif (dim==6);
247         r(1:10) =
                [-0.993128599185;-0.963971927278;-0.912234428251;-0.839116971822;-0.74633190646;...
                -0.636053680727;-0.510867001951;-0.373706088715;-0.227785851142;-0.07652652113];
                r(11:20)=-fliplr(r(1:10));
248         w(1:10)=[ 0.017614007068; 0.040601429882; 0.062672048298; 0.083276741551;
                0.10193011983;...
                0.118194531969; 0.131688638458; 0.142096109327; 0.149172986482;
                0.15275338714]; w(11:20)= fliplr(w(1:10));
249
250     end
251
252
253     ww = w'*w;
254     rlat = clat+.5.*wlat.*r;
255     rlon = clon+.5.*wlon.*r;
256
257     [rrlat,rrlon] = meshgrid(rlat,rlon);
258     angp = acos(sin(rrlat(:)).*sin(olat)+cos(rrlat(:)).*cos(olat).*cos(rrlon(:)-
                olon));
259     [grnp] = greenp(angp,indx);
260     gauss = sum(ww(:).*grnp(:)./(angp(:).*earthr)).*1E-12.*area./4;
261
262     if abs(1-gausst./gauss) < 0.0001; break; end; gausst=gauss;
263 end
264 end

```

## Appendix B. Code associated with Chapter 2

---

```
265
266
267
268 function [area] = areasph(cclat,cclon,wlat,wlon)
269 % GRACE data are date on each 1x1deg grid of the earth. This function compute
270 %the area of each 1x1deg compartement; It depends on where we are on the
271 %earth (latitude, pole)
272
273 earthr = 6.371e6;
274
275 if wlat*wlon > 3e-5 ;
276     alat = cclat-0.5.*wlat; alon = cclon-0.5.*wlon;
277     blat = cclat+0.5.*wlat; blon = cclon-0.5.*wlon;
278     clat = cclat+0.5.*wlat; clon = cclon+0.5.*wlon;
279     dlat = cclat-0.5.*wlat; dlon = cclon+0.5.*wlon;
280
281     [sinab,cosab] = angrad(alat,alon,blat,blon);
282     [sinbc,cosbc] = angrad(blat,blon,clat,clon);
283     [sincd,coscd] = angrad(clat,clon,dlat,dlon);
284     [sinac,cosac] = angrad(alat,alon,clat,clon);
285     [sinbd,cosbd] = angrad(blat,blon,dlat,dlon);
286     [sinda,cosda] = angrad(dlat,dlon,alat,alon);
287
288     a = acos((cosbd-cosab.*cosda)./(sinab*sinda));
289     b = acos((cosac-cosab.*cosbc)./(sinab*sinbc));
290     c = acos((cosbd-coscd.*cosbc)./(sincd*sinbc));
291     d = acos((cosac-coscd.*cosda)./(sincd*sinda));
292
293     area = (a+b+c+d-2*pi).*earthr.*earthr;
294
295     for i=1 : length(cclat)
296
297         if area(i)==0 || isnan(area(i));
298             area(i) = wlat(i).*wlon(i).*earthr.*earthr.*cos(cclat(i)).*cos(0.5*
299                 wlat(i));
300
301         end
302     else
303         area = wlat.*wlon.*earthr.*earthr.*cos(cclat).*cos(0.5*wlat);
304     end
305 end
306
307 function [sinang,cosang] = angrad(alat,alon,blat,blon)
```

```

308 cosang = sin(alat).*sin(blat)+cos(alat).*cos(blat).*cos(alon-blon);
309 sinang = sqrt(1-cosang.*cosang);
310 end
311
312
313 function readf(grnfile)
314 % This function extract prem.data. Theses data are compute for a spherical
315 % perfectly elastic Earth Model based on load Love numbers theory.
316
317 global ang grn
318 deg2rad = pi/180;
319 tmp = reshape(dlmread(grnfile, ''),50,8);
320 grn = tmp(:,2:8);
321 ang = tmp(:,1).*deg2rad;
322 end
323
324 function [grnp] = greenp(angp,indx)
325 global ang grn
326 n = length(angp);
327 m = length(ang);
328 mind = (1:m)'; mind = mind(:,ones(1,n));
329 nind = (1:n)'; nind = nind(:,ones(1,m));
330 dang = ang(mind);
331 dgrn = grn(:,indx); dgrn = dgrn(mind);
332 [tmp,sind] = sort(abs(dang-angp(nind)'));
333 tmp = dang(sind); x(1:3,:) = tmp(1:3,:);
334 tmp = dgrn(sind); y(1:3,:) = tmp(1:3,:);
335 [grnp] = quadr(x,y,angp');
336 end
337
338 function [yp] = quadr(x,y,xp)
339 xa = x(2,:)-x(1,:);
340 ya = y(2,:)-y(1,:);
341 xb = x(3,:)-x(2,:);
342 yb = y(3,:)-y(2,:);
343 xc = x(1,:)-x(3,:);
344 xxc = 1.0./(xa.*xb.*xc);
345 a = -(xa.*yb-xb.*ya).*xxc;
346 b = -(ya.*xb.*(x(2,:)+x(3,:)) -...
347     yb.*xa.*(x(1,:)+x(2,:))).*xxc;
348 c = -(y(1,:).*x(2,:).*x(3,:).*xb +...
349     x(1,:).*y(2,:).*x(3,:).*xc +...
350     x(1,:).*x(2,:).*y(3,:).*xa).*xxc;
351 yp = xp.*(a.*xp + b) + c;

```

## Appendix B. Code associated with Chapter 2

---

```
352 end
353
354
355 function [az] = azrad(alat,alon,blat,blon)
356 %Compute azimuth of a point in rad
357
358 az = atan2(cos(alat).*sin(alon-blon),cos(blat).*sin(alat)-sin(blat).*cos(alat).*
    cos(alon-blon));
359
360 end

1 function plot_disp_ts
2
3 % Plots East/North/Vertical displacement time series at (y)
4 % all locations specified in 'cgps_location' file or (n) at specific
5 % location using station name
6 %
7 % Input: none
8 %
9 % Output: - (y) disp_gps/figures folder with .eps figures of displacement time
10 %          series at all locations in 'cgps_location' file
11 %          - (n) disp_gps/figures folder with .eps figures of displacement time
12 %          series at specific location using station name
13
14 % Loads: disp_gps/displacements_cgps, from model_seasonal_var.m
15 %
16 % Calls: none
17 % Called by: none
18 %
19 % K. Chanard, last modified 20-03-14
20
21
22 load disp_gps/displacements_cgps
23 prompt1 = 'Plot and save all time series? y/n : ';
24 str1 = input(prompt1,'s');
25
26 if ~exist('disp_gps/figures', 'dir')
27     mkdir('disp_gps/figures');
28 end
29
30 if str1=='y'
31
32     figure(1);
```

```

33
34     for i=1:ngps
35
36         subplot(3,1,1); plot(time,ee(:,i),'r','LineWidth',2); % East
37         title(rname{i}, 'FontSize',14); xlabel('Year'); ylabel('East (mm)');
38         xlim([2002.6 2012.6])
39         subplot(3,1,2); plot(time,nn(:,i),'r','LineWidth',2); % North
40         xlabel('Year'); ylabel('North (mm)');
41         xlim([2002.6 2012.6])
42         subplot(3,1,3); plot(time,uu(:,i),'r','LineWidth',2); % Vertical
43         xlabel('Year'); ylabel('Vertical (mm)');
44         xlim([2002.6 2012.6])
45
46         filename=sprintf('disp_gps/figures/%s',rname{i});
47         print('-depsc2','-painters', filename)
48         clf;
49     end
50
51 else
52     prompt2 = 'Plot and save single time series - Enter name of station ';
53     str2 = input(prompt2,'s');
54     tmp=strcmp(str2,rname);
55     [ind,~]=find(tmp==1);
56     if isempty(ind)==1
57         disp('non-existing station')
58     else
59         figure(1);
60         subplot(3,1,1); plot(time,ee(:,ind),'r','LineWidth',2); % East
61         title(rname{ind}, 'FontSize',14);
62         xlabel('Year','FontSize',12); ylabel('East (mm)','FontSize',12);
63         xlim([2002.6 2012.6])
64         subplot(3,1,2); plot(time,nn(:,ind),'r','LineWidth',2); % North
65         xlabel('Year','FontSize',12); ylabel('North (mm)','FontSize',12);
66         xlim([2002.6 2012.6])
67         subplot(3,1,3); plot(time,uu(:,ind),'r','LineWidth',2); % Vertical
68         xlabel('Year','FontSize',12); ylabel('Vertical (mm)','FontSize',12);
69         xlim([2002.6 2012.6])
70         filename=sprintf('disp_gps/figures/%s',rname{ind});
71         print('-depsc2','-painters', filename)
72     end
73 end
74
75 end

```

## Appendix B. Code associated with Chapter 2

---

```
1 function plot_grace_ts(flon,flat)
2
3 % Plots Equivalent Water Height (EWH) time series derived from GRACE at a
4 % specific lon/lat points given as inputs
5 %
6 % Input: - lon, lat: vectors of longitude and latitudes of points where
7 %         you wish to plot EWH
8 %
9 % Output: - disp_zone/figures folder with .eps figures of EWH at each point
10 %         of lon/lat vectors
11 %
12 % Loads: grace_extract/grace_ts, from model_seasonal_var.m
13 %
14 % Calls: none
15 % Called by: none
16 %
17 % K. Chanard, last modified 20-03-14
18
19
20 if ~exist('grace_extract/figures', 'dir')
21     mkdir('grace_extract/figures');
22 end
23
24 load grace_extract/grace_ts
25
26 for i=1:length(flat)
27
28     ind = find(flon(i)==iclone & flat(i)==iclone);
29
30     figure(1);
31     plot(time,tloads(:,ind),'r','LineWidth',2);
32     tname=sprintf('Point lat=%3.1f, lon=%3.1f',flat(i),flon(i));
33     title(tname,'FontSize',14); xlabel('Year','FontSize',14); ylabel('
34         Equivalent Water Height (mm)','FontSize',14);
35     xlim([2002.6 2012.6])
36
37     filename=sprintf('grace_extract/figures/Point_lat_%3.1f_lon_%3.1f',flat(i)
38         ),flon(i));
39     print('-depsc2','-painters', filename);
40     clf;
41 end
42 end
```

```

1 function plot_tmaps(lon,lat,fdate)
2
3 % Plots GRACE loading map and East/North/Vertical displacement maps for
4 % extracted (lon,lat) zone at specific date (fdate)
5 %
6 % Input: - lat: latitude vector of loading zone
7 %        - lon: longitude vector of loading zone
8 %        - fdate (one of the grace files names, ex: '2002_08_08_2002_08_17')
9 %
10 % Output: - disp_zone/figures folder with .eps maps of GRACE loading and
11 %          East/North/Vertical displacements at time fdate
12 %
13 % Loads: - disp_zone/FDATE_de-dn-du.mat files, from model_seasonal_var.m
14 %         - grace_extract/FDATE load file
15 %
16 % Calls: none
17 % Called by: none
18 %
19 % K. Chanard, last modified 20-03-14
20
21 if ~exist('disp_zone/figures', 'dir')
22     mkdir('disp_zone/figures');
23 end
24
25 feast=sprintf('disp_zone/%s_de.mat',fdate);load(feast);
26 fnorth=sprintf('disp_zone/%s_dn.mat',fdate);load(fnorth);
27 fvertical=sprintf('disp_zone/%s_du.mat',fdate);load(fvertical);
28
29 floads=sprintf('grace_extract/%s',fdate);
30 [~,~,ewh]=textread(floads,'%f%f%f');
31
32 nlat = length(lat); nlon = length(lon);
33 mloads = zeros(nlat,nlon);
34
35 for i=1:nlat;
36     for j=1:nlon;
37         mloads(i,j) = ewh((nlon*nlat)+j-(i*nlon));
38     end
39 end
40
41 [olon,olat] = meshgrid(lon,lat);
42 figure(1);
43 subplot(2,2,1); contourf(olon,olat,mloads);colorbar;
44 xlabel('Longitude','FontSize',14);ylabel('Latitude','FontSize',14);

```

## Appendix B. Code associated with Chapter 2

---

```
45 title('EWH from GRACE (mm)','FontSize',14);
46 subplot(2,2,2); contourf(olon,olat,tmpc);colorbar;
47 xlabel('Longitude','FontSize',14);ylabel('Latitude','FontSize',14);
48 title('East disp. (mm)','FontSize',14);
49 subplot(2,2,3); contourf(olon,olat,tmpn);colorbar;
50 xlabel('Longitude','FontSize',14);ylabel('Latitude','FontSize',14);
51 title('North disp.(mm)','FontSize',14)
52 subplot(2,2,4); contourf(olon,olat,tmpu);colorbar;
53 xlabel('Longitude','FontSize',14);ylabel('Latitude','FontSize',14);
54 title('Vertical disp. (mm)','FontSize',14);
55
56 filename=sprintf('disp_zone/figures/%s',fdate);
57 print('-depsc2','-painters', filename)
58
59 end
```

## BIBLIOGRAPHY

- Ader, T., Avouac, J.-P., Liu-Zeng, J., Lyon-Caen, H., Bollinger, L., Galetzka, J., Genrich, J., Thomas, M., Chanard, K., Sapkota, S. N., et al. (2012a). Convergence rate across the nepal himalaya and interseismic coupling on the main himalayan thrust: Implications for seismic hazard. *Journal of Geophysical Research: Solid Earth (1978–2012)*, 117(B4).
- Ader, T. J., Ampuero, J.-P., & Avouac, J.-P. (2012b). The role of velocity-neutral creep on the modulation of tectonic tremor activity by periodic loading. *Geophysical Research Letters*, 39(16).
- Ader, T. J. & Avouac, J.-P. (2013). Detecting periodicities and declustering in earthquake catalogs using the schuster spectrum, application to himalayan seismicity. *Earth and Planetary Science Letters*, 377, 97–105.
- Agnew, D. C. (1996). *SPOTL: Some programs for ocean-tide loading*. Institute of Geophysics and Planetary Physics, University of California, San Diego, Scripps Institution of Oceanography.
- Agnew, D. C. (1997). Nloadf: A program for computing ocean-tide loading. *Journal of Geophysical Research*, 102(B3), 5109–5110.
- Akaogi, M., Tanaka, A., & Ito, E. (2002). Garnet–ilmenite–perovskite transitions in the system mg<sub>4</sub>si<sub>4</sub>o<sub>12</sub>–mg<sub>3</sub>al<sub>2</sub>si<sub>3</sub>o<sub>12</sub> at high pressures and high temperatures: phase equilibria, calorimetry and implications for mantle structure. *Physics of the Earth and Planetary Interiors*, 132(4), 303–324.
- Altamimi, Z., Collilieux, X., & Métivier, L. (2011). Itrf2008: an improved solution of the international terrestrial reference frame. *Journal of Geodesy*, 85(8), 457–473.
- Amiri-Simkooei, A. (2013). On the nature of gps draconitic year periodic pattern in multivariate position time series. *Journal of Geophysical Research: Solid Earth*, 118(5), 2500–2511.

## Bibliography

---

- Amos, C. B., Audet, P., Hammond, W. C., Bürgmann, R., Johanson, I. A., & Blewitt, G. (2014). Uplift and seismicity driven by groundwater depletion in central California. *Nature*.
- Anderson, D. L. (1989). *Theory of the Earth*. Blackwell Scientific Publications.
- Anderson, D. L. & Minster, J. B. (1979). The frequency dependence of  $q$  in the earth and implications for mantle rheology and Chandler wobble. *Geophysical Journal International*, 58(2), 431–440.
- Argand, E. (1924). *La tectonique de l'Asie. Conférence faite à Bruxelles, le 10 août 1922*.
- Bassin, C. (2000). The current limits of resolution for surface wave tomography in North America. *Eos Trans. AGU*.
- Baud, P. & Meredith, P. (1997). Damage accumulation during triaxial creep of Darley Dale sandstone from pore volumetry and acoustic emission. *International Journal of Rock Mechanics and Mining Sciences*, 34(3), 24–e1.
- Beaumont, C., Jamieson, R. A., Nguyen, M., & Lee, B. (2001). Himalayan tectonics explained by extrusion of a low-viscosity crustal channel coupled to focused surface denudation. *Nature*, 414(6865), 738–742.
- Beaumont, C., Jamieson, R. A., Nguyen, M. H., & Medvedev, S. (2004). Crustal channel flows: 1. Numerical models with applications to the tectonics of the Himalayan-Tibetan orogen. *Journal of Geophysical Research: Solid Earth (1978–2012)*, 109(B6).
- Beeler, N. & Lockner, D. (2003). Why earthquakes correlate weakly with the solid Earth tides: Effects of periodic stress on the rate and probability of earthquake occurrence. *Journal of Geophysical Research: Solid Earth (1978–2012)*, 108(B8).
- Benjamin, D., Wahr, J., Ray, R. D., Egbert, G. D., & Desai, S. D. (2006). Constraints on mantle anelasticity from geodetic observations, and implications for the  $J_2$  anomaly. *Geophysical Journal International*, 165(1), 3–16.
- Bettinelli, P., Avouac, J., Flouzat, M., Bollinger, L., Ramillien, G., Rajaure, S., & Sapkota, S. (2008). Seasonal variations of seismicity and geodetic strain in the Himalaya induced by surface hydrology. *Earth and Planetary Science Letters*, 266, 332–344.

- Bettinelli, P., Avouac, J., Flouzat, M., Jouanne, F., Bollinger, L., Willis, P., & Chitrakar, G. (2006). Plate motion of India and interseismic strain in the Nepal Himalaya from GPS and DORIS measurements. *Journal of Geodesy*, 80, 567–589.
- Beutler, G., Rothacher, M., Schaer, S., Springer, T., Kouba, J., & Neilan, R. (1999). The international gps service (igs): an interdisciplinary service in support of earth sciences. *Advances in Space Research*, 23(4), 631–653.
- Bevis, M., Alsdorf, D., Kendrick, E., Fortes, L., Forsberg, B., Smalley Jr, R., & Becker, J. (2005). Seasonal fluctuations in the mass of the Amazon River system and Earth's elastic response. *Geophysical Research Letters*, 32.
- Bills, B. G., Adams, K. D., & Wesnousky, S. G. (2007). Viscosity structure of the crust and upper mantle in western Nevada from isostatic rebound patterns of the late Pleistocene Lake Lahontan high shoreline. *Journal of Geophysical Research: Solid Earth (1978–2012)*, 112(B6).
- Bills, B. G. & May, G. M. (1987). Lake Bonneville—constraints on lithospheric thickness and upper mantle viscosity from isostatic warping of Bonneville, Provo, and Gilbert stage shorelines. *Journal of Geophysical Research Atmospheres*.
- Bina, C. R. & Helffrich, G. (1994). Phase transition Clapeyron slopes and transition zone seismic discontinuity topography. *Journal of Geophysical Research: Solid Earth (1978–2012)*, 99(B8), 15853–15860.
- Blewitt, G. & Clarke, P. (2003). Inversion of Earth's changing shape to weigh sea level in static equilibrium with surface mass redistribution. *Journal of Geophysical Research: Solid Earth (1978–2012)*, 108(B6).
- Blewitt, G. & Lavallée, D. (2002). Effect of annual signals on geodetic velocity. *J. Geophys. Res.*, 107.
- Blewitt, G., Lavallee, D., Clarke, P., & Nurutdinov, K. (2001). A new global mode of Earth deformation: Seasonal cycle detected. *Science*, 294, 2342–2345.
- Boehm, J., Niell, A., Tregoning, P., & Schuh, H. (2006). 2 global mapping function (gmf): A new empirical mapping function 3 based on numerical weather model data. *J. geophys. Res.*, 33, L07304.

## Bibliography

---

- Bollinger, L., Avouac, J., Cattin, R., & Pandey, M. (2004). Stress buildup in the Himalaya. *Journal of Geophysical Research: Solid Earth (1978–2012)*, 109(B11).
- Bollinger, L., Perrier, F., Avouac, J., Sapkota, S., Gautam, U., & Tiwari, D. (2007). Seasonal modulation of seismicity in the Himalaya of Nepal. *Geophysical Research Letters*, 34.
- Bouille, F., Cazenave, A., Lemoine, J., & Crétaux, J. (2000). Geocentre motion from the Doris space system and laser data to the Lageos satellites: Comparison with surface loading data. *Geophysical Journal International*, 143(1), 71–82.
- Bourbie, T. & Zinszner, B. (1985). Hydraulic and acoustic properties as a function of porosity in Fontainebleau sandstone. *Journal of Geophysical Research: Solid Earth (1978–2012)*, 90(B13), 11524–11532.
- Boussinesq, J. (1885). *Application des potentiels à l'étude de l'équilibre et du mouvement des solides élastiques*. Gauthier-Villars.
- Brantut, N., Heap, M., Meredith, P., & Baud, P. (2013). Time-dependent cracking and brittle creep in crustal rocks: A review. *Journal of Structural Geology*, 52, 17–43.
- Brantut, N., Schubnel, A., & Guéguen, Y. (2011). Damage and rupture dynamics at the brittle-ductile transition: The case of gypsum. *Journal of Geophysical Research: Solid Earth (1978–2012)*, 116(B1).
- Braunmiller, J., Nábělek, J. L., & Tréhu, A. M. (2014). A seasonally modulated earthquake swarm near Maupin, Oregon. *Geophysical Journal International*, 197(3), 1736–1743.
- Brodsky, E. E., Karakostas, V., & Kanamori, H. (2000). A new observation of dynamically triggered regional seismicity: Earthquakes in Greece following the August 1999 Izmit, Turkey earthquake. *Geophysical Research Letters*, 27(17), 2741–2744.
- Brodsky, E. E. & Prejean, S. G. (2005). New constraints on mechanisms of remotely triggered seismicity at Long Valley Caldera. *Journal of Geophysical Research: Solid Earth (1978–2012)*, 110(B4).
- Brodsky, E. E. & van der Elst, N. J. (2014). The uses of dynamic earthquake triggering. *Annual Review of Earth and Planetary Sciences*, 42, 317–339.

- Brown, L., Zhao, W., Nelson, K., Hauck, M., Alsdorf, D., Ross, A., Cogan, M., Clark, M., Liu, X., & Che, J. (1996). Bright spots, structure, and magmatism in southern tibet from indepth seismic reflection profiling. *Science*, 274(5293), 1688–1690.
- Bruinsma, S., Lemoine, J., Biancale, R., & Valès, N. (2010). CNES/GRGS 10-day gravity field models (release 2) and their evaluation. *Advances in Space Research*, 45(4), 587–601.
- Čadek, O. & Fleitout, L. (2003). Effect of lateral viscosity variations in the top 300 km on the geoid and dynamic topography. *Geophysical Journal International*, 152(3), 566–580.
- Carrère, L. & Lyard, F. (2003). Modeling the barotropic response of the global ocean to atmospheric wind and pressure forcing-comparisons with observations. *Geophysical Research Letters*, 30(6).
- Cathles, L. M. (1975). *The viscosity of the Earth's mantle*, volume 386. Princeton University Press Princeton, NJ.
- Cattin, R. & Avouac, J. (2000). Modeling mountain building and the seismic cycle in the himalaya of nepal. *Journal of Geophysical Research*, 105(B6), 13389–13407.
- Chanard, K., Avouac, J., Ramillien, G., & Genrich, J. (2014). Modeling deformation induced by seasonal variations of continental water in the himalaya region: sensitivity to earth elastic structure. *Journal of Geophysical Research: Solid Earth*.
- Chandrasekhar, D., Bürgmann, R., Reddy, C., Sunil, P., & Schmidt, D. A. (2009). Weak mantle in nw india probed by geodetic measurements following the 2001 bhuj earthquake. *Earth and Planetary Science Letters*, 280(1), 229–235.
- Chen, J., Wilson, C., Eanes, R., & Nerem, R. (1999). Geophysical interpretation of observed geocenter variations. *Journal of Geophysical Research: Solid Earth (1978–2012)*, 104(B2), 2683–2690.
- Chen, J., Wilson, C., Tapley, B., & Grand, S. (2007). Grace detects coseismic and postseismic deformation from the sumatra-andaman earthquake. *Geophysical Research Letters*, 34(13).
- Christensen, U. R. (1985). Mantle phase transitions and postglacial rebound. *Journal of Geophysical Research: Solid Earth (1978–2012)*, 90(B13), 11312–11318.

## Bibliography

---

- Christiansen, L., Hurwitz, S., Saar, M., Ingebritsen, S., & Hsieh, P. (2005). Seasonal seismicity at western united states volcanic centers. *Earth and Planetary Science Letters*, 240(2), 307–321.
- Cochran, E. S., Vidale, J. E., & Tanaka, S. (2004). Earth tides can trigger shallow thrust fault earthquakes. *Science*, 306(5699), 1164–1166.
- Costain, J. & Bollinger, G. (1996). Climatic changes, streamflow, and long-term forecasting of intraplate seismicity. *Journal of Geodynamics*, 22(1), 97–117.
- Crétaux, J.-F., Soudarin, L., Davidson, F. J., Gennero, M.-C., Bergé-Nguyen, M., & Cazenave, A. (2002). Seasonal and interannual geocenter motion from slr and doris measurements: Comparison with surface loading data. *Journal of Geophysical Research: Solid Earth (1978–2012)*, 107(B12), ETG–16.
- Dahl-Jensen, T., Larsen, T. B., Voss, P. H., et al. (2010). Greenland ice sheet monitoring network (glisn): a seismological approach. *Geological Survey of Denmark and Greenland Bulletin*, 20, 55–58.
- Das, S. & Scholz, C. H. (1981). Off-fault aftershock clusters caused by shear stress increase? *Bulletin of the Seismological Society of America*, 71(5), 1669–1675.
- Davis, J., Elósegui, P., Mitrovica, J., & Tamisiea, M. (2004). Climate-driven deformation of the solid Earth from GRACE and GPS. *Geophys. Res. Lett*, 31, 24.
- DeVries, P. M. & Meade, B. J. (2013). Earthquake cycle deformation in the tibetan plateau with a weak mid-crustal layer. *Journal of Geophysical Research: Solid Earth*, 118(6), 3101–3111.
- Dieterich, J. (1994). A constitutive law for rate of earthquake production and its application to earthquake clustering. *Journal of Geophysical Research: Solid Earth (1978–2012)*, 99(B2), 2601–2618.
- Dieterich, J. H. (1979). Modeling of rock friction: 1. experimental results and constitutive equations. *Journal of Geophysical Research: Solid Earth (1978–2012)*, 84(B5), 2161–2168.
- Dieterich, J. H. (1992). Earthquake nucleation on faults with rate-and state-dependent strength. *Tectonophysics*, 211(1), 115–134.

- Doin, M.-P., Twardzik, C., Ducret, G., Lasserre, C., Guillaso, S., & Jianbao, S. (2015). In-sar measurement of the deformation around siling co lake: Inferences on the lower crust viscosity in central tibet. *Journal of Geophysical Research: Solid Earth*.
- Döll, P., Kaspar, F., & Lehner, B. (2003). A global hydrological model for deriving water availability indicators: model tuning and validation. *Journal of Hydrology*, 270(1-2), 105–134.
- Dong, D., Dickey, J., Chao, Y., & Cheng, M. (1997). Geocenter variations caused by atmosphere, ocean and surface ground water. *Geophysical Research Letters*, 24(15), 1867–1870.
- Dong, D., Fang, P., Bock, Y., Cheng, M., & Miyazaki, S. (2002). Anatomy of apparent seasonal variations from GPS-derived site position time series. *J. geophys. Res*, 107.
- Dragert, H., Wang, K., & James, T. S. (2001). A silent slip event on the deeper cascadia subduction interface. *Science*, 292(5521), 1525–1528.
- Durand, S., Chambat, F., Matas, J., & Ricard, Y. (2012). Constraining the kinetics of mantle phase changes with seismic data. *Geophysical Journal International*, 189(3), 1557–1564.
- Dziewonski, A. & Anderson, D. (1981). Preliminary reference Earth model. *Physics of the Earth and Planetary Interiors*, 25, 297–356.
- Elósegui, P., Davis, J., Mitrovica, J., Bennett, R., & Wernicke, B. (2003). Crustal loading near great salt lake, utah. *Geophys. Res. Lett*, 30(3), 1111.
- Farrell, W. (1972). Deformation of the Earth by surface loads. *Reviews of Geophysics*, 10.
- Fischer, A. D., Sammis, C. G., Chen, Y., & Teng, T.-L. (2008). Dynamic triggering by strong-motion p and s waves: Evidence from the 1999 chi-chi, taiwan, earthquake. *Bulletin of the Seismological Society of America*, 98(2), 580–592.
- Flouzat, M., Bettinelli, P., Willis, P., Avouac, J., Héritier, T., & Gautam, U. (2009). Investigating tropospheric effects and seasonal position variations in gps and doris time-series from the nepal himalaya. *Geophysical Journal International*, 178(3), 1246–1259.
- Fu, Y., Argus, D. E., Freymueller, J. T., & Heflin, M. B. (2013). Horizontal motion in elastic response to seasonal loading of rain water in the amazon basin and monsoon water in

## Bibliography

---

- southeast asia observed by gps and inferred from grace. *Geophysical Research Letters*, 40(23), 6048–6053.
- Fu, Y., Argus, D. E., & Landerer, F. W. (2015). Gps as an independent measurement to estimate terrestrial water storage variations in washington and oregon. *Journal of Geophysical Research: Solid Earth*.
- Fu, Y. & Freymueller, J. T. (2012). Seasonal and long-term vertical deformation in the nepal himalaya constrained by gps and grace measurements. *Journal of Geophysical Research*, 117(B3), B03407.
- Fu, Y., Freymueller, J. T., & Jensen, T. (2012). Seasonal hydrological loading in southern alaska observed by gps and grace. *Geophysical Research Letters*, 39(15).
- Gomberg, J., Blanpied, M. L., & Beeler, N. (1997). Transient triggering of near and distant earthquakes. *Bulletin of the Seismological Society of America*, 87(2), 294–309.
- Gomberg, J. & Johnson, P. (2005). Seismology: Dynamic triggering of earthquakes. *Nature*, 437(7060), 830–830.
- Grapenthin, R., Sigmundsson, F., Geirsson, H., Árnadóttir, T., & Pínel, V. (2006). Icelandic rhythms: Annual modulation of land elevation and plate spreading by snow load. *Geophysical Research Letters*, 33.
- Greff-Lefitz, M. & Legros, H. (1997). Some remarks about the degree-one deformation of the earth. *Geophysical Journal International*, 131(3), 699–723.
- Griffiths, J. & Ray, J. R. (2013). Sub-daily alias and draconitic errors in the igs orbits. *GPS solutions*, 17(3), 413–422.
- Guo, J., Li, Y., Huang, Y., Deng, H., Xu, S., & Ning, J. (2004). Green's function of the deformation of the earth as a result of atmospheric loading. *Geophysical Journal International*, 159, 53–68.
- Hainzl, S., Kraft, T., Wassermann, J., Igel, H., & Schmedes, E. (2006). Evidence for rainfall-triggered earthquake activity. *Geophysical Research Letters*, 33.

- Han, S.-C., Sauber, J., Luthcke, S. B., Ji, C., & Pollitz, F. F. (2008). Implications of postseismic gravity change following the great 2004 sumatra-andaman earthquake from the regional harmonic analysis of grace intersatellite tracking data. *Journal of Geophysical Research: Solid Earth (1978–2012)*, 113(B11).
- Han, S.-C., Shum, C., Bevis, M., Ji, C., & Kuo, C.-Y. (2006). Crustal dilatation observed by grace after the 2004 sumatra-andaman earthquake. *Science*, 313(5787), 658–662.
- Hatanaka, Y., Sawada, M., Horita, A., Kusaka, M., Johnson, J. M., & Rocken, C. (2001). Calibration of antenna-radome and monument-multipath effect of geonet—part 2: Evaluation of the phase map by geonet data. *Earth, planets and space*, 53(1), 23–30.
- Heinz, D., Jeanloz, R., & O’Connell, R. J. (1982). Bulk attenuation in a polycrystalline earth. *Journal of Geophysical Research: Solid Earth (1978–2012)*, 87(B9), 7772–7778.
- Heki, K. (2003). Snow load and seasonal variation of earthquake occurrence in Japan. *Earth and Planetary Science Letters*, 207, 159–164.
- Herring, T. (2005). Globk: Global kalman filter vlbi and gps analysis program, v.10.2. *Mass. Inst. of Tech.*
- Hill, D. & Prejean, S. (2007). Dynamic triggering. *Treatise on Geophysics*, 4, 257–292.
- Hill, D., Reasenber, P., Michael, A., Arabaz, W., Beroza, G., Brumbaugh, D., Brune, J., Castro, R., Davis, S., Ellsworth, W., et al. (1993). Seismicity remotely triggered by the magnitude 7.3 landers, california, earthquake. *Science*, 260(5114), 1617–1623.
- Hill, D. P., Pollitz, F., & Newhall, C. (2002). Earthquake-volcano interactions. *Physics Today*, 55(11), 41–47.
- Hilley, G., Bürgmann, R., Zhang, P.-Z., & Molnar, P. (2005). Bayesian inference of plastosphere viscosities near the kunlun fault, northern tibet. *Geophysical Research Letters*, 32(1).
- Hoechner, A., Sobolev, S. V., Einarsson, I., & Wang, R. (2011). Investigation on afterslip and steady state and transient rheology based on postseismic deformation and geoid change caused by the sumatra 2004 earthquake. *Geochemistry, Geophysics, Geosystems*, 12(7).

## Bibliography

---

- Hugentobler, U., Van der Marel, H., & Springer, T. (2006). Identification and mitigation of gnss errors. In *Position paper, IGS 2006 workshop proceedings*.
- Husker, A. L. & Brodsky, E. E. (2004). Seismicity in idaho and montana triggered by the denali fault earthquake: A window into the geologic context for seismic triggering. *Bulletin of the Seismological Society of America*, 94(6B), S310–S316.
- Ide, S. & Tanaka, Y. (2014). Controls on plate motion by oscillating tidal stress: Evidence from deep tremors in western japan. *Geophysical Research Letters*, 41(11), 3842–3850.
- Irifune, T. (1993). Phase transformations in the earth's mantle and subducting slabs: Implications for their compositions, seismic velocity and density structures and dynamics. *Island Arc*, 2(2), 55–71.
- Ita, J. & Stixrude, L. (1992). Petrology, elasticity, and composition of the mantle transition zone. *Journal of Geophysical Research: Solid Earth (1978–2012)*, 97(B5), 6849–6866.
- Ito, T. & Simons, M. (2011). Probing asthenospheric density, temperature, and elastic moduli below the western united states. *Science*.
- Jamieson, R. A., Beaumont, C., Medvedev, S., & Nguyen, M. H. (2004). Crustal channel flows: 2. numerical models with implications for metamorphism in the himalayan-tibetan orogen. *Journal of Geophysical Research: Solid Earth (1978–2012)*, 109(B6).
- Jiang, Y., Dixon, T., & Wdowinski, S. (2010). Accelerating uplift in the north atlantic region as an indicator of ice loss. *Nature Geoscience*, 3(6), 404–407.
- Kang, K., Wahr, J., Heflin, M., & Desai, S. (2015). Stacking global gps verticals and horizontals to solve for the fortnightly and monthly body tides: Implications for mantle anelasticity. *Journal of Geophysical Research: Solid Earth*, 120(3), 1787–1803.
- Kang, Z., Tapley, B., Chen, J., Ries, J., & Bettadpur, S. (2009). Geocenter variations derived from gps tracking of the grace satellites. *Journal of Geodesy*, 83(10), 895–901.
- Kaniuth, K. & Vetter, S. (2006). Estimating atmospheric pressure loading regression coefficients from GPS observations. *GPS Solutions*, 10(2), 126–134.

- Katsura, T. & Ito, E. (1989). The system  $\text{Mg}_2\text{SiO}_4\text{-Fe}_2\text{SiO}_4$  at high pressures and temperatures: Precise determination of stabilities of olivine, modified spinel, and spinel. *Journal of Geophysical Research: Solid Earth (1978–2012)*, 94(B11), 15663–15670.
- King, M. A. & Watson, C. S. (2010). Long gps coordinate time series: multipath and geometry effects. *Journal of Geophysical Research: Solid Earth (1978–2012)*, 115(B4).
- King, R. & Bock, Y. (2000). Documentation for the gamit gps software analysis version 9.9. *Mass. Inst. of Technol., Cambridge*.
- King, R. & Bock, Y. (2005). Documentation for the gamit gps analysis software, release 10.2. *Mass. Inst. of Tech., Scripps Inst. Oceanogr.*
- Krásná, H., Böhm, J., & Schuh, H. (2013). Tidal love and shida numbers estimated by geodetic vlbi. *Journal of Geodynamics*, 70, 21–27.
- Krien, Y. & Fleitout, L. (2010). Accommodation of volume changes in phase transition zones: Macroscopic scale. *Journal of Geophysical Research: Solid Earth (1978–2012)*, 115(B3).
- Lemoine, J., Bruinsma, S., Loyer, S., Biancale, R., Marty, J., Perosanz, F., & Balmino, G. (2007). Temporal gravity field models inferred from GRACE data. *Advances in Space Research*, 39, 1620–1629.
- Lockner, D. (1993). Room temperature creep in saturated granite. *Journal of Geophysical Research: Solid Earth (1978–2012)*, 98(B1), 475–487.
- Lockner, D. A. & Beeler, N. M. (1999). Premonitory slip and tidal triggering of earthquakes. *Journal of Geophysical Research: Solid Earth (1978–2012)*, 104(B9), 20133–20151.
- Lomb, N. R. (1976). Least-squares frequency analysis of unequally spaced data. *Astrophysics and space science*, 39(2), 447–462.
- Longman, I. (1962). A Green's Function for Determining the Deformation of the Earth under Surface Mass Loads 1. Theory. *Journal of Geophysical Research*, 67(2), 845–850.
- Longman, I. (1963). A Green's Function for Determining the Deformation of the Earth under Surface Mass Loads 2. Computations and Numerical Results. *Journal of Geophysical Research*, 68(2), 485–496.

## Bibliography

---

- Love, A. E. H. (1911). *Some Problems of Geodynamics: Being an Essay to which the Adams Prize in the University of Cambridge was Adjudged in 1911*. Cambridge.
- Lowry, A. R. (2006). Resonant slow fault slip in subduction zones forced by climatic load stress. *Nature*, 442(7104), 802–805.
- Main, I. G. (2000). A damage mechanics model for power-law creep and earthquake aftershock and foreshock sequences. *Geophysical Journal International*, 142(1), 151–161.
- Main, I. G., Sammonds, P. R., & Meredith, P. G. (1993). Application of a modified griffith criterion to the evolution of fractal damage during compressional rock failure. *Geophysical Journal International*, 115(2), 367–380.
- Manga, M. & Brodsky, E. (2006). Seismic triggering of eruptions in the far field: volcanoes and geysers. *Annu. Rev. Earth Planet. Sci*, 34, 263–291.
- Mantovani, M. S., Shukowsky, W., de Freitas, S. R., & Brito Neves, B. B. (2005). Lithosphere mechanical behavior inferred from tidal gravity anomalies: a comparison of africa and south america. *Earth and Planetary Science Letters*, 230(3), 397–412.
- Matsuo, K. & Heki, K. (2010). Time-variable ice loss in Asian high mountains from satellite gravimetry. *Earth and Planetary Science Letters*.
- McGarr, A., Simpson, D., & Seeber, L. (2002). Case histories of induced and triggered seismicity. *International Geophysics Series*, 81(A), 647–664.
- Métivier, L., de Viron, O., Conrad, C. P., Renault, S., Diament, M., & Patau, G. (2009). Evidence of earthquake triggering by the solid earth tides. *Earth and Planetary Science Letters*, 278(3), 370–375.
- Monsalve, G., Sheehan, A., Schulte-Pelkum, V., Rajaure, S., Pandey, M., & Wu, F. (2006). Seismicity and one-dimensional velocity structure of the Himalayan collision zone: Earthquakes in the crust and upper mantle. *J. geophys. Res*, 111, B10301.
- Mooney, W. D., Laske, G., & Masters, T. G. (1998). Crust 5.1: A global crustal model at 5 × 5. *Journal of Geophysical Research: Solid Earth (1978–2012)*, 103(B1), 727–747.

- Munekane, H. (2007). Ocean mass variations from grace and tsunami gauges. *Journal of Geophysical Research: Solid Earth (1978–2012)*, 112(B7).
- Nahmani, S., Bock, O., Bouin, M.-N., Santamaría-Gómez, A., Boy, J.-P., Collilieux, X., Metivier, L., Panet, I., Genthon, P., Linage, C., et al. (2012). Hydrological deformation induced by the west african monsoon: Comparison of gps, grace and loading models. *Journal of Geophysical Research: Solid Earth (1978–2012)*, 117(B5).
- Ogawa, R. & Heki, K. (2007). Slow postseismic recovery of geoid depression formed by the 2004 sumatra-andaman earthquake by mantle water diffusion. *Geophysical research letters*, 34(6).
- Pandey, M., Tandukar, R., Avouac, J., Lave, J., & Massot, J. (1995). Interseismic strain accumulation on the himalayan crustal ramp (nepal). *Geophysical Research Letters*, 22(7), 751–754.
- Pariisky, N. (1965). The regional heterogeneity of the mantle as revealed by earth-tide observations. *Tectonophysics*, 1(5), 439–442.
- Peltier, W. (1974). The impulse response of a Maxwell Earth. *Rev. Geophys. Space Phys*, 12(4), 649–669.
- Peng, Z., Hill, D. P., Shelly, D. R., & Aiken, C. (2010). Remotely triggered microearthquakes and tremor in central california following the 2010 mw 8.8 chile earthquake. *Geophysical Research Letters*, 37(24).
- Petit, G. & Luzum, B. (2010). *IERS conventions (2010)*. Technical report, DTIC Document.
- Pollitz, F. F. (2003). Transient rheology of the uppermost mantle beneath the mojave desert, california. *Earth and Planetary Science Letters*, 215(1), 89–104.
- Pollitz, F. F. (2005). Transient rheology of the upper mantle beneath central alaska inferred from the crustal velocity field following the 2002 denali earthquake. *Journal of Geophysical Research: Solid Earth (1978–2012)*, 110(B8).
- Pollitz, F. F., Bürgmann, R., & Banerjee, P. (2006). Post-seismic relaxation following the great

## Bibliography

---

- 2004 sumatra-andaman earthquake on a compressible self-gravitating earth. *Geophysical Journal International*, 167(1), 397–420.
- Pollitz, F. F., Stein, R. S., Sevilgen, V., & Bürgmann, R. (2012). The 11 april 2012 east indian ocean earthquake triggered large aftershocks worldwide. *Nature*, 490(7419), 250–253.
- Pollitz, F. F. & Thatcher, W. (2010). On the resolution of shallow mantle viscosity structure using postearthquake relaxation data: Application to the 1999 hector mine, california, earthquake. *Journal of Geophysical Research: Solid Earth (1978–2012)*, 115(B10).
- Prawirodirdjo, L., Ben-Zion, Y., & Bock, Y. (2006). Observation and modeling of thermoelastic strain in southern california integrated gps network daily position time series. *Journal of Geophysical Research: Solid Earth (1978–2012)*, 111(B2).
- Prejean, S., Hill, D., Brodsky, E., Hough, S., Johnston, M., Malone, S., Oppenheimer, D., Pitt, A., & Richards-Dinger, K. (2004). Remotely triggered seismicity on the united states west coast following the mw 7.9 denali fault earthquake. *Bulletin of the Seismological Society of America*, 94(6B), S348–S359.
- Press, W. H., Teukolsky, S. A., Vetterling, W. T., & Flannery, B. P. (1992). Numerical recipes (cambridge.
- Ramillien, G., Famiglietti, J., & Wahr, J. (2008). Detection of Continental Hydrology and Glaciology Signals from GRACE: A Review. *Surveys in Geophysics*, 29, 361–374.
- Ramillien, G., Frappart, F., Cazenave, A., & Güntner, A. (2005). Time variations of land water storage from an inversion of 2 years of GRACE geoids. *Earth and Planetary Science Letters*, 235, 283–301.
- Ramillien, G., Frappart, F., Guntner, A., Ngo-Duc, T., Cazenave, A., & Laval, K. (2006). Time variations of the regional evapotranspiration rate from Gravity Recovery and Climate Experiment (GRACE) satellite gravimetry. *Water Resources Research*, 42, 104–103.
- Ray, J., Altamimi, Z., Collilieux, X., & van Dam, T. (2008). Anomalous harmonics in the spectra of gps position estimates. *GPS Solutions*, 12(1), 55–64.

- Ray, J., Griffiths, J., Collilieux, X., & Reischung, P. (2013). Subseasonal gnss positioning errors. *Geophysical Research Letters*, 40(22), 5854–5860.
- Resovsky, J., Trampert, J., & Van der Hilst, R. (2005). Error bars for the global seismic q profile. *Earth and Planetary Science Letters*, 230(3), 413–423.
- Ricard, Y., Matas, J., & Chambat, F. (2009). Seismic attenuation in a phase change coexistence loop. *Physics of the Earth and Planetary Interiors*, 176(1), 124–131.
- Rietbroek, R., Fritsche, M., Brunnabend, S.-E., Daras, I., Kusche, J., Schröter, J., Flechtner, F., & Dietrich, R. (2012). Global surface mass from a new combination of grace, modelled obp and reprocessed gps data. *Journal of Geodynamics*, 59, 64–71.
- Ringwood, A. E. (1970). Phase transformations and the constitution of the mantle. *Physics of the Earth and Planetary Interiors*, 3, 109–155.
- Rodriguez-Solano, C., Hugentobler, U., Steigenberger, P., Bloßfeld, M., & Fritsche, M. (2014). Reducing the draconitic errors in gnss geodetic products. *Journal of Geodesy*, 88(6), 559–574.
- Rogers, G. & Dragert, H. (2003). Episodic tremor and slip on the cascadia subduction zone: The chatter of silent slip. *Science*, 300(5627), 1942–1943.
- Rubinstein, J., Beroza, G., Brown, J., Brudzinski, M., Gomberg, J., Malone, S., Oppenheimer, D., Peng, Z., Prejean, S., Savage, H., et al. (2011). Widespread triggering of earthquakes and tremor by the 2011 m 9.0 off-tohoku earthquake. *Seismol. Res. Lett.*, 82(2), 273–361.
- Ryder, I., Bürgmann, R., & Pollitz, F. (2011). Lower crustal relaxation beneath the tibetan plateau and qaidam basin following the 2001 kokoxili earthquake. *Geophysical Journal International*, 187(2), 613–630.
- Saar, M. O. & Manga, M. (2003). Seismicity induced by seasonal groundwater recharge at mt. hood, oregon. *Earth and Planetary Science Letters*, 214(3), 605–618.
- Sakumura, C., Bettadpur, S., & Bruinsma, S. (2014). Ensemble prediction and intercomparison analysis of grace time-variable gravity field models. *Geophysical Research Letters*, 41(5), 1389–1397.

## Bibliography

---

- Sauber, J. M. & Molnia, B. F. (2004). Glacier ice mass fluctuations and fault instability in tectonically active southern alaska. *Global and Planetary Change*, 42(1), 279–293.
- Savage, J. & Cockerham, R. (1984). Earthquake swarm in long valley caldera, california, january 1983: evidence for dike inflation. *Journal of Geophysical Research: Solid Earth (1978–2012)*, 89(B10), 8315–8324.
- Scargle, J. D. (1982). Studies in astronomical time series analysis. ii-statistical aspects of spectral analysis of unevenly spaced data. *The Astrophysical Journal*, 263, 835–853.
- Scholz, C. H. (2002). *The mechanics of earthquakes and faulting*. Cambridge university press.
- Schubnel, A., Brunet, F., Hilairet, N., Gasc, J., Wang, Y., & Green, H. W. (2013). Deep-focus earthquake analogs recorded at high pressure and temperature in the laboratory. *Science*, 341(6152), 1377–1380.
- Schuster, A. (1897). On lunar and solar periodicities of earthquakes. *Proceedings of the Royal Society of London*, 61(369-377), 455–465.
- Shida, T. (1912). On the body tides of the earth, a proposal for the international geodetic association. *Tokyo Sugaku-Buturigakkwai Kizi Dai 2 Ki*, 6(16), 242–258.
- Smith, M. L. & Dahlen, F. (1981). The period and q of the chandler wobble. *Geophysical Journal International*, 64(1), 223–281.
- Steckler, M., Nooner, S., Akhter, S., Chowdhury, S., Bettadpur, S., Seeber, L., & Kogan, M. (2010). Modeling Earth deformation from monsoonal flooding in Bangladesh using hydrographic, GPS, and Gravity Recovery and Climate Experiment (GRACE) data. *Journal of Geophysical Research*, 115(B8), B08407.
- Stolz, A. (1976). Changes in the position of the geocentre due to seasonal variations in air mass and ground water. *Geophysical Journal International*, 44(1), 19–26.
- Sun, W. & Okubo, S. (1993). Surface potential and gravity changes due to internal dislocations in a spherical earth—i. theory for a point dislocation. *Geophysical Journal International*, 114(3), 569–592.

- Swenson, S., Chambers, D., & Wahr, J. (2008). Estimating geocenter variations from a combination of grace and ocean model output. *Journal of Geophysical Research: Solid Earth (1978–2012)*, 113(B8).
- Szeliga, W., Melbourne, T., Santillan, M., & Miller, M. (2008). Gps constraints on 34 slow slip events within the cascadia subduction zone, 1997–2005. *Journal of Geophysical Research: Solid Earth (1978–2012)*, 113(B4).
- Talwani, P. (1998). On the nature of reservoir-induced seismicity. In *Seismicity Associated with Mines, Reservoirs and Fluid Injections* (pp. 473–492). Springer.
- Tamisiea, M. & Wahr, J. (2002). Phase transitions and short timescale sinusoidal motions. *Earth and Planetary Science Letters*, 198(3), 459–470.
- Tanaka, S. (2010). Tidal triggering of earthquakes precursory to the recent sumatra megathrust earthquakes of 26 december 2004 (mw 9.0), 28 march 2005 (mw 8.6), and 12 september 2007 (mw 8.5). *Geophysical Research Letters*, 37(2).
- Tanaka, S. (2012). Tidal triggering of earthquakes prior to the 2011 tohoku-oki earthquake (mw 9.1). *Geophysical Research Letters*, 39(7).
- Tanaka, S., Ohtake, M., & Sato, H. (2002). Evidence for tidal triggering of earthquakes as revealed from statistical analysis of global data. *Journal of Geophysical Research: Solid Earth (1978–2012)*, 107(B10), ESE–1.
- Tanaka, S., Ohtake, M., & Sato, H. (2004). Tidal triggering of earthquakes in japan related to the regional tectonic stress. *Earth, planets and space*, 56(5), 511–515.
- Tapley, B., Bettadpur, S., Ries, J., Thompson, P., & Watkins, M. (2004). GRACE measurements of mass variability in the Earth system. *Science*, 305, 503–505.
- Tapley, B., Ries, J., Bettadpur, S., Chambers, D., Cheng, M., Condi, F., Gunter, B., Kang, Z., Nagel, P., Pastor, R., et al. (2005). GGM02—An improved Earth gravity field model from GRACE. *Journal of Geodesy*, 79(8), 467–478.
- Tarantola, A. (2005). *Inverse problem theory and methods for model parameter estimation*. siam.

## Bibliography

---

- Thomas, A., Bürgmann, R., Shelly, D., Beeler, N., & Rudolph, M. (2012). Tidal triggering of low frequency earthquakes near parkfield, california: Implications for fault mechanics within the brittle-ductile transition. *Journal of Geophysical Research: Solid Earth (1978–2012)*, 117(B5).
- Tregoning, P. & Watson, C. (2009). Atmospheric effects and spurious signals in gps analyses. *Journal of Geophysical Research: Solid Earth (1978–2012)*, 114(B9).
- Tregoning, P. & Watson, C. (2011). Correction to “atmospheric effects and spurious signals in gps analyses”. *Journal of Geophysical Research: Solid Earth (1978–2012)*, 116(B2).
- Tregoning, P., Watson, C., Ramillien, G., McQueen, H., & Zhang, J. (2009). Detecting hydrologic deformation using grace and gps. *Geophysical Research Letters*, 36(15).
- Trubienko, O., Fleitout, L., Garaud, J.-D., & Vigny, C. (2013). Interpretation of interseismic deformations and the seismic cycle associated with large subduction earthquakes. *Tectonophysics*, 589, 126–141.
- Tsai, V. C. (2011). A model for seasonal changes in gps positions and seismic wave speeds due to thermoelastic and hydrologic variations. *Journal of Geophysical Research: Solid Earth (1978–2012)*, 116(B4).
- Turcotte, D. L. & Schubert, G. (2014). *Geodynamics*. Cambridge University Press.
- Van Dam, T., Wahr, J., Milly, P., Shmakin, A., Blewitt, G., Lavallee, D., & Larson, K. (2001). Crustal displacements due to continental water loading. *Geophys. Res. Lett.*, 28, 651–654.
- van der Elst, N. J., Savage, H. M., Keranen, K. M., & Abers, G. A. (2013). Enhanced remote earthquake triggering at fluid-injection sites in the midwestern united states. *Science*, 341(6142), 164–167.
- Vergnolle, M., Walpersdorf, A., Kostoglodov, V., Tregoning, P., Santiago, J., Cotte, N., & Franco, S. (2010). Slow slip events in Mexico revised from the processing of 11 year GPS observations. *Journal of Geophysical Research*, 115(B8), B08403.
- Vidale, J. E., Agnew, D. C., Johnston, M. J., & Oppenheimer, D. H. (1998). Absence of earthquake

- correlation with earth tides: An indication of high preseismic fault stress rate. *Journal of Geophysical Research: Solid Earth* (1978–2012), 103(B10), 24567–24572.
- Wagner, C., McAdoo, D., Klokočník, J., & Kostelecký, J. (2006). Degradation of geopotential recovery from short repeat-cycle orbits: application to grace monthly fields. *Journal of Geodesy*, 80(2), 94–103.
- Wahr, J., Khan, S., Dam, T., Liu, L., Angelen, J. H., Broeke, M. R., & Meertens, C. M. (2013). The use of gps horizontals for loading studies, with applications to northern california and southeast greenland. *Journal of Geophysical Research: Solid Earth*, 118(4), 1795–1806.
- Wang, H.-S., Xiang, L.-W., Wu, P., Steffen, H., Jia, L., Jiang, L.-M., & Shen, Q. (2013). Effects of the tibetan plateau crustal structure on the inversion of water trend rates using simulated grace/gps data. *Terrestrial, Atmospheric and Oceanic Sciences*, 24(4I), 505–512.
- Weidner, D. J. & Li, L. (2010). Impact of phase transitions on p wave velocities. *Physics of the Earth and Planetary Interiors*, 180(3), 189–194.
- Wu, P. & Peltier, W. (1983). Glacial isostatic adjustment and the free air gravity anomaly as a constraint on deep mantle viscosity. *Geophysical Journal International*, 74(2), 377–449.
- Wu, X., Argus, D. F., Heflin, M. B., Ivins, E. R., & Webb, F. H. (2002). Site distribution and aliasing effects in the inversion for load coefficients and geocenter motion from gps data. *Geophysical research letters*, 29(24), 63–1.
- Wu, X., Ray, J., & van Dam, T. (2012). Geocenter motion and its geodetic and geophysical implications. *Journal of Geodynamics*, 58, 44–61.
- Yuan, L., Chao, B. F., Ding, X., & Zhong, P. (2013). The tidal displacement field at earth's surface determined using global gps observations. *Journal of Geophysical Research: Solid Earth*, 118(5), 2618–2632.
- Zhao, W., Mechie, J., Brown, L., Guo, J., Haines, S., Hearn, T., Klemperer, S., Ma, Y., Meissner, R., Nelson, K., et al. (2001). Crustal structure of central tibet as derived from project indepth wide-angle seismic data. *Geophysical Journal International*, 145(2), 486–498.

## **Bibliography**

---

Zhao, W.-L. & Morgan, W. J. (1987). Injection of indian crust into tibetan lower crust: A two-dimensional finite element model study. *Tectonics*, 6(4), 489–504.